Comprehensive population synthesis predictions for massive binary stars in the Small Magellanic Cloud

Dissertation
zur
Erlangung des Doktorgrades (Dr. rer. nat.)
der
Mathematisch-Naturwissenschaftlichen Fakultät
der
Rheinischen Friedrich-Wilhelms-Universität Bonn

von
Xiao-Tian Xu
aus
Beijing, China

Bonn 2024

Angefertigt mit Genehmigung der Mathematisch-Naturwissenschaftlichen Fakultät der Rheinischen Friedrich-Wilhelms-Universität Bonn

1. Gutachter:	Prof. Dr. Norbert Langer
2. Gutachterin:	Prof. Dr. Frank Bertoldi
Tag der Promotion:	18.01.2024
Erscheinungsjahr:	2024

Abstract

The past and ongoing gravitational wave detections have fostered a wide interest in understanding the formation of binary black holes (BBHs). Several formation scenarios have been proposed, including the evolution of isolated massive binaries. While most of the observed merging black holes are at cosmological distances, and thus likely at low metallicity, the Small Magellanic Cloud (SMC) — one of the satellite galaxies of the Milky Way — provides a unique laboratory to probe the binary scenario thanks to its rich massive star population and low metallicity. In this thesis, we provide comprehensive synthetic SMC populations of massive binary stars throughout all their different evolutionary stages, based on a dense grid of more than 50,000 detailed binary evolution models.

As stars expand when they age, mass transfer occurs in most of our models. This leads to a spin-up of the mass gainers to produce rapidly rotating so called Be/Oe emission line stars, which are abundant in the SMC. The mass donors, if massive enough, may form so called Wolf-Rayet (WR) stars, which are hydrogen deficient and have emission line dominated spectra. Our models predict 7 so called WR + main sequence star (MS) binaries in the SMC, which roughly matches the observed number, even though our models produce more long-period WR binaries than observed. At the same time, our synthetic population contains $\sim$ 200 BH+MS binaries, mostly associated with Be/Oe stars, which are so far undetected. We show that this is not in contradiction to the small number of wind-accreting BH+MS binaries observed through their X-ray emission. We also predict a neutron star (NS) +MS population, for which our models reproduce the orbital period distribution of the observed rich Be/X-ray binary population, but not their number. On the other hand, we predict a so far undiscovered group of X-ray quiet NS binaries with orbital periods below 10 days.

We then use semi-analytic methods to investigate which of our BH+MS binaries can evolve into a BH+WR system, which of those evolve further into a BBH, and which of those can merge within the Hubble time. Our results predict a high BH companion fraction for WR stars, and 2-3 BH+WR binaries in the SMC. Our prediction on merging BBHs is sensitive to several model assumptions. The main features of the observed merging BBH population can be reproduced by our model, with common envelope evolution and stable mass transfer evolution contributing about equally.

In conclusion, while our model in part agrees with the observed populations, it also raises new questions. In particular, there is an apparent lack of long-period massive evolved binaries with WR or BH components. As those are harder to detect than the shorter period counterparts, we hope that future observing campaigns will have the power to resolve this issue.

Contents

CHAPTER 1

Introduction

"上知天文, 下知地理"

"know the astronomy above, and know the geography below"

– An ancient Chinese proverb

1.1 From ancient China to gravitational waves

The word astronomy in Chinese is 天文. Here the character 天 has the meanings of sky, Universe, and heaven. While the character 文 nowadays usually means article or literature, in ancient times it had the meaning of principle. Like the meaning of 天文 (heaven's principle), ancient Chinese astronomers believed that what they observed is the palace of God and constellations are the officials in heaven (in Chinese 星官 , where 星 is star and 官 is official). It was believed that the changes in the Universe should suggest what will happen on the ground. Hence, to better rule the country, ancient Chinese emperors hired astronomers to observe the Universe.

Guest stars are great examples to illustrate the function of astronomy in ancient China. Figure 1.1 shows a government report in AD 1054. The author wrote that a star suddenly appeared last year and is still shining until now. In this report the star is called the evil star (in Chinese 妖星), which was seen as a sign of disasters. The author was suggesting the emperor to be prepared for upcoming turmoil. After about 21 months this star finally faded away (Green and Stephenson, 2003), which is known as a guest star afterwards.

In modern astronomy, we know that this guest star is actually a catastrophic explosion of a dying massive star, called supernova. During this explosion, the envelope of the star was ejected and left an extremely compact object made mostly of neutrons (neutron star), which has a size similar to Bonn but is as heavy as the Sun. The ejected material formed the Crab Nebula. After one thousand years, we are able to reveal the details of the remnant of this supernova event. Figure 1.2 shows the multi-wavelength

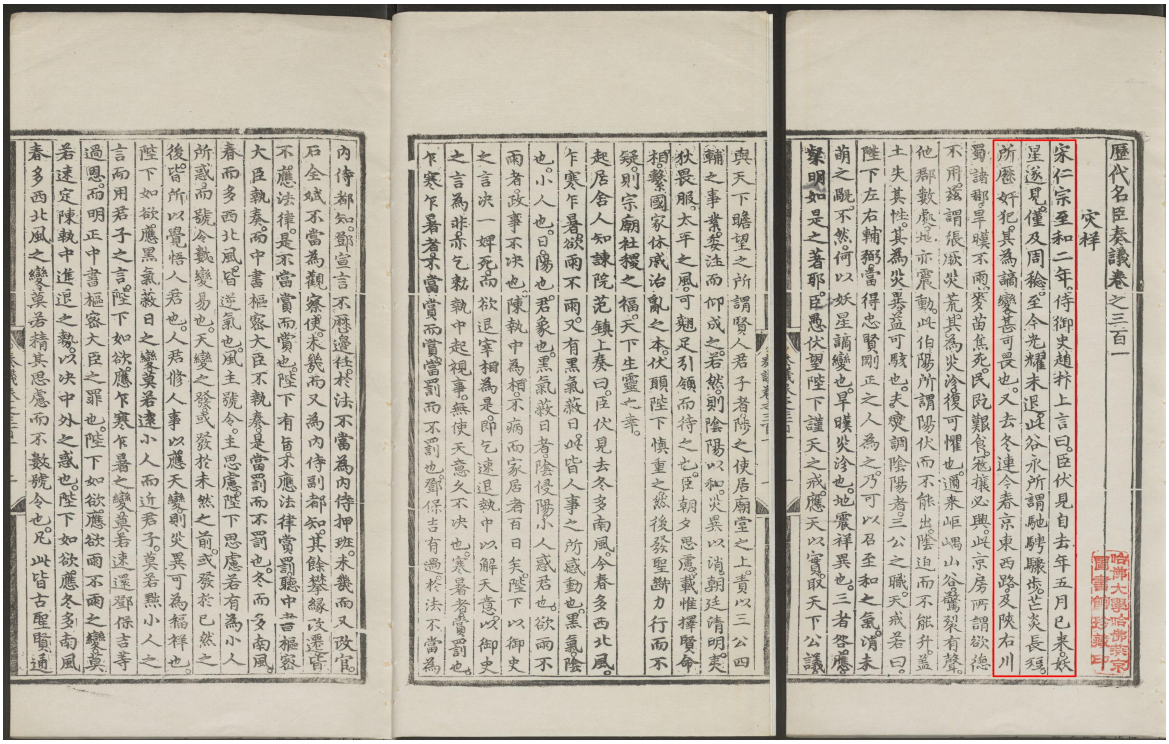

Figure 1.1: Scanned copy of 历代名臣奏议：三百五十卷 provided by Harvard College Library Harvard-Yenching Library (https://iiif.lib.harvard.edu/manifests/view/drs:428463547$4i), where highlighted text describes the observation of an evil star. This suddenly appearing star is seen as s sight of upcoming disasters, which is known as a guest star afterwards.

observations of the Crab Nebula, which contain the results from three space telescopes, Chandra, Hubble, and Spitzer. Zooming into the center of the Crab Nebula, we can see a disc-like structure, which is related to the central fast-rotating neutron star. While ancient astronomers could only observe the Universe with human eyes, their records are still valuable for modern astronomy. For example, the record of the guest star gives us one of the most accurate measurements of the age of a celestial object, which firmly proves the magnetic dipole model for neutron stars (section 10.5 in Shapiro and Teukolsky, 1986).

Nowadays, besides electromagnetic waves, gravitational waves open a new window for us. As a consequence of General Relativity, the existence of gravitational waves was predicted by Einstein more than one hundred years ago. In the 50s and 60s, physicists realized that a binary star could become a gravitational-wave emitter. At the same time, the fundamental ideas of the gravitational wave detector appeared, which led to the birth of the Laser Interferometer Gravitational-Wave Observatory (LIGO) (Saulson, 2011). Interestingly, binary black holes were not mentioned at that time, which are currently the main contributors to the observed gravitational wave events. In 1975, Hulse and Taylor (1975) reported the discovery of a binary neutron star, whose orbital evolution perfectly matches the prediction by General Relativity. This indirect demonstration of the existence of gravitational waves further motivated scientists to directly detect gravitational waves. On September 14th 2015, the first direct detection of gravitational wave was achieved by the LIGO and Virgo Collaboration

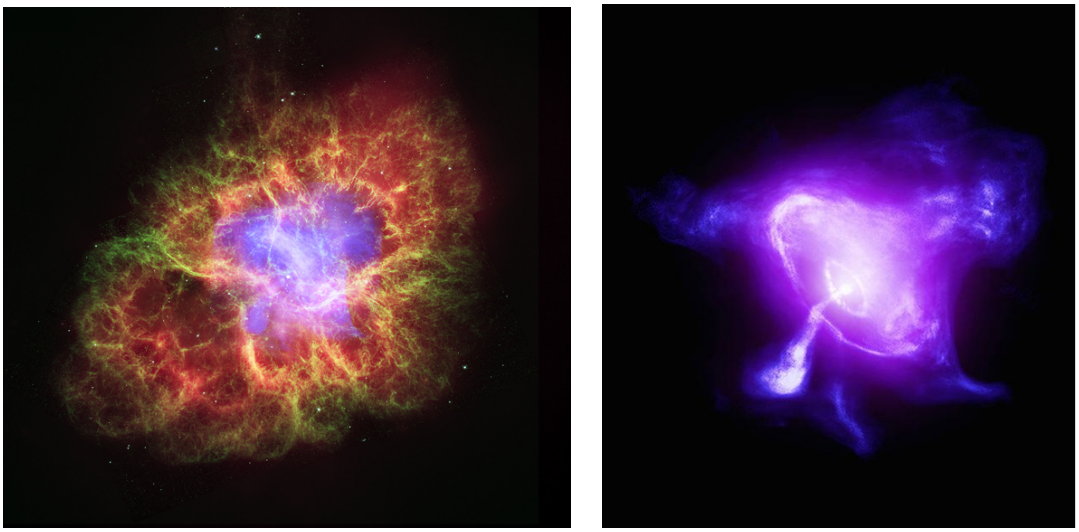

Figure 1.2: Left panel: multiwavelength observation of the Crab Nebula. Credit: (1) X-ray: NASA/CXC/ASU/J.Hester et al., (2) Optical: NASA/ESA/ASU/J.Hester & A.Loll, (3) Infrared: NASA/JPL-Caltech/Univ. Minn./R.Gehrz. Right panel: X-ray observation of the pulsar wind nebula inside the Crab Nebula. Credit: X-ray (IXPE: NASA), (Chandra: NASA/CXC/SAO), Image processing: NASA/CXC/SAO/K. Arcand & L. Frattare.

(B. P. Abbott, R. Abbott, T. D. Abbott, Abernathy et al., 2016), which came from the merger of a binary black hole. Up to now, more than one hundred gravitational wave events were reported (see Fig. 1.3 for a chart of the detections from observational runs O1, O2, and O3). Besides the mergers of binary black holes, the mergers of neutron star or black hole + neutron star systems were also detected. Especially, the electromagnetic counterpart of the merger of a binary neutron star (GW170817) were identified, which provides a direct demonstration for our understanding of short gamma-ray bursts (B. P. Abbott, R. Abbott, T. D. Abbott, Acernese et al., 2017).

Black hole is the most mysterious object in the Universe and the detection of binary black holes has fostered a wide interest in understanding the formation of such objects in the astrophysics community (Mapelli, 2020). One route is that black holes are formed from single massive stars, and then two black holes form a binary system through dynamical interaction. The other route is that binary black holes are products of the interaction in isolated massive binary stars, based on the fact that most of massive stars are born in binaries (Sana et al., 2012). What we have observed is likely a mixture of these two routes but each route's contribution is still under debate. This thesis focuses on the route involving binary interaction. Before talking about binary stars, firstly we need to understand single stars.

1.2 Single stars

1.2.1 Our Sun and stellar equilibrium

The Sun is the closest star to us, which is an excellent laboratory for us to study the physics of stars. Figure 1.4 presents a detailed observation of the Sun. Our Sun is a hot gas ball made of ionised plasma. The reason that it has the shape of a ball is that stars are gravitationally self-bound and the

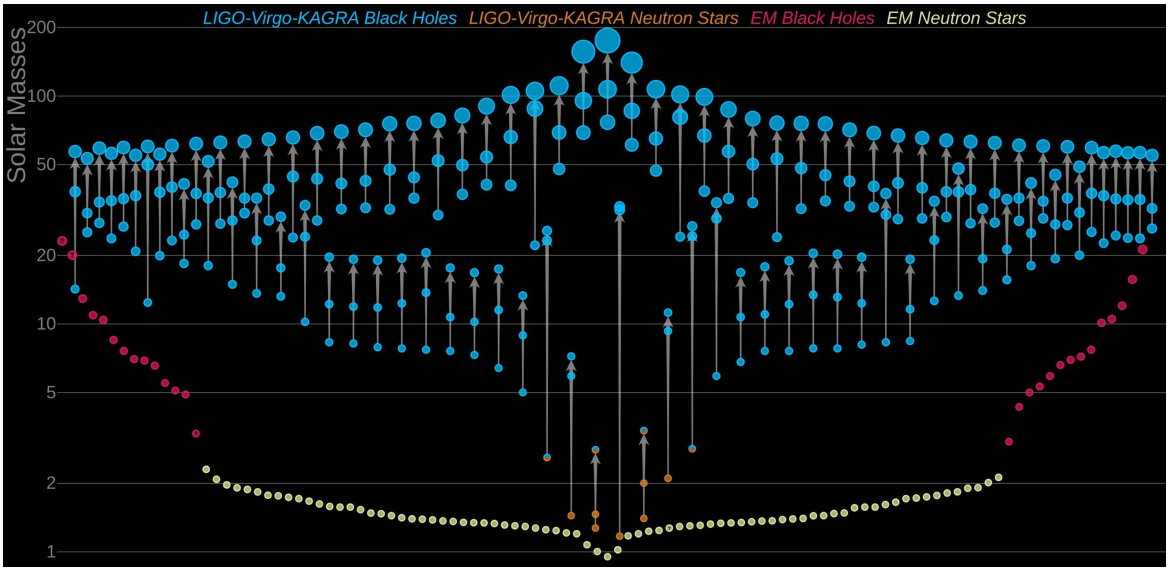

Figure 1.3: Masses of announced gravitational-wave detections since 2015, where blue and orange circles correspond to black holes and neutron stars. The pre-merger binary components and merger product are related through a grey arrow, pointing towards the merger products. The red and light yellow circles show the masses of the black holes and neutron stars constrained through electromagnetic observations. Credit: LIGO-Virgo / Aaron Geller / Northwestern University. Source: https://www.ligo.caltech.edu/image/ligo20211107a .

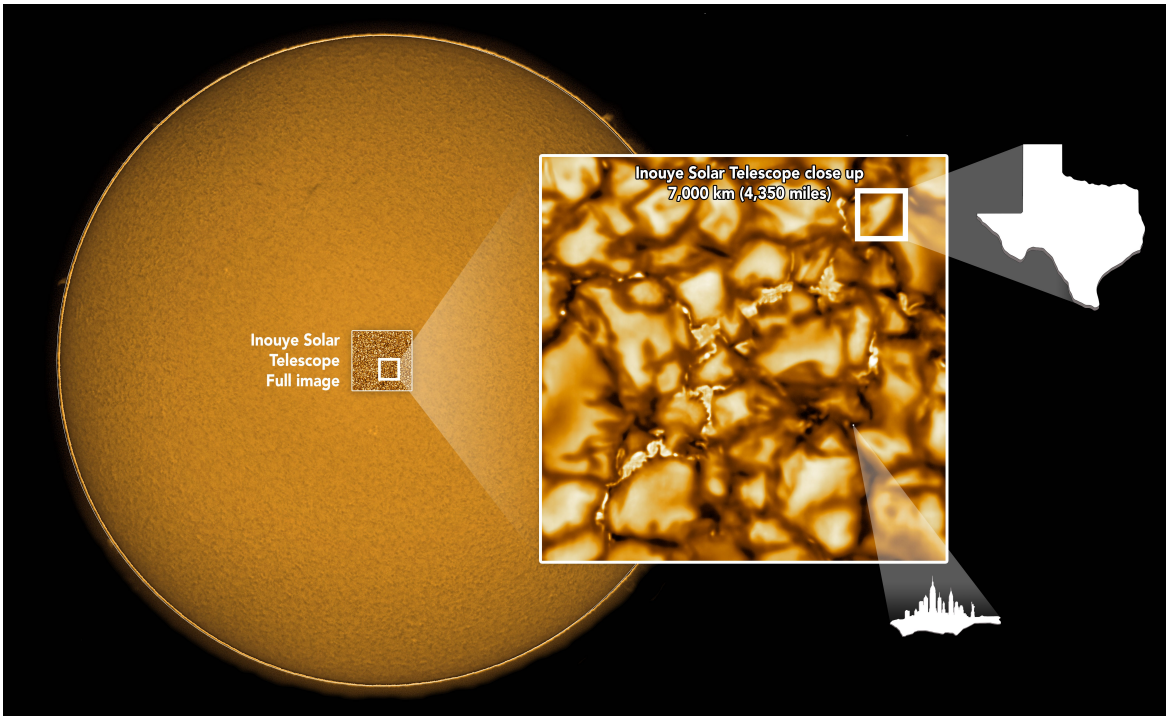

Figure 1.4: Sun observed by the NSF's Inouye Solar Telescope, where the cell-like structures are hundreds of kilometers across. Credit: NSO/AURA/NSF.

gravity of a point mass only depends on the distance to this point mass. While rotation can distort the shape of stars through centrifugal force, the rotational period of the Sun is about 27 days, which is too slow to change the shape of the Sun. Also due to gravity, stars always tend to contract. We have not observed any significant contraction of the Sun because its own weight is supported by the internal pressure gradient. This balance between gravity and pressure gradient is defined as hydrostatic equilibrium. This equilibrium can be violated. For the Sun, once hydrostatic equilibrium is violated, it will be rapidly restored within an hour, which causes small-scale oscillation on the solar surface. This timescale is defined as the dynamical timescale, which is about the time of an object at the surface freely falling to the center. If hydrostatic equilibrium can not be restored, a supernova may take place.

In Chinese, stars are called 恒星, where 恒 means constant or forever. The lifetime of stars is too long for human lives to observe the changes of stars. Several energy sources were proposed to understand this long lifetime and their high luminosity, like chemical reaction and gravitational contraction. However both of them predict a solar lifetime shorter than the age of the Earth. Therefore a much more efficient energy generation mechanism, nuclear reaction, is needed. The energy generated by a nuclear reaction is calculated by the Einstein mass-energy relation $E = \Delta M c^2$, where c is the speed of light, and ΔM is the mass difference between fuel and products. Nuclear reaction was not considered in the first place because one needs to overcome a strong Coulomb barrier to get two protons close enough to trigger nuclear reaction. This requires the input energy to be much higher than the output energy. With the development of quantum mechanics, people realized that nuclear reaction actually occurs at a much lower temperature than the previous estimation because of the quantum tunneling, which makes it a perfect energy source for stars. The time it takes to deplete nuclear fuel is defined as the nuclear timescale. The Sun is currently burning hydrogen and the corresponding product is helium. The nuclear timescale of Sun-like stars is about 10^{10} years, which is comparable with the age of the Universe ($\simeq 1.4 \times 10^{10}$ years). Nuclear reaction becomes more intense for stars more massive than the Sun. While they have more fuel to burn, the enhanced nuclear reaction makes their lifetimes shorter than the Sun.

To keep a steady internal structure, the energy generated in the center should be equal to the energy released at the surface. This condition is defined as the thermal equilibrium. Once the core runs out of hydrogen fuel, it will evolve on the thermal timescale, which is the time of a star to lose its internal energy through radiation. For the Sun, its thermal timescale is about 10^7 years. Inside stars, there are two ways to transfer energy from the core to the surface, radiation and convection. Radiation is the most direct way to transfer energy. However, stellar material is very hot and dense, making it opaque to photons. It takes about 10^7 years for a photon to slowly walk from the core to the surface. On the other hand, since photons are trapped by stellar material, the bulk motion of the material can also carry energy to the surface, i.e., convection. Convection occurs because heated material tends to move upwards due to buoyancy, while cool material tends to move inwards.

1.2.2 Convection and mixing process

Whether energy transport is dominated by radiation or convection can be determined by the Schwarzschild's criterion. Considering a heated gas blob, its higher temperature makes it expands to achieve pressure balance with its environment, which reduces the density of this gas blob. Then buoyancy force makes it move upwards. During this process, the pressure and the density of the environment decrease, and accordingly this gas blob keeps expanding to achieve pressure balance. If the density of this blob decreases faster than that of the environment, this blob will keep moving upwards, i.e. convection

takes place. Convection prefers to occur with high energy generation rate or high opacity because, in these cases, a gas blob will be heated up efficiently. The efficiency of energy transfer depends on the distance a gas blob can travel upwards, which is modelled by the so-called mixing length theory (Böhm-Vitense, 1958). Variation in composition can also play a role in triggering convection. A layer with higher mean molecular weight is harder to penetrate, which can help stabilize the up-floating blob. The criterion further considering the effect of the mean molecular weight gradient is called Ledoux's criterion. In the case of the Sun, it has a radiative core and a convective envelope. The convective envelope extends to its surface, and up-floating gas blobs form the granule structure on the solar surface (see Fig. 1.4). For more massive stars, the core becomes convective, and the envelope becomes radiative due to the increasing energy generation rate in the core. In addition, a gas blob can keep moving upwards due to its inertia when crossing the boundary of the convection zone determined by the Ledoux's criterion. This process is known as convective overshooting, which enlarges the convective zone.

Convection can not only transfer energy but also help mix the material inside stars. During this mixing process, for massive stars the fuel for nuclear reaction gets replenished, and for Sun-like stars the nuclear-reaction processed material can be transferred to the surface. After the depletion of core hydrogen fuel, a strong chemical gradient builds up. As a consequence, a region is stable according to the Ledoux's criterion but unstable due to the Schwarzschild's criterion appears (Kato, 1966; Langer, K. J. Fricke and Sugimoto, 1983). In this region a gas blob can not keep moving upwards due to insufficient buoyancy, while it is hotter than its environment, which makes it lose energy, becomes denser, and sink faster. This process is known as semiconvection and plays essential roles in the mixing process.

Besides convection, rotation also plays an important role in the mixing process (see Heger and Langer, 2000, for a detailed description). Rotation-induced mixing can occur through two types of hydrodynamic instabilities, which are

- Kelvin–Helmholtz instability: this instability is also known as shearing instability, which takes place when two fluid layers move at different velocities. This process leads to a wave-like structure at the boundary between these two layers, which is common in a planet's atmosphere (see Fig. 1.5 for an example). Stars are made of highly ionised plasma, the shearing motion of which can produce strong magnetic field. This process is known as the Spruit–Taylor dynamo (Spruit, 2002). The internal magnetic field can force star to rotate rigidly, which prevents the occurrence of Kelvin-Helmholtz instability.

- Rayleigh–Taylor instability: this instability happens when a heavy fluid pushing on a light fluid, like water above oil. Due to the difference in density, the heavy fluid tends to penetrate the light fluid, forming a finger-like structure. For example, the structure of the Crab Nebula is formed by the interaction between fast-expending wind and ejected material from the past supernova event (Fig. 1.2). This instability can occur inside a rotating star because the inner dense material tends to move outwards due to the centrifugal force. Due to the inward gravity, the radial density gradient has a stabilising effect against this instability. Meanwhile, the outwards displaced fluid element can induce heat diffusion, which counterbalances the stabilising effect of the radial density gradient. This condition is known as the Goldreich-Schubert-Fricke criterion (Goldreich and Schubert, 1967; K. Fricke, 1968).

In addition, rotation can lead to a large-scale circulation, which is known as the Eddington-Sweet

Figure 1.5: A cloud formed through the Kelvin-Helmholtz instability. This photo is picked from BBC news (https://www.bbc.com/news/world-us-canada-63912257).

circulation (Eddington, 1929; Sweet, 1950). The appearance of stars is shaped by gravity, which reflects the surface of equipotential. For non-rotating stars, temperature keeps constant on the surface of equipotential. However, for rotating stars, the surface of equipotential is distorted by centrifugal force, and consequently the polar region is hotter than the equatorial region, which forces the occurrence of the large-scale circulation.

1.2.3 Example of single star evolution

In astronomy, the most commonly used tool to study stars is the Hertzsprung–Russell diagram. Figure 1.6 gives an example of the Hertzsprung–Russell diagram, where the x-axis is surface temperature, and the y-axis is luminosity. Different features on the Hertzsprung–Russell diagram are associated with different evolutionary stages. The hydrogen burning phase is the most long-lived stage, which forms the so-called main sequence extending diagonally on the Hertzsprung–Russell diagram. Once the stellar core runs out of its hydrogen, the nuclear reaction eases, and internal pressure can not support the weight anymore, which pushes the star to evolve towards the giant branch. To illustrate how a star evolves, we provide the evolutionary track of a 31.6 $M_{\odot}$ star (Fig. 1.7), which is computed with a metallicity designed for the Small Magellanic Cloud (Brott et al., 2011).

At point A, the stellar core becomes hot enough to ignite hydrogen burning, which marks the beginning of the main-sequence phase. The ignition of nuclear reaction makes the core convective and the envelope radiative. Here the size of the convective core determines how much fuel can be used for nuclear reaction. With the consumption of nuclear fuel, the core gradually contracts, which further enhances nuclear reaction. This increasing in energy generation pushes the envelope to expand and cool down. The lifetime of the main-sequence phase is related to the overshooting process, which

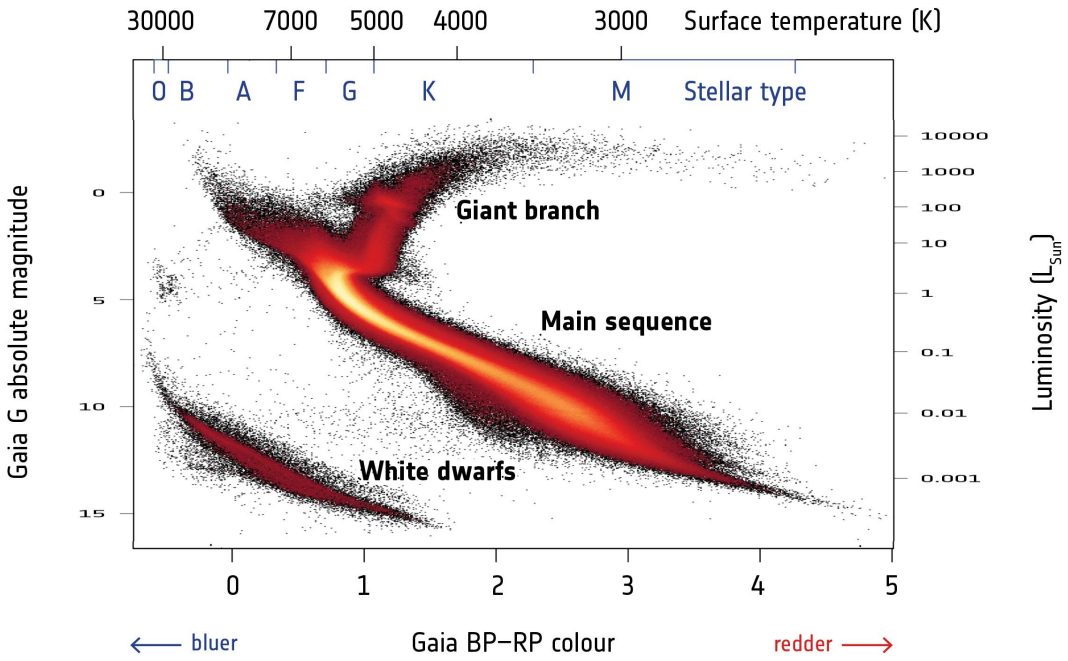

Figure 1.6: Hertzsprung-Russell diagram of the low-extinction stars from Gaia's second data release (Gaia Collaboration et al., 2018), where low extinction is defined by $E(B-V) < 0.015$ mag. There are over four million stars plotted.

changes the size of the convective core and how much fuel can be used for hydrogen burning. The strength of overshooting can be constrained by the observed width of the main sequence (Brott et al., 2011).

After 6.2 million years, the convective core depletes hydrogen and reaches point B. In response to the termination of the central nuclear reaction, the star contracts until igniting the hydrogen shell above the hydrogen-depleted core, and then it evolves through the Hertzsprung gap (the region between point B and point C). During this phase, the hydrogen-depleted core contracts and heats up the burning shell. In turn, the burning shell pushes the outer envelope to expand, and the nuclear-reaction-processed material helps the core grow in mass. Above the burning shell, semiconvection takes place due to the building up of a strong chemical gradient. This can largely alter the post-main-sequence evolution by changing the energy generation rate of the burning shell (Schwarzschild and Härm, 1958; Chiosi and Summa, 1970; Langer, El Eid and K. J. Fricke, 1985). Efficient semiconvection makes stars expand less and ignite central helium at a small radius, forming blue supergiants. In our model, a moderate semiconvection is assumed with an efficiency parameter $\alpha_{\rm SC} = 1$. The ratio of blue and red supergiants in the Small Magellanic Cloud suggests that semiconvection might be very efficient ($\alpha_{\rm SC} > 10$ by Schootemeijer, Langer, Grin et al., 2019).

The stellar envelope cools down with its expansion. At point C, this star appears as a red supergiant, and its envelope is cool enough to become convective. One key feature of a convective envelope is that it keeps expanding in response to mass loss, which means that mass transfer becomes unstable if the donor star fills its Roche lobe during this phase (see section 1.3.2). The convective region can reach down to the core and bring the ash of nuclear reaction to the surface, which is known as the

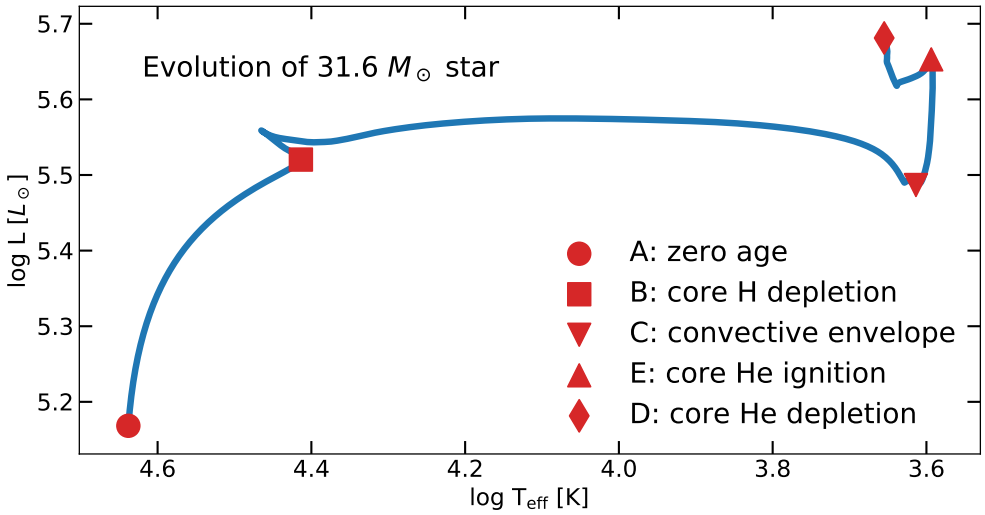

Figure 1.7: Evolution of a non-rotating 31.6 $M_\odot$ star with the Small Magellanic Cloud metallicity. This model is computed from core hydrogen ignition until core helium depletion.

dredge-up process. Meanwhile, the nuclear ash of the burning shell falls into the hydrogen-depleted core, supporting it keeps growing.

At point E, the stellar core becomes massive enough to ignite central helium, which burns more intensely than hydrogen burning. The ignition of central helium helps the star restore its thermal equilibrium. It takes about 10% of the nuclear timescale of hydrogen burning to deplete core helium (point D). After core helium depletion, the star rapidly goes through a series of advanced nuclear burning stages, which finally produces an onion-like structure. The innermost core is made of iron, and the layers above are the ashes of different nuclear burning stages. Once an iron core is formed, there is no way for a star to support its own weight anymore. The hydrogen-depleted core collapses and forms a black hole. It is very unclear how much material can be ejected during this process and whether there is a momentum kick on the newborn black hole.

1.3 Binary stars

1.3.1 Roche lobe and stable mass transfer

A binary system is made of two stars bound by gravity and orbiting each other. While our understandings about stars are built upon isolated stars, most of massive stars are living in binary systems (Sana et al., 2012), where binary interaction has tremendous impacts on stellar evolution, supernova explosion, and the formation of compact objects (see Langer, 2012, for a detailed review).

Whether binary interaction can take place or not is determined by gravity. Considering a test particle moving in the binary system, which receives the gravity from two stars and a centrifugal force caused by the orbital motion. The corresponding potential is called the Roche potential. The left panel of Fig. 1.8 presents the section at the orbital plane of the Roche potential of a binary with a mass ratio of 0.25. There are five points where the net force acting on the test particle is zero, which are

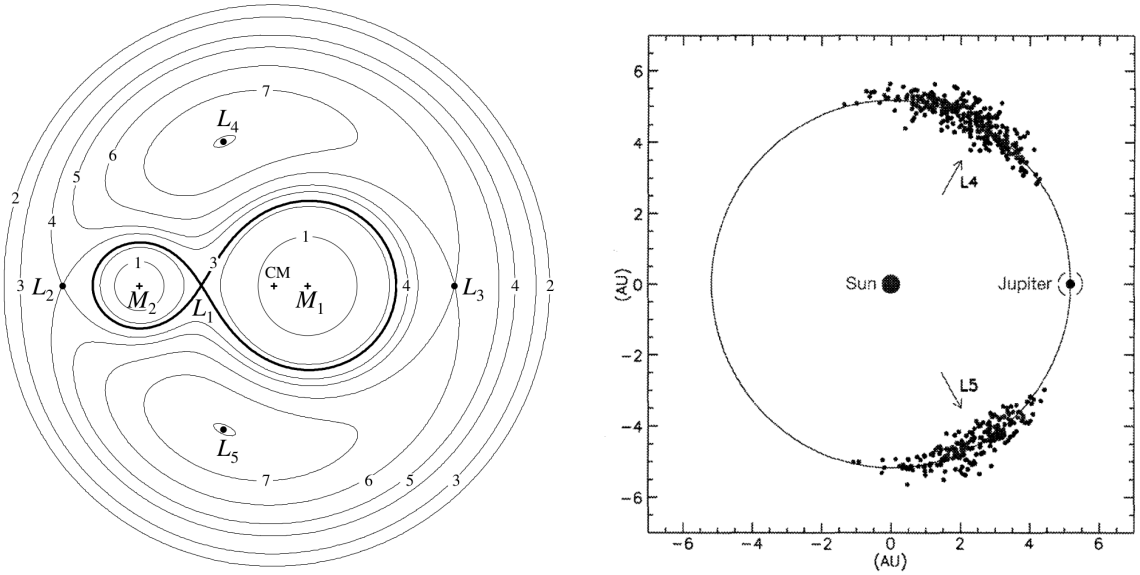

Figure 1.8: Left panel: the section at the orbital plane of the Roche potential of a binary with a mass ratio of 0.25, where L_{1-5} are the Lagrangian points, CM is the center of mass, and $M_{1\text{ or }2}$ is the mass of the binary component. This figure is picked from Frank, King and Raine (2002a). Right panel: observed asteroids that captured by the L_4 and L_5 points of the Sun-Jupiter system Jewitt, Sheppard and Porco (2004).

known as the Lagrangian points, labelled by L_1, L_2, L_3, L_4, and L_5. The L_4 and L_5 points are usually stable, which has been proved by asteroid observation in the solar system. The right panel of figure 1.8 shows the observed asteroids sharing the same orbit as Jupiter, which are captured by the L_4 and L_5 points of the Sun-Jupiter system. The asteroids captured by the L_4 and L_5 points are also known as the Trojan objects. The L_1, L_2, and L_3 points are always unstable, which means that material can easily flow through these positions. Specifically the equipotential surface crossing the L_1 point is called the Roche lobe, below which material is bound to the star by gravity. Once a star reaches its Roche lobe, its envelope material flows towards the other star through the L_1 point. As shown by Fig. 1.8, the Roche lobe has a non-spherical shape, which can hardly be included in current binary evolution codes. To describe the size of the Roche lobe, Eggleton (1983) proposed an equieffective radius, which is the radius of a sphere that has the same volume as the Roche lobe, and mass transfer starts once the stellar radius reaches this equieffective radius, which is most commonly adopted assumption in modern binary evolution computations (e.g., Hurley, Tout and Pols, 2002; Belczynski, Kalogera et al., 2008; Shao and X.-D. Li, 2014; Paxton, Marchant et al., 2015).

The Roche lobe filling can be achieved by two processes, stellar expansion and orbital shrinkage. The latter one can happen because binary systems keep losing their orbital angular momentum during their lifetimes. There are three mechanisms responsible for this angular momentum loss, which are

- Gravitational-wave radiation: As a consequence of General Relativity, binary stars keep generating gravitational wave, which carries away orbital energy and causes orbital shrinkage. This process has already been observationally demonstrated by the Hulse-Taylor pulsar system (Fig. 2 in Weisberg, Nice and Taylor, 2010).

- Wind mass loss: during stellar evolution, stars lose their material through wind, which carries

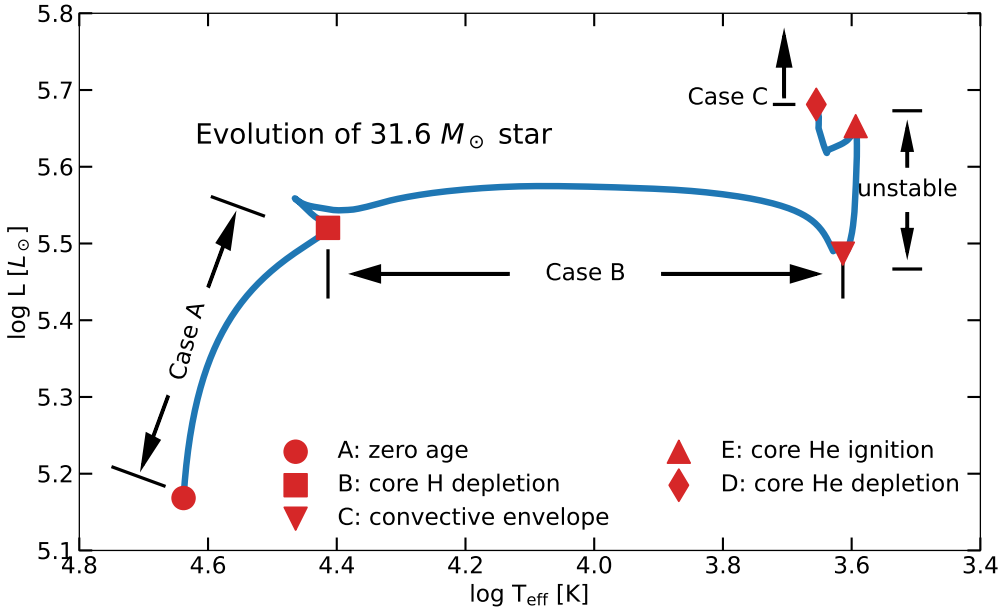

Figure 1.9: Locations of stable mass transfer (Case A, Case B, and Case C) and unstable mass transfer caused by convective envelope on the Hertzsprung–Russell diagram if taking a 31.6$M_\odot$ star from the Small Magellanic Cloud as a mass donor.

away rotational and specific orbital angular momentum. For core-hydrogen-burning stars, the loss of orbital angular momentum is too weak to considerably change the orbital separation (Fig. 10 in El Mellah, Bolte et al., 2020).

- Tidal interaction: tidal torque in binary systems has been studied since the 70s (Zahn, 1977; Hut, 1981) but is still poorly understood until now. A star in nature is not a point mass, and its companion's gravity can distort its surface. The gravity of the nonspherical-symmetric part of the distorted star makes it tends to rotate at the same period as the orbital motion. If a star rotates slower than the orbital motion, tidal torque spins it up by taking orbital angular momentum and vice versa. The state that the rotational period matches the orbital period is called tidal locking. For example, the Moon is tidally locked by the Earth such that on the Earth we can only see one side of the Moon. In tidally locked systems, the rotational angular momentum loss through stellar wind is compensated by tide. As a result, orbital angular momentum is indirectly extracted. For low-mass stars, their winds are magnetised and this process is known as magnetic braking (Verbunt and Zwaan, 1981; Rappaport, Verbunt and Joss, 1983).

Once Roche lobe is reached, material starts to overflow through the L_1 point. The effects of mass transfer on stellar evolution depends on the evolutionary stage of the mass donor at the moment of the Roche lobe filling, which leads to the following classification (Kippenhahn, Kohl and Weigert, 1967),

- Case A: Roche lobe overflow occurs with a hydrogen-burning mass donor. Since stars do not expand significantly during the main-sequence evolution, Case A mass transfer only takes place

in close binaries. The more massive star first fills its Roche lobe and triggers a fast Case A phase proceeding on the thermal timescale. After the reversal of mass ratio, a slow Case A phase follows, which is driven by stellar expansion and proceeds on the nuclear timescale.

- Case B: Roche lobe overflow occurs with a core hydrogen-depleted mass donor. After the core hydrogen depletion, stars evolve on the thermal timescale and expand significantly. Usually the entire hydrogen-rich envelope gets stripped during this process, exposing the helium core of the donor star.

- Case C: Roche lobe overflow occurs with a core helium-depleted mass donor. After core helium depletion, strong stellar expansion is resumed, filling the Roche lobe again. Compared with Case A and Case B, Case C is much rarer since stars evolve very fast after core helium depletion. In the low-metallicity environment, Case C mass transfer becomes more often since stars become more compact and can ignite core helium at an earlier stage (S. E. de Mink, Cantiello et al., 2008). Meanwhile, the ignition of core helium can help stars restore the thermal equilibrium, forming slowly-expanding core-helium-burning stars, which may lead to a new type of mass transfer (Klencki et al., 2020).

Mass transfer can redistribute the orbital angular momentum of a binary system by changing the masses of the two stars. Meanwhile, lots of material escapes from the binary carrying away orbital angular momentum. Here how much material can be accreted by the mass gainer is unclear. One way to determine the accretion efficiency is to consider the accretion-induced spin up. According to Packet (1981), stars can be easily spun up to critical rotation during mass transfer. It is fair to assume that a star can not gain more angular momentum once it reaches critical rotation. As a result, how much material can be accreted depends on the strength of tidal torque. In close binaries, critical rotation can be avoided with the help of strong tides, and hence a large amount of mass can be accreted, while almost all material is ejected in wide binaries. This orbital-period-dependent accretion efficiency is supported by the studies on massive close binaries (S. E. de Mink, Pols and Hilditch, 2007; Sen, Langer et al., 2022). However, the luminosity of the Be stars in Be X-ray binaries suggests that about half of the transferred material can be accreted in wide binaries (Shao and X.-D. Li, 2014; Vinciguerra et al., 2020; Schürmann, Langer, X.-T. Xu et al., 2023).

1.3.2 Common envelope evolution

Figure 1.9 presents the regions of stable mass transfer (Case A, Case B, and Case C) and unstable mass transfer caused by the convective envelope of the mass donor on the Hertzsprung–Russell diagram. If the mass transfer is unstable, the system is expected to enter the common envelope phase. The concept of common envelope evolution was first proposed by Paczynski, Ostrike, and Webbink (Paczynski, 1976) and nowadays is believed to be necessary for forming very close binaries (see Ivanova et al., 2013, for detailed review). The stability of mass transfer is determined by the responses of the donor star and its Roche lobe to mass variation. Considering a case that the donor star tends to expand but its Roche lobe tends to shrink in response to the mass loss caused by the Roche lobe overflow, the interplay between the stellar expansion and the Roche lobe shrinking further enhances the Roche lobe overflow, which in turn makes the donor star expands, and its Roche lobe shrinks even more. In this case, mass transfer is unstable. This condition was quantified by Soberman, Phinney and van den

Heuvel (1997), who showed that a common envelope evolution can happen with the mass donor much more massive than the mass gainer or the mass donor having a strongly convective envelope.

While the common envelope phase only lasts about 1000 years, a binary with orbital periods exceeding 1000 days can shrink to about 1 day after this phase. This strong orbital shrinkage makes the common envelope phase play a key role during binary evolution. Once mass transfer becomes unstable, mass transfer rate is so large that the mass gainer is engulfed by the envelope of the donor star. During this process, orbital energy is rapidly converted into thermal energy through the friction between the spiral-in mass gainer and the envelope material of the donor star. Consequently, the envelope is rapidly dissipated, and the orbit shrinks significantly. To survive the common envelope evolution, the mass gainer should be massive enough to expel the donor star's envelope, and the orbital separation should be large enough to avoid merger. If a merger is avoided, the mass donor loses its entire envelope, leaving a naked core, while the properties of the mass gainer keep unchanged. The outcome of a common envelope evolution can be estimated by considering the energy budget that the binding energy of the envelope should be equal to the difference in the orbital energy before and after interaction (Webbink, 1984), which is still the mostly adopted assumption in binary evolution modelling. This estimation sensitively depends on various factors like the efficiency of expelling envelope material, the determination of stellar core, and so on. The short lifetime of this phase makes it difficult to constrain observationally, casting large uncertainties on the outcomes of binary evolution simulations.

1.3.3 Example of binary star evolution

Figure 1.10 presents the evolution of a binary made of a 31.6 $M_\odot$ primary star and a 25.2 $M_\odot$ secondary star with a 100 days initial orbital period. Initial orbit period determines the beginning point of the Roche lobe overflow. For this binary, the primary star fills its Roche lobe during the Hertzsprung gap, which triggers a Case B mass transfer. The hydrogen-rich envelope is rapidly stripped, which meanwhile reduces the luminosity of the donor star. During this process, the mass gainer is rapidly spun up to critical rotation. Since a critically rotating star can not further accrete angular momentum, most of the transferred material is ejected out of the binary.

After mass transfer, the mass gainer keeps critically rotating until the end of its main-sequence phase. The secondary star is cooler than its single star counterpart because rotation reduces its surface gravity, which cools down the envelope. Due to the same reason, the envelope material can easily flow away at the equator, which forms a circumstellar decretion disc, producing Balmer line emission. This is known as the Be phenomenon (Rivinius, Carciofi and Martayan, 2013). While Be stars can also be formed through single star evolution (Hastings, Wang and Langer, 2020), the apparent lack of main-sequence companions for observed Be stars suggests that the majority of them are binary-interaction products (Bodensteiner, Shenar and Sana, 2020). For the donor star, it leaves a naked helium-rich core, which keeps contracting until the beginning of stable core helium burning. If the stripped star is massive enough, it appears as a Wolf-Rayet star due to its strong and optically thick wind. Wolf-Rayet stars can also be formed through self-stripping through stellar wind, which is much less efficient than the stripping through mass transfer (Shenar, Gilkis et al., 2020).

Due to the numerical limitations of our binary evolution code, the evolution of the primary star after its core helium depletion is not presented in Fig. 1.10. After this point, the stripped star is expected to form a black hole, while the secondary star is still burning hydrogen. If the orbit of this black hole + O star binary is close enough, the black hole can capture the wind material from the companion

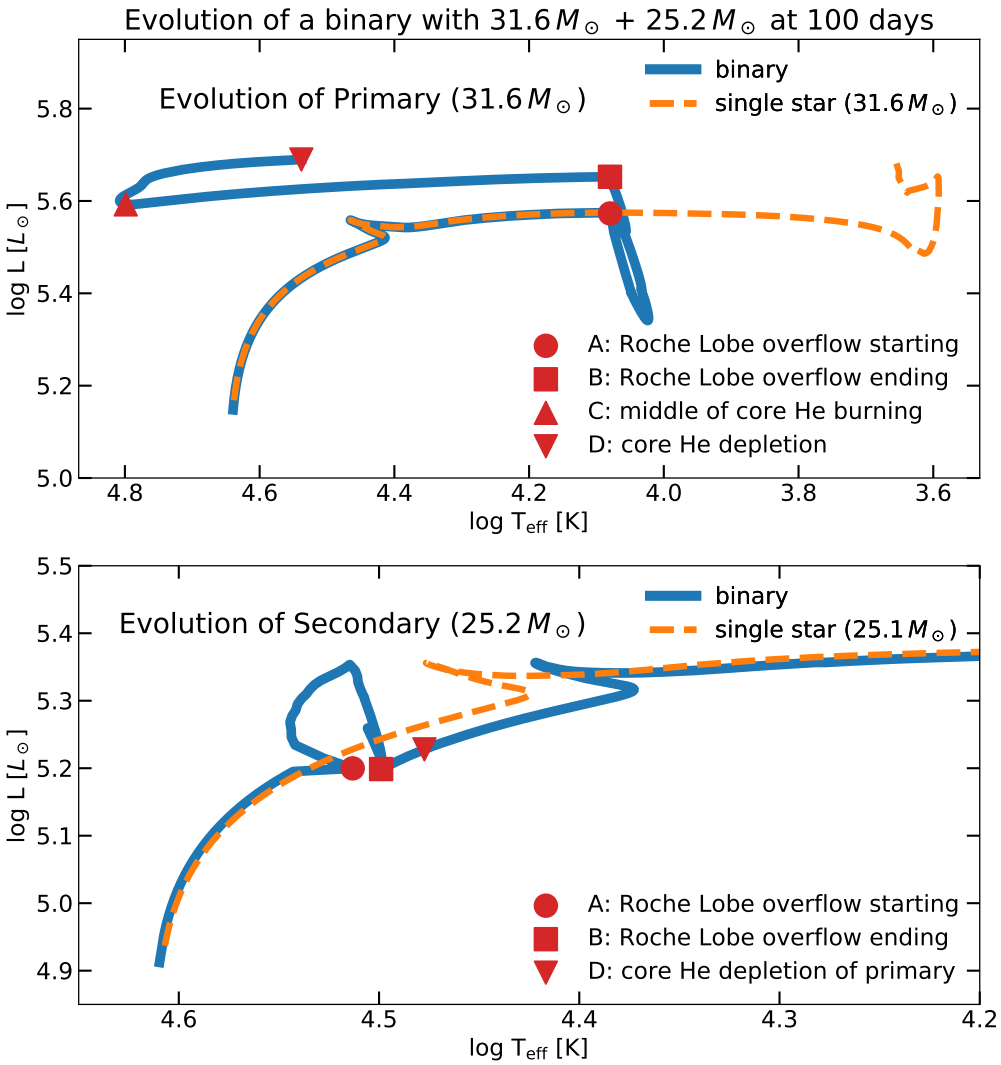

Figure 1.10: Evolution of a binary composed of a 31.6 $M_\odot$ primary star and a 25.2 $M_\odot$ secondary star with 100 days initial orbital period on the Hertzsprung-Russell diagram (upper panel for the primary star and lower panel for the secondary star). The blue solid lines are the tracks of binary evolution, and the yellow dashed lines are the evolution of the single star counterparts.

and produce strong X-ray emission (Iben and Tutukov, 1996; Vanbeveren et al., 2020; Sen, X.-T. Xu et al., 2021). The secondary star starts to expand once its core depletes hydrogen. Then its Roche lobe filling triggers the mass transfer onto the black hole, making the system become X-ray binaries. After that, a binary made of a black hole and a Wolf-Rayet star could be produced. With the end of the core helium burning of the secondary star, a binary made of two black holes is formed, which ends up with a merger.

1.4 The Small Magellanic Cloud as a laboratory for studying binary evolution

While the above picture of binary evolution is widely accepted, each step through the pathway to the final binary black hole merger should be treated carefully. Various factors like accretion efficiency, stability of mass transfer, and supernova kicks can significantly change the properties of the outcome binary black holes but all of them are still poorly constrained. The Small Magellanic Cloud provides a nice laboratory to improve our understanding of stars and binaries. It is one of our closest neighbours, whose distance is well known (about 62 kpc Graczyk et al., 2020). Its metallicity is relatively low, corresponding to the average metallicity at a redshift of ~ 5, which means stellar wind is weak, and we can focus on the effects of binary interaction. It is a star-forming galaxy so that there is a large population of massive stars, which allows us to test our model predictions.

- Be X-ray binaries: this object contains a neutron star and a Be star, the majority of which have eccentric orbits. During the periastron passage, the interaction between the neutron star and the Be disc produces strong X-ray emission. There are over 100 Be X-ray binaries detected in the Small Magellanic Cloud with orbital periods from several days to thousand days (Haberl and Sturm, 2016).

- Black hole + OB star binaries: while no black hole + OB star binary has been observed in the Small Magellanic Cloud yet, it is fair to believe that there is a large population of such binaries. Most of massive stars should have a companion (Sana et al., 2012), and about 800 massive stars have been found in the Small Magellanic Cloud (Schootemeijer, Langer, D. Lennon et al., 2021). We have already found plenty of neutron star + Be star binaries (Be X-ray binaries). Black hole progenitors are just more massive than neutron star progenitors. The no detection of black hole + OB star binaries could be caused by their dim X-ray emission (Casares et al., 2014).

- Wind-fed black hole X-ray binaries: black hole + OB star binaries can become strong X-ray emitters unless their orbits are close enough that wind material can be captured by the black hole and form an accretion disc (Vanbeveren et al., 2020; Sen, X.-T. Xu et al., 2021). There is no wind-fed black hole X-ray binaries detected in the Small Magellanic Cloud so far. This fact also put a constraint on our model predictions.

- Wolf-Rayet star + O star or black hole binaries: there are 12 Wolf-Rayet stars in the Small Magellanic Cloud, where 4 Wolf-Rayet star + O star binaries, 1 Wolf-Rayet star + Wolf-Rayet star binaries, and 7 apparently single Wolf-Rayet stars (see Schootemeijer and Langer, 2018, and references therein). The chance to observe an object should be proportional to its lifetime if the star formation rate is constant, and a Wolf-Rayet star + O star binary should have a similar

lifetime as a Wolf-Rayet star + black hole binary (van den Heuvel, Portegies Zwart and S. E. de Mink, 2017a). This means that some of these single Wolf-Rayet stars could actually have a black hole companion.

1.5 Population synthesis with detailed models

There are two ways to compare our model predictions with observations.

- Focusing on the properties of individual objects. One needs to perform detailed modelling for each observed object and adjust the input physics to fit the observed properties.
- Focusing on the properties of whole populations. One needs to compute plenty of models to simulate a population and compare with the observed population.

In this thesis, we adopt the latter way, which is known as population synthesis. The most adopted and direct approach to achieve this purpose is the Monte Carlo method. Knowing of the possibility distributions of initial parameters, one can generate a large sample of binaries and compute their evolutionary outcomes. Usually, at least 10^5 binaries are required to obtain a statistically meaningful population. However, it can take hours to compute only one detailed binary model. In order to save computational time, people use tabulated data and design fitting formulas to describe the evolutionary histories computed by detailed models, which allows people to compute the evolution of millions of binaries within several minutes.

The first well-built open-source rapid population synthesis tool is the BSE code by Hurley (Hurley, Pols and Tout, 2000; Hurley, Tout and Pols, 2002), which is based on the stellar models computed by Pols, Schröder et al. (1998). Nowadays, most of population synthesis codes are the updated versions of the BSE code (e.g. Izzard et al., 2006; Belczynski, Kalogera et al., 2008; Shao and X.-D. Li, 2014; Mapelli and Giacobbo, 2018). The authors of these BES-type codes usually adopt the stellar models used in the original version of the BSE code. Until recent years, rapid codes based on updated stellar models are published, e.g., ComBinE (Kruckow et al., 2018) and POSYDON (Fragos et al., 2023). While these rapid codes can help us to quickly compute a large population, they have many disadvantages. Firstly, due to the absence of detailed physics, these rapid codes can not provide information like surface abundance and can not accurately compute stellar rotation. Rapid codes usually assume that the hydrogen-rich envelope of donor stars is completely stripped during mass transfer. As a consequence, these codes can not handle Case A mass transfer properly. Detailed simulations have shown that the envelope of donor stars is partly stripped (Laplace, Götberg et al., 2020). In addition, some authors combine the model data computed by different detailed codes with the BSE code to build their population synthesis tools, which is not a self-consistent way and can cause potential uncertainties. One direct way to overcome the above disadvantages is to use detailed models. The BPASS code by Eldridge, Stanway et al. (2017) is based on several detailed single and binary star model grids computed by an updated version of the STARS code first developed by Eggleton (1971). However, several important physical processes are still missing in the STARS model, like semiconvection and rotational mixing. For binary evolution, the BPASS code only follows one star with detailed computation, while the other star is estimated by the fitting formulas in the BSE code.

In this thesis we perform population synthesis with the detailed binary evolution code MESA (Modules for Experiments in Stellar Astrophysics version 8845, Paxton, Bildsten et al., 2011; Paxton,

Cantiello et al., 2013; Paxton, Marchant et al., 2015), which includes detailed physics like convection, semiconvection, rotation, mixing, tide, and mass transfer. Our analysis relies on a dense detailed binary model grid computed by Wang, Langer et al. (2020) with a tailored metallicity for the Small Magellanic Cloud, which contains 53298 detailed binary models and took months to compute. The input parameter space is described in the following:

- Initial primary masses $M_{1,\mathrm{i}}$ from 5 $M_\odot$ to 100 $M_\odot$ with intervals of $\Delta \log(M_{1,\mathrm{i}}/\mathrm{M}_\odot) = 0.05$;
- Initial mass ratios q_i from 0.3 to 0.95 with an interval of $\Delta\, q_\mathrm{i} = 0.05$;
- Initial orbital periods $P_{\mathrm{orb,i}}$ from 1 day to 3162 days with intervals of $\Delta \log\,(P_{\mathrm{orb,i}}/\mathrm{day}) = 0.025$.

Instead of the Monte Carlo method, we evaluate each model by a statistic weight. For a binary model with initial primary mass $M_{1,\mathrm{i}}$, initial mass ratio q_i, and initial orbital period $P_{\mathrm{orb,i}}$, the predicted number N_{binary} is

$$N_{\mathrm{binary}} \propto f_{\mathrm{IMF}} \times f_{q_\mathrm{i}} \times f_{P_{\mathrm{orb,i}}} \times \mathrm{lifetime} \times \mathrm{SFR}, \tag{1.1}$$

where f_{IMF} is the initial mass function, f_{q_i} is the probability distribution function of initial mass ratios, $f_{P_{\mathrm{orb,i}}}$ is the probability distribution function of initial orbital periods, lifetime is the lifetime of an evolutionary stage, and SFR is the star formation rate. This approach allows us to populate binaries within an acceptable computational time, and the model grid is dense enough to produce statistically meaningful distributions. Due to the numerical limitations of the MESA code, our binary evolution is terminated at the core helium depletion of the primary star, and after that we keep evolving the secondary star as a single star. Additional assumptions are required to investigate the properties of black hole + OB star binaries, Wolf-Rayet star + black hole binaries, and binary black holes. We determine the types of the outcome compact objects by checking the final status of the stars. Since the properties of black hole + OB star or neutron star + OB star binaries remain unchanged most of time, we can take a snapshot of the systems at the moment of the compact object formation to represent the typical properties of the binaries.

Compared with rapid codes, the disadvantage of our method is that our analysis relies on the pre-computed massive MESA model grid. Using rapid codes, one can easily repeat a Monte Carlo simulation with different input physics. However, in our case, it is not wise to compute another model grid with slightly different input physics because it not only consumes lots of computation resources but also takes very large space to save the output model data. It would be nice if our prediction could well match observations but very unlikely. If it does not match, the discrepancy between observations and the model prediction can guide us to modify our models and improve our understanding of binary evolution.

1.6 This thesis

As discussed above, the binary pathway towards the gravitational-wave event involves Roche-lobe overflow, mass transfer, common envelope evolution, supernova, and BH formation, which plays crucial roles but are still poorly understood. The population synthesis method is a great tool to study binary evolution. Currently, most population synthesis studies in the market are performed with rapid binary evolution codes, which lose many important physical processes.

The primary aim of this thesis is to provide a comprehensive population synthesis calculation covering all the evolutionary stages of massive binary stars from the pre-interaction phase until the

formation of a binary black hole by using the detailed dense binary model grid mentioned in Sect. 1.5. We compare our model prediction with the observed rich massive star population in the Small Magellanic Cloud to gain a better understanding of the binary evolution at low metallicity and of the role of isolated binaries in producing gravitational-wave events (Chapters 2 and 3).

While the Small Magellanic Cloud has a rich massive star population, no black hole high-mass X-ray binary has been confirmed yet. There are three dynamically confirmed black hole + O star X-ray binaries in the local Universe, Cygnus X-1 (Orosz, McClintock, Aufdenberg et al., 2011), LMC X-1 (Orosz, Steeghs et al., 2009), and M33 X-7 (Orosz, McClintock, Narayan et al., 2007; Ramachandran et al., 2022), one of which is in the Milky Way. It was recently proposed that strong momentum kicks are required to understand the dearth of such binaries, while our fiducial population synthesis model does not include kicks for newborn black holes. It is also possible that only a small fraction of black hole + O star binaries are able to produce observable X-ray. We revisit the formation of wind-fed black hole high-mass X-ray binaries with an emphasis on the condition of producing strong X-ray emission in Chapter 4.

1.6.1 Populations of evolved massive binary stars in the Small Magellanic Cloud I: Predictions from detailed binary evolution models

In Chapter 2, we provide population synthesis predictions for OB star + Wolf-Rayet (WR) star binaries, OB star + neutron star (NS) binaries, and OB star + black hole (BH) binaries. We adopt the supernova window computed by the ComBinE code (Kruckow et al., 2018; Schürmann, Langer, X.-T. Xu et al., 2023) since the resolution of our model grid is not good enough to distinguish different types of supernovae. Our fiducial population synthesis model predicts 7 OB+WR binaries, 25 OB+NS binaries, and 211 OB+BH binaries, which can well match the observed O+WR and O+BH binaries. For NS binaries, we only predict one fourth of the observed number.

Most of our OB+WR binaries have orbital periods of 100 days, while the observed O+WR binaries are below 20 days. The reason that the long-period binaries are missing could be that their small orbital velocities are hard to observe. In addition, many predicted OB+WR binaries have mass ratios (WR star mass divided by companion mass) above 0.6, which means that WR stars could outshine their companions, making such OB+WR binaries difficult to identify.

Similar to OB+WR binaries, the predicted OB+BH binaries have a typical orbital period of around 100 days, which we expect to be X-ray quiet. The comparison between the predicted OB+BH binaries and the observed O+BH binaries also shows a lack of long-period binaries. In the Milky Way, a Be+BH binary with a orbital period of 60 days is observed, which may support the existence of long-period BH binaries. In addition, due to the accretion-induced spin up, most BHs have a near-critically-rotating main-sequence companion, which means that we have a large chance of finding BHs in Oe star binaries. Compared with the observed massive stars, we estimate 7-10% of them to have BH companions. We expect long-period OB+WR and OB+BH binaries to be identified by future observations.

For OB+NS binaries, despite the large discrepancy between our model prediction and the observed number, our results still have important implications. The observed orbital period distribution of Be X-ray binaries is partly reproduced by our model, and we find a small group of NS binaries having orbital periods near 10 days. There is no observed Be X-ray binary having an orbital period below 10 days. In our model, these NS binaries have rather slow-rotating companions and low eccentricities, making them X-ray quiet. Once the companions leave the main sequence, they may form supergiant X-ray binaries like SMC X-1.

1.6.2 Population synthesis predictions for Wolf-Rayet star-black hole binaries in the Small Magellanic Cloud and their implications for merging binary black holes

In Chapter 2, we have investigated the binary evolution until the time when the initially less massive star leaves the main sequence. In this Chapter we use the OB+WR and OB+BH binaries predicted by the fiducial model in Chapter 2 to investigate further the evolution until the final merger of a binary black hole (BBH). The observed O+WR and OB+BH binaries can be well recovered by our fiducial model, which forms a solid ground for the study into the later phases, WR+BH and BBH.

In consistent with Chapter 2, we adopt the same assumption on BH formation and method for population synthesis. Since our binary evolution model does not compute the mass transfer onto BH, we rely on analytical estimates for the second mass transfer, which also enables us to take into account common envelope evolution. To study the properties of merging BBH in the local Universe, we propagate our predicted BBH population to all redshifts by assuming all galaxies have similar metallicity as the Small Magellanic Cloud.

Our fiducial population synthesis model predicts 2-3 WR+BH binaries in the Small Magellanic Cloud, 0.15 of which are formed from common envelope evolution. The typical orbital period of WR+BH binaries is similar to that of O+WR and OB+BH binaries, which is 100 days. Our prediction can recover the observed WR+BH candidates NGC300 X-1 and IC10 X-1. Due to the difference in metallicity, our model can hardly explain the galactic object Cygnus X-3.

The predicted merging BBH population is highly sensitive to the treatment of the stability of mass transfer and the common envelope evolution. Our result suggests that stable mass transfer and common envelope evolution may contribute equally to the observed merging BBH near zero redshift. Particularly, all merging BBHs formed from stable mass transfer undergo Case A mass transfer, which was not seen in previous works performed with rapid binary evolution codes.

In the previous Chapter, we have predicted 7 O+WR binaries in the Small Magellanic Cloud, and in this Chapter we predict 2-3 WR+BH binaries. This leads to a strikingly high fraction of the WR stars having BH companions, which can be explained by the comparable lifetimes of the O+WR and WR+BH phases. There are 7 apparently single WR stars in the Small Magellanic Cloud. We expect some of them are actually long-period WR+O or WR+BH binaries. However, the recent monitoring campaign did not found any clear siguature of orbital motion in these single WR stars. The reason might be that six observation nights are not enough to resolve the orbital motion of long-period binaries. If these WR stars are truly single, the lack of long-period O+WR and WR+BH binaries may imply that wide massive binaries undergo very strong orbital shrinkage during the first mass transfer, and the long-period OB+BH binaries may not exist either.

1.6.3 X-ray emission from black hole + O star binaries expected to descend from the observed galactic Wolf-Rayet star + O star binaries

There is a long-standing discussion on whether newborn BHs receive momentum kicks. Since BHs are much more massive than NSs, it is believed that BH kicks are weaker than NS kicks if BHs do receive kicks. In our fiducial population synthesis model presented in Chapter 2 and 3, we assume that BHs do not receive kicks, and our parameter study confirms that the main conclusions of these two Chapters remain valid if considering non-extreme BH kicks. However, Vanbeveren et al. (2020) suggested that the lack of wind-fed BH high-mass X-ray binaries implies that BH kicks could be quite strong, which disrupts most BH binaries. In this Chapter, we revisit their analysis to test whether

strong BH kicks are necessary.

Without a solid surface, a BH becomes a strong X-ray emitter only if there is an accretion disc around it, where potential energy is efficiently converted into radiation through viscosity. It requires the circularisation radius of the captured material to be larger than the radius of the innermost stable orbit of the BH to form an accretion disc. This criterion is highly sensitive to various factors, including the wind velocity of O stars, which is underestimated by a factor of 2.6 in Vanbeveren et al. (2020). With the updated criterion, our fiducial model predicts that the galactic WR+O binaries produce 2-3 wind-fed BH X-ray binaries in the Milky Way (over 100 in Vanbeveren et al., 2020), while one observed (Cygnus X-1). Considering the uncertainties in disc formation, we conclude that large BH kicks are not necessary to explain the sparsity of wind-fed BH high-mass X-ray binaries.

CHAPTER 2

Populations of evolved massive binary stars in the Small Magellanic Cloud I: Predictions from detailed binary evolution models

Xiao-Tian Xu[a], Christoph Schürmann[a,b], Norbert Langer[a,b], Chen Wang[c]

[a]Argelander-Institüt für Astronomie, Universität Bonn, Auf dem Hügel 71, 53121 Bonn, German
[b]Max-Planck-Institut für Radioastronomie, Auf dem Hügel 69, 53121 Bonn, Germany
[c]Max Planck Institute for Astrophysics, Karl-Schwarzschild-Strasse 1, 85748 Garching, Germany

To be submitted to Astronomy and Astrophysics

Author contributions: X.-T.X. analysed the data from the detailed binary evolution model grid computed by C.W., interpreted the results together with N.L. and C.S., and wrote this article. C.S. performed the population synthesis calculation with the ComBinE code and helped improve the plots. N.L. and C.S. reviewed the first draft of this article.

Abstract

Context. Massive stars are rarely alone, but most of them have a close binary companion. How this affects their evolution and fate is still largely uncertain, especially at low metallicity.

Aims. Here, we derive theoretical predictions for the distribution functions of massive post-interaction binary products. Some of them are readily compared to corresponding observed presumably complete populations in the Small Magellanic Cloud (SMC), and provide valuable constraints on uncertain model parameters.

Methods. We analyse 53,298 detailed evolutionary models of massive binary stars computed with MESA, with an initial chemical composition tailored to that of the present-day interstellar medium of the Small Magellanic Cloud, and an initial primary mass range of 5...100 $M_\odot$. The quasi-simultaneously computed model stars in a binary include the physics of rotation, non-conservative mass and angular momentum transfer, magnetic internal angular momentum transport, and tidal spin-orbit coupling. The high density of the binary model grid allows to predict the detailed property distributions even

in sparsely populated parts of the parameter space. Our models cover the first mass transfer and the donor star death, and end when the mass gainer leaves the main sequence.

Results. In many of our models, the mass gainer is spun up and may form an Oe/Be star; their predicted population corresponds well to the observed one. While our fiducial model population underpredicts the number of Be/X-ray binaries in the SMC, their orbital period distribution is well reproduced. It also predicts the properties of the observed WR stars in the SMC well. We find that most Oe stars should be associated with BH companions, with orbital periods of ~10...1000 days, which are expected to be X-ray silent. We vary critical assumptions in our population synthesis, which helps to recover some but not all observational constraints.

Conclusions. While the comparison with the observed SMC stars supports many physics assumptions in our high-mass binary models, a match to the large number of Be/X-ray binaries likely requires on average higher mass transfer efficiencies in the models. For BH systems, our fiducial model expects 211 OB+BH binaries in the SMC, the majority of which has orbital periods of 100 days and fast-rotating main-sequence companions. Finding such objects can provide further constraints on binary evolution, improving our understanding on binary black hole mergers.

2.1 Introduction

On September 14th, 2015, a new window to the Universe was opened by the first detection of gravitational waves, emitted by the merging of two stellar-mass black holes (B. P. Abbott, R. Abbott, T. D. Abbott, Abernathy et al., 2016). Up to now, more than 90 compact object merger events are detected in this way (The LIGO Scientific Collaboration et al., 2021). Several formation channels have been proposed (Mapelli, 2020), including their formation in isolated massive binaries. Due to the cosmological distance of these sources, and considerable delay times between the compact object formation and the merger, the majority of them will have formed at low metallicity.

An understanding of the formation of tight double-compact binaries through binary evolution is intimately linked to an understanding of massive stars as such, since most of them are born with a close companion with which they will interact (Sana et al., 2012). Massive star feedback, be it via emitting newly synthesised chemical elements, kinetic energy, or ionising radiation, is strongly affected by the presence of a companion, which is therefore important for the evolution of star forming galaxies (Fichtner et al., 2022).

While this holds for all redshifts, we can study metal-rich individual massive stars and binaries in detail in many sources nearby. Star forming galaxies are found at redshifts beyond 10 (Finkelstein et al., 2023) but individual stars at high redshift remain inaccessible to us (except for compact object merger!).

In this respect, the Small Magellanic Cloud (SMC) provides an ideal laboratory to investigate massive single star and binary evolution at conditions prevalent in the early universe. Its metallicity of only $\sim 1/5$th solar (Hill, Andrievsky and Spite, 1995; Korn et al., 2000; Davies et al., 2015) corresponds to the average metallicity of star forming galaxies at a redshift of ≈ 5 (Langer and Norman, 2006). Yet, with a distance of only 61.9 ± 0.6 kpc (de Grijs and Bono, 2015), and with a current star formation rate of $\sim 0.05\ M_\odot\ \mathrm{yr}^{-1}$ (Harris and Zaritsky, 2004; Rubele, Girardi et al., 2015; Hagen et al., 2017; Rubele, Pastorelli et al., 2018; Schootemeijer, Langer, D. Lennon et al., 2021), it shows us a rich population of massive stars.

The SMC is also an ideal testbed for massive star evolution for other reasons. Firstly, due to its low

metallicity, the winds of hot star are weak (Mokiem et al., 2007), such that the uncertainty in their mass and angular momentum loss is reduced. Secondly, the SMC being a dwarf galaxy, the extinction towards most of the stars is very low. Except for the youngest massive stars (Schootemeijer, Langer, D. Lennon et al., 2021), it is thus generally assumed that the we see their complete population, which makes the SMC well suited for population synthesis studies.

Figure 2.1 presents a schematic picture of the evolutionary phases of massive close binary systems, up to the time where the initially less massive star leaves the main sequence. It demonstrates that binary evolution models may be compared with the properties of several observed populations of evolved massive binaries in the SMC. Particularly rich is the SMC's massive X-ray binary population, with about 150 objects, of which $\sim$ 100 are identified to be Be/X-ray binaries (BeXBs, Haberl and Sturm, 2016). Furthermore, Schootemeijer, D. Lennon et al. (2022) identified more than 1700 OBe stars brighter than $M_{\rm V} \simeq 3\,{\rm mag}$ ($\gtrsim 9\,M_{\odot}$), most of which are thought to represent spun-up mass gainers in binary systems (Shao and X.-D. Li, 2014). The SMC also harbors 11 Wolf-Rayet stars, of which about half show a close OB star companion (Shenar, Hainich, Todt, Sander et al., 2016).

While the predictions of population synthesis models can be easily compared with these observed samples of post-interaction binaries, for several binary evolutionary stages we basically lack any observed counterparts. This holds in particular for rich predicted populations of stripped mass donors, which lack the strong winds to make them appear as Wolf-Rayet stars (Wellstein, Langer and Braun, 2001; Götberg, S. E. de Mink et al., 2018; Langer, Baade et al., 2020), and of wind accreting black holes with OB star companions (Shao and X.-D. Li, 2019; Langer, Schürmann et al., 2020; Janssens et al., 2022), which may lack any X-ray emission (Casares et al., 2014; Sen, X.-T. Xu et al., 2021), and of which very few are known in the Galaxy and LMC (Orosz, Steeghs et al., 2009; Orosz, McClintock, Aufdenberg et al., 2011; Casares et al., 2014; Shenar, Sana et al., 2022), but none so far in the SMC. Here, population synthesis predictions are useful to refine targeted searches for such objects.

We aim to provide predictions for the evolved phases of massive binary stars in the SMC based on detailed binary evolution models. Our work is closely related to that of Schürmann, Langer, X.-T. Xu et al. (2023), who undertake a similar effort using the rapid binary evolution code ComBinE (Kruckow et al., 2018). Our paper is organized as following. In Sect. 2.2, we introduce the grid of detailed binary evolution models used for our analysis, and describe the essential input physics. In Sect. 2.3, we present the results of our fiducial population synthesis model, and describe the result of parameter variations in Sect. 2.4. In Sect. 2.6, we compare our results with previous works, and we discuss the key uncertainties in our calculations in Sect. 2.7, before summarizing our results in Sect. 2.8.

2.2 Method

This work is based on a dense grid of detailed massive binary evolution (Wang, Langer et al., 2020), which is calculated with the one-dimensional stellar evolution code MESA (Modules for Experiments in Stellar Astrophysics version 8845) using a tailored metallicity appropriate for the SMC, as in Brott et al. (2011). The detailed description of this code can be found in Paxton, Bildsten et al. (2011), Paxton, Cantiello et al. (2013) and Paxton, Marchant et al. (2015). Using statistical weights depending on the initial distributions and lifetimes allows us to perform population synthesis. In the following subsections, we describe our method in detail.

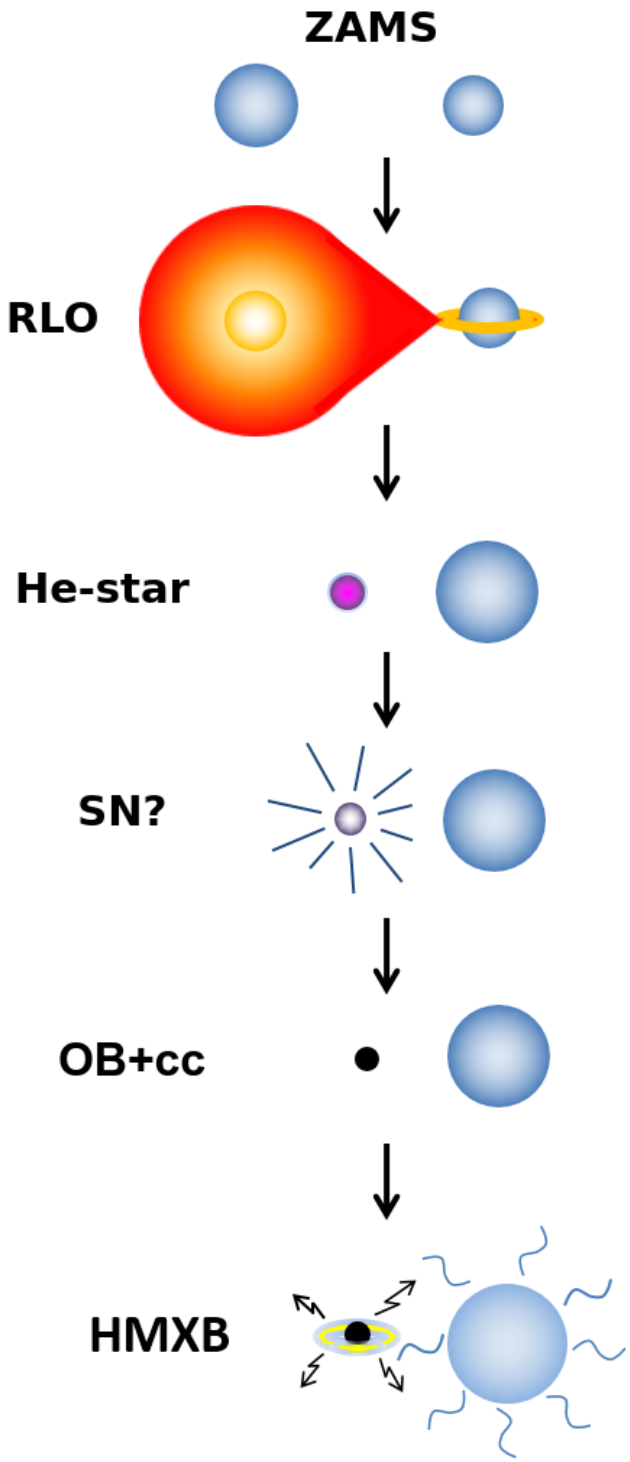

Figure 2.1: Schematic evolution of a massive binary system through the six evolutionary phases considered in this paper: pre-interaction, Roche lobe overflow (RLO), stripped envelope star (subdwarf, helium star or Wolf-Rayet star), compact object (WD/NS/BH) formation possibly connected with a supernova explosion, X-ray silent compact object binary, and high-mass X-ray binary. After the 2nd stage, a fraction of the mass gainers may be fast rotating and appear as Oe or Be stars, and after NS formation as OBe/X-ray binary. Notably, many systems do not survive the 2nd, 4th and 6th stage as a binary, i.e., the number of systems evolving from top to bottom is being reduced at these stages. The figure is adapted from Kruckow et al. (2018).

2.2.1 MESA input physics

Here we briefly summarize our input physics for the MESA models. In order to model convection, the traditional mixing length theory is adopted with parameter $\alpha_{\rm MLT} = 1.5$ (Böhm-Vitense, 1958), and we use the Ledoux criterion to determine the size of convective region combined with overshooting parameter $\alpha_{\rm OV} = 0.335$ (Brott et al., 2011). We model semiconvection with $\alpha_{\rm SC} = 1$ (Langer, 1991; Brott et al., 2011), which happens in regions unstable to the Schwarzschild criterion but stable to the Ledoux criterion. We follow Cantiello and Langer (2010) to model thermohaline mixing with the efficiency parameter $\alpha_{\rm th} = 1$. Rotation-induced mixing is modelled as in Heger and Langer (2000), including the dynamical (Endal and Sofia, 1978) and secular shear instability (Maeder, 1997), Goldreich-Schubert-Fricke instability (Goldreich and Schubert, 1967; K. Fricke, 1968) and Eddington-Sweet circulation (Eddington, 1929) for large-scale circulation. In addition, the Spruit-Taylor dynamo is included for the internal angular momentum transport (Spruit, 2002).

Mass loss follows the treatment in Brott et al. (2011), which includes the so-called bi-stability jump (Vink, de Koter and Lamers, 1999). The first jump temperature is near 22 kK, below which OB stars' mass loss is computed according to (Nieuwenhuijzen and de Jager, 1990; Vink, de Koter and Lamers, 2000; Vink, de Koter and Lamers, 2001). Above the first jump temperature, with the increasing of surface helium abundance from 0.3 to 0.7, the mass-loss rate is smoothly switched from the OB star case (Vink, de Koter and Lamers, 2001) to the Wolf-Rayet stars case (Hamann, Koesterke and Wessolowski, 1995). In addition, enhanced mass loss by rotation is assumed as in (Heger and Langer, 2000) though see Hastings, Langer and Puls (2023)

The orbit evolution of our binary model is determined by mass transfer (Tauris and van den Heuvel, 2006) and tidal interaction (Hut, 1981; Hurley, Tout and Pols, 2002; Sepinsky et al., 2007). We use the `Hut_rad` scheme coded in MESA to calculate radiative-damping dominated tide interaction (Detmers et al., 2008). Mass transfer takes place when the radius of the primary star excesses the radius of its Roche Lobe, where the Roche Lobe radius is calculated by the empirical formula by Eggleton (1983). In order to take into account for long-term contact phases, the `contact` scheme in MESA is adopted (Marchant, Langer, Podsiadlowski, Tauris and Moriya, 2016). During mass transfer, accretors can be spun up to critical rotation (Packet, 1981). Once a mass gainer rotates critically, we assume it can not accrete anymore and the transferred material is ejected. This leads to a rotation-dependent accretion efficiency. In wide-orbit binaries, where tides are inefficient, the accretion efficiency is often below 10%, while it can reach 60% in narrow-orbit binaries. The material that can not be accreted by the mass gainer is assumed to be ejected through a radiation-powered wind. We set an upper limit on the mass transfer rate $\dot{M}_{\rm limit}$ by assuming that the radiation energy of the stars are completely used to drive the wind, which is (Marchant, 2017)

$$\log \frac{\dot{M}_{\rm limit}}{M_\odot\ {\rm yr}^{-1}} = -7.19 + \log\frac{L_1 + L_2}{L_\odot} - \log\frac{M_2}{M_\odot} + \log\frac{R_2}{R_\odot}, \tag{2.1}$$

where L_1 and L_2 are the luminosities of mass donor and mass gainer, M_2 is the mass of mass gainer, and R_2 is the radius of mass gainer. Above this limit, mass transfer is unstable. With the above condition, the critical mass ratio for unstable mass transfer in our models is very sensitive to initial orbital period and initial primary mass of the system (see section 2.2.2 and Fig. 2.2). In addition, we also assume unstable mass transfer if the mass transfer rate reaches $0.1 M_\odot\ {\rm yr}^{-1}$ (an artificial upper limit), if inverse mass transfer occurs with a post-main-sequence (post-MS) donor, and if L2 overflow

occurs.

Our stellar models evolve from zero-age main-sequence (ZAMS) binaries to core carbon depletion. If the donor star has a helium core mass above 13 $M_\odot$, we terminate the evolution at the core helium depletion to avoid convergence issues. After the termination of primary star, we further evolve the secondary star as single star by setting the orbital separation to infinity (cf. Sect. 2.2.6 and 2.2.7).

2.2.2 Binary model Grid

Our SMC binary model grid (Wang, Langer et al., 2020) contains 53298 detailed evolution models. We assume that the stars are initially tidally locked. Therefore, the evolution is determined by initial primary mass $M_{1,\mathrm{i}}$, initial mass ratio q_i, and initial orbital period $P_{\mathrm{orb,i}}$. Our model grid is computed with the following parameter space:

- Initial primary masses $M_{1,\mathrm{i}}$ are in the range $5 - 100\,\mathrm{M}_\odot$, logarithmically $\log\,(M_{1,\mathrm{i}}/\mathrm{M}_\odot)$ between 0.7 and 2, with intervals $\Delta\log(M_{1,\mathrm{i}}/\mathrm{M}_\odot) = 0.05$;
- Initial mass ratios q_i between 0.3 and 0.950 with an interval $\Delta\, q_\mathrm{i} = 0.05$;
- Initial orbital periods $P_{\mathrm{orfb,i}}$ from 1 day to 3162 days, logarithmically $\log(P_{\mathrm{orb,i}}/\mathrm{day}) = 0.0{-}3.50$, with intervals $\Delta\log\,(P_{\mathrm{orb,i}}/\mathrm{day}) = 0.025$.

Fig. 2.2 provide an overview of the outcomes of our binary evolution models with $\mathrm{M}_{1,\mathrm{i}} = 17.8\,M_\odot$. At this mass, our Case A mass donors form neutron stars, and our Case B mass donors form black holes (cf. Sect. 2.2.5). The widest binaries do not experience any binary interactions and serve as a grid of single star models. In our closest binaries, the primary star fills its Roche Lobe during its core hydrogen burning phase (Case A). Above about 5 days initial orbital period, the mass transfer takes place with a shell hydrogen burning donor (Case B binaries). Above about 300 days, mass transfer rate violates our upper limit $0.1 M_\odot\,\mathrm{yr}^{-1}$. Here mass transfer is expected to become unstable due to the convective envelope of the donor star.

Based on our stability criterion Eq. (2.1), we find that a large fraction of models undergoes unstable mass transfer (labelled by "Upper_mdot_limit" in Fig. 2.2). For higher initial primary masses, fewer binary models undergo unstable mass transfer (cf. Figs. A.1 and A.2) and the Case A/B boundary is shifted to larger initial orbital periods, even exceeding 1000 days. This is caused by the so-called envelope inflation (Sanyal et al., 2015), which is the result of adopting the traditional mixing length theory. Due to the iron bump in opacity, the Eddington limit can be reached below the surface of massive stars. With the traditional mixing length theory, convection is not efficient to transfer the energy to surface. Consequently, radiation pushes the outer envelope to a very large radius during core H burning phase.

2.2.3 OBe stars

Observationally, the Be phenomenon is mainly featured by Hα emission line and an infrared excess, which is believed to occur in fast-rotating stars with a circumstellar disk (Reig, 2011; Rivinius, Carciofi and Martayan, 2013). While Be stars are fast rotators, it is unclear how close they are to their critical rotation. R. H. D. Townsend, Owocki and Howarth (2004) suggested that considering gravitational darkening, all Be stars are very close to their critical rotation. On the other hand, many works suggest that Be stars can rotate sub-critically (e.g. Huang, Gies and McSwain, 2010; El-Badry et al., 2022;

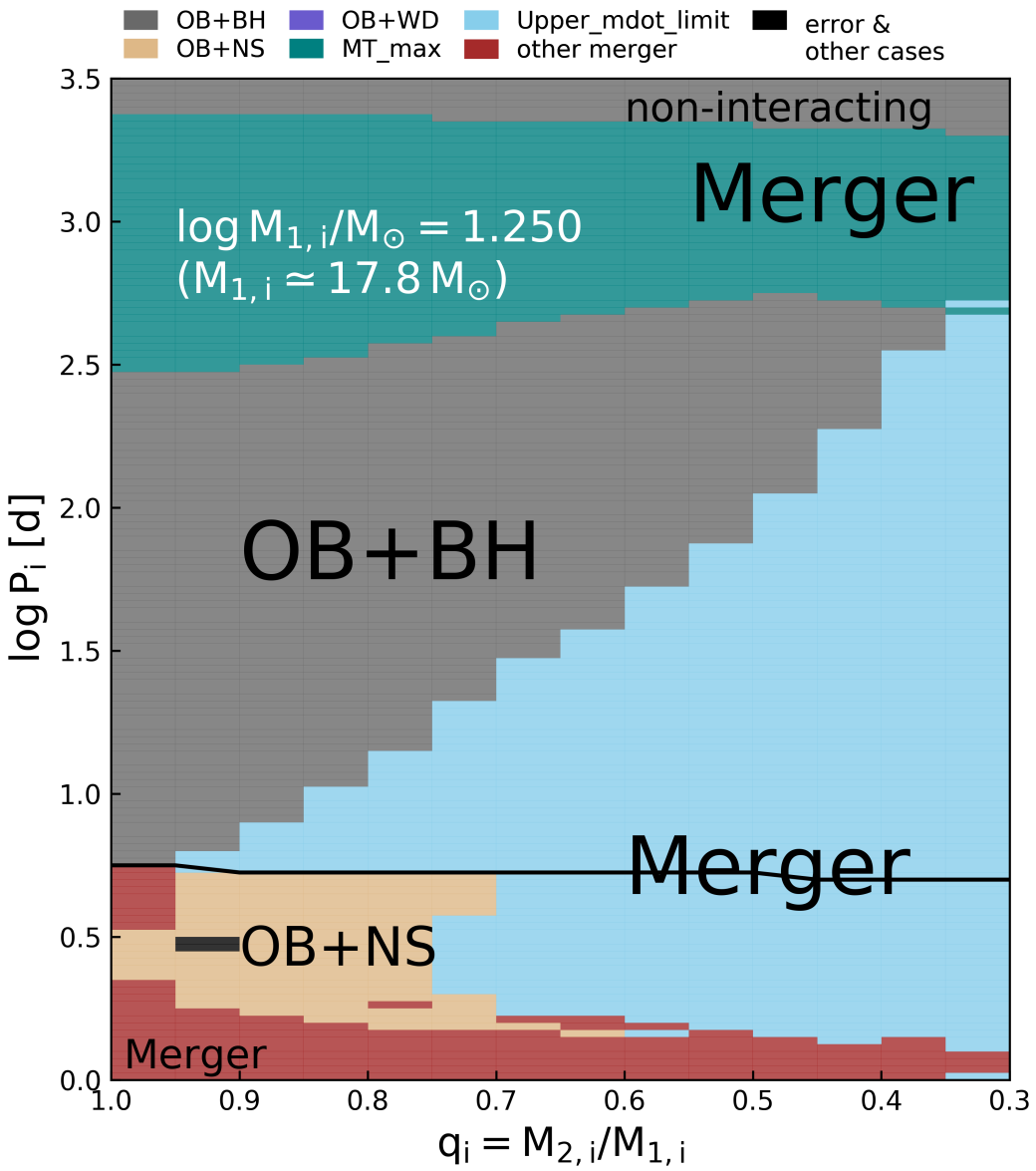

Figure 2.2: The outcomes of our detailed binary evolution models with initial primary mass 17.78 $M_\odot$. In this figure, each pixel represents one detailed MESA binary evolution model, and the related evolutionary outcome is color-coded (see top legend). Here, "OB+cc" (cc= BH, NS, WD) implies that the corresponding model produced a OB+cc phase, with the compact companion type indicated by the corresponding color. In all other cases, OB+cc are not produced. Systems indicated as "Upper_mdot_limit" or "MT_max" are terminated during their first mass transfer phase as the mass transfer rate exceeds limiting values (see text), and those indicated as "merger" undergo L2-overflow in a contact situation. For all three cases, we assume that both stars in the binary system merge. Corresponding plots for different initial donor star masses can be found in App. A.

Dufton, D. J. Lennon et al., 2022). Following R. H. D. Townsend, Owocki and Howarth (2004), in our fiducial model, we define Be stars as rotating faster than 0.95 of their critical rotation velocity ($\upsilon_{\rm crit}$). We will discuss the effects of different threshold values in Sec. 2.4. Golden-Marx et al. (2016) showed that Oe stars are the high-mass extension of Be stars, and therefore we also adopt $0.95\,\upsilon_{\rm crit}$ to define Oe stars. the detailed properties of the circumstellar discs are not considered.

2.2.4 Helium stars and Wolf-Rayet stars

Following the common nomenclature, we define helium stars (HeSs) as stripped-envelope core helium burning stars, and accordingly their lifetime is determined by the period of core He burning. Classical Wolf-Rayet stars (WR stars) are HeSs with optically thick wind, which can form through self-stripping by a stellar wind or envelope-stripping by mass transfer. Observationally, Shenar, Gilkis et al. (2020) found a metallicity-dependent luminosity threshold for the WR phenomenon, as $\log L/L_\odot \approx 4.9, 5.25,$ and 5.6 for the Galaxy, the LMC, and the SMC respectively. Based on this result, we assume HeSs with $\log L/L_\odot > 5.6$ are WR stars. In addition, we define hydrogen-free (H-free) WR stars by a surface H abundance less 0.05 according to the errors of the observed H abundance in Shenar, Hainich, Todt, Sander et al. (2016).

2.2.5 Formation of black holes and neutron stars

We determine the types of compact objects according to the final state of our model. Sukhbold, Woosley and Heger (2018) performed detailed simulation on the explodability of stars. They found a sudden increase in the compactness parameter of pre-supernova (pre-SN) stars at a final He core mass of $6.6\,M_\odot$, which marks the formation of BHs. We assume accordingly that BH forms if the final mass of a helium core $M_{\rm He,c}$ reaches $6.6\,M_\odot$. For simplicity, the non-monotonous behaviour of the compactness parameter (O'Connor and Ott, 2011; Sukhbold, Ertl et al., 2016; Sukhbold, Woosley and Heger, 2018) is ignored. Since our models do not reach the pre-SN state, this assumption may overestimate the number of low-mass BH (Langer, Schürmann et al., 2020). The mass of the BH is computed by the same assumption as in the ComBinE code (Kruckow et al., 2018; Schürmann, Langer, X.-T. Xu et al., 2023), that 20% of the mass of the He-rich envelope of the core He depleted star is ejected and after that 20% of the remaining mass is lost due to the release of the gravitational binding energy.

Stars with very massive helium cores become unstable due to the production of electron–positron pairs, and consequently a series of energetic pulses and strong mass ejections occurs (Heger and Woosley, 2002; Chatzopoulos and Wheeler, 2012; Marchant, Renzo et al., 2019). This process is known as pulsational pair-instability. Marchant, Renzo et al. (2019) simulates the mass ejections during PPISNe with the MESA code. We perform a polynomial fitting to the helium core mass at core helium depletion and the remaining mass $M_{\rm rem}$ after the pulsations following Marchant, Renzo et al.

(2019), which is

$$\begin{aligned} M_{\rm rem}/\,M_{\odot} = &-8.658\times10^{-8}\,M_{\rm He,c}^{8} + 3.252\times10^{-5}\,M_{\rm He,c}^{7} \\ &- 0.005318\,M_{\rm He,c}^{6} + 0.4946\,M_{\rm He,c}^{5} \\ &- 28.61\,M_{\rm He,c}^{4} + 1054\,M_{\rm He,c}^{3} \\ &- 2.414\times10^{4}\,M_{\rm He,c}^{2} + 3.145\times10^{5}\,M_{\rm He,c} \\ &- 1.783\times10^{6}, \end{aligned} \tag{2.2}$$

where $M_{\rm He,c}$ is in solar mass.

We assume that stars with $M_{\rm He,c}$ less than $6.6\,M_{\odot}$ form NSs or WDs. The mass of our NSs is fixed to be $1.4\,M_{\odot}$. Neutron star formation is accompanied by a SN explosion due to the collapsing core. Core collapse in the lowest-mass SN progenitors is triggered by electron capture, producing electron-capture supernovae (ECSNe, Nomoto, 1984). While ECSNe may happen in a very narrow mass range in single star case (Poelarends, Herwig et al., 2008; Janka, 2012), the ECSN window can be broadened by binary interaction (Podsiadlowski et al., 2004; Langer, 2012; Shao and X.-D. Li, 2014; Poelarends, Wurtz et al., 2017; Siess and Lebreuilly, 2018; Vinciguerra et al., 2020). Since ECSN produces weak momentum kick on newborn NSs (Janka, 2017), it plays an important role in the formation of Be X-ray binaries (BeXBs). Detailed simulations have shown that even taking into account the effects of binary interaction, the mass window of ECSNe is still narrower than $1\,M_{\odot}$ (Poelarends, Wurtz et al., 2017; Siess and Lebreuilly, 2018), which can not be well resolved by our model grid. Therefore, we apply the SNe scheme adopted in the ComBinE code (See App. A for details). There are four types of SNe considered in the ComBinE code: 1) normal core collapse SN (CCSN) if the pre-SN star has a final carbon core mass larger than $1.435\,M_{\odot}$ and a H-rich envelope, 2) H-envelope-stripped SN (CCSN-He) if the H-rich envelope is stripped by mass transfer and a HeS remains, 3) He-envelope-stripped SN (CCSN-C) if the He-rich envelope is stripped by mass transfer and a carbon star remains, 4) ECSN if the final carbon core is in the mass range of 1.37 - $1.435\,M_{\odot}$ (Nomoto, 1984). Different types of SNe are associated with different kick velocity distributions, which are introduced in the next subsection.

2.2.6 Natal kick

During the SN explosion, asymmetries in the ejecta can generate a momentum kick in the newborn NSs. The more energetic the explosion, the stronger is the kick (Janka, 2012). We adopt the Monte Carlo method to take into account the dynamical effects of SNe. For each pre-SN binary, we determine the type of SN with the SN scheme explained above. Then we randomly draw a sample of kick velocities from the corresponding kick velocity distribution. Here we adopt the same kick distributions as the ComBinE code, which is summarized in Tab. 2.1.

For normal CCSNe, the kick velocity distribution is assumed to be the Maxwell-Boltzmann distribution $f(\upsilon_{\rm K},\,\sigma)$ with a root-mean-square velocity $\sigma = 265{\rm km\,s^{-1}}$, which is based on the proper motion analysis of young pulsar (Hobbs et al., 2005), where

$$f(\upsilon_{\rm K},\,\sigma) = \sqrt{\frac{2}{\pi}}\frac{\upsilon_{\rm K}^{2}}{\sigma^{3}}\exp\left(-\frac{\upsilon_{\rm K}^{2}}{\sigma^{2}}\right). \tag{2.3}$$

Table 2.1: Kick velocity distributions imparted on newborn neutron stars

ECSN	flat distribution, $0-50\,\mathrm{km\,s^{-1}}$	
normal CCSN	Maxwell-Boltzmann distribution with $\sigma = 265\mathrm{km\,s^{-1}}$ [a]	
stripped CCSN	bi-modal Maxwell-Boltzmann distribution	
	σ_1 [a]	σ_2 [a]
– CCSN-He [b]	$120\,\mathrm{km\,s^{-1}}$	$200\,\mathrm{km\,s^{-1}}$
– CCSN-C [b]	$60\,\mathrm{km\,s^{-1}}$	$200\,\mathrm{km\,s^{-1}}$

Notes. [(a)] Parameters σ, $\sigma_{1/2}$ are root-mean-square velocity of the Maxwellian and bi-modal Maxwellian distributions respectively. [(b)] CCSN-He/C stand for pre-SN stars having their hydrogen/helium envelope stripped.

The SNe from stripped stars are thought to be less energetic and therefore generate weaker kicks. On the other hand, observed double pulsar binaries imply that large kicks may happen in close binaries (Tauris, Kramer et al., 2017, and references therein). Accordingly, for stripped SNe we adopt a bi-modal Maxwellian distribution $f_2(\upsilon_\mathrm{K},\,\sigma_1,\,\sigma_2)$ with a 80% low-kick component and a 20% high-kick component,

$$f_2(\upsilon_\mathrm{K},\,\sigma_1,\,\sigma_2) = \sqrt{\frac{2}{\pi}}\left[0.8\frac{\upsilon_\mathrm{K}^2}{\sigma_1^3}\exp\left(-\frac{\upsilon_\mathrm{K}^2}{\sigma_1^2}\right) + 0.2\frac{\upsilon_\mathrm{K}^2}{\sigma_2^3}\exp\left(-\frac{\upsilon_\mathrm{K}^2}{\sigma_2^2}\right)\right]. \tag{2.4}$$

Based on the observed migration of galactic high-mass X-ray binaries (Coleiro and Chaty, 2013), the low-kick component σ_1 is taken to be $120\mathrm{km\,s^{-1}}$ and $60\mathrm{km\,s^{-1}}$ for CCSN-He and CCSN-C respectively, and the high-kick component σ_2 is taken to be $200\mathrm{km\,s^{-1}}$(Tauris, Kramer et al., 2017). For ECSNe, based on the observed low-eccentricity X-ray binary X Persei (Pfahl et al., 2002; Podsiadlowski et al., 2004), a flat distribution in $[0,\,50]\mathrm{km\,s^{-1}}$ is adopted.

The momentum kick imparted on BHs is highly uncertain. It has been proposed that the low-mass BHs can have a natal kick due to material fallback during BH formation (e.g. Belczynski, Kalogera et al., 2008; Fryer, Belczynski et al., 2012; Belczynski, Holz et al., 2016; Janka, 2017; Mandel and Müller, 2020). In our fiducial model, we simply assume no kick for all BHs.

Besides the additional kinetic energy injected by natal kick, mass loss during the SN weakens the gravitational bounding of a binary (Blaauw, 1961). Whether a binary can survive a SN depends on the orbital energy of the post-SN system $E_\mathrm{orb,post-SN}$. Binary disruption happens when $E_\mathrm{orb,post-SN} \geq 0$. If the binary remains bound, the parameters of the post-SN orbit are calculated by the formulas in the appendix A.1 of Hurley, Tout and Pols (2002).

2.2.7 Population synthesis

Different from the commonly adopted Monte Carlo method, we perform population synthesis through statistical weights (see App. A for detailed formulas). Each binary is evaluated by a statistical weight determined by initial mass function (IMF, f_IMF), initial distributions for mass ratio f_{q_i} and orbital period $f_{\log P_\mathrm{orb,i}}$, and the lifetime of the corresponding phase τ. For a OB+cc binary, its lifetime is determined by we determine the lifetime of OB+cc by checking the age at compact object formation

and the age when the secondary star leaves the MS or fills its Roche Lobe. We adopt the IMF in Kroupa (2001),

$$f_{\rm IMF} \propto M_{\rm 1,i}^{-\alpha}, \tag{2.5}$$

where

$$\begin{cases} \alpha = 0.3 & 0.01 \leq M_{\rm 1,i}/M_\odot < 0.08 \\ \alpha = 1.3 & 0.08 \leq M_{\rm 1,i}/M_\odot < 0.50 \\ \alpha = 2.3 & 0.50 \leq M_{\rm 1,i}/M_\odot \end{cases} . \tag{2.6}$$

For our fiducial model, initial distributions of mass ratio and orbital period are taken from Sana et al. (2012), which is derived from the O star population in open clusters. The Sana distribution shows a preference for short orbital periods and a near flat mass ratio distribution,

$$f_{q_{\rm i}} \propto q_{\rm i}^{-0.1} \tag{2.7}$$

and

$$f_{\log P_{\rm orb,i}} \propto \log P_{\rm orb,i}^{-0.55}. \tag{2.8}$$

In addition, a constant star formation rate of $0.05 M_\odot\ {\rm yr}^{-1}$ is adopted (Harris and Zaritsky, 2004; Rubele, Girardi et al., 2015; Hagen et al., 2017; Rubele, Pastorelli et al., 2018; Schootemeijer, Langer, D. Lennon et al., 2021) in our fiducial model.

During the OB+cc phase, the orbits may slowly expand or shrink due to the stellar wind from the main-sequence companions (Quast, Langer and Tauris, 2019; El Mellah, Bolte et al., 2020). Considering the low mass loss rate of OB stars in the SMC, we do not expect significant changes in orbital separation during OB+cc phase. Therefore, we simply assume the orbital parameters remain unchanged. Also, stellar parameters are assumed to remain constant during this phase. For stellar rotation, we consider the tidal interaction during the OB+cc phase by calculating the synchronization timescale at the beginning of the OB+cc phase. We found that tides during the OB+cc phase is too weak to further spin down the OB star (See App. A for details).

For HeSs, we determine their parameters at the middle of core helium burning, i.e., when the core He mass fraction dropped to 0.5, and the lifetime is determined by their core He burning time. For WR stars, we go through the evolutionary tracks of core He burning phase step by step to check whether the stars are luminous enough to be observed as WR stars.

We define O stars as MS stars with effective temperatures hotter than 31.6 kK. Here we adopt the relation between spectral type and temperature derived by Schootemeijer, Langer, D. Lennon et al. (2021). In order to count O stars regardless of the types of companions, we go through the evolutionary tracks of all MS stars in our binary model grid. Only the visually brighter star in a binary is counted. Here merger products are not considered.

2.3 Properties of our fiducial synthetic population

In contrast to rapid binary population synthesis, where different binary model parameters can easily be explored, we only have one fixed binary evolution grid to work with. However, in order to construct a synthetic population from that model grid, parameters are introduced, which can be varied later-on. This concerns in particular the birth kicks of compact objects, the core mass ranges defining the emerging compact object type, the threshold rotation for assuming OBe stars, and the star formation

history. In this section we present the main properties of our synthetic model population based on our fiducial parameter choice, as explained above (see App. A for further model details). In Sect. 2.4, we discuss the effects of variations of the mentioned parameters, and we compare our predictions with the observed numbers in Sect. 2.5.

2.3.1 Numbers of post-interaction binaries

The numbers of the various types of binary systems consisting of a main sequence star (the mass gainer) and a post-main sequence companion predicted to exist in the SMC are shown in Tab. 2.2 and Fig. 2.3. In Tab. 2.2, we distinguish core-helium burning stripped mass donors originating from three different initial donor mass ranges, which roughly correspond to those forming WDs, NSs, and BHs, respectively, according to our assumptions. Note, however, that while such initial mass limits are well defined for Case B binaries, the emerging helium star mass in Case A systems is not only a function of the initial donor mass but also of the initial orbital period (Wellstein, Langer and Braun, 2001). We can see the effect of this in Fig. 2.2, which shows that 17.8 $M_\odot$ donors form BHs in Case B systems but NSs in Case A evolution (see also the plot for the initial donor mass of 10 $M_\odot$ in Fig. A.1). Table 2.2 further gives the predicted number of OB+WR binaries, and those for the much smaller fraction in which the WR star is expected to be hydrogen-free. Finally, Tab. 2.2 lists the predicted number of OB stars with NS and BH companions. We also count the number of binaries, which were broken up due to the adopted NS birth kick. Since our fiducial model ignores BH birth kicks, none of our model binary is broken up when a BH is formed.

In Tab. 2.2 and Fig. 2.3, we also distinguish systems in which the mass gainer is spun-up to close-to-critical rotation and designate them as OBe systems. Notably, we find that 60. . . 100% of the post-interaction systems contain an OBe star. Besides the high efficiency of the spin-up process, these numbers reflect the generally low mass loss rates of our SMC main sequence models. Figure 2.3 shows that the OBe fraction is a decreasing function of of the OB stars mass.

We expect that the numbers in Tab. 2.2 and Fig. 2.3 are complete, except for the WD progenitors ($M_{\rm i,1} \leq 10\,M_\odot$). The plot for 10 $M_\odot$ donors in Fig. A.1 shows that we expect the lowest mass main sequence stars which have a NS companion to weigh $\sim 6.5\,M_\odot$.

Similarly, Fig. 2.2 shows the lowest mass OB+BH progenitors have initial mass ratios near ~ 0.35, implying BH companion masses above $\sim 6.2\,M_\odot$. This means we do not expect NS or BH binaries in mass bins to the left of the $6-8\,M_\odot$ bin in Fig. 2.3. The numbers on top of the bins in Fig. 2.3 show that the numbers of systems we are missing for $M_{\rm OB} > 100\,M_\odot$ is negligible.

As shown in Figs. 2.2 and A.1, we expect Case C mass transfer in a small range of initial orbital periods for initial donor masses $\lesssim 15.8\,M_\odot$. We ignore those in our statistics, because they have a negligible lifetime as post-interaction binary. Only a very small fraction of them undergoes stable mass transfer, while the vast majority is expected to merge in a common envelope evolution. During the core helium burning phase of the mass donor, they may be nearly indistinguishable from systems in which both components never interact.

To interpret the numbers shown in Tab. 2.2 and Fig. 2.3, it is helpful to consider some basic trends in our summary plots (Fig. 2.2 and App. A.1). For the lowest initial donor masses, we see a small corner in the Case A regime and a somewhat larger triangular region in the high mass ratio region of the Case B regime which indicate those binaries which are thought to avoid merging (as the non-interacting systems with the largest orbital periods). This shows, in agreement with many previous detailed binary evolution calculations (Pols, 1994; Wellstein, Langer and Braun, 2001; S. E. de Mink, Pols and

Table 2.2: Number of post-main sequence companions of OB stars in our fiducial synthetic SMC population. Besides the total numbers, we give the numbers emerging from Case A mass transfer, from Case B mass transfer, and from chemically homogeneous evolution (CHE). For WR stars and BHs, we also give the numbers emerging from chemically homogeneous evolution (CHE). As OBe stars, we count OB mass gainers which rotate faster than 95% of critical rotation. For core-helium burning mass donors, we distinguish three different initial mass ranges as indicated, as well as stars with $\log L/L_\odot > 5.6$ as WR stars.

	Total		Case A		Case B	
	OBe	OB	OBe	OB	OBe	OB
He-stars	223	12	57	12	166	1
- $M_{1,\mathrm{i}} \leq 10\,M_\odot$	191	0	51	0	140	0
- $M_{1,\mathrm{i}}$, $10-17\,M_\odot$	18	3	5	3	13	0
- $M_{1,\mathrm{i}} \geq 17\,M_\odot$	14	9	1	9	13	1
- WR	4	3	1	3	3	0
- H-free WR	0.02	0.2	0.02	0.2	0	0
NSs	92	6	8	7	85	0
-bound	20	4	5	4	15	0
-disrupted	72	2	3	3	70	0
BHs	171	40	6	22	165	18
- CHE BH	0	0.32				

Hilditch, 2007), that only ~10% of all binary systems in this mass range are expected to survive their first mass transfer, and appear in Tab. 2.2 and Fig. 2.3; ~90% do not[1]. For larger initial donor masses, the surviving fraction increases and reaches about 60% above $30\,M_\odot$.

The implication is that our synthesis models predicts a similar number of OB+HeS systems in the SMC for the those formed from the initial mass ranges of NS ($M_\mathrm{i} \simeq 10\ldots17\,M_\odot$: 21) and BH progenitors ($M_\mathrm{i} \gtrsim 17\,M_\odot$: 23). This is so because the IMF predicts a similar number of systems in both mass ranges, and the shorter lifetime of the more massive binaries is compensated by a smaller merger fraction. Notably, our fiducial model also predicts 7 WR+O star binaries.

As then most NS-forming binaries are broken up due to the NS birth kick, while — in our fiducial model — BH forming binaries are not, many more BH-binaries (211) than NS-binaries (24) are predicted to exist in the SMC all mostly with OBe type main-sequence companions.

Figure 2.3 shows the predicted relative fractions of compact companions to OB stars as the function of mass. The total BH fraction is nearly constant at about 70%. Here, most MS star companions below $\sim 15\,M_\odot$ are Be stars. For higher masses, the OBe+BH fraction drops, which reflects the increasing importance of wind braking. The NS fraction reaches a maximum near $M_\mathrm{OB} = 8\,M_\odot$ with a value about 20% and then decreases to zero near $30\,M_\odot$. The most massive O+NS binaries form in Case A systems, which feature a strong tidal interaction and a high accretion efficiency. The HeS fraction is nearly constant with ~ 20%, which is in the range inferred by El-Badry et al. (2022). A distribution of OB star masses in NS and BH binaries is provided in Fig. A.5.

[1] Our employed initial orbital period and mass ratio distributions do not deviate strongly from flat distributions in $\log P_\mathrm{i}$ and q_i, such that the area in the summary plots are roughly representatives of the number of systems born in these areas, at the considered initial donor mass.

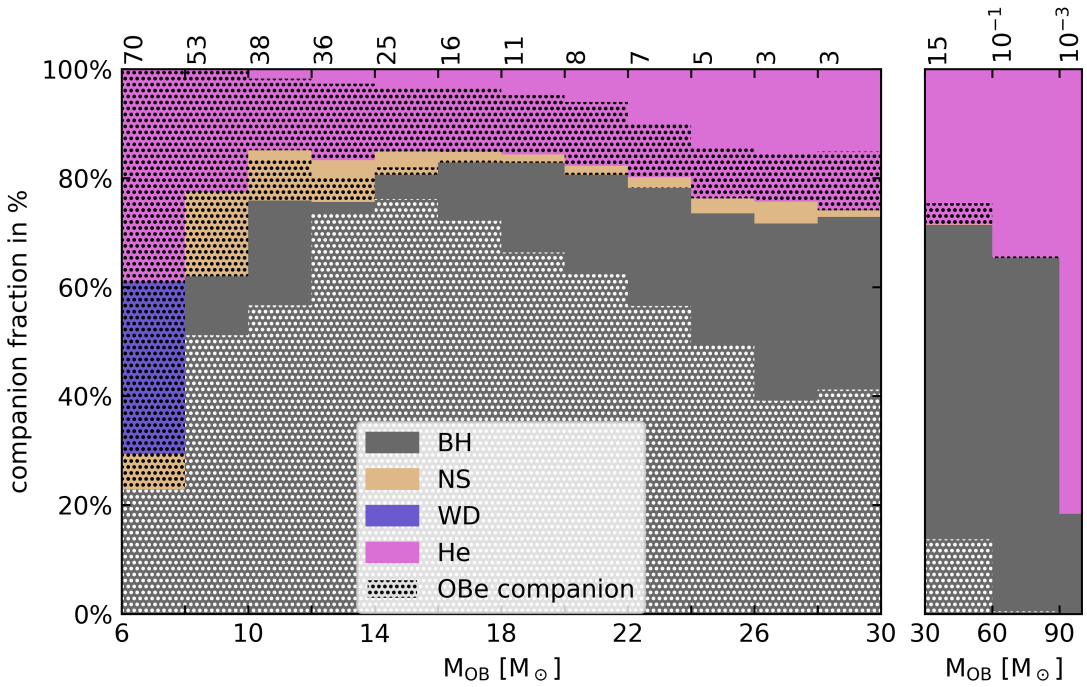

Figure 2.3: The relative fractions of different types of post-main sequence companions of OB stars in our fiducial synthetic binary population, as the function of the mass of the OB star. For the companions, we distinguish core-helium burning stars (purple), white dwarfs (blue), neutron stars (yellow) and black holes (gray). For the OB stars, shading identifies those which are predicted to rotate with more than 95% of their critical rotational velocity. The absolute number of binaries with post-main sequence companions expected in the SMC is given on top of each mass bin. The high-mass end (30 - 100 $M_\odot$) is presented with a wider bin width.

2.3.2 Properties of OB+WR binary systems

The top panel of Fig. 2.4 shows the predicted OB+WR binaries in the Hertzsprung Russell diagram (HRD). The majority of our WR stars has surface temperature $T_{\rm eff} \simeq 8 \times 10^4$ K ($\log T_{\rm eff} = 4.9$) and luminosity $L \simeq 5 \times 10^5\, L_\odot$ ($\log L = 5.7$). The distribution is sharply cut off at $\log L = 5.6$ due to the threshold luminosity for defining WR stars (see Sect. 2.2.4). Towards high-luminosity end, the predicted number is reduced by the effects of the IMF. While the H-rich envelope of the donor stars gets nearly completely stripped by mass transfer, the remaining H can largely reduce the surface temperature of stripped stars (Gilkis et al., 2019; Laplace, Götberg et al., 2020). In our prediction, the WR stars with $\log T_{\rm eff} = 4.9$ have surface H mass fraction about 0.3. Above $\log T_{\rm eff} = 5.1$, H-free WR stars remain.

The bottom panel of Fig. 2.4 shows that most of the WR stars in the OB+WR binaries have orbital velocities of 50km s^{-1}, which is related to orbital periods of 300. . . 1000 days. The number suddenly drops below 50km s^{-1} due to the boundary of interacting binaries. The number drops towards lower orbital periods because of the adopted initial orbital period distribution (Eq. 2.7). Meanwhile, accretion efficiency increases. This produces a flat distribution for the orbital velocities of the WR stars from 200km s^{-1} to 350km s^{-1}. In addition, H-free WR stars have orbital periods below 10 days, where primary stars are deeply stripped.

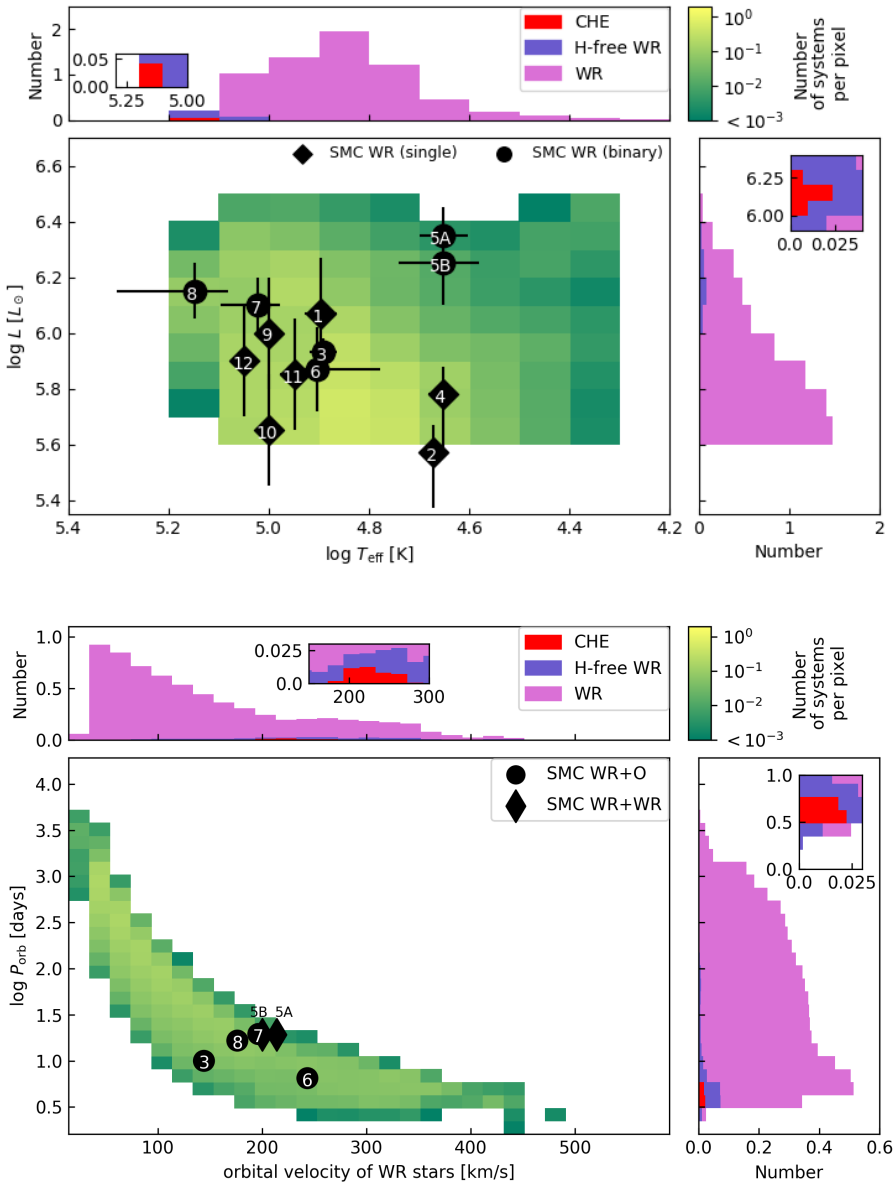

Figure 2.4: Predicted OB+WR binaries in the Hertzsprung Russell diagram (top) and in the orbital velocity of WR star - logarithmic orbital period plane (bottom). The number in each pixel is color-coded. The black circles, diamonds (top panel), thin diamonds (bottom panel) are the observed WR binaries, single WR stars, and WR+WR binary (SMC AB5) (Foellmi, Moffat and Guerrero, 2003; Foellmi, 2004; Koenigsberger et al., 2014; Hainich et al., 2015; Shenar, Hainich, Todt, Sander et al., 2016; Shenar, Hainich, Todt, Moffat et al., 2018), where the numbers are related to the identifier, e.g., SMC AB1. In the 1D projections, H-free WR stars and CHE WR stars are distinguished.

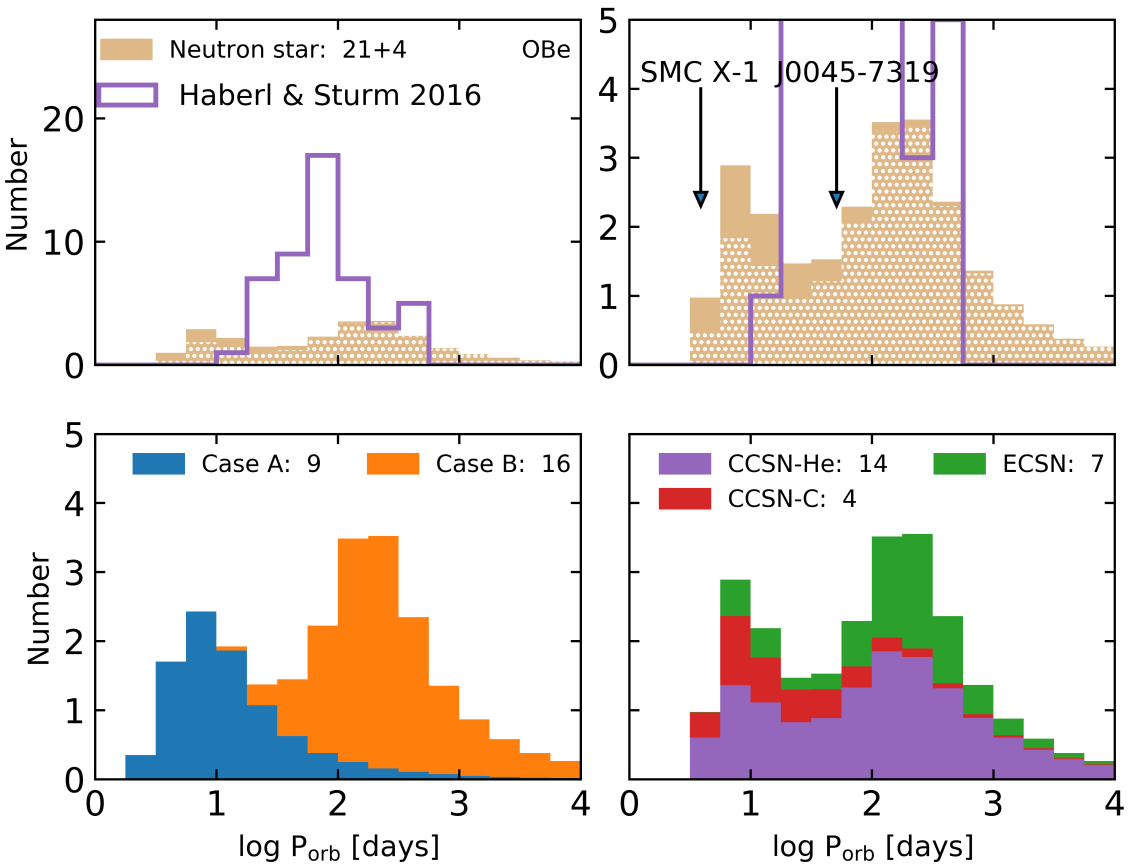

Figure 2.5: Distributions of orbital periods of OB+NS binaries. Upper left: distribution with OBe feature indicated (shaded area). The observed sample by Haberl and Sturm (2016) is plotted with purple. The B star + radio pulsar binary J0045-7319 (Bell et al., 1995) and the supergiant X-ray binary SMC X-1 (Rawls et al., 2011; Falanga et al., 2015) are indicated by arrows. Upper right: a zoom-in version of the upper left panel. Lower left: distribution with Case A and Case B (blue and orange) systems indicated. Lower right: distribution with the types of SNe indicated [green for electron-capture supernova; red for helium-envelope-stripped SN (CCSN-C); purple for hydrogen-envelope-stripped SN (CCSN-He)].

2.3.3 Properties of OB+NS binary systems

Figure 2.5 presents the orbital period distribution of OB+NS binaries. There are two distinct subpopulations with orbital periods peaking near 10 days and 200 days, which are associated with the different modes of mass transfer. As seen in Fig. 2.2 and A.1, OB+NS binaries are formed from two clearly-separated triangular regions in the Case A and Case B regimes due to the upper limit on mass transfer rate set by Eq. (2.1). In addition, some OB+NS binaries have orbital periods exceeding the upper initial orbital period bound ($\simeq 3000$ days), which are broadened by SN kicks. The observed orbital period distributions is overplotted. The large discrepancy between our model prediction and the observed number is discussed in Sect. 2.7.

Neutron stars formed through different SN types are distinguished. There are 7 NS binaries undergoing ECSN, 14 CCSN-He, and 4 CCSN-C. Electron-capture SNe also contribute a considerable

Figure 2.6: Distribution of eccentricities of OB+NS binaries with the types of SNe indicated [green for electron-capture supernova; red for helium-envelope-stripped SN (CCSN-C); purple for hydrogen-envelope-stripped SN (CCSN-He)].

fraction at orbital period around 200 days, where the second dredge up of primary star is avoided due to mass transfer, making ECSNe occurs more frequently (Podsiadlowski et al., 2004). He-envelope-stripped SN prefers narrow orbit since the binary has to be close enough to get the donor star deeply stripped. H-envelope-stripped SN does not show strong orbital period preference.

Figure 2.6 presents the distribution of eccentricities e of OB+NS binaries. Eccentricities e peaks at around 0.3. The OB stars of highly eccentric binaries have large chance to fill the Roche Lobe during periastron passage, which causes the number drop in the high-e region. Due to the difference in the magnitudes of kicks, ECSN mainly contributes binaries with $e \sim 0.3$, while stripped SN contributes most of high-e binaries.

We further present the distribution of OB+NS binaries in the $\log P_{\rm orb} - e$ plane in Fig. 2.7. Wide binaries trend to have high e since they are more easily disrupted than close binaries. The upper left edge is due to the Roche Lobe overflow during periastron passage.

We present the distributions of OB+cc binaries in the Hertzsprung–Russell diagram (HRD) in Fig. 2.8 (left panel for NS and right panel for BH). Since fast rotators dominate the population, the predicted population are generally cooler than the ZAMS stars. We expect all Be stars have spectral types earlier than B3, which is consistent with the observed spectral types of the SMC BeXBs (McBride et al., 2008). Both BH and NS prefer $\log L/L_\odot$ about 4, corresponding to $10\,M_\odot$. Above about $10^5 L_\odot$, only BH systems remains. For these massive OB stars, happening of envelope inflation makes them much cooler than ZAMS.

2.3.4 Properties of OB+BH binary systems

Figure 2.9 gives an overview of the properties of the predicted OB+BH binaries in the SMC. The upper panel presents the distribution in the OB star mass $M_{\rm OB}$ - BH mass $M_{\rm BH}$ plane. Our OB+BH binaries mostly concentrate in the area with $M_{\rm OB} \simeq 10\,M_\odot$ and $M_{\rm BH} \simeq 6\,M_\odot$. For the OB star mass, the number drop towards higher masses is caused by the effect of the IMF. Below $10\,M_\odot$, the chance decreases that the pre-SN star is massive enough for BH formation. The BH mass distribution is also affected by the IMF. The lightest BH we predict is about $4.9\,M_\odot$. The pre-SN star is $6.6\,M_\odot$. About $0.5\,M_\odot$ helium-rich envelope is ejected. After that $1.2\,M_\odot$ is lost due to the release of gravitational binding energy. The most massive BH is about $35\,M_\odot$, whose mass ejection is set by PPISN Marchant, Renzo et al. (2019).

The middle panel of Fig. 2.9 presents the distribution in the OB star mass - logarithmic orbital period $\log P_{\rm orb}$ panel. The majority of our OB+BH binaries have orbital periods around 100 days. Above 3000 days, binaries are broadened by PPISNe. Due to the difference in tides, OBe feature dominates wide binaries ($P_{\rm orb} > 10$ days), while slow rotators dominate close binaries. A small amount of wide binaries contain slow rotators because of wind braking. Massive OB stars are more likely to be produced in close binaries due to the rather high accretion efficiency, where the highest OB star mass is about $70\,M_\odot$. Otherwise, the masses are limited by strong stellar wind. Our model even expect OB stars above $90\,M_\odot$, which are very rare and not presented in the figure. Comparing with the orbital period distribution of NS binaries (Fig. 2.5), the signatures of the different modes of

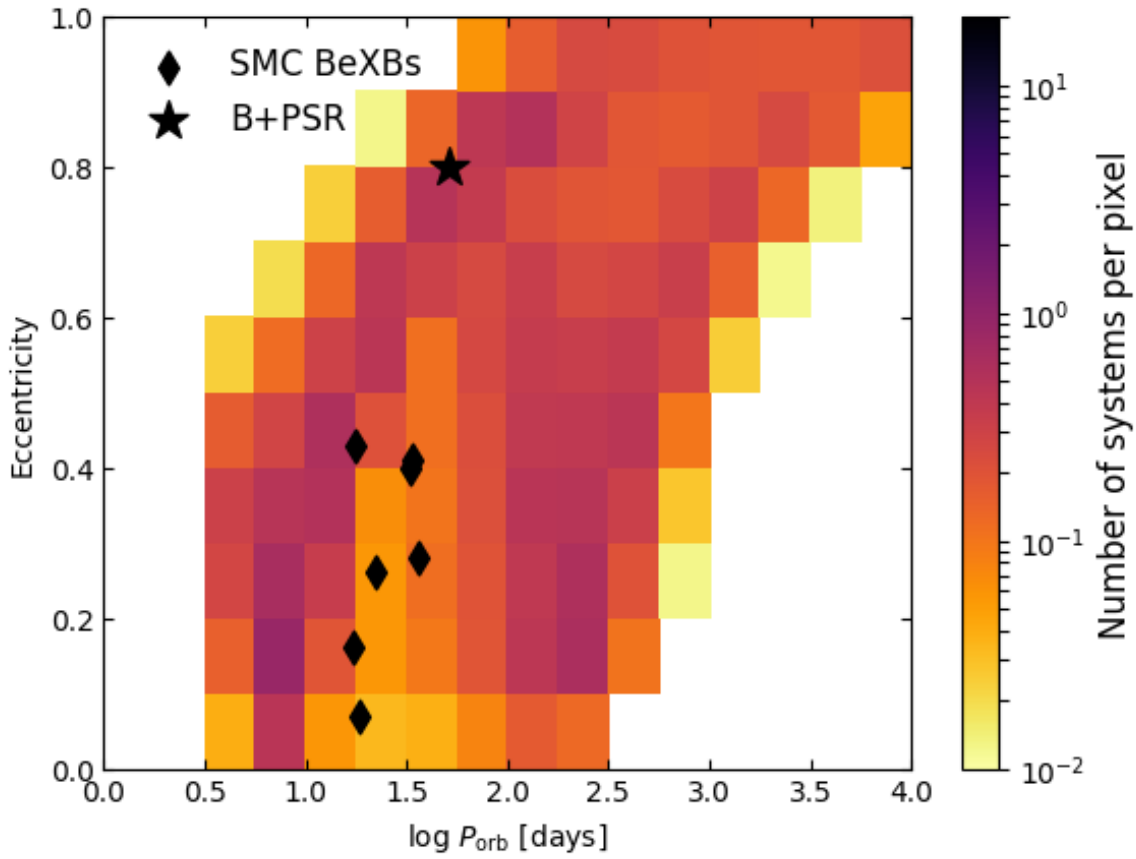

Figure 2.7: Predicted OB+NS binaries in the logarithmic orbital period - eccentricity plane. The number in each pixel is color-coded.. There are 7 SMC Be X-ray binaries having eccentricity measurements (L. J. Townsend et al., 2011; Coe and Kirk, 2015), indicated by black diamonds. The B star + radio pulsar binary (Kaspi et al., 1994; Bell et al., 1995) is indicated by black star.

mass transfer disappear. The reason is that the parameter space of BH formation is much larger than that of NS formation (see Fig. A.2).

The lower panel of Fig. 2.9 presents the distribution in the OB star mass - orbital velocity semi-amplitude of OB star $K_{\rm OB}$ plane. Here, $K_{\rm OB}$ is defined by

$$K_{\rm OB} = \frac{M_{\rm cc}}{(M_{\rm cc} + M_{\rm OB})} \sqrt{\frac{G(M_{\rm cc} + M_{\rm OB})}{a(1-e^2)}}, \tag{2.9}$$

where $M_{\rm cc}$ is the mass of compact object. For BH systems, the effect of e can be ignored since no BH kick is assumed in our fiducial model. Corresponding to the orbital period of 100 days seen in the middle panel, our OB+BH binaries have $K_{\rm OB}$ peaking near 40km s^{-1}. The highest $K_{\rm OB}$ we predict is about 250km s^{-1}, which is near the initial orbital period boundary between stable mass transfer and L2 overflow (see Figs. 2.2, A.1, and A.2).

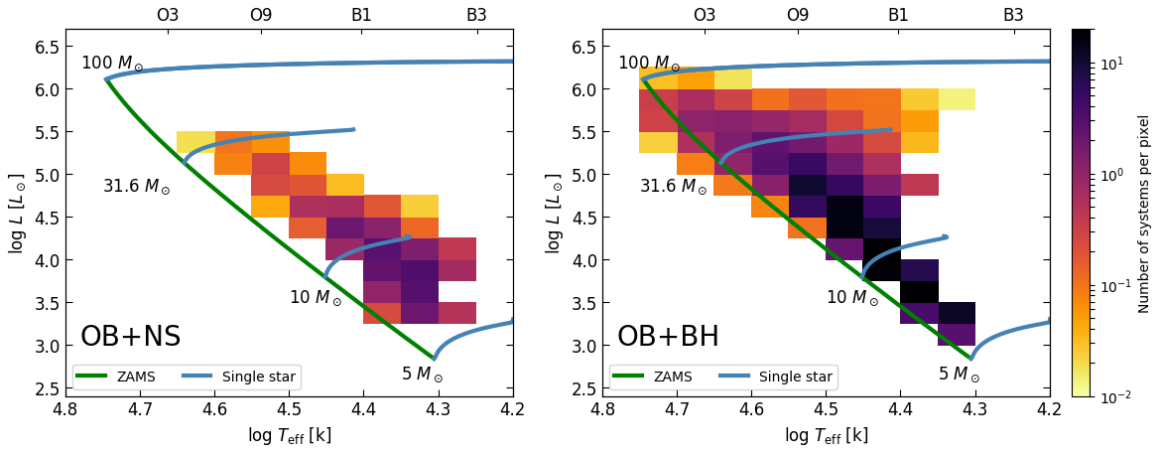

Figure 2.8: Distribution of OB+NS (left) and OB+BH binaries (right) in the Hertzsprung–Russell diagram. The green line is the zero-age main sequence. The blue lines are the evolutionary tracks of non-rotating single stars, where the initial masses are indicated by the texts near the zero-age main sequence.

2.4 Parameter variations

In this subsection, we perform a parameter study to explore the effects of several of our assumptions on our results. To do this we introduce the following population synthesis models:

- Kick-265: the distribution of kick velocities is taken to be the Maxwellian distribution with $\sigma = 265\mathrm{km\,s^{-1}}$ for all types of SNe;
- Kick-0: Kick velocities are fixed to zero;
- Kick-BH: we take a flat distribution in [0, 200]$\mathrm{km\,s^{-1}}$ for natal kick imparted to newborn BHs (Kruckow et al., 2018; Schürmann, Langer, X.-T. Xu et al., 2023);
- logPq-flat: the initial distributions of $q_{\rm i}$ and $\log P_{\rm orb,i}$ are taken to be flat distributions;
- SFH-S: we assume a SFR rapidly decrease to zero within last 7 Myrs (see the upper panel in Fig. 2.11), which is proposed to explain the dearth of young massive stars in the SMC (Schootemeijer, Langer, D. Lennon et al., 2021);
- SFH-R: we assume a SFR with a recent peak $\sim 20-40$ Myrs ago (see the lower panel in Fig. 2.11), which is inferred from the VMC survey (Rubele, Girardi et al., 2015);
- $\upsilon_{\rm crit}$-0.98: the threshold value of $\upsilon_{\rm rot}/\upsilon_{\rm crit}$ for defining OBe stars is taken to be 0.98;
- $\upsilon_{\rm crit}$-0.8: the threshold value of $\upsilon_{\rm rot}/\upsilon_{\rm crit}$ for defining OBe stars is taken to be 0.8;
- NS-limit: we assume all stars with $M_{\rm He,c} > 6.6\,M_\odot$ end up with NSs.

Table 2.3 summarizes the predictions of these different models. Figure 2.10 compares the

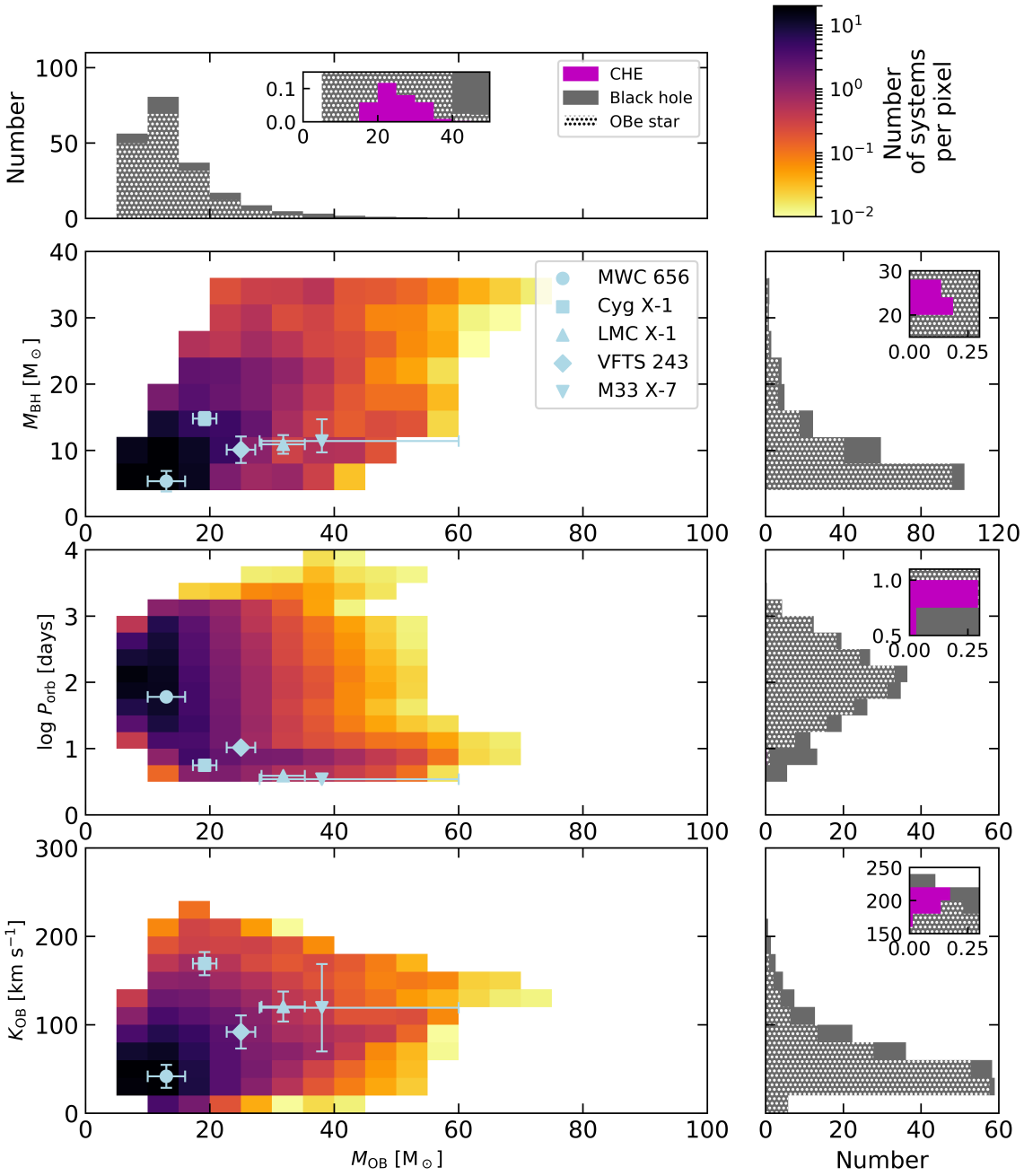

Figure 2.9: Predicted OB+BH binaries in the OB star mass M_{OB} - BH mass M_{BH} plane (upper panel), OB star mass - logarithmic orbital period log P_{orb} (middle panel), and OB star mass - orbital velocity semi-amplitude of OB star K_{OB} (lower panel). The Be feature and CHE BHs are indicated in the 1D projection. The number in each pixel is color-coded. The observed BH systems are overplotted, which are MWC 656 (Casares et al., 2014), Cyg X-1 (Orosz, McClintock, Aufdenberg et al., 2011), LMC X-1 (Orosz, Steeghs et al., 2009), M33 X-7 (Ramachandran et al., 2022), and VFTS 243 (Shenar, Sana et al., 2022). The values of K_{OB} for observed systems are calculated by Eq. (2.9) with the observed masses and orbital periods. The errors are calculated by error propagation.

distributions of orbital periods and the V-band magnitude[2] of OB stars in OB+cc binaries. Except the SFH-S model, our population synthesis models always expect over 1000 O stars in the SMC. Except the NS-limit model, we always predict a large population of wide-orbit OBe+BH binaries in the SMC, which have V-band magnitude about 16-17. For the NS population, the discrepancy between our predictions and observation can not solved by changing our assumptions in a reasonable range, suggesting that the main factor limiting our NS population is the merger criterion. Now we discuss the differences among the predictions of these models in detail in the following subsections.

2.4.1 Natal kicks

Momentum kick imparted on newborn NSs is one of the major uncertainties for the formation of NS binaries. In this work, we adopt the same kick distributions as the ComBinE code, where the kicks from ECSNe and stripped SNe are included. Observationally, the constraint on kick velocity is still inconclusive. The eccentricity of high-mass X-ray binaries (Pfahl et al., 2002) and double pulsar binaries (Vigna-Gómez et al., 2018) imply that stripped SNe produce weak momentum kick. (Hobbs et al., 2005) found the spatial velocity of young pulsars can be described by the Maxwellian distribution with $\sigma = 265\mathrm{km\,s^{-1}}$. With a sample of 28 young pulsars having VLBI measurements, Verbunt, Igoshev and Cator (2017) suggests that there is a slow-moving group of young pulsar.

To account for different kick velocities, we consider two extreme models: i) Kick-265 and ii) Kick-0. Comparing with the fiducial model, OBe+NS binaries given by the Kick-265 model is reduced from 21 to 3 and OB+NS binaries from 4 to 2. Almost all Case B binaries are disrupted (see the upper left panel of Fig. 2.10). On the other hand, there is no disruption in the Kick-0 model. Consequently, the Kick-0 model predicts binaries have more wide-orbit binaries than the fiducial model. The upper right panel of Fig. 2.10 shows that the most probable value of OB star mass is in 8-10 $M_\odot$ through different kick models, while the predicted number in 8-10 $M_\odot$ is highly reduced by increasing kick velocities. In addition, different kick velocities can change the age when the OB star fills the Roche Lobe during the OB+NS phase, which makes the total number of NS systems (NS binaries + disrupted systems) slightly different through these models.

Newborn BH may receive momentum kicks due to partial material fallback (Janka, 2012). We examine the effect BH kicks in the Kick-BH model. There are 30 OB+BH binaries and 96 OBe+BH binaries. There are 83 BH binaries disrupted by kicks, which largely reduces the number of the binaries with 100 days orbital period and 10 $M_\odot$ OB star.

2.4.2 Initial distributions

The initial distributions adopted in the fiducial model prefer close binaries and low mass ratio (see Eq. (2.8) and (2.7)). We change to flat distribution for q_i and $\log P_\mathrm{orb,i}$ in the logPq-flat model.

Comparing with the Sana distributions (Sana et al., 2012), flat distribution has a larger fraction of wide-orbit binaries. Hence the logPq-flat model predicts more OB+cc binaries in 100 - 300 days and less below 20 days than the fiducial model (Fig. 2.10). The total number of BH systems is boosted from 211 to 268. While the total number of NS binaries roughly keeps unchanged, there are more disrupted systems. The increased fraction of wide binaries leads to a larger fraction of fast rotating

[2] V-band magnitude: the distance modulus of the SMC is taken to be 18.91 (Hilditch, Howarth and Harries, 2005) and we calculate the bolometric correction by using a polynomial fit to MIST values (Dotter, 2016; Choi et al., 2016). Extinction and Be-correction are not included

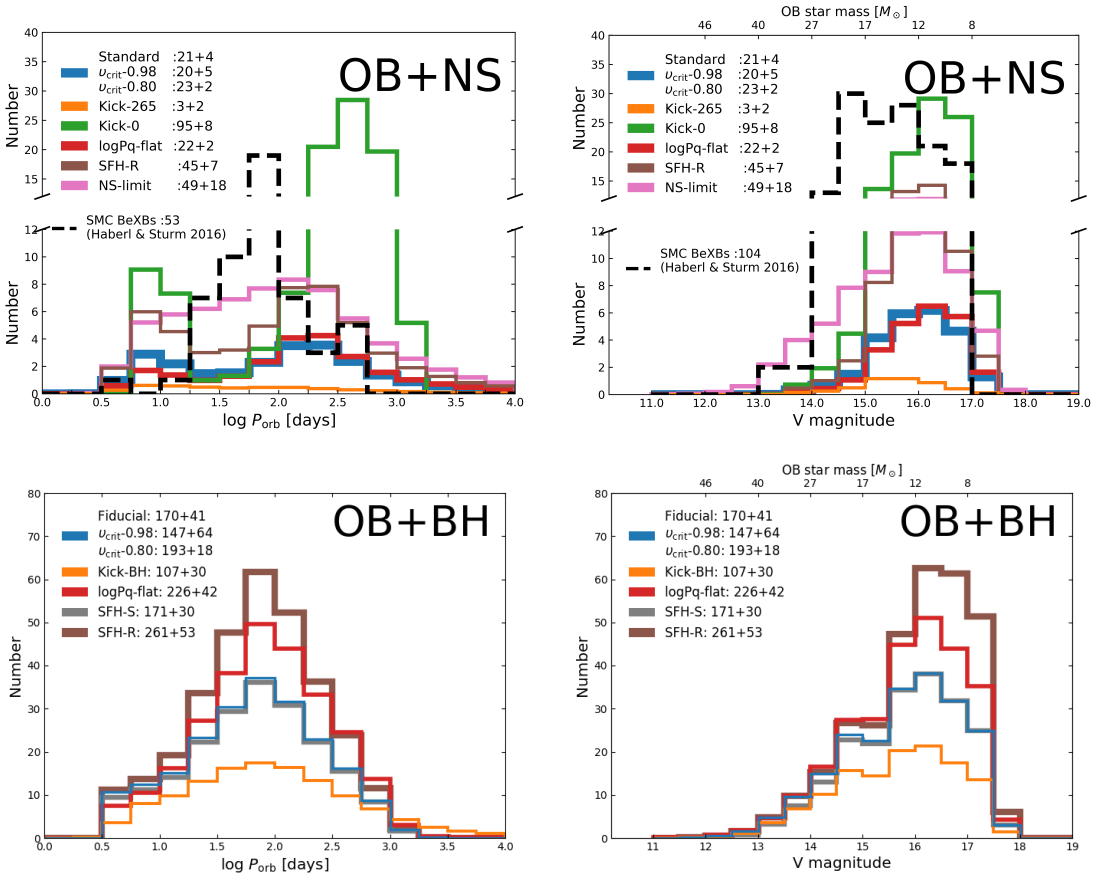

Figure 2.10: Parameter study on the properties of OB+cc binaries. The upper and lower rows present the properties of NS and BH populations. The left and right columns are the distributions of log P_{orb} and V-band magnitude. The predictions from different models are color coded. The two numbers indicate the predicted number of normal OB stars and OBe stars, e.g., fiducial: 21+4 means that our fiducial model expects 4 normal OB stars and 20 OBe stars. The models that have the same predictions as the fiducial models are not shown in the corresponding plots. The models υ_{crit}-0.98/0.80 alter the number of OBe stars but the total number of NS systems keeps unchanged. We therefore only present the predicted numbers in the legends. In addition, we also plot the observed SMC BeXBs in the upper panels with black dashed line. The observed orbital periods and V-band magnitudes of SMC BeXBs are from Haberl and Sturm (2016).

stars with V-band magnitude around 16. This effect is less significant for NS population than that for BH population because in our model the window allowing NS formation is much narrower than that of BH formation (Fig. 2.2).

The stripped stars formed in close binaries have relatively long lifetime and contribute a considerable fraction to the HeS population. Therefore, changing to a flat distribution slightly reduces the HeS number. On the other hand, the lifetimes of massive HeSs are roughly the same and the flat distribution gives more WR+O binaries.

2.4.3 Star formation history

Our fiducial model adopts a constant star formation rate with the typical literature value $0.05 M_{\odot}\ \mathrm{yr}^{-1}$. There are evidences suggesting non-constant star formation rate. The population of high-mass X-ray binaries in the SMC implies a peak in star formation rate tens of million years ago (Antoniou, Zezas, Hatzidimitriou et al., 2010; Antoniou, Zezas, Drake et al., 2019), which may be questionable (Schootemeijer, Langer, D. Lennon et al., 2021; Schürmann, Langer, X.-T. Xu et al., 2023). Rubele, Girardi et al. (2015) identified two peaks at ~ 30 Myrs and ~ 5 Gyrs. Rubele, Pastorelli et al. (2018) confirmed the existence of the bi-modality, while the recent peak was shifted to recent 10 Myrs. On the other hand, Schootemeijer, Langer, D. Lennon et al. (2021) found that one needs star formation rate decreases to zero with 7 Myrs to explain the dearth of young massive stars in the SMC.

To account the effects of different star formation histories, we construct two models SFH-S and SFH-R (see Fig. 2.11 for the star formation histories adopted in these two models). In the SFH-S model, star formation history decreases to zero, while in the SFH-R model star formation is most efficient 30 Myrs ago.

All NS systems have ages older than 7 Myrs and therefore do not get affected by the SFH-S model. For BH systems, the SFH-S model reduces the number of BH+OB binaries from 40 (the fiducial model) to 30. The SFH-S model expects 403 O stars in the SMC. Considering a peak in star formation rate 30 Myrs age can significantly enhance the number of OB+cc populations, where NS and BH systems are respectively boosted by factors about 2 and 1.5. Since BH progenitors are short-lived comparing with NS progenitors, BH population is less affected by this star formation history. Due to the same reason, the number of O stars is not sensitive with the star burst model.

2.4.4 Be phenomenon

R. H. D. Townsend, Owocki and Howarth (2004) proposes that most of Be stars are very close to their critical rotation. Following this idea, we assume that a star shows the Be phenomenon when it reaches $0.95\upsilon_{\mathrm{crit}}$. However, sub-critically rotating Be stars are observed (Rivinius, Carciofi and Martayan, 2013, and references therein). Recent study shows that Be stars can rotate at $0.68\upsilon_{\mathrm{crit}}$ (Dufton, D. J. Lennon et al., 2022). To account the uncertainties in defining OBe stars, we set the threshold value of $\upsilon_{\mathrm{rot}}/\upsilon_{\mathrm{crit}}$ to be 0.98 and 0.80 in the υ_{crit}-0.98 model and υ_{crit}-0.8 model respectively.

Our results show that the effects of changing the $\upsilon_{\mathrm{rot}}/\upsilon_{\mathrm{crit}}$ threshold value are only considerable in the high-mass end, where wind braking becomes significant. Increasing the $\upsilon_{\mathrm{rot}}/\upsilon_{\mathrm{crit}}$ threshold from 0.80 to 0.98, we expect BH+OBe binaries decreasing 194 to 147 and WR+Oe binaries 2 to 5.

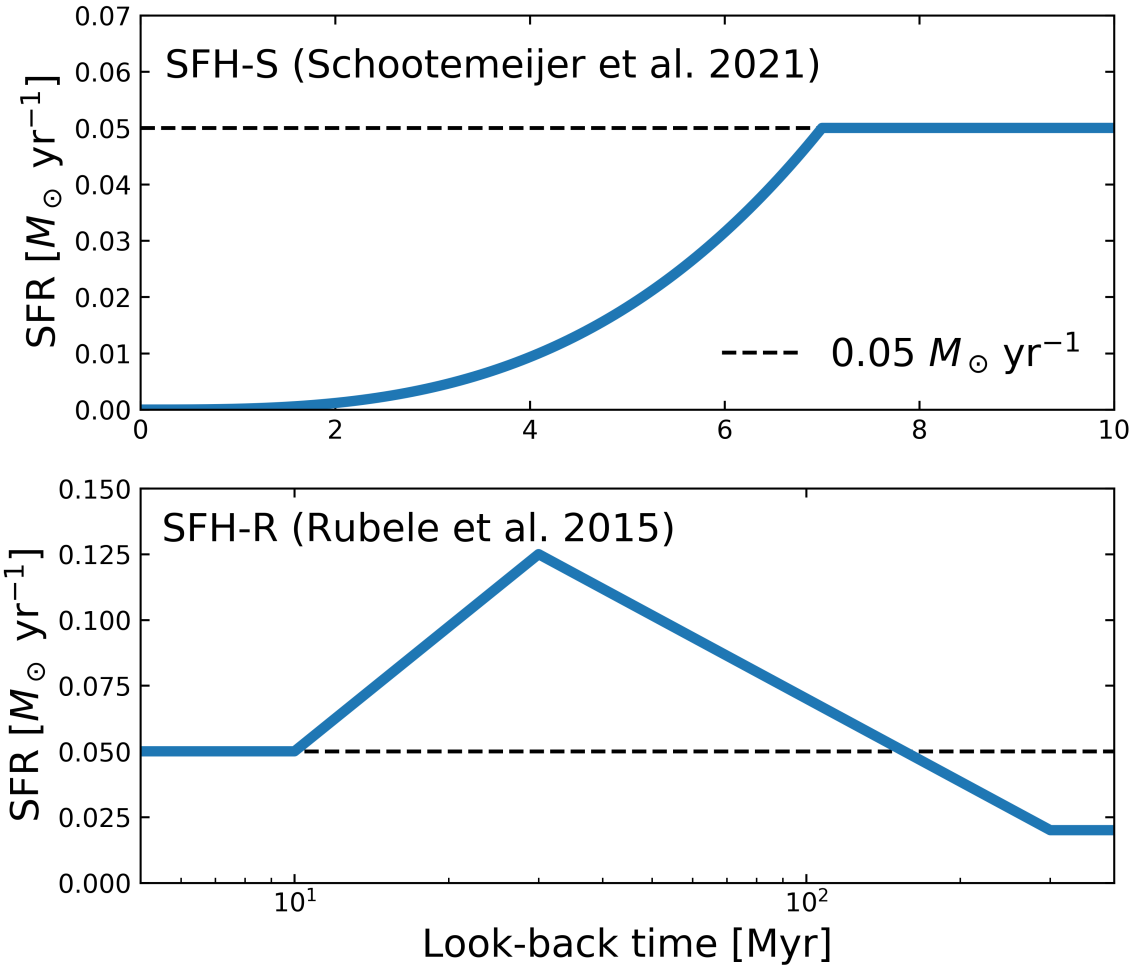

Figure 2.11: The star formation history adopted in the model SFH-S (upper panel, Schootemeijer, Langer, D. Lennon et al., 2021) and SFH-R (lower panel, Rubele, Girardi et al., 2015), where the dashed lines indicate the constant SFR $0.05 M_\odot$ yr^{-1} adopted in the fiducial model.

2.4.5 Boundary between BH and NS

In the fiducial model, if a star haves helium core mass $M_{\rm He,c}$ larger than 6.6 $M_\odot$ at the core helium depletion, we expect it to produce a BH. This assumption is based on the detailed simulation on the compactness of pre-SN stars (Sukhbold, Woosley and Heger, 2018). In order to examine how this assumption affects our NS population, here we consider an extreme case (the NS-limit model) that all stars with $M_{\rm He,c}$ exceeding 6.6 $M_\odot$ end up with NSs.

While the fiducial model predicts over 200 BHs, the NS-limit model only predicts 66 NS binaries because natal kick is included and more mass is ejected during SN than the case of BH. The systems with orbital periods between 10 and 300 days are largely enhanced so that the bi-modality found in the fiducial model is smoothed out The V-band magnitude can reach up to 13.

2.5 Comparisons with observations

2.5.1 OBe stars

Our fiducial model predicts 1254 O stars in the SMC, which includes the O stars in pre- and post-interaction binaries, which drops to 403 in the SFH-S model (Sect. 2.4.3). Here merger product is not counted. This result is consistent with the result of (Schootemeijer, Langer, D. Lennon et al., 2021) that there should be over 1000 O stars in the SMC but only 259 observed[3] and this dearth of young mass stars can be explained by a decreasing star formation rate. However, the SFH-S model only predicts 3 WR+O binaries, which is below the observed number. O stars can also be produced by the merger of MS+MS binaries, which takes place in close binaries with low initial mass ratios. With increasing initial primary mass, the parameter space of MS+MS merger narrows. Therefore, we do not expect our result to be largely affected by merger products.

Most OB stars keep rotating close to critical unless they undergo strong wind braking (Fig. 2.3). This suggests that we have a large chance to find compact objects in OBe star binaries. This conclusion is independent with our assumptions (see Sec. 2.4). While the OBe fraction predicted in post-interaction binaries exceeds 80%, it drops to about 7% if the OB stars in pre-interaction binaries are included (Fig. 2.12), which is below the observed OBe fraction in the SMC (Schootemeijer, D. Lennon et al., 2022). This discrepancy also suggests that our merger criterion is too restrictive at the low-mass end.

2.5.2 Wolf-Rayet stars

There are 12 WR stars observed in the SMC, where 4 are WR+O binaries and 1 WR+WR binary (Foellmi, Moffat and Guerrero, 2003; Foellmi, 2004; Koenigsberger et al., 2014; Hainich et al., 2015; Shenar, Hainich, Todt, Sander et al., 2016; Shenar, Hainich, Todt, Moffat et al., 2018; Schootemeijer and Langer, 2018). We expect 7 WR+O(e) binaries in the SMC, which is consistent with the observed number. In addition, we expect $\sim$ 0.2 H-free WR stars and one observed (SMC AB8 Shenar, Hainich, Todt, Sander et al., 2016). Due to the small sample size, this may not be a discrepancy. We expect 3 WR+Oe binaries but all observed O star companions seem to be slow rotators (projected velocities below $\sim$ 200 km s^{-1}, Shenar, Hainich, Todt, Sander et al., 2016; Shenar, Hainich, Todt, Moffat et al.,

[3] The sample adopted in Schootemeijer, Langer, D. Lennon et al. (2021) contains 780 stars, whose completeness is about 40% - 50%. Adopting the O star fraction obtained from population synthesis (Tab. 2 in Schootemeijer, Langer, D. Lennon et al., 2021), it results in over 1000 O stars in the SMC.

Table 2.3: Predicted population with different initial conditions. The predictions of fiducial model are listed for comparison purpose, which are computed by the Kroupa IMF (Eq. 2.6), the Sana distributions for initial mass ratios and orbital periods (Eq. 2.7 and Eq. 2.8) with our fiducial kick velocity distributions (Tab. 2.1). Be feature is assumed with $\upsilon_{\rm rot}/\upsilon_{\rm crit} > 0.95$ and BH forms with He core mass above 6.6 $M_{\odot}$ at the core He depletion. We vary these assumptions in different models (see text). In the table, "=" means the same value as the fiducial model.

	Fiducial[a]	Kick-265	Kick-0	Kick-BH	logPq-flat
WR+O	3	=	=	=	=
WR+Oe	4	=	=	=	5
H-free WR	0.22	=	=	=	0.20
He+OB	12	=	=	=	8
He+OBe	223	=	=	=	200
BH+OB	40	=	=	30	42
BH+OBe	171	=	=	96	226
NS+OB	4	2	8	=	2
NS+OBe	21	3	95	=	22
OB disr.	3	5	0	2+8	2
OBe disr.	71	91	0	71+75	93
O stars	1254	=	=	=	1139
	SFH-S	SFH-R	$\upsilon_{\rm rot}$-0.98	$\upsilon_{\rm rot}$-0.8	NS-limit
WR+O	1	=	5	2	=
WR+Oe	2	=	2	5	=
H-free WR	0.04	0.23	=	=	=
He+OB	10	15	15	9	=
He+OBe	221	347	220	226	=
BH+OB	30	53	64	17	0
BH+OBe	171	261	147	194	0
NS+OB	=	7	5	2	4+14
NS+OBe	=	45	20	23	21+28
OB disr.	=	5	3	1	2+25
OBe disr.	=	155	71	73	71+138
O stars	403	1256	=	=	=

Notes. [(a)] The fiducial model is listed for comparison purpose and see section 2.4 for the definitions of other models; [(b)] "=" means the same value as in the fiducial model; [(c)] The runway OB and OBe stars from disrupted binaries.

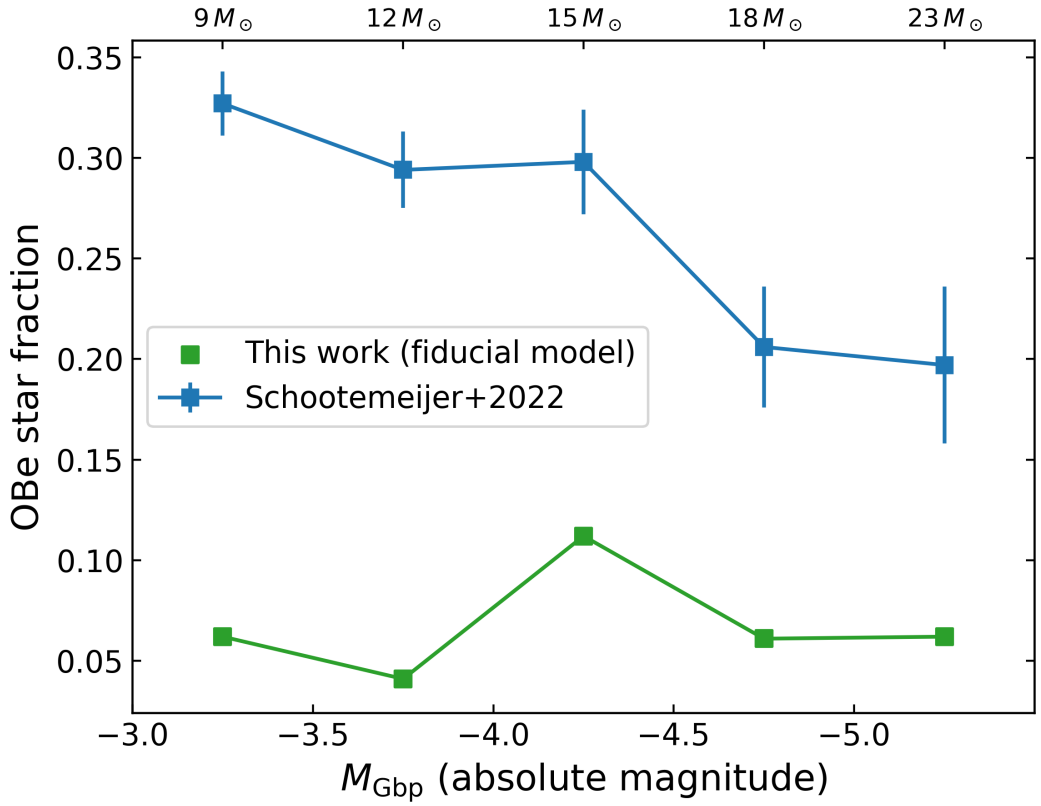

Figure 2.12: Predicted OBe star fraction by our fiducial model as a function of absolute magnitude (green). The OB stars in pre-interaction binaries are included. The observed OBe star fraction is plotted with blue (Schootemeijer, D. Lennon et al., 2022). On the top we show the averaged evolutionary mass in each bin (Schootemeijer, D. Lennon et al., 2022).

2018). This may suggest that the circumstellar disc is easily disrupted by O star or our evolutionary models underestimate the effect of wind braking.

As already shown in Fig. 2.4, the observed parameters of all WR binaries can be covered by our prediction. Particularly, the only WO+O system SMC AB8 is covered by our H-free models ($\log T_{\mathrm{eff}}/\mathrm{K} > 5.1$). SMC AB7 is near the H-free region and observationally this WR stars has the lowest surface hydrogen abundance compared to SMC AB6 and SMC AB3. SMC AB6 was found to have super-Eddington luminosity (Shenar, Hainich, Todt, Sander et al., 2016) but was later identified as part of a high-order multiple system (Shenar, Hainich, Todt, Moffat et al., 2018). For the double WR star binary SMC AB5, it may be formed through the tide-induced chemically homogeneous evolution in equal-mass binaries (S. E. de Mink and Mandel, 2016; Marchant, Langer, Podsiadlowski, Tauris and Moriya, 2016), which is beyond the scope of this work.

All observed systems have projected orbital velocities above $150\,\mathrm{km\,s^{-1}}$ and orbital periods below 20 days, which can be covered by our predictions (bottom panel of Fig. 2.4). Above orbital period of 20 days, our fiducial model predicts 4 WR+O binaries. It may be their small orbital velocities ($40...60\,\mathrm{km\,s^{-1}}$) that makes them difficult to be identified in past observations. On the other hand,

below orbital period of 10 days a considerable fraction of binaries with velocities above 150km s^{-1} is also missing in observations. The reason may be that the WR stars outshine their companions due to their rather high mass ratios ($M_{\rm WR}/M_{\rm O} > 0.6$, Fig. A.4)[4]. If these high-mass-ratio WR+O binaries do not exist, it may require a different merger criterion or a different orbital evolution history for the binaries with low initial mass ratios.

For CHE, the observed O+WR binaries are unlikely to be formed from this scenario. Only SMC AB8 is hot enough to reach the CHE region. However, it has wider orbital period than the CHE region. Moreover, CHE produces mass ratio over one, while the observed values are below 0.6 (Fig. A.4).

In addition, our prediction can cover the observed apparently single WR stars (the top panel in Fig. 2.4). Therefore it would not be surprising if these single WR stars have undetected companions. For SMC AB2 and AB4, their cool surface temperature may suggest that they are core-hydrogen-burning WR stars (Schootemeijer and Langer, 2018), formed from the initial secondary stars (Pauli et al., 2023), or shallowly-stripped core-helium-burning WR stars (this work).

2.5.3 Be/X-ray binaries

There are about 150 high-mass X-ray binaries are found in the SMC, while about 100 of them are identified to be Be X-ray binaries (Haberl and Sturm, 2016). However, our fiducial model only predicts 25 OBe+NS binaries (Sect. 2.4). This large difference is mainly caused by our merger criterion, which leads to a high merger rate below the initial primary mass of 20 $M_\odot$ (see Fig. 2.2 and App. 3.2). This may be solved by a different merger criterion (see Sect. 2.7.1). While most NSs have B(e) type companions, O+NS binaries can exist but are very rare (Fig. 2.3). Due to their extreme mass ratio and narrow orbit, they should merge due to the common envelope evolution once the O star fills the Roche Lobe.

Observationally, Knigge, Coe and Podsiadlowski (2011) found two subpopulations of Be X-ray binaries, which are featured by close orbits with slow pulsation periods and wide orbits with long pulsation periods. We find a similar feature in our $\log P_{\rm orb}$ distribution of Be+NS binaries , which is generated by our merger criterion and the two peaks are related to Case A and Case B binaries respectively. About pulsation periods, our model does not include the spin evolution of X-ray pulsars. The observed bimodal feature in pulsation period distribution could be understood by supernova mechanism (Knigge, Coe and Podsiadlowski, 2011) or accretion modes (Cheng, Shao and X. .-. Li, 2014; X.-T. Xu and X.-D. Li, 2019). We note that there is no observed BeXB with $P_{\rm orb} < 10$ days, while we find a considerable fraction of Be+NS binaries in such close orbits. This difference could be explained by the tide-induced disk truncation. Okazaki and Negueruela (2001) have shown that in low-eccentricity binaries the gap between the circumstellar disc and the L1 point is so large that the NS can not generate strong X-ray emission. The observed supergiant X-ray binaries SMC X-1 is close to the Roche-lobe filling and has an orbital period of 3.9 days (Rawls et al., 2011; Falanga et al., 2015), which may imply the existence of these close B+NS binaries.

As shown in Fig. 2.7, observed BeXBs have eccentricity e below 0.4 (R. H. D. Townsend, Owocki and Howarth, 2004; Coe and Kirk, 2015), while we expect half of the population to have eccentricity above that. These high-e binaries also have wide orbit, making the periastron passages of NSs very fast and hence hard to be identified as BeXBs. Tidal circularization and the interaction between the NS and the Be disc, which may make binaries less eccentric, are not considered.

[4] This mechanism could also apply to wide WR+O binaries.

In the SMC, a B-type star + radio pulsar is observed (PSR J0045-7319 Kaspi et al., 1994; Bell et al., 1995). This binary is highly eccentric with an orbital period of 51 days (Fig. 2.7) but does not have X-ray emission. It could be formed through Case A mass transfer, after which the orbit widened due to supernova explosion.

2.5.4 BH-binaries

There are four confirmed O+BH binaries, Cyg X-1 (Orosz, McClintock, Aufdenberg et al., 2011), LMC X-1 (Orosz, Steeghs et al., 2009), M33 X-7 (Orosz, McClintock, Narayan et al., 2007; Ramachandran et al., 2022), and VFTS 243 (Shenar, Sana et al., 2022). The first three sources are wind-fed X-ray binaries. The recently discovered VFTS 243 is X-ray quiet and has the widest orbit ($\sim$ 10 days). M33 X-7 was reported to have a 70 $M_\odot$ O star and a 15.6 $M_\odot$ BH (Orosz, McClintock, Narayan et al., 2007), which was recently revised to be 38 $M_\odot$ for the O star and 11.4 for the BH (Ramachandran et al., 2022). While the Be+BH nature of MWC 656 (Casares et al., 2014) is challenged by new spectral data (Rivinius, Klement et al., 2022), We still include it as an OB+BH binary. As seen in Fig. 2.9, we can explain the observed BH binaries. The observed BH masses ($\sim$ 10 $M_\odot$) are close to the low end of the IMF MWC 656 matches the peak values of our OB+BH population very well. All observed O+BH binaries have orbital periods below 10 days, where only 10% of our OB+BH binaries is located. Wider binaries are missing may be due to their low orbital velocities. In addition, our model suggests that the observed O+BH binaries can not be formed from the CHE since the observed BH masses are far below the values predicted by CHE.

In our synthetic population, most BHs have a fast-rotating MS companion. Particularly, most Oe star binaries contain BH companions (Fig. 2.3). This suggests that observationally we have a large chance to find BHs by examining fast-rotating O stars. Besides Oe star, we expect many Be stars also have BH companions like MWC 656.

There are 780 massive stars are observed in the SMC with $\log L/L_\odot > 4.5$ (Bonanos et al., 2010; Schootemeijer, Langer, D. Lennon et al., 2021). Schootemeijer, Langer, D. Lennon et al. (2021) pointed out that many young massive stars could still be embedded in their birth cloud, which leads to about missing 300 O stars. Our model expects about 71 OB+BH binaries in this luminosity range. Hence we would expect 7-10% of the observed SMC massive stars to have BH companions.

2.6 Comparisons with previous works

In parallel with this work, Schürmann, Langer, X.-T. Xu et al. (2023) studied the population of SMC OB+cc binaries with the rapid evolution code ComBinE (Kruckow et al., 2018, and references therein), which arrives at the similar conclusion that there is a large population of undiscovered wide-orbit OB(e)+BH binaries in the SMC.

The key differences between the two works lies in the accretion efficiency and merger criterion. Schürmann, Langer, X.-T. Xu et al. (2023) assume a fixed accretion efficiency and use the overflow of the outer Lagrangian point to determine the stability of mass transfer. During mass transfer, the mass gainers could expand significantly, reaching the outer Lagrangian point and then triggering unstable mass transfer. In their study, Schürmann, Langer, X.-T. Xu et al. (2023) connect the swelling of the accretor to the accretion efficiency by the thermal imbalance in the mass changing star. With this criterion, the authors find that it requires an average $q_{\rm min}$ of around 0.5 at an accretion efficiency

of around 0.6 to explain the observed BeXBs. However, their model, even at the highest accretion efficiencies, underpredicts the total number of Be stars by a factor of about 2. In our MESA models, wide binaries have a near-zero accretion efficiency and we assume that mass transfer becomes unstable if radiation is not powerfully enough to eject accreting material when mass gainers rotate critically. This assumption can fit the observed WR binaries but can only form 1/4 of the observed BeXBs. Schürmann, Langer, X.-T. Xu et al. (2023) also find that fitting the SMC WR+O binaries requires lower average $q_{\rm min}$ (~ 0.3) at a lower accretion efficiency (below 0.1). In addition, Schürmann, Langer, X.-T. Xu et al. (2023)'s merger criterion predicts that close binaries have more chance to undergo stable mass transfer than wide binaries, which may explain the current lack of massive evolved binaries in observations.

ComBinE and MESA treat the stripping by mass transfer differently. ComBinE assumes that the envelope of donor is completely lost after the mass transfer, while MESA expects almost all stripped stars to have a H-rich outer layer. As pointed out by Laplace, Götberg et al. (2020), this H-rich outer layer can expand to very large radius, which can fill the Roche Lobe. This largely widens the parameter space for interacting stripped star compared to rapid code like ComBinE (Kruckow et al., 2018) and BSE (Hurley, Tout and Pols, 2002). We notice that many models get terminated when their H-rich envelope still fills their Roche Lobe. It is unclear whether this process has effect on kick velocities.

Langer, Schürmann et al. (2020) studied the OB+BH binaries in the LMC by using a detailed binary model grid computed by the MESA code with the LMC metallicity. This LMC binary model grid was computed with the same MESA version and the same input physics (except metallicity) as the SMC model grid adopted in this work. Higher metallicity leads to stronger stellar wind, which widens the orbital periods a little bit. The properties of OB+BH binaries predicted by our work are quite similar to that by Langer, Schürmann et al. (2020) that the authors also expect a large fraction of wide-orbit OB+BH binaries. In particular, the LMC model grid adopts the same merger criterion as we do, resulting in a clear bi-modal feature in the orbital period distribution of the LMC OB+BH binaries (Langer, Schürmann et al., 2020). About the BH formation, we calculate BH mass differently. While Langer, Schürmann et al. (2020) takes the He core mass at core He depletion as the mass of BHs, we include the effect of fallback and the release of gravitation binding energy, which makes our BHs generally lighter than that in Langer, Schürmann et al. (2020). In the high-mass end, PPISNe is considered in this work, producing most massive BH about $30\,M_{\odot}$. The maximum initial primary mass of the LMC model grid is about $40\,M_{\odot}$, which corresponds to a $20\,M_{\odot}$ BH. Due to the same reason, strong envelope inflation does not take place in Langer, Schürmann et al. (2020).

2.7 Discussion

2.7.1 Stability of mass transfer

The major uncertainty of this work comes from our merger criterion. Different from the commonly adopted criterion proposed by Soberman, Phinney and van den Heuvel (1997), we further take into account the ability of driving wind of critically rotating star during mass transfer. According to this assumption, the minimum mass ratio of stable mass transfer $q_{\rm min}$ highly depends on stellar mass and orbital period. On average we obtain $q_{\rm min} > 0.6$ in the low-mass end and close to 0.3 in the high-mass end. This assumption works well in the high-mass end but produces too many mergers in the low-mass end. While Soberman, Phinney and van den Heuvel (1997) give $q_{\rm min}$ about 0.2-0.3 (also see Vinciguerra et al., 2020), many works suggest that $q_{\rm min}$ is about 0.5 if the donor star is in

the Hertzsprung gap (Pols, Cote et al., 1991; Hurley, Tout and Pols, 2002; Shao and X.-D. Li, 2014; Schürmann, Langer, X.-T. Xu et al., 2023). However, these population synthesis works assume a high accretion efficiency, which is physically motivated because it allows critically rotating stars to keep accrete angular momentum. On the other hand, Hastings, Langer, Wang et al. (2021) found that the Be fraction in clusters may suggest a mass-dependent $q_{\rm min}$. Hence it seems that our model is in the right direction.

The idea proposed by Pauli (2020) may help us to get one step further. During mass transfer, the luminosity of the donor is largely reduced and binary can easily merge according to our criterion. Pauli (2020) suggests that binary does not merge immediately. The accreted material could stay around the system and can be expelled once the star restores equilibrium. This assumption allows much more Be stars to survive mass transfer (see section 3.3.3 in Pauli, 2020).

2.7.2 Accretion efficiency

In our binary models, the accretor can not accrete any more if it rotates critically. During the mass transfer phase, the accretor can be easily spun up if tide is weak. As a consequence, the mass transfer efficiency depends on the orbital periods. In Case B binaries it is close to zero, while in Case A binaries mass transfer efficiency can be up to 60%, which is still far below the conservative case. This feature has already been noticed by S. E. de Mink, Pols and Hilditch (2007). The authors investigated a sample of 50 double-lined eclipsing binaries in the SMC. Their best fitting mass transfer efficiency trends to decrease with orbital period (cf. Fig.7 in S. E. de Mink, Pols and Hilditch, 2007). This rotation-dependent accretion efficiency can explain the observed massive Algol systems (Sen, X.-T. Xu et al., 2021) and the observed WR+O binaries (Petrovic, Langer and van der Hucht, 2005; Shao and X.-D. Li, 2016, and this work).

On the other hand, some population synthesis works on Be X-ray binaries suggest that the accretion efficiency can be up to 50%. Shao and X.-D. Li (2014) and Vinciguerra et al. (2020) investigated the Be X-ray binaries in the Milky Way and SMC respectively. Both of the works suggest high accretion efficiency. We notice that if they assume near-zero accretion efficiency, they always predicts too many low-mass Be stars, which is also found in the ComBinE results (Schürmann, Langer, X.-T. Xu et al., 2023). This could be solved by a different merger criterion. If wide-orbit binaries do have larger mass transfer efficiency, the mass of the OB stars will increase and make the mass ratio reverse more easily, leading to a wider orbit. Due to the increasing in mass, their main-sequence lifetime could be shorter. This effect can slightly reduce the predicted number of OB+BH binaries.

2.7.3 Supernova windows

The supernova windows play important roles by determining the magnitude of kick velocities. However, the resolution of our SMC model grid is not good enough to distinguish different types of SNe and we therefore adopt the SN windows computed by the ComBinE code (Kruckow et al., 2018; Schürmann, Langer, X.-T. Xu et al., 2023). Taking ECSN as an example, Podsiadlowski et al. (2004) proposed that binary interaction can broaden the mass window of ECSN. However, detailed simulations show that even including mass transfer it is still narrower than 1 $M_\odot$ (Poelarends, Wurtz et al., 2017; Siess and Lebreuilly, 2018). The ZAMS mass window computed by the ComBinE code is about [9.5, 10.2] $M_\odot$. However, around this mass range, the SMC model grid only have three mass slices of 8.91 $M_\odot$, 10 $M_\odot$, and 11.22 $M_\odot$. Instead of interpolating, we simply use our grid points to calculate the systems

undergoing ECSN with a fraction factor (see App. C for details). While this could cast uncertainties on our NS populations, it should be a minor effect comparing with merger criterion.

The ComBinE code like other rapid codes assumes that the envelope of donor star is completely stripped by mass transfer. This allows it to calculate the product of Case BB or Case BC mass transfer. However, there could be a considerable fraction of envelope left after mass transfer at low metallicity (Laplace, Götberg et al., 2020). We find similar feature in our model grid. The remaining H-rich outer layer helps the core keep growing, which may shift the boundary between NS and WD (Ercolino et al., in prep). Furthermore, the H-rich outer layer can expand to very large radius and trigger the mass transfer from a partially stripped star. Usually, the partially stripped star is less massive than the accretor, making mass transfer widen the orbit. The parameter space of helium-envelope-stripped supernova could be narrowed by this process. In addition, due to the remaining material, stars could explode when they still fill their Roche lobe (Laplace, Götberg et al., 2020). The asymmetric structure of pre-SN star may have effects on the kick velocities.

2.7.4 Envelope inflation

Sanyal et al. (2015) have shown that in massive main-sequence stars the maximum Eddington factor can exceed one inside the stars due to the Fe-bump of opacity. Radiation then pushes the envelope to a very large radius, leading to core-hydrogen burning supergiant models. Envelope inflation is sensitive to the treatment of convection and can cause convergence issues in calculation. The LMC binary models adopted in Langer, Schürmann et al. (2020) can not handle the effects of envelope inflation well and therefore do not have models with initial primary mass larger than about 40 $M_\odot$. While envelope inflation can be avoided by assuming stronger convection (Paxton, Cantiello et al., 2013), we do not see the reason to assume that the traditional mixing length theory becomes invalid (Böhm-Vitense, 1958).

Since the inflated envelope is highly convective (Sanyal et al., 2015), Langer, Schürmann et al. (2020) assume that the mass transfer from a inflated star is unstable. In our SMC models we do find the binaries undergoing envelope inflation reach the OB+BH phase. Above 50 $M_\odot$ initial primary mass, the effect of envelope inflation becomes more and more significant. As a consequence, the orbital period window of Case A systems largely widens. With a more efficient convection, the inflated envelope will expend less and fill the Roche Lobe at a later time, which could slightly increase the mass of the stripped star. Since there are only 11 OB+BH binaries having initial primary mass above 50 $M_\odot$, we do not expect our result to be largely affected by this uncertainty.

2.8 Conclusions

In this paper, we have performed a population synthesis study on the properties of evolved massive binaries in the SMC by using a dense model grid of detailed binary evolution models. Comparing with rapid population synthesis calculations, our models include detailed calculations like stellar rotation, convection, envelope inflation, and mass transfer through Roche Lobe overflow. Instead of using a fixed accretion efficiency, we adopt a rotation-dependent accretion efficiency assuming that a critically rotating star can not accrete anymore. When a mass gainer critically rotates, we assume the transferred material is ejected as radiation-driven wind. In the case of radiation power is too weak to driven wind, mass transfer is expected to be unstable. For supernovae and kicks, we adopt the same supernova

windows and kick distributions as the ComBinE code (Kruckow et al., 2018; Schürmann, Langer, X.-T. Xu et al., 2023).

We compared the observed WR+O binaries with our predictions on the HRD and the orbital velocity - $\log P_{\rm orb}$ plane. Our results are consistent with the observed parameters. Particularly, the only one H-rich system SMC AB8 can be explained by our model. We predict that many WR+O binaries having orbital periods above 100 days, which are not observed yet. Since OB+BH binaries are the direct offspring of WR+O binaries, our results on WR+O binaries builds a solid foundation for our predictions on OB+BH binaries. On the other hand, moving to low-mass regime, we can hardly explain the observed Be X-ray binaries due to high merger rate. The assumption on the stability criterion needs further investigation.

We expected over 200 OB+BH binaries in the SMC and most of them harbour OBe stars. This conclusion is not affected by the choosing of initial distributions and star formation history (Sect. 2.4). The expected OB+BH population have OB star mass $\sim 10\,M_\odot$, BH mass $\sim 6\,M_\odot$ and orbital period ~ 100 days. In consistent with our predicted WR+O population, the majority of OB+BH binaries have wide orbits and hence are expected to be X-ray quiet. They can be identified through orbital motion and surface properties of OB stars. These OB stars have orbital velocities around $40\mathrm{km\,s^{-1}}$ and are fast rotators with rotational velocity around $600\mathrm{km\,s^{-1}}$. The surface abundance is enhanced by mass transfer. Our predictions are consistent with the observed OB+BH binaries.

Our study suggests a large population of undetected wide-orbit OB+BH binaries. The detection of such systems could largely improve our understanding of massive binary evolution and their role in producing BH merger. In future work, we will use our predicted OB+BH binaries to further investigate the properties of WR+BH binaries and BH+BH binaries.

CHAPTER 3

Population synthesis predictions for Wolf-Rayet star-black hole binaries in the Small Magellanic Cloud and their implications for merging binary black holes

Xiao-Tian Xu[a], Norbert Langer[a,b], Tomer Shenar[c], Abel Schootemeijer[a], Chen Wang[d]

[a] Argelander-Institüt für Astronomie, Universität Bonn, Auf dem Hügel 71, 53121 Bonn, German
[b] Max-Planck-Institut für Radioastronomie, Auf dem Hügel 69, 53121 Bonn, Germany
[c] Anton Pannekoek Institute for Astronomy, Science Park 904, NL-1098 XH Amsterdam, the Netherlands
[d] Max Planck Institute for Astrophysics, Karl-Schwarzschild-Strasse 1, 85748 Garching, Germany

To be submitted to Astronomy and Astrophysics

Author contributions: X.-T.X. analysed the data from the detailed binary evolution model grid computed by C.W., interpreted the results together with N.L., T.S., and A.S, and wrote this article. N.L. reviewed the first draft of this article.

Abstract

Context. The majority of massive stars have nearby companions, which play an important role in forming merging binary black holes (BBHs). However, many key factors of binary evolution are still poorly understood, rendering the predictions of BBH mergers uncertain.

Aims. We perform a population synthesis study of the evolved massive binaries in the Small Magellanic Cloud (SMC) and compare with the observed post-interaction binary products. Previously, we have studied the evolution up to the time when the initially less massive stars leave the main sequence. In this work, we investigate the evolution further until the final BBH merger.

Methods. Our analysis is based on a dense MESA binary model grid, which contains 53,298 detailed binary evolution models computed with the metallicity tailored for the SMC, and the OB+WR and OB+BH binary population derived from this model grid. The observed SMC WR+O binaries and

BH+O binaries are well recovered by our fiducial synthetic population, which forms a solid foundation for our study of the later phases.

Results. Our result indicates that 2-3 of the 7 apparently single WR stars in the SMC could have BH companions with expected orbital periods of 30 - 100 days, corresponding to orbital velocities of $\sim$50 km s^{-1} for the WR stars, and with mass ratios near one. This high predicted fraction of WR+BH binaries is due to the comparable lifetimes of the WR+O and BH+WR phases. Except for Cygnus X-3, our predictions recover the main properties of the observed WR+BH candidates in the Local Group. Case A mass transfer is found to produces a large fraction of merging BBHs at low redshift due to its long delay time. However, the observed merging BBHs may not necessarily be dominated by high-redshift binaries due to the short delay time produced by common envelope evolution.

Conclusions. Our prediction suggests that we might find WR+BH binaries amongst the apparently single WR stars in the SMC. If these SMC WR stars are truly single, it may imply that wide massive binaries undergo strong orbital shrinkage during the first mass transfer.

3.1 Introduction

Since 2015, over 90 gravitational-wave events have been detected (R. Abbott et al., 2023), most of which originate from the merger of two stellar-mass black holes. Massive isolated binary stars may play an essential role in forming such objects (Dominik et al., 2013; Belczynski, Buonanno et al., 2014; Eldridge and Stanway, 2016; Mapelli, Giacobbo et al., 2017; Kruckow et al., 2018; Mapelli, 2020; Marchant, Pappas et al., 2021; Shao and X.-D. Li, 2021; Belczynski, Doctor et al., 2022; Briel, Stevance and Eldridge, 2022).

The binary pathway towards gravitational-wave events involves Roche-lobe overflow, common envelope evolution, BH formation, and mass transfer, which play crucial roles in massive binary evolution but are still poorly understood (Janka, 2012; Langer, 2012; Ivanova et al., 2013; Laplace, Götberg et al., 2020; Laplace, Justham et al., 2021). In addition, the observed BBH mergers have redshifts below $\sim$ 1.25 (R. Abbott et al., 2023). Considering the merger delay time, They may be formed from binaries at high redshift, where massive stars behave very differently from those in the local universe (Langer, 2012).

The Small Magellanic Cloud provides an ideal testbed to study binary evolution and BBH formation. Its low metallicity (1/5 of solar value, Hill, Andrievsky and Spite, 1995; Korn et al., 2000; Davies et al., 2015) reduces stellar wind mass loss rate (Mokiem et al., 2007) and is related to the average metallicity at a reshift of about 5 (Langer and Norman, 2006). The SMC is a star forming galaxy with an average star formation rate of 0.05 $M_\odot$ yr^{-1} (Harris and Zaritsky, 2004; Rubele, Girardi et al., 2015; Hagen et al., 2017; Rubele, Pastorelli et al., 2018; Schootemeijer, Langer, D. Lennon et al., 2021), which contain a rich population of massive stars (Schootemeijer, Langer, D. Lennon et al., 2021; Schootemeijer, D. Lennon et al., 2022), including $\sim$150 high-mass X-ray binaries (Haberl and Sturm, 2016). There are 12 WR stars observed (Shenar, Hainich, Todt, Sander et al., 2016; Shenar, Hainich, Todt, Moffat et al., 2018; Schootemeijer, Langer, Grin et al., 2019), of which 5 have detected O star companion. This sample is near complete (Shenar, Gilkis et al., 2020). There are three WR+BH candidates, Cygnus X-3 (Lommen et al., 2005; Zdziarski, Mikolajewska and Belczynski, 2013; Antokhin et al., 2022), NGC300 X-1 (Crowther, Carpano et al., 2007; B. Binder et al., 2011), IC10 X-1 (Bauer and Brandt, 2004; Clark and Crowther, 2004; Laycock, Cappallo and Moro, 2015), but none of them was found in the SMC (Clark and Crowther, 2004; Zdziarski, Mikolajewska and

Belczynski, 2013; Laycock, Maccarone and Christodoulou, 2015; B. A. Binder et al., 2021; Antokhin et al., 2022). Also, the nature of the compact objects in these WR binaries is still under debate (van den Heuvel and De Loore, 1973; Dewi et al., 2002; Lommen et al., 2005; Linden, Valsecchi and Kalogera, 2012; Zdziarski, Mikolajewska and Belczynski, 2013; Tutukov, Fedorova and Cherepashchuk, 2013; van den Heuvel, Portegies Zwart and S. E. de Mink, 2017b; Antokhin et al., 2022). As pointed out by van den Heuvel, Portegies Zwart and S. E. de Mink (2017b), the WR+O phase and WR+BH phase should have comparable lifetimes, and therefore it is reasonable to believe that some of the single SMC WR stars have undetected BH companions, while they do not clearly show any signatures of binary interaction (Schootemeijer and Langer, 2018). Population synthesis can help refine the search for such systems in the SMC. Previous population synthesis studies targeting stripped star + compact object binaries are mainly preformed for galactic metallicity (e.g., Lommen et al., 2005; Götberg, Korol et al., 2020; Shao and X.-D. Li, 2020).

Binary black holes may be the direct offsprings of WR+BH binaries. Many previous population synthesis works performed with rapid binary evolution codes have shown that common envelope evolution plays a crucial role in forming BBHs (e.g. Belczynski, Kalogera et al., 2008; Dominik et al., 2013; Mapelli, Giacobbo et al., 2017; Kruckow et al., 2018; Shao and X.-D. Li, 2021), also found in the detailed code BPASS (Eldridge and Stanway, 2016), which is challenged by recent detailed simulations (Klencki et al., 2020; Marchant, Pappas et al., 2021; Gallegos-Garcia et al., 2021). The orbital period window for common envelope evolution found in these detailed simulations is much narrower than that found in rapid population synthesis codes, and this leads to a much lower merger rate (Gallegos-Garcia et al., 2021), suggesting that the formation of merging BBHs may be dominated by the stable mass transfer channel.

X.-T. Xu, Schürmann et al. (2023) (hereafter Paper I) have studied the evolution of massive binary systems with MESA up to the time when the initially less massive stars leave the main sequence (MS). Our fiducial population model in Paper I predicts 7 WR+O binaries in the SMC, which is consistent with the observed number (Shenar, Hainich, Todt, Sander et al., 2016; Shenar, Hainich, Todt, Moffat et al., 2018; Schootemeijer, Langer, Grin et al., 2019). This leads to the prediction of 211 OB+BH binaries with properties that cover the properties of the observed OB+BH binaries (Orosz, McClintock, Narayan et al., 2007; Orosz, Steeghs et al., 2009; Orosz, McClintock, Aufdenberg et al., 2011; Casares et al., 2014; Ramachandran et al., 2022; Shenar, Sana et al., 2022). This result builds the ground for our study on the later evolutionary stages in this work.

Here we provide population synthesis prediction for the WR+BH phase and try to understand the role of stable mass transfer in BBH formation. In Sect. 3.2 we introduce our detailed binary models and method. We present the predicted SMC WR+BH population and merging BBH population in Sect. 3.3 and make comparisons with observations in Sect. 3.4. We discuss the uncertainties and implications of our results in Sect. 3.6. Finally, we summarize our work in Sect. 3.7.

3.2 Method

Figure 3.1 shows the schematic evolution of a massive binary up to the binary black hole (BBH) and an outline of our method. Our MESA model covers the evolution from pre-interaction until the initial secondary star leaves the main sequence (Paper I). Afterwards, we rely on analytical estimates on the mass transfer onto BH.

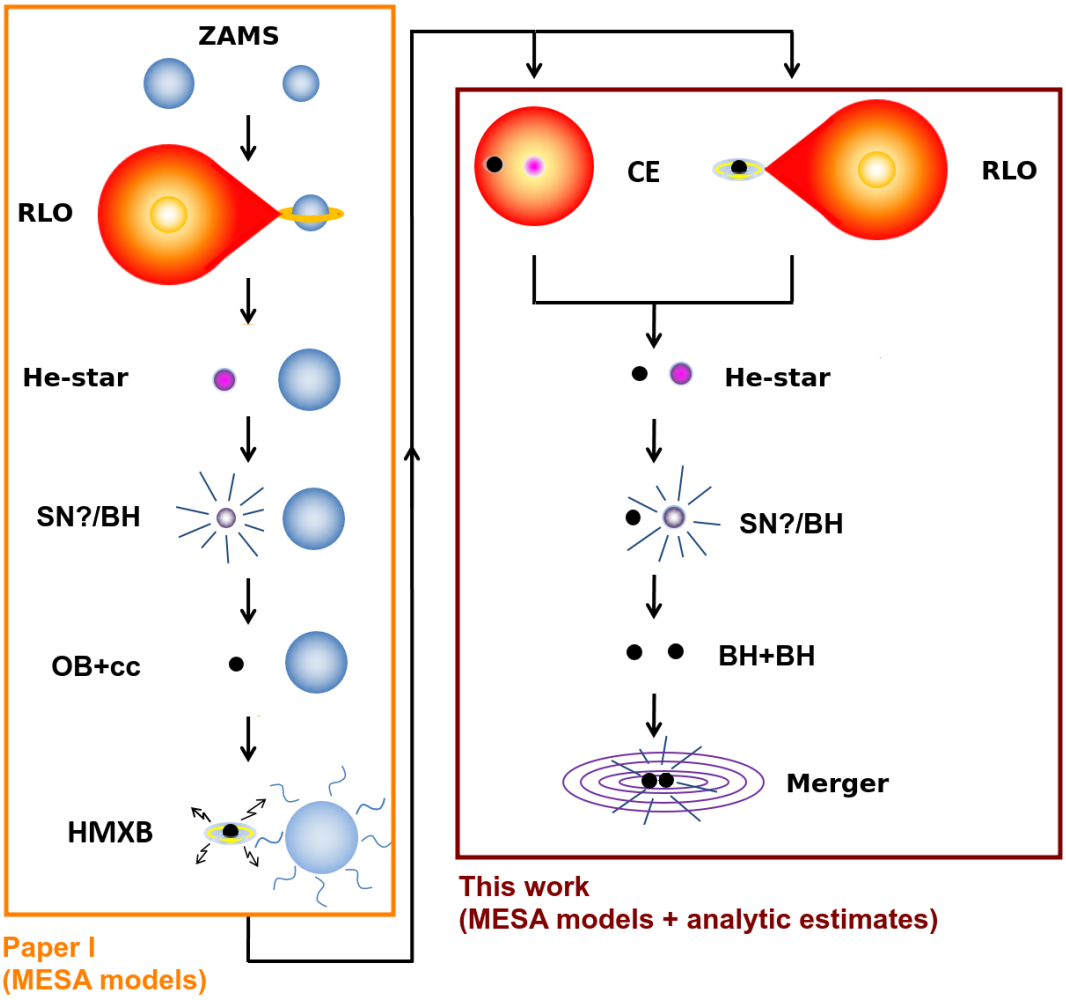

Figure 3.1: Schematic evolution of a massive binary system until the compact object merger. Paper I considered the phases from pre-interaction binaries until the initially less massive star leaves main sequence. In this work we consider the later phases: second mass transfer (Roche-lobe overflow or common envelope evolution), second black hole formation, and compact object merger. This plot is adapted from Kruckow et al. (2018)

3.2.1 MESA input physics and binary model grid

Our analysis is based on a dense detailed binary model grid (see Wang, Langer et al., 2020; X.-T. Xu, Schürmann et al., 2023, for details), which is computed using the MESA code (Modules for Experiments in Stellar Astrophysics version 8845, Paxton, Bildsten et al., 2011; Paxton, Cantiello et al., 2013; Paxton, Marchant et al., 2015) with a tailored metallicity appropriate for the SMC (Brott et al., 2011). This model grid contains 53,298 detailed binary evolution models, covering initial primary mass $M_{1,\mathrm{i}}$ of 5...100 $M_\odot$ with intervals $\Delta \log M_{1,\mathrm{i}} = 0.05$, initial mass ratio of q_i 0.3...0.95 with interval $\Delta q_\mathrm{i} = 0.05$, and initial orbital period $P_{\mathrm{orb,i}}$ of 1...3000 days with intervals $\Delta \log P_{\mathrm{orb,i}} = 0.025$. Binary evaluations are terminated if primary stars deplete core carbon, or if primary stars deplete core helium for the stars with helium core mass above 13 $M_\odot$. When this happens, we expect the primary star to become a neutron star or a black hole, and we keep evolving the secondary star as a single star.

During binary evolution a self-consistent accretion efficiency is adopted. Due to accretion-induced spin-up, mass gainers can reach critical rotation (Packet, 1981) unless tidal torque is strong. Consequently, our wide binaries have near-zero accretion efficiency, while close binaries up to 60%. Once mass gainers reach critical rotation, we assume that transferred material is expelled by radiation and mass transfer becomes unstable if radiation is not powerful enough to drive wind (Marchant, 2017; Wang, Langer et al., 2020; X.-T. Xu, Schürmann et al., 2023), which sets an upper limit on mass transfer rate. Besides this condition, unstable mass transfer is also expected if L2 overflow happens, or if mass transfer rate violates upper limit 0.1 $M_\odot\,\mathrm{yr}^{-1}$. In Paper I unstable mass transfer is not considered as shown in Fig. 3.1.

3.2.2 Black hole formation

To keep consistent, we adopt the same BH formation prescription as the fiducial model in Paper I. We determine the type of the outcome compact objects by the mass of the final helium core. According to the compactness computed by Sukhbold, Woosley and Heger (2018), BHs form if the helium core mass at core helium depletion is above 6.6 $M_\odot$. We do not assume any momentum kick acting on newborn BHs. The BH mass is computed by the formula in Kruckow et al. (2018) that 20% of the helium-rich envelope is ejected during fallback process, and then 20% of the remaining mass is lost due to the release of gravitational bounding energy. Without kick, this process generates eccentricities less than 0.1. In addition, if final helium core is larger than 35 $M_\odot$, pair-instability supernova takes place, which is computed by an empirical relation based on Marchant, Renzo et al. (2019) (see Paper I for details).

3.2.3 Mass transfer onto black hole

As mentioned in Sect. 3.2.1, our binary models do not compute the mass transfer onto BH. We keep evolving the secondary stars as single stars after the primary stars becoming BHs. The single star model data allows us to determine the Roche-lobe filling moment for the mass transfer onto BHs and the properties of the outcome stripped star (Sect. 3.2.4).

The orbital periods of OB+BH binaries are assumed to remain unchanged since the orbital angular momentum lost through the OB star wind can be ignored (El Mellah, Grinberg et al., 2020). Roche-lobe overflow takes place when the radius of the secondary star reaches its Roche Lobe radius R_L, where

$R_{\rm L}$ is given by (Eggleton, 1983)

$$\frac{R_{\rm L}}{a} = \frac{0.49 q_{\rm d}^{2/3}}{0.6 q^{2/3} + \ln(1 + q_{\rm d}^{1/3})}, \tag{3.1}$$

where $q_{\rm d}$ is the mass ratio (mass donor / mass gainer), and a is the orbital semi-major axis.

Whether mass transfer is stable depends on how the fast donor star and its Roche lobe response to mass loss (Soberman, Phinney and van den Heuvel, 1997). It is unstable if the donor star can not be enclosed by its Roche Lobe, which happens if the mass donor is much more massive than the mass gainer, or if the mass donor has a strongly convective envelope. These two conditions are respectively corresponding to a minimum mass ratio $q_{\rm min}$ (mass gainer/mass donor) and a maximum orbital period $P_{\rm orb,max}$ for stable mass transfer, having typical values of 0.3 (Soberman, Phinney and van den Heuvel, 1997) and 1000 days (Fig. 2 and App. C in X.-T. Xu, Schürmann et al., 2023).

For stable mass transfer (StableMT), orbital evolution is determined by the evolution of orbital angular momentum $J_{\rm orb}$, which is

$$J_{\rm orb} = \frac{M_1 M_2}{M} \sqrt{G M a}, \tag{3.2}$$

where M_1 and M_2 are the stellar masses, $M = M_1 + M_2$, and G is the gravitational constant. The logarithmic derivative of this equation gives

$$\frac{\dot{J}_{\rm orb}}{J_{\rm orb}} = \frac{\dot{M}_1}{M_1} + \frac{\dot{M}_2}{M_2} - \frac{1}{3}\frac{\dot{M}}{M} + \frac{1}{3}\frac{\dot{P}_{\rm orb}}{P_{\rm orb}}, \tag{3.3}$$

where a is replaced by orbital period $P_{\rm orb}$ through the Kepler's Third Law. Assuming that mass escapes the system as isotropic wind, Eq. (3.3) has the following solution (Tauris and van den Heuvel, 2006) [1],

$$\begin{aligned}\left(\frac{a_{\rm f}}{a_{\rm i}}\right)_{\rm RLO} = &\left(\frac{q_{\rm f}^{-1}}{q_{\rm i}^{-1}}\right)^{2(\alpha_{\rm RLO}-1)} \left(\frac{q_{\rm f}^{-1}+1}{q_{\rm i^{-1}}+1}\right)^{(-\alpha_{\rm RLO}-\beta_{\rm RLO})(1-\epsilon)^{-1}} \\ &\times \left(\frac{\epsilon q_{\rm f}^{-1}+1}{\epsilon q_{\rm i}^{-1}+1}\right)^{3+2(\alpha_{\rm RLO}\epsilon^2+\beta_{\rm RLO})[\epsilon(1-\epsilon)]^{-1}},\end{aligned} \tag{3.4}$$

where $a_{\rm f}$ and $a_{\rm i}$ are the semi-major axes after and before interaction, $q_{\rm f}$ is the mass ratio after interaction (BH mass / stripped star mass), $q_{\rm i}$ is the mass ratio before interaction (mass gainer / mass donor), $\alpha_{\rm RLO}$ and $\beta_{\rm RLO}$ are the fractions of mass lost from the mass donor and the mass gainer, and ϵ is the accretion efficiency, i.e., $\epsilon = 1 - \alpha_{\rm RLO} - \beta_{\rm RLO}$. We assume no mass lost at the vicinity of the donor star ($\alpha_{\rm RLO} = 0$). The accretion onto a BH is expected to be limited by the Eddington limit, which is much lower than the mass transfer rate under thermal timescale (see App. B). This means that almost all transferred material is ejected out of the systems by the BH, and we accordingly take

[1] In Tauris and van den Heuvel (2006), the authors define mass ratio by mass donor divided by mass gainer, while we in this work define mass ratio by mass gainer divided by mass donor.

$\beta_{\rm RLO} = 1$ and $\epsilon = 0$. In this case, Eq. (3.4) becomes

$$\lim_{\epsilon\to 0}\left(\frac{a_{\rm f}}{a_{\rm i}}\right)_{\rm RLO} = \left(\frac{q_{\rm f}^{-1}}{q_{\rm i}^{-1}}\right)^{2(\alpha_{\rm RLO}-1)} \left(\frac{q_{\rm f}^{-1}+1}{q_{\rm i}^{-1}+1}\right)^{-1} \times \exp\left[2\beta_{\rm RLO}(q_{\rm f}^{-1}-q_{\rm i}^{-1})\right]. \tag{3.5}$$

If mass transfer becomes unstable, common envelope evolution (CEE) is going to take place, during which mass transfer rate is so large that the mass gainer is engulfed by the envelope of the donor star (Ivanova et al., 2013). While CEE only lasts for about 1000 years, the friction between the mass gainer and the envelope material leads to dramatic orbital shrinkage. We adopt the commonly adopted formula to compute the outcome of a CEE (Webbink, 1984; de Kool, 1990),

$$\frac{GM_{\rm donor}M_{\rm env}}{\lambda_{\rm bind}R_{\rm donor}} = \eta_{CE}\left[\frac{GM_{\rm He,core}M_{\rm BH}}{2a_{\rm f}} - \frac{GM_{\rm O}M_{\rm BH}}{2a_{\rm i}}\right], \tag{3.6}$$

where $R_{\rm donor}$ is the radius of donor star, $M_{\rm donor}$ is the mass of donor star, $M_{\rm BH}$ is the BH mass, $M_{\rm He,core}$ is the mass of stripped star (see Sect. 3.2.4), $M_{\rm env} = M_{\rm donor} - M_{\rm He,core}$, $\eta_{\rm CE}$ is the efficiency of expelling envelope, $\lambda_{\rm bind}$ captures the effects of stellar structure on the binding energy of the envelope. This equation gives

$$\left(\frac{a_{\rm f}}{a_{\rm i}}\right)_{\rm CE} = \frac{M_{\rm He,core}M_{\rm BH}}{M_{\rm donor}} \frac{1}{M_{\rm BH}+2M_{\rm env}/[\eta_{CE}\lambda_{\rm bind}(R_{\rm L}/a_{\rm i})]}, \tag{3.7}$$

where $R_{\rm donor}$ is replaced by $R_{\rm L}$ since we have $R_{\rm donor} = R_{\rm L}$ at the Roche-lobe filling. In our fiducial model, $\eta_{\rm CE}$ is fixed to be 1. The binding energy parameter $\lambda_{\rm bind}$ is computed by our MESA model by

$$\int_{M_{\rm He,core}}^{M_{\rm donor}} \frac{Gm\,{\rm d}m}{r} = \frac{GM_{\rm donor}M_{\rm env}}{\lambda_{\rm bind}R_{\rm donor}}, \tag{3.8}$$

where m and r are the mass and radius coordinate.

3.2.4 Stripped star and Wolf-Rayet star

For Case B mass transfer, the stripped star can be determined by the H-depleted core of the donor star, which evolves independently of its H-rich envelope. We assume that the H-rich envelope is completely stripped by Roche-lobe overflow like most of rapid codes (e.g. Hurley, Tout and Pols, 2002; Shao and X.-D. Li, 2014; Kruckow et al., 2018), while the remaining H layer may have important effects (Laplace, Götberg et al., 2020, and section 7 in Paper I). We take the He core at the middle of core He burning in our secondary star models as the outcome stripped star.

While the majority of our models undergoes Case B mass transfer onto BHs, a few close binaries undergo Case A mass transfer. In this case, the growth of stripped star is limited by the stripping during the MS phase of the donor star (S. E. de Mink, Pols and Hilditch, 2007). In our models, only late Case A mass transfer can occur[2], whose effect on the He core in the post-MS phase is ignorable. Hence we assume that the donor stars completely lose their H-rich envelope after Case AB mass

[2] Secondary stars have core H mass fraction less than 0.16 when filling their Roche lobe.

transfer. The outcome stripped stars are also given by the He core at the middle of core He burning.

Stripped stars become as Wolf-Rayet (WR) stars if their winds are strong enough. In this work, only classic WR star is considered. Based on the observed minimum luminosity of the SMC WR stars (Shenar, Gilkis et al., 2020), in Paper I we define WR stars by core He burning stars with luminosity higher than $10^{5.6}\,L_{\odot}$, which in our MESA model is related to a threshold mass of 14.3 $M_{\odot}$. In this work, we define WR stars as stripped stars with mass above 14.3 $M_{\odot}$.

3.2.5 Binary black holes

Delay time of binary black hole merger

The delay time of a BBH merger $\tau_{\rm delay}$ is the time from the birth of the BBH progenitor (zero-age main-sequence binary) until the final BBH merger, i.e.,

$$\tau_{\rm delay} = \tau_{\rm evo} + \tau_{\rm merge}, \tag{3.9}$$

where $\tau_{\rm evo}$ is the evolutionary time when the secondary star becomes BH (core He depletion), and $\tau_{\rm merge}$ is the merger timescale of the BBH. The orbital evolution of BBH is solely determined by gravitational-wave radiation. The corresponding orbital angular momentum loss rate $\dot{J}_{\rm gr}$ is given by (Eq. (16.14) in Tauris and van den Heuvel, 2006),

$$\frac{\dot{J}_{\rm gr}}{J_{\rm orb}} = -\frac{32G^3}{5c^5}\frac{M_1 M_2 (M_1+M_2)}{a_{\rm BBH}^4}, \tag{3.10}$$

where $a_{\rm BBH}$ is the orbital semi-major axis at the birth of the BBH. With this, the merger timescale $\tau_{\rm merge}$ is defined as

$$\tau_{\rm merge} = \frac{J_{\rm orb}}{|\dot{J}_{\rm gr}|}. \tag{3.11}$$

In addition, the BBHs having $\tau_{\rm delay}$ less than the Hubble time is defined as merging BBHs.

Cosmological calculation

We adopt the same method for cosmological calculation as in Dominik et al. (2013). Different from Dominik et al. (2013), we assume galaxies at all redshifts are SMC-like. For given redshift z, the corresponding cosmic time t is given by

$$t(z) = t_{\rm H}\int_{z}^{\infty}\frac{{\rm d}\,z'}{(1+z')E(z')}, \tag{3.12}$$

where $t_{\rm H}$ is the Hubble time and

$$E(z) = \sqrt{\Omega_{\rm M}(1+z)^3 + \Omega_{\rm k}(1+z)^2 + \Omega_{\lambda}}, \tag{3.13}$$

where $(\Omega_{\rm M},\ \Omega_{\rm k},\ \Omega_\Lambda)$ is taken to be $(0.3,\ 0.7,\ 0.0)$. The relation between $t(z)$ and z given by Eq. (3.12) can be well-described by an fitting formula, which is

$$t(z) = \frac{C_1}{C_2 + (C_3 + z)^2} \tag{3.14}$$

where C_{1-3} have values of 70.9, -5.2, and 3.2 respectively (also see Carmeli, Hartnett and Oliveira, 2006).

In order to compute cosmic merger rate density, we create time bins from the birth of the universe to the current universe with a bin size of 100 Myrs. In each bin, star formation rate (SFR) is assumed to be constant with the value at the bin center, which is given by (Strolger et al., 2004)

$$\mathrm{SFR}(t) = 10^9 a(t^b e^{-t/c} + d e^{d(t-t_0)/c})\ M_\odot\ \mathrm{yr}^{-1}\ \mathrm{Gpc}^{-3}, \tag{3.15}$$

where t is in the unit of Gyrs, t_0 is the current age of the universe, and $(a,\ b,\ c,\ d) = (0.182,\ 1.26,\ 1.865,\ 0.071)$. The progenitors of BBHs are expected to emerge evenly in each time bin. Considering a BBH progenitor born at $t_{\rm birth}$, it produces a BBH merger event at $t_{\rm birth} + \tau_{\rm delay}$. The merger rate density of each time bin is the sum of the birth rates of all BBHs that merge in this bin.

3.2.6 Population synthesis method

We use the same population synthesis method as in Paper I that the number $N_{\rm b}$ and birth rate $R_{\rm b}$ of a binary with initial parameter $(M_{1,\rm i},\ q_{\rm i},\ \log P_{\rm orb,i})$ are evaluated by a statistic weight (see App. A in Paper I for detailed formulas),

$$N_{\rm b} \propto \mathrm{SFR} \times \text{ lifetime} \times f_{\rm IMF} \times f_{q_{\rm i}} \times f_{\log P_{\rm orb,i}} \tag{3.16}$$

and

$$R_{\rm b} \propto \mathrm{SFR} \times f_{\rm IMF} \times f_{q_{\rm i}} \times f_{\log P_{\rm orb,i}}, \tag{3.17}$$

where $f_{\rm IMF}$ is the initial mass function (IMF), $f_{q_{\rm i}}$ is the distribution for initial mass ratio, and $f_{\log P_{\rm orb,i}}$ for initial orbital period. In consistent with the fiducial model in Paper I, we take the IMF in Kroupa (2001) for the primary stars,

$$f_{\rm IMF} \propto M_{1,\rm i}^{-2.3}, \tag{3.18}$$

and the orbital period and mass ratio distributions in Sana et al. (2012),

$$\begin{aligned} f_{q_{\rm i}} &\propto q_{\rm i}^{-0.1}, \\ f_{\log P_{\rm orb,i}} &\propto \log P_{\rm orb,i}^{-0.55}. \end{aligned} \tag{3.19}$$

For the SMC, SFR is assumed to be constant with a rate of $0.05\ M_\odot\ \mathrm{yr}^{-1}$ (Harris and Zaritsky, 2004; Rubele, Girardi et al., 2015; Hagen et al., 2017; Rubele, Pastorelli et al., 2018; Schootemeijer, Langer, D. Lennon et al., 2021). For cosmological calculation, SFR is given by Eq. (3.15).

3.3 Properties of our fiducial synthetic population

In this section, we presents the predicted WR+BH population (Sect. 3.3.2) and merging BBH population (Sect. 3.3.3) expected by our fiducial model described in Sect. 3.2. To better interpret our population synthesis results, we firstly introduce some basic features of our models (Sect. 3.3.1). In Sect. 3.4, we compare our predictions with the observed WR+BH candidates and the merging BBH population inferred from GWTC-3. In App. B, we provide a detailed parameter study regarding the criterion of the stability of mass transfer, accretion efficiency, the efficiency of expelling envelope material during common envelope evolution, and BH kicks.

3.3.1 Outcomes of MESA model grid

Similar to Paper I, we summary the outcomes of models in initial mass ratio $q_{\rm i}$ - logarithmic orbital period log $P_{\rm orb,i}$ plane. Here we further distinguish the parameter spaces for forming WR+BH binaries, BBHs from stable mass transfer, BBHs from CEE, merging BBHs, and pulsational pair-instability supernovae. Four slices of initial primary mass $M_{1,\rm i}$ are presented, 20 $M_\odot$, 31.6 $M_\odot$, 50.1 $M_\odot$, and 79.4 $M_\odot$, i.e., 1.3, 1.5, 1.7, and 1.9 in logarithm.

The minimum initial primary mass to form BBHs binaries is 20 $M_\odot$ (upper left panel of Fig 3.2). Most of BBHs are formed through the StableMT channel (orange regions in Fig. 3.2) with $q_{\rm i} > 0.9$, while a few close binaries can produce BBHs with slightly lower mass ratios. This is because secondary stars in close binaries can be spun down by tides and accrete considerable mass before rotating critically. Around $P_{\rm orb,i} = 300$ days, secondary stars develop convective envelope when filling their Roche lobes, triggering unstable mass transfer. Most of them can survive the CEE and produce BBHs with delay times within the Hubble time (merging BBHs, red regions in Fig. 3.2). For the binaries with larger initial orbital periods, unstable mass transfer takes place when the primary stars fill the Roche lobe, which are not considered in this work and Paper I. Common envelope evolution can also take place in close orbit. At around 3 days, the rather high accretion efficiency produces mass ratios below $q_{\rm min}$ for their OB+BH phases. As a consequence, these binaries end up with mergers caused by CEE (blue regions in Fig. 3.2).

The parameter space of forming BBHs largely widens with increasing initial primary mass. For $M_{1,\rm i} = 31.6\,M_\odot$ (upper right panel of Fig. 3.2), BBHs can form with $q_{\rm i} = 0.55$. Different from $M_{1,\rm i} = 20\,M_\odot$, WR+BH binaries emerge at this mass slice (diagonal-hatched regions in Fig. 3.2). Around 3 days and close to the CEE-merger region, secondary stars accrete enough mass to form WR stars. At the same orbital period range, merging BBHs are formed from the StableMT channel.

For higher $M_{1,\rm i}$ (lower two panels of Fig. 3.2, left panel for $M_{1,\rm i} = 50.1\,M_\odot$ and right panel for $M_{1,\rm i} = 79.4\,M_\odot$), the parameter spaces for forming BBHs and having WR+BH phase further widen. However, the formation of merging BBHs from the StableMT channel becomes more difficult due to the widening parameter spaces for L2 overflow (grey regions near log $P_{\rm orb,i} = 0$ in Fig. 3.2) and convergence errors (white regions in Fig. 3.2). In addition, with $M_{1,\rm i} = 79.4\,M_\odot$ most of models are expected to experience pulsational pair-instability supernovae.

3.3.2 Wolf-Rayet star + black hole binaries

In Paper I we predicted 211 OB+BH binaries and 7 OB+WR binaries in the SMC. This leads to 2.61 WR+BH binaries, where the StableMT channel dominates the population (StableMT: 2.61, CEE:

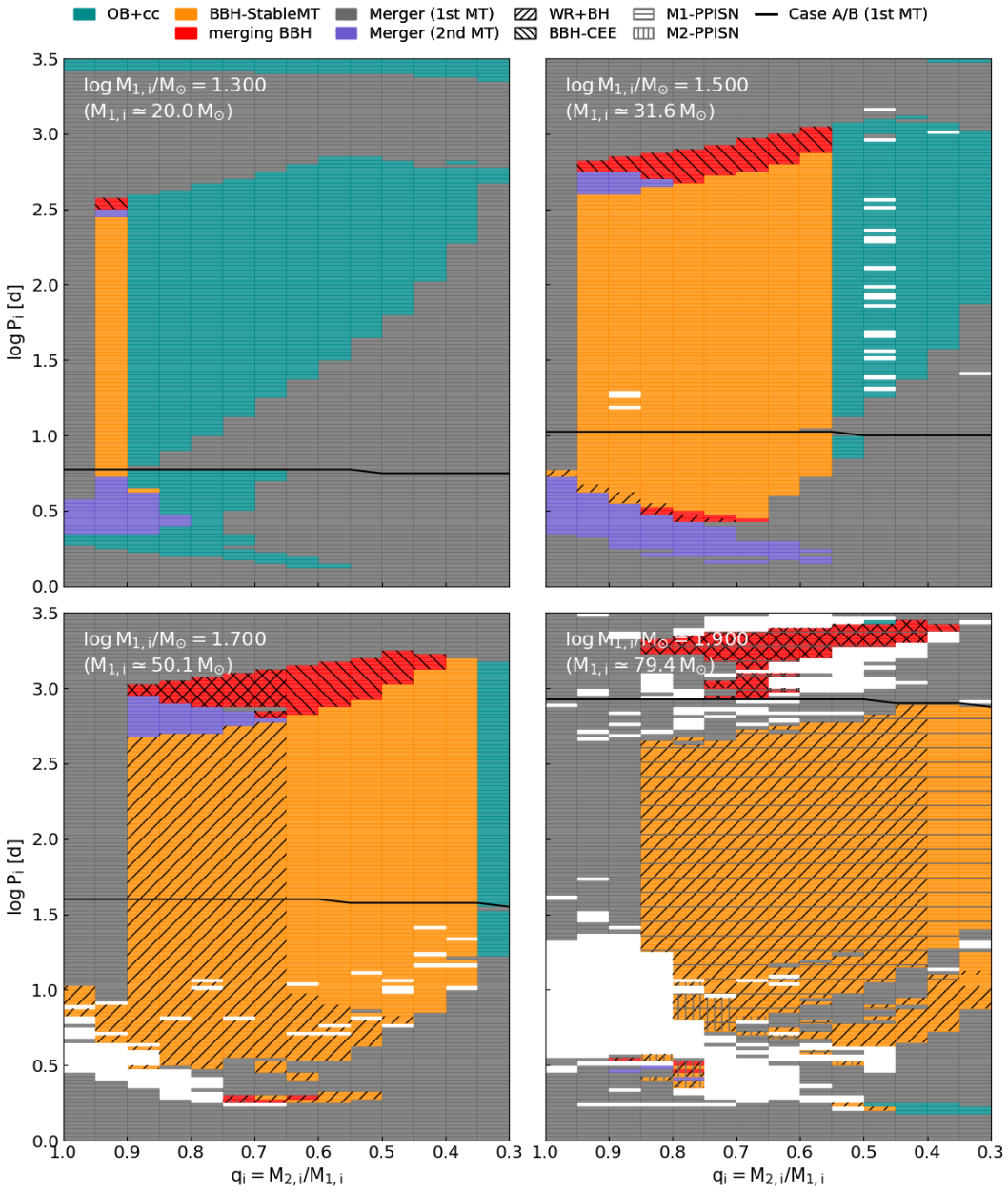

Figure 3.2: Overview of the end points of the computed binary evolution models. The fixed initial primary mass $M_{1,\mathrm{i}}$ is indicated by the white text in each panel. The X-axis and Y-axis are initial mass ratio q_{i} and logarithmic initial orbital period $\log P_{\mathrm{i}}$. Each pixel corresponds to one binary model. The evolutionary outcomes are indicated by colors, lines, and hatches (see top legend). Here, "WR+BH" implies that the model evolves through a WR+BH phase. We distinguish the BBHs formed from the StableMT channel, and the CEE channel, and the BBHs having merger delay time less than the Hubble time ("merging BBH"). In other cases, binaries either are not massive enough to evolve through BBH or WR+BH phases ("OB+cc", where cc=BH,NS, see Paper I for more details on OB+cc phase) or end up merging before the double compact binary stage. Here the mergers occur during the first and second mass transfer are distinguished. The white pixels correspond to the models suffering from numerical problems. In addition, pulsational pair-instability supernova are indicated by the hatched region, "M1-PPISN" for primary star and "M2-PPISN" for secondary star. The black horizontal line is the boundary between Case A and Case B systems.

0.15). Only 0.22 WR+BH binaries undergo Case A mass transfer onto BHs. The variations of input physics does not largely change our predicted number (see App. B). In the following subsections we discuss the properties of our fiducial WR+BH population in detail (Fig. 3.3).

BH masses and WR star masses

We study the distribution of BH masses $M_{\rm BH}$ in the panel (a) of Fig. 3.3. Most of BHs have masses between 17 $M_\odot$ and 22 $M_\odot$, which is the result of two completing factors, i) secondary stars have to be massive enough to become WR stars, ii) the number of massive binaries is limited by the effects of the IMF and lifetime. As shown in Fig. 3.2, below $M_{1,\rm i} = 31.6\ M_\odot$ only a few Case A systems can have WR+BH phases, which causes the sharp number drop at $M_{\rm BH} = 12\ M_\odot$. Towards higher mass, the number drop at 27 $M_\odot$ is related to our grid interval[3].

The panel (b) of Fig. 3.3 presents the distribution of WR star masses $M_{\rm WR}$. This distribution is dominated by the effects of IMF, peaking at 14 $M_\odot$ and decreasing to 33 $M_\odot$. The cutoff below 14 $M_\odot$ reflects our definition of WR stars (see Sect. 3.2.4). The 33 $M_\odot$ WR star is related to a secondary star with initial masses of 67 $M_\odot$ ($(\log M_{1,\rm i},\ q_{\rm i}) = (1.9,\ 0.85)$).

The panel (c) of Fig. 3.3 presents the distribution of mass ratios $q_{\rm BH/WR}$ ($M_{\rm BH}/M_{\rm WR}$). This distribution peaks near $q_{\rm BH/WR} = 1$. Producing small mass ratio requires high initial mass ratio and close orbit, i.e., high accretion efficiency. This results in a minimum mass ratio of 0.4. The opposite occurs in the high-$q_{\rm BH/WR}$ region, where the highest mass ratio (2.4) is related to the lower bound of our initial mass ratio 0.3.

Orbital parameters

The panel (d) of Fig. 3.3 presents the distribution of orbital periods $P_{\rm orb}$. The StableMT channel produces a roughly flat distribution between 3 days and 300 days with a bump at around 40 - 100 days. This result is consistent with our OB+BH population predicted in Paper I, which has typical orbital period of 100 days. The WR+BH binaries from the StableMT and CEE channels are clearly separated by the merger caused by L2 overflow during the first mass transfer episode. Below 0.3 day, the CEE survivors dominate the population with a typical period near 2 hrs, some of which can appear as wind-fed X-ray binaries (see Sect. 3.6.7).

We further study the orbital velocities of WR stars $\upsilon_{\rm WR}$ in the panel (e) of Fig. 3.3. The majority of WR stars move at 50km s^{-1}, corresponding to orbital periods of $\sim$ 300 days. Above $\upsilon_{\rm WR} = 140\,{\rm km\,s^{-1}}$, we expect a flat distribution in $[140,\ 240]\,{\rm km\,s^{-1}}$, which are the binaries with $P_{\rm orb}$ in $[1,\ 10]$ days. For the CEE channel, the WR stars have a orbital velocity of $\sim 900\,{\rm km\,s^{-1}}$ due to their tight orbits.

3.3.3 Merging binary black holes

In this subsection, we firstly present the merging BBH population in the SMC, and then we study the merging BBH population at zero redshift by propagating our SMC population to all redshifts.

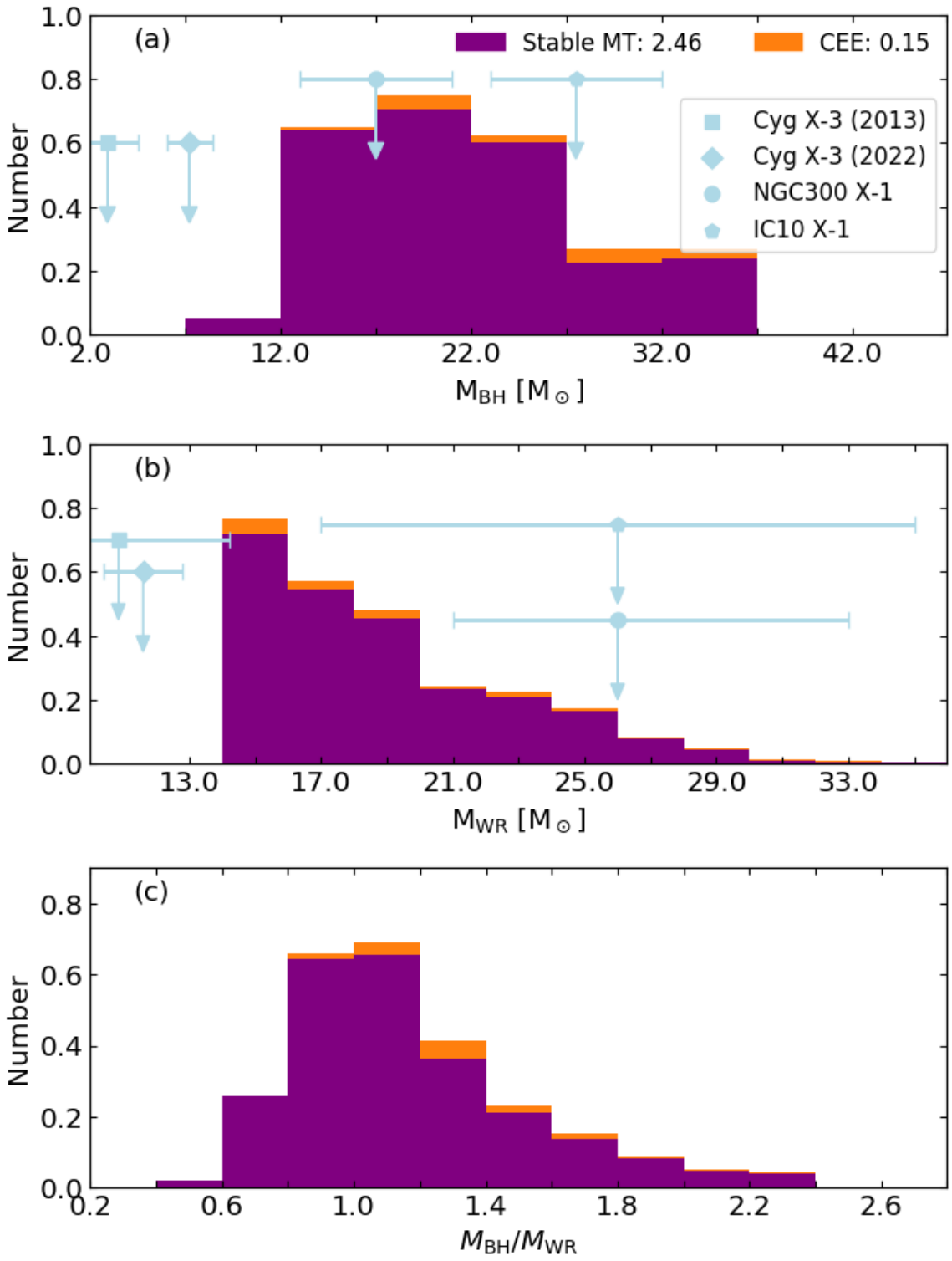

Figure 3.3: Properties ofthe predicted WR+BH binaries in the SMC (histograms), where panels (a) to (c) show the distributions of BH masses $M_{\rm BH}$, WR star masses $M_{\rm WR}$, and mass ratios $M_{\rm BH}/M_{\rm WR}$. Different formation channels are coded in color (orange: CEE, purple: StableMT), and the corresponding total numbers are indicated in the legend in panel (a). The light blue arrows indicate the observed WR+BH candidates (see Tab. 3.1).

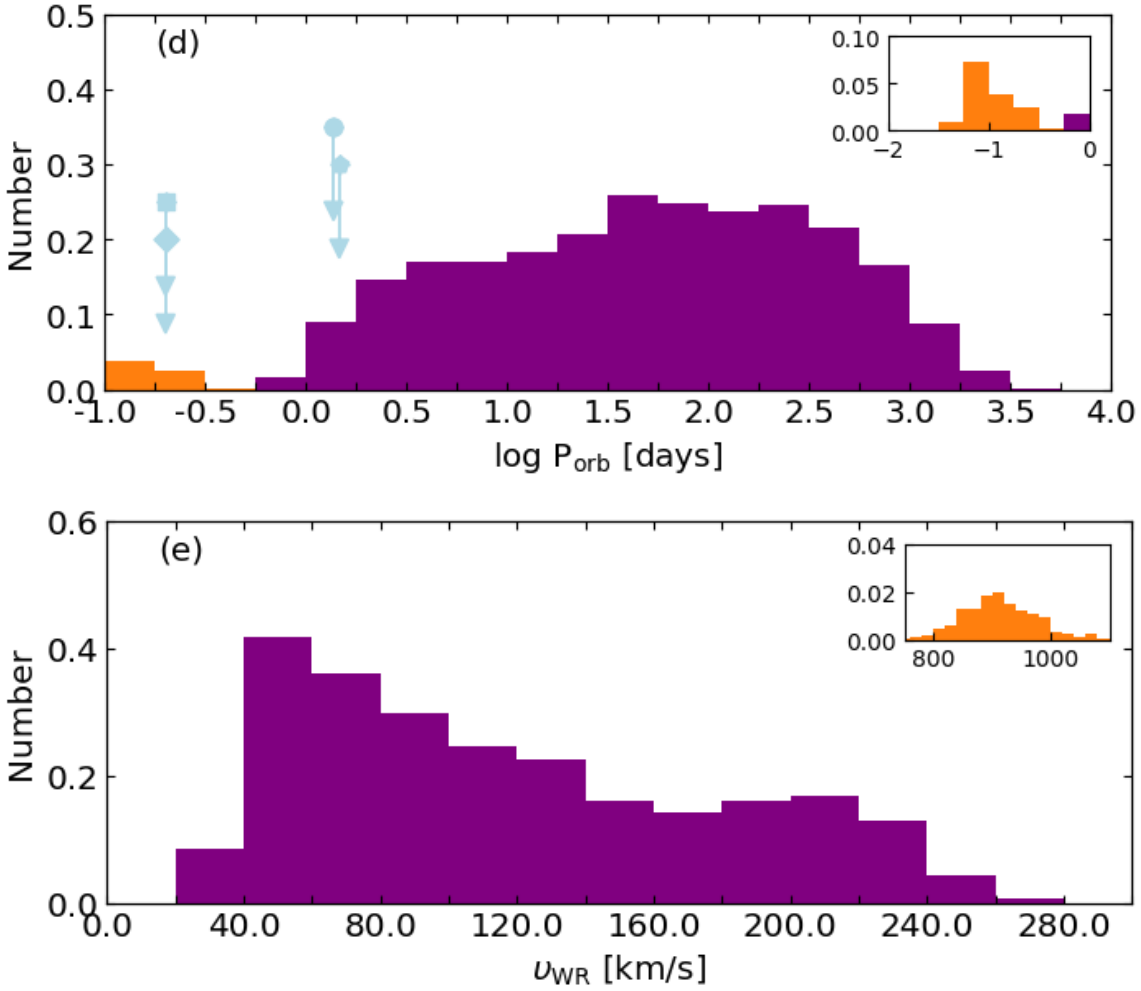

Figure 3.4: Properties ofthe predicted WR+BH binaries in the SMC (histograms), where panels (d) and (e) show the distributions of orbital periods P_{orb} and orbital velocities of the WR stars υ_{WR}. Different formation channels are coded in color (orange: CEE, purple: StableMT). The subplots each panels provide zoom-ins for the CEE channel. The light blue arrows indicate the observed WR+BH candidates (see Tab. 3.1).

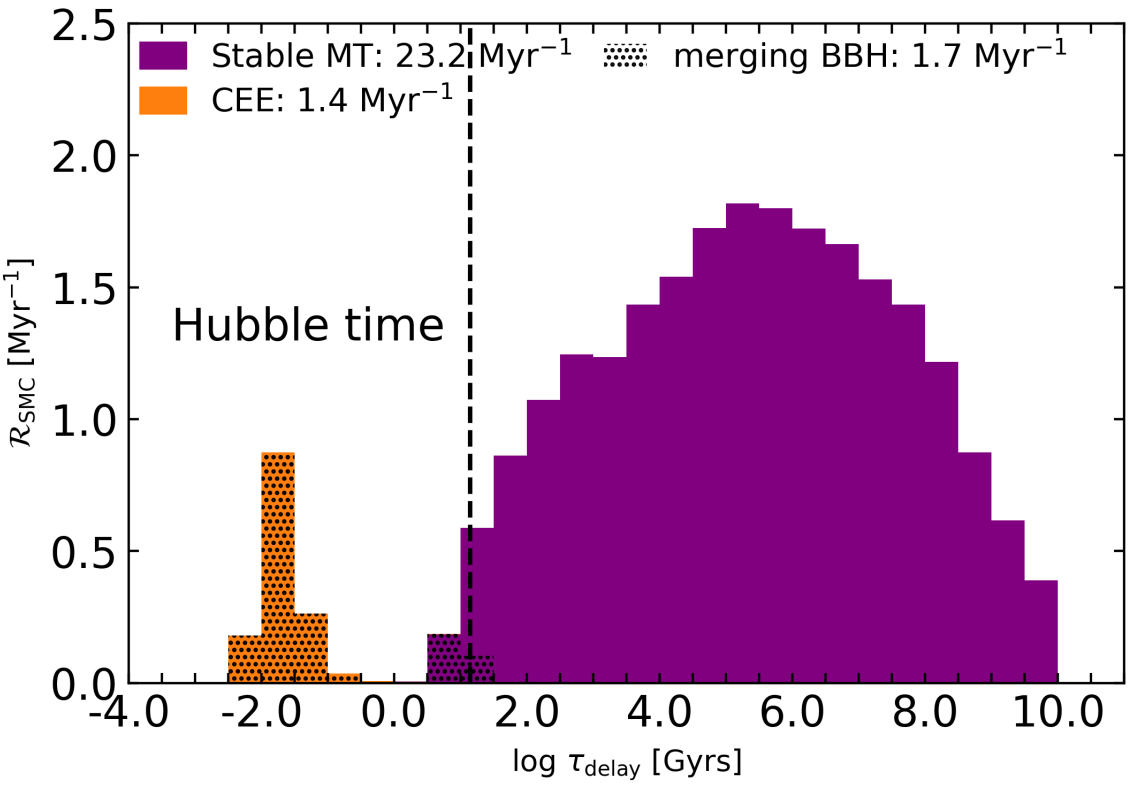

Figure 3.5: Predicted distribution of the merger delay time $\tau_{\rm delay}$ of BBHs in the SMC. The Y-axis shows the birth rate in unit of Myr^{-1}. Different formation channels are coded in color (orange: CEE, purple: StableMT). The total birth rate through each channel is indicated by the text in the legend. The shaded area corresponds to the BBHs with merger delay time less than the Hubble time. The vertical dashed line corresponds to the Hubble time.

Merging BBHs in the SMC

Figure 3.5 presents the distribution of the delay time $\tau_{\rm delay}$ of SMC BBHs. We expect a total birth rate of 24.6 Myr^{-1} for the SMC BBHs, where 1.7 Myr^{-1} of them can merge within the Hubble time (CEE channel: 1.4 Myr^{-1}). The StableMT channel produces very long delay time with a peak near 10^5 Gyrs, and the CEE channel near $\tau_{\rm delay} = 10^{-1.75}$ Gyrs (17.78 Myrs). This distribution resembles the orbital period distribution of WR+BH phase since delay time is usually dominated by merger time, which is highly sensitive to orbital separation (see Eq. (3.10)). In the following results, we focus on the properties of these merging BBHs.

The panel (a) of Fig. 3.6 presents the distribution of the masses of the BHs formed from primary stars $M_{\rm BH,1}$. As shown in Fig. 3.2, the mass window for the StableMT channel very narrow, and this leads to a cutoff at $M_{\rm BH,1} = 18\ M_\odot$. On the contrary, the parameter space of the CEE channel

[3] The mass intervals of our model grid are $\Delta \log M_{1,\rm i} = 0.05$. The BHs in the [22 $M_\odot$, 27 $M_\odot$] bin are mainly formed with $\log M_{1,\rm i} = 1.8$ (63 $M_\odot$) and $\log M_{1,\rm i} = 1.75$ (56 $M_\odot$), while the BHs in the [27 $M_\odot$, 32 $M_\odot$] bin from $\log M_{1,\rm i} = 1.85$ (71 $M_\odot$).

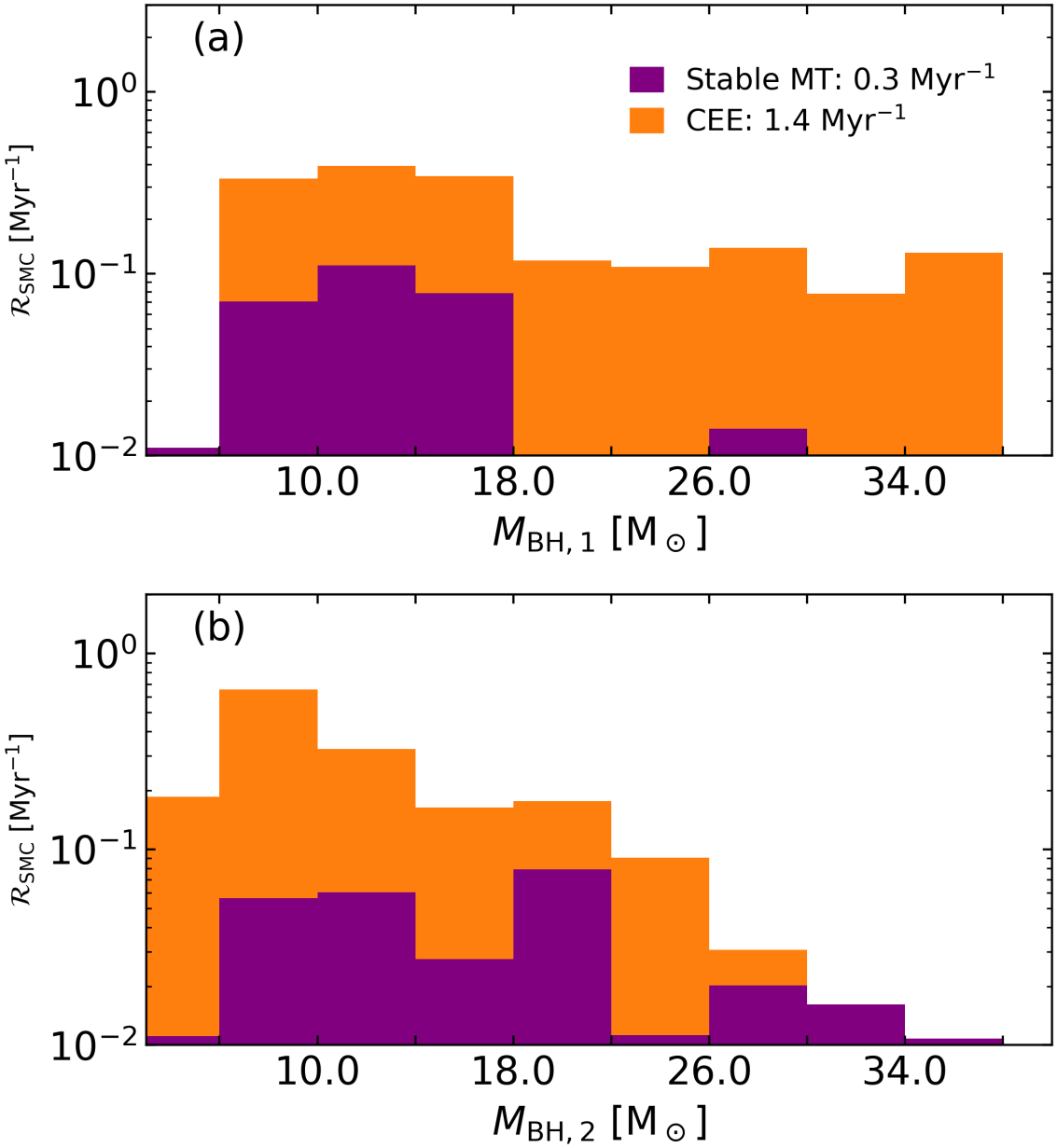

Figure 3.6: Properties of the predicted merging BBHs in the SMC (histograms), where panels (a) and (b) show the distributions of the masses of the BHs formed from the initial primary stars $M_{\rm BH,1}$ and the masses of the BHs formed from the initial secondary stars $M_{\rm BH,2}$. The Y-axis shows birth rate in unit of Myr^{-1}. Different formation channels are coded in color (orange: CEE, purple: StableMT), and the total merger rates are indicated in the legend in panel (a).

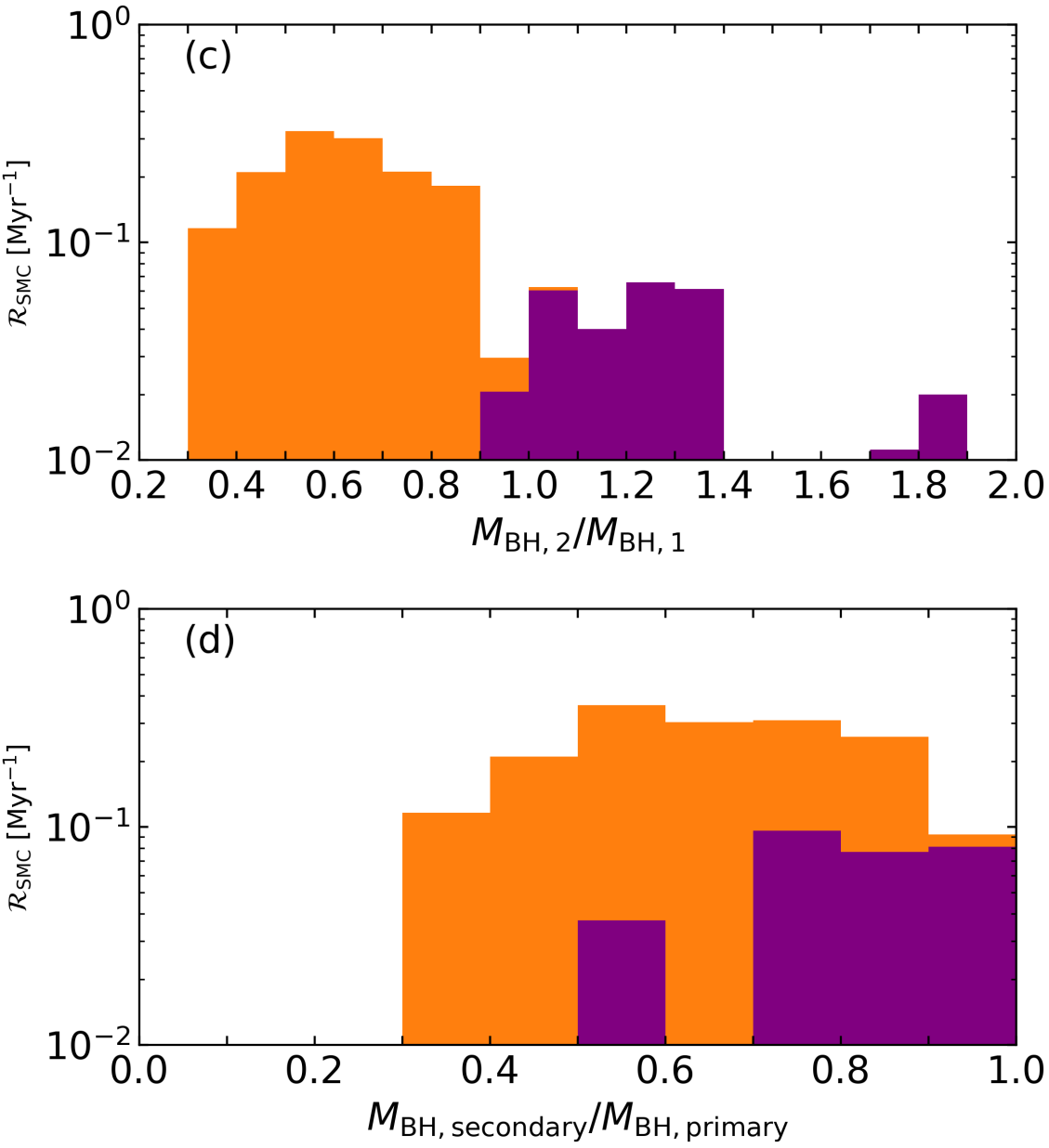

Figure 3.7: Properties of the predicted merging BBHs in the SMC (histograms), where panels (c) to (d) show the distributions of mass ratios defined by $M_{\rm BH,2}/M_{\rm BH,1}$ and mass ratios defined by $M_{\rm BH,secondary}/M_{\rm BH,primary}$, $M_{\rm BH,secondary}$ and $M_{\rm BH,primary}$ are the masses of the primary and secondary BHs respectively. The Y-axis shows birth rate in unit of Myr^{-1}. Different formation channels are coded in color (orange: CEE, purple: StableMT).

increases with $\log M_{1,i}$. The interplay between this widening process and the effect of the IMF leads to a flat distribution between 18 $M_\odot$ and 38 $M_\odot$.

The panel (b) of Fig. 3.6 presents the distribution of the masses of the BHs formed from secondary stars $M_{\rm BH,2}$. This distribution peaks at 8 $M_\odot$ and decreases to 34 $M_\odot$. For the CEE channel, it requires high initial mass ratio to produce massive BHs. The number drop towards high-mass end is caused by the narrowing of the initial mass ratio window. The most massive BHs formed from secondary stars come from the StableMT channel due to the high accretion efficiency during the first mass transfer episode.

The panel (c) and (d) of Fig. 3.6 present the distributions of mass ratios. In panel (c), mass ratio is defined by $M_{\rm BH,2}/M_{\rm BH,1}$, while in panel (d) mass ratio is defined by primary BH $M_{\rm BH,secondary}$ divided by secondary BH $M_{\rm BH,primary}$ [4]. Due to the difference in accretion efficiency, the mass ratio of the BBHs from the CEE channel roughly reflect the initial mass ratio of the binaries, i.e., 0.3. . . 0.95, while the most of the BBHs from the StableMT channel have $M_{\rm BH,2}/M_{\rm BH,1} > 1$, dominating the population with $M_{\rm BH,secondary}/M_{\rm BH,primary} > 0.9$.

Merging BBHs at zero redshift

Figure 3.8 presents the cosmic merger rate density of BBHs $\mathcal{R}_{\rm cosmic}$ if all galaxies are SMC-like. At zero redshift ($z = 0$), we expect a merger rate density about $1000\,{\rm yr}^{-1}\,{\rm Gpc}^{-3}$, where the StableMT and CEE channels contribute equally. While in the SMC the birth rate of the merging BBHs from the StableMT channel is about 1/5 of the CEE channel, their long delay time (see Fig. 3.5) allows BBHs formed at high redshift to merge at $z = 0$. Similarly, the merging BBHs at $z = 0$ from the CEE channel should be born at a redshift near zero, and the corresponding cosmic merger rate density is roughly proportional to the cosmic SFR density (Eq. (3.15) Strolger et al., 2004).

Figure 3.9 presents the distributions of $M_{\rm BH,primary}$ and $M_{\rm BH,secondary}/M_{\rm BH,primary}$ of merging BBHs at $z = 0$. In agreement with Fig. 3.8, the StableMT channel is largely enhanced comparing with the SMC population (Fig. 3.6). Massive primary BHs ($> 22\,M_\odot$) are mainly formed from the CEE channel. Both the StableMT and CEE channels do not produce primary BHs more massive than 38 $M_\odot$ due to the limit set by pulsation pair-instability supernova. For the mass ratio distributions, the StableMT channel dominates the population with $M_{\rm BH,secondary}/M_{\rm BH,primary} > 0.7$.

3.4 Comparisons with observations

3.4.1 Wolf-Rayet star + black hole binaries

Observed WR+BH candidates in the local Universe

There are three WR+BH candidates, Cygnus X-3 (Lommen et al., 2005), NGC300 X-1 (Crowther, Carpano et al., 2007), and IC10 X-1 (Bauer and Brandt, 2004; Clark and Crowther, 2004). Due to the lack of reliable measurements of masses, the nature of these compact objects are still under debate (Barnard, Clark and Kolb, 2008; Crowther, Barnard et al., 2010; B. Binder et al., 2011; Zdziarski, Mikolajewska and Belczynski, 2013; Laycock, Cappallo and Moro, 2015; Laycock, Maccarone and Christodoulou, 2015; B. A. Binder et al., 2021; Veledina et al., 2023). In this work, we take them as BHs, and the adopted parameters are summarized in Tab. 3.1. As already shown in the panels (a), (b),

[4] Here primary (secondary) BH refers to the more (less) BH in a BBH.

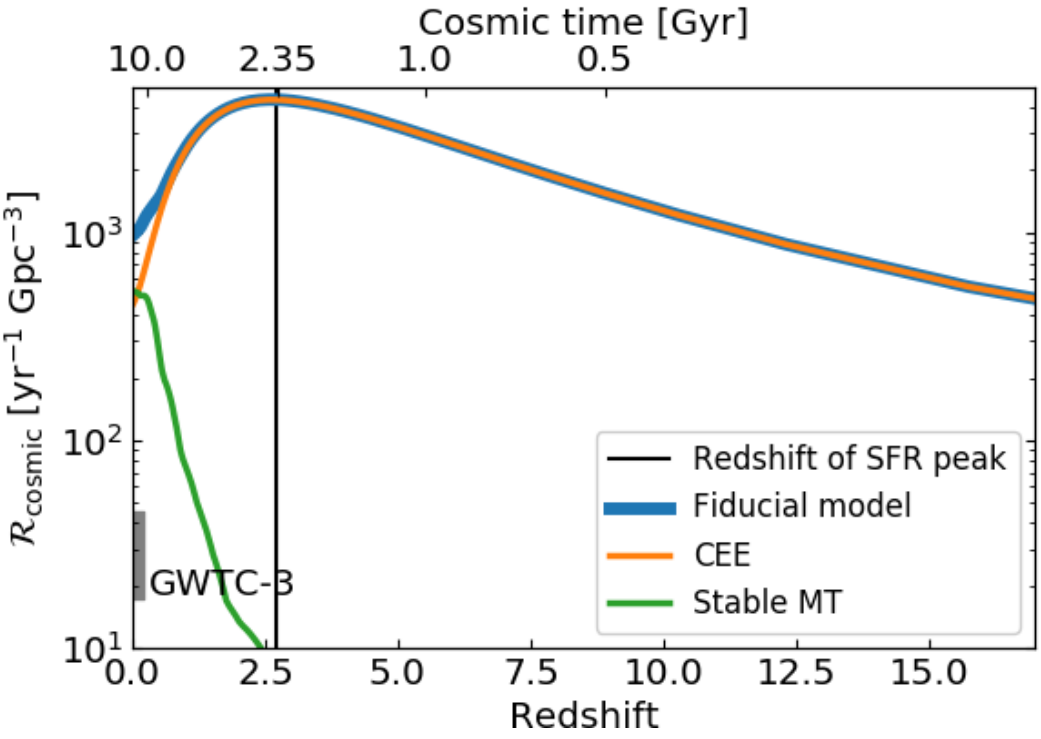

Figure 3.8: Predicted cosmic merger rate density of BBHs assuming all galaxies are SMC-like. The blue thick line shows the total merger rate density predicted by our fiducial model. The contributions of the CEE and StableMT channels are plotted with orange and green respectively. The Y-axis shows the merger rate density in unit of yr^{-1} Gpc^{-3}. The grey region means that the Y-axis shows the merger rate density inferred from GWTC-3 (R. Abbott et al., 2023).

Table 3.1: Observed WR+BH binary candidates in the local Universe

Name	Galaxy	average metallicity	refs	BH mass [$M_\odot$]	WR star mass [$M_\odot$]	orbital period [hr]	refs
Cygnus X-3	Milky Way	$\sim 0.7 z_\odot$	(1)	1.3-4.5	7.5-14.2	4.8	(4)
				6.0-8.4	10.4-12.8	4.8	(5)
NGC300 X-1	NGC300	$\sim 0.4 z_\odot$	(2)	13-21	21-33	32.8	(6)
IC10 X-1	IC10	$\sim 0.25 z_\odot$	(3)	23-32	17-35	35	(7) & (8)

Notes. (1) Brott et al. (2011), (2) Kudritzki et al. (2008), (3) Magrini and Gonçalves (2009), (4) Zdziarski, Mikolajewska and Belczynski (2013), (5) Antokhin et al. (2022), (6) B. A. Binder et al. (2021), (7) Clark and Crowther (2004), (8) Laycock, Maccarone and Christodoulou (2015)

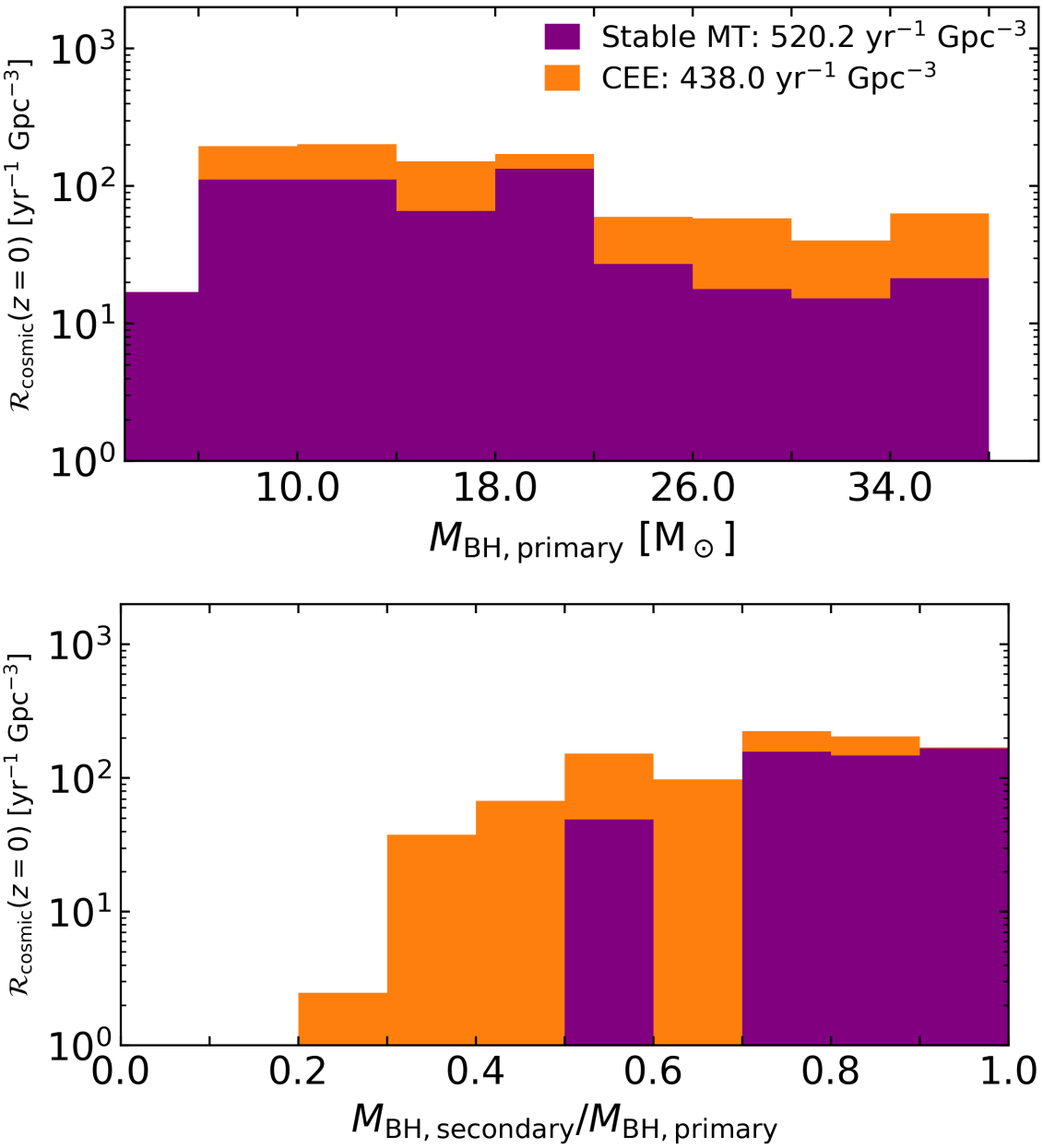

Figure 3.9: Predicted merging BBHs population at zero redshift. The Y-axis shows the merger rate density at zero redshift in unit of yr^{-1} Gpc^{-3}. The top and bottom panels show the distributions of the masses of the primary BHs $M_{\rm BH,primary}$ and the mass ratios $M_{\rm BH,secondary}/M_{\rm BH,primary}$ respectively. Different formation channels are coded in color (orange: CEE, purple: StableMT), and the total merger rate densities are indicated by the number in the legend in the top panel.

and (d) of Fig. 3.3, our prediction can cover NGC300 x-1 and IC10 X-1 but hardly explain Cygnus X-3. One reason is that the metallicity of the Milky Way (MW) is much higher than that of the SMC, which allows WR stars to be formed with less massive stripped stars. The compact object in Cygnus X-3 may lie in the mass gap between NS and BH, which may be formed through a different fallback factor (Olejak et al., 2022) or accretion-induced collapse (van den Heuvel and De Loore, 1973). In addition, our orbital period distribution suggests that Cygnus X-3 would probably have survived a past common envelope phase.

Observed radial velocities of SMC WR stars

Foellmi, Moffat and Guerrero (2003) monitored the SMC WR stars expect SMC AB12 and found 6 single WR stars by taking a radial velocity (RV) semi-amplitude of $30\,\mathrm{km\,s^{-1}}$ as their detection threshold, which can cause a missing of wide orbit systems (Fig. 4 in Paper I and Fig. 3.3 in this work). Schootemeijer, Shenar et al. (in prep) have preformed a monitoring campaign to examine whether these WR stars are truly single. The authors obtain maximum RVs of $\sim 5\,\mathrm{km\,s^{-1}}$ for SMC AB10 and $\sim 10\,\mathrm{km\,s^{-1}}$ for the other single WR stars by using N V lines, which are generally smaller than the values measured by He II 4686 Å(Foellmi, Moffat and Guerrero, 2003; Schootemeijer, Shenar et al., in prep).

In general, the small RVs measured by Schootemeijer, Shenar et al. (in prep) still have room for binarity. Wide WR binaries have a typical orbital velocity of $50\,\mathrm{km\,s^{-1}}$. Considering a inclination of 30°, the RV is below $15\mathrm{km\,s^{-1}}$ during 40% of one orbital period. In addition, Schootemeijer, Shenar et al. (in prep) have 6 spectra for each object, which may not be sufficient for resolving the orbital motion of long-period binaries.

If these SMC WR stars are truly single, there are severe consequences. Firstly, long-period OB+BH binaries seem not to exist neither, which also means that the CEE channel for forming merging BBHs does not exist. Secondly, it suggests a rather low binary fraction, while most massive stars are believed to have nearby companions (Sana et al., 2012). The lack of long-period massive evolved binaries may suggest that newborn BHs receive very strong kicks, which, however, can not explain the lack of wide WR+O binaries. It would be more likely that wide massive binaries undergo large orbital shrinkage during the first mass transfer due to overflow through outer Lagrangian points or common envelope evolution, and single WR stars are formed from merger products.

3.4.2 Merging binary black holes

The inferred merger rate density at $z = 0.2$ from GWTC-3 is 17.9 - $44\,\mathrm{yr^{-1}\,Gpc^{-3}}$ (R. Abbott et al., 2023), which is much lower than the value expected by our fiducial model (Fig. 3.8). Both the StableMT and CEE channels predict higher rate than the GWTC-3 result. Our predictions are highly sensitive to the treatment of the stability of mass transfer (see App. B), and we find that the GWTC-3 result can be reproduced by $q_{\rm min} = 0.34$ if the StableMT channel dominates the population at $z = 0$ or $\eta_{\rm CE} = 0.4$ if the CEE channel dominates (see App. B for details). Figure 3.10 compares the predicted population by our fiducial model, the StableMT channel with $q_{\rm min} = 0.34$ (hereafter $q_{\rm min}$-0.34 model), and the CEE channel with $\eta_{\rm CE} = 0.4$ (hereafter $\eta_{\rm CE}$-0.4 model) with the inferred population from GWTC-3 (R. Abbott et al., 2023).

The masses of primary BHs from GWTC-3 is featured by two peaks at around 8 $M_\odot$ and 35 $M_\odot$. Both the $q_{\rm min}$-0.34 model and $\eta_{\rm CE}$-0.4 model can produce similar feature with a mass gap between

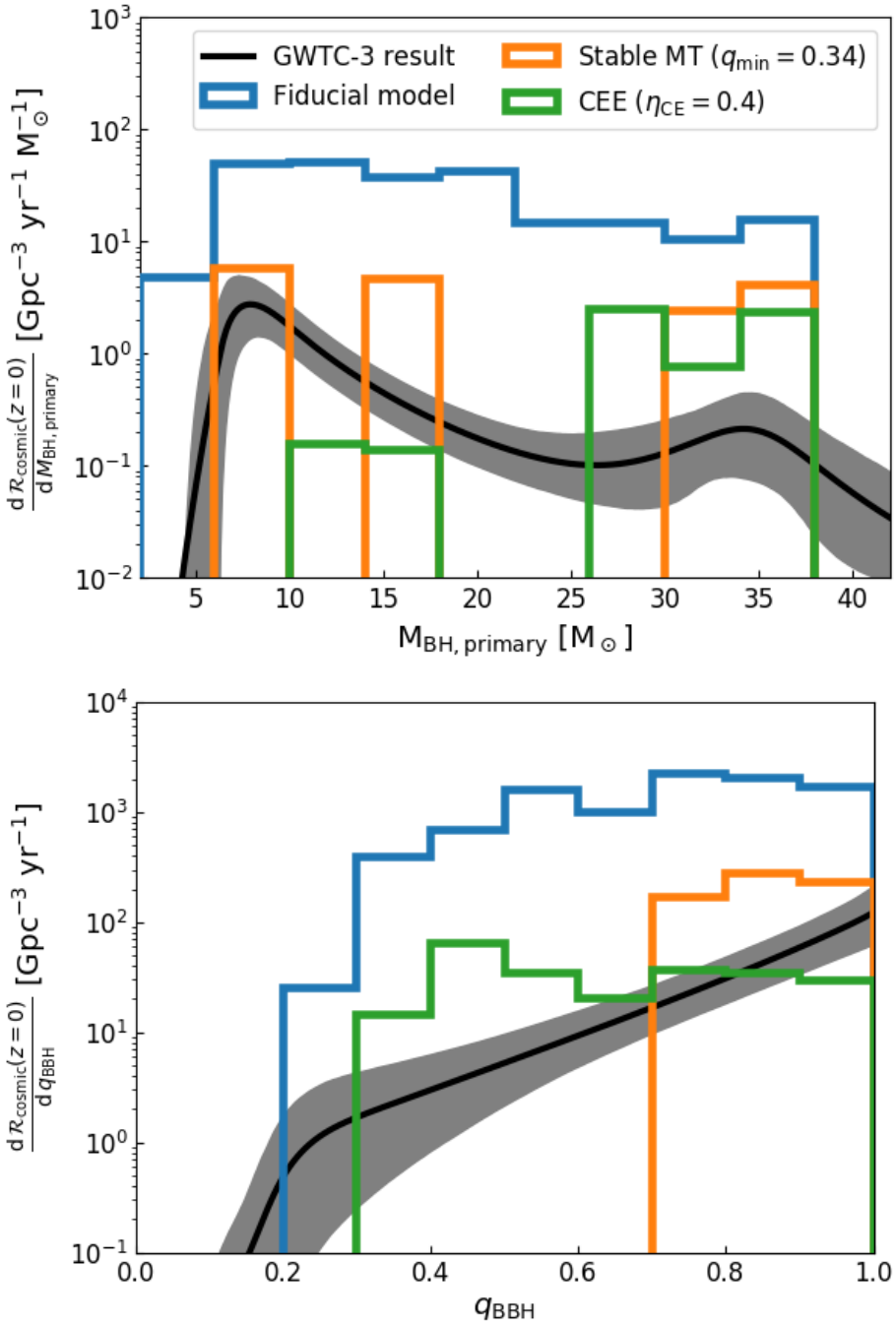

Figure 3.10: Predicted merging BBH population at zero redshift by the fiducial model (blue), the $q_{\rm min}$-0.34 model (orange), and the $\eta_{\rm CE}$-0.4 model (green). Top and bottom panels display the masses of primary BHs $M_{\rm BH,primary}$ and mass ratios $q_{\rm BBH}$ defined by $M_{\rm BH,secondary}/M_{\rm BH,primary}$. The black solid lines and the grey regions correspond to the median rates and the 90% credible interval given by the power law + peak model in R. Abbott et al. (2023).

20 $M_\odot$ and 25 $M_\odot$. In the $\eta_{\rm CE}$-0.4 model, this gap is related to the change in the binding energy parameter $\lambda_{\rm bind}$ of the envelope of the donor star at the Roche-lobe filling, whose value decrease with increasing masses. Above the mass gap the BH accretors are massive enough to avoid merger. For the $q_{\rm min}$-0.34 model, the mass gap is related to the lower orbital separation bound caused by L2 overflow, which become higher with increasing initial primary mass. Above this gap, BBHs are massive enough to merge within the Hubble time, while they have rather wide orbits. In addition, considering the rarity of our models that producing merging BBHs from the StableMT channel (Fig. B.4), this feature may change if our model grid is denser.

The distribution of mass ratio $q_{\rm BBH}$ inferred from GWTC3-3 peaks near 1 and rapidly decreases to 0.2. The $q_{\rm min}$-0.34 model expects all BBHs to have $q_{\rm BBH} > 0.7$ due to their high accretion efficiency during the first mass transfer episode, while the $\eta_{\rm CE}$-0.4 model predicts a near flat distribution between 0.3 and 1, reflecting the initial mass ratios of our model grid. This comparison suggests that the StableMT and CEE channels may contribute equally in the observed merging BBH population.

3.5 Comparisons with previous works

Previous population synthesis studies on WR+BH phase were performed with the Milky Way (MW) metallicity (Lommen et al., 2005; Shao and X.-D. Li, 2020). Both Lommen et al. (2005) and Shao and X.-D. Li (2020) expect $\sim$ 30 WR+BH binaries in the MW if assuming WR stars are stripped stars with masses larger than 7 $M_\odot$ (see Fig. 4 in Lommen et al. 2005 and Fig. 6 in Shao and X.-D. Li 2020). By checking whether an accretion disc can be formed around BHs, Lommen et al. (2005) predicted 1 wind-fed WR+BH X-ray binaries in the MW, while Shao and X.-D. Li (2020) assumes all WR+BH binaries can emit X-ray through wind accretion. In our work, WR+BH binaries are generally more massive than that in Shao and X.-D. Li (2020) due to the difference in metallicity. Our WR+BH binaries shares similar features with Shao and X.-D. Li (2020) that the CEE and StableMT channels are clearly separated in orbital period distribution. For the StableMT channel, we find more WR+BH binaries at around 1 day. The reason could be the difference in treating Case A systems. In addition, we expect 0.1 out of 2.6 WR+BH binaries in the SMC to become wind-fed X-ray binaries (see Sect. 3.6.7). This fraction is close to the result of Lommen et al. (2005). In addition, while Götberg, Korol et al. (2020) mainly focus on stripped star + neutron star or stripped star + white dwarf systems, we find similar orbital periods for the CEE survivors.

Different from other population synthesis studies performed by rapid codes (e.g. Dominik et al., 2013; Kruckow et al., 2018; Spera et al., 2019; Shao and X.-D. Li, 2021), we find that the StableMT channel can contribute a significant fraction of merging BBHs at zero redshift. This is also due to the difference in treating Case A systems. In our population, all merging BBHs formed from the StableMT channel are Case A systems (Fig. 3.2), while most of them undergo Case B mass transfer when the secondary star fills the Roche lobe. The stripping during the MS phase limits the growth of the inner core (S. E. de Mink, Pols and Hilditch, 2007), and the secondary star accretes a large amount of mass due to the high accretion efficiency. These processes produce rather extreme mass ratios for the OB+BH phase, which leads to large orbital shrinkage when the secondary star fills the Roche lobe. Many rapid population synthesis codes (e.g., Hurley, Tout and Pols, 2002) model mass transfer by assuming that H-rich envelope of donor star is completely stripped by Roche-lobe overflowing, which can not self-consistently compute the outcome of Case A mass transfer.

We note that our fiducial model predicts a merger rate density much higher than that by other

population synthesis studies. The main reason is that the parameters $q_{\rm min}$ and $\eta_{\rm CE}$ are treated differently through different works. For example, Kruckow et al. (2018) obtained a merger rate density of $16.8\,{\rm yr}^{-1}\,{\rm Gpc}^{-3}$ at $z = 0$ with $(\eta_{\rm CE},\, q_{\rm min}) = (0.5,\, 0.4)$. Adopting the same values as in Kruckow et al. (2018), we obtain a rate of $20\,{\rm yr}^{-1}\,{\rm Gpc}^{-3}$ at $z = 0$. Particularly, with $q_{\rm min} = 0.4$, the StableMT channel in our model can not produce merging BBHs anymore (see App. B and B).

In most previous studies, CEE plays an important or even dominating role in forming merging BBHs, which is challenged by recent detailed simulations (Klencki et al., 2020; Marchant, Pappas et al., 2021; Gallegos-Garcia et al., 2021). The reason for this difference could be the efficient semiconvection adopted in these detailed simulations (Sect. 3.6.3). Furthermore, Marchant, Pappas et al. (2021) find that stable mass transfer can take place even with mass ratio ($M_{\rm BH}/M_{\rm OB}$) down to 0.1, which is much lower than our model. Both Marchant, Pappas et al. (2021) and Gallegos-Garcia et al. (2021) do not consider the evolution before the first BH formation, which leads to a larger parameter space for forming merging BBHs through stable mass transfer than that in our model (Fig. 3.2). For example, the BH binaries with mass ratios of 0.1 in Marchant, Pappas et al. (2021) can not be formed in our model since it would require a very large mass loss during the first BH formation, and the BH binaries with orbital periods of 1 day in Gallegos-Garcia et al. (2021) are expected to merge during the first mass transfer in our model due to L2 overflow (see Paper I).

3.6 Discussion

3.6.1 Stability of mass transfer

During the first mass transfer, the stability of mass transfer is mainly determined by the ability of expelling transferred material when the mass gainer rotates critically (Marchant, 2017; Wang, Langer et al., 2020, and Paper I). This condition makes low-mass binaries with low initial mass ratio and close orbits merge easily (bottom-right grey regions in Fig. 3.2). Consequently, the fiducial model in Paper I expects 1/4 of the observed number of Be X-ray binaries (Haberl and Sturm, 2016) but can match observed number of WR+O binaries (Shenar, Hainich, Todt, Sander et al., 2016; Schootemeijer and Langer, 2018). In this work, we consider the binaries with initial primary mass above 20 $M_\odot$ and high initial mass ratio (Fig. 3.2). Therefore, our do not expect our WR+BH and BBH populations to be affected by this uncertainty.

The above criterion only applies to main-sequence mass gainers. For BH mass gainers, we adopt a parameterised criterion (Sect. 3.2.3) with $q_{\rm min} = 0.3$ and $P_{\rm orb,max} = 1000\,{\rm days}$ in our fiducial model. The values of these two parameters depend various factors like metallicity (Klencki et al., 2020), semiconvection (Klencki et al., 2020), and evolutionary stages (Ge, Webbink and Han, 2020). Particularly, there are cumulative evidences suggesting that $q_{\rm min}$ must be mass-dependent. To explain the observed Be X-ray binaries, it requires $q_{\rm min} = 0.5$ (Shao and X.-D. Li, 2014; Vinciguerra et al., 2020; Schürmann, Langer, X.-T. Xu et al., 2023), while the observed WR+O binaries suggest $q_{\rm min}$ close to 0.3 (Shao and X.-D. Li, 2016; Schürmann, Langer, X.-T. Xu et al., 2023; X.-T. Xu, Schürmann et al., 2023), also see Hastings, Langer, Wang et al. (2021). To address this uncertainty, we explore $q_{\rm min} = (0,\, 0.6)$ and $P_{\rm orb,max} = (500,\, 1500)$ days in App. B. We always expect 1 - 3 WR+BH binaries in the SMC. Expect the $q_{\rm min} = 0.6$ case, the typical values of $P_{\rm orb}$ and $\upsilon_{\rm WR}$ by different input parameters are similar to that by the fiducial model. In addition, the efficiency of expelling envelope during CEE $\eta_{\rm CE}$ does not have considerable effects on our WR+BH population since CEE survivors only takes a very small fraction.

Different from the SMC WR+BH binaries, the merging BBH population at $z = 0$ is highly sensitive with the values of $q_{\rm min}$ (Figs. B.2 and B.3). While the two formation channels contribute equally at $z = 0$ with $(q_{\rm min}, \eta_{\rm CE}) = (0.3, 1)$, there is no merging BBH formed from the StableMT channel with $q_{\rm min} = 0.4$ (also see Fig. B.4), and the merger rate predicted by the CEE is reduced by 2 orders of magnitude by varying $\eta_{\rm CE}$ from 1 to 0.3. For BH accretors, BH mass may also play an role in the stability of mass transfer (Shao and X.-D. Li, 2021). What makes the situation for the CEE channel even worse is that the $\eta_{\rm CE}$ parameter is coupled with the binding energy parameter $\lambda_{\rm bind}$ of the envelope of the donor star (see Eq. (3.7)), which is also not well understood (Sect. 3.3 in Wang, Jia and X.-D. Li, 2016; Ivanova et al., 2013; Marchant, Pappas et al., 2021). These factors cast large uncertainties on our merging BBH population.

3.6.2 Accretion efficiency

In our fiducial model, we fix accretion efficiency to zero since the accretion onto a BH is expected to be limited by the Eddington limit (App. B). There are works suggesting that stellar-mass BHs are able to accrete at a super-Eddington rate (Poutanen et al., 2007; Fabrika et al., 2015). If we allow BHs to accrete supercritically, the post-interaction BHs are more massive than our fiducial model. Moreover, this also means that less orbital angular momentum is lost through isotropic wind, and therefore orbits shrink less. This process produces longer delay time, which reduces the fraction of the merging BBHs formed from the StableMT channel at $z = 0$ (see the panel (c) in Fig. B.2).

For the first mass transfer (see section 6.2 in Paper I for details), higher accretion efficiency can result in wider orbits for the OB+BH phases, slightly enhancing the fraction of binaries entering the CE phase. It is unclear how this changes the number of the CEE survivors since donor star becomes more massive with higher accretion efficiency.

3.6.3 Semiconvection

Recent detailed simulations with the MESA code have shown that the maximum orbital period for stable mass transfer $P_{\rm orb,max}$ is underestimated in previous studies with rapid code (Klencki et al., 2020; Marchant, Pappas et al., 2021), which consequently leads to a much lower merger rate (Gallegos-Garcia et al., 2021). The reason is that both Klencki et al. (2020) and Marchant, Pappas et al. (2021) adopt a strong semiconvection suggested by Schootemeijer, Langer, Grin et al. (2019). Through the ratio of red supergiants (RSGs) and blue supergiants (BSGs) in the SMC, Schootemeijer, Langer, Grin et al. (2019) suggested a parameter of $\alpha_{\rm SC} > 10$ for semiconvection. Efficient semiconvection can wash out the chemical gradient above H-burning shell and enhance the energy generation rate of shell burning. Consequently, the envelope in the post-MS phase becomes less convective, resulting in larger $P_{\rm orb,max}$. Our SMC binary grid takes $\alpha_{\rm SC} = 1$ (Wang, Langer et al., 2020), which leads to $P_{\rm orb,max}$ about 500 - 1000 days (Fig. 3.2 and App. C in Paper I).

Whether semiconvection is efficient is still unclear since the role of binary interaction on forming BSGs is not well understand yet (Schneider et al., 2019; Klencki et al., 2020). If massive stars do have efficient semiconvection, we will have more OB+BH binaries with orbital periods around 1000 days, some of which may produce merging BBHs through common envelope evolution. Consequently, we will need lower $\eta_{\rm CE}$ to fit the merger rate density from GWTC-3.

In addition, Klencki et al. (2020) also showed that a low metallicity has similar effects to a strong semiconvection that the envelope of post-MS star becomes less convective and expands less.

Furthermore, this can form slowly-expanding core-helium-burning stars (Klencki et al., 2020), mass transfer from which is not well understood yet.

3.6.4 Chemically homogeneous evolution

The evolutionary pathways involving chemically homogeneous evolution (CHE) are not included in the WR+BH and BBH population predicted in this work. CHE in close can produce BBHs though two ways, (1) primary star evolves homogeneously, requiring low initial mass ratio (Marchant, Langer, Podsiadlowski, Tauris and Moriya, 2016), (2) both stars evolve homogeneously, requiring high initial mass ratio (Marchant, Langer, Podsiadlowski, Tauris, S. de Mink et al., 2017).

In the first case, binaries evolve though the OB+WR and OB+BH phases but only takes a small fraction of the whole population (see Paper I). Before the first BH formation, no Roche-lobe overflow takes place, and orbits largely widens due to the wind mass loss. Orbits widens further after the second mass transfer since the BHs are usually more massive than their companions (Fig. E.2 in Paper I). Hence we do not expect this channel to largely change our results, while it may produce BBHs with large mass ratio.

In the second case, both stars enter the WR star phase and produce BHs simultaneously. Our MESA models may be able to compute this channel properly since most massive close binaries with high initial mass ratio suffer from numerical errors in our model grid (Fig. 3.2). Mandel and S. E. de Mink (2016) and du Buisson et al. (2020) found that the merger rate density at zero redshift corresponding to this channel is below 10 $\mathrm{Gpc}^{-3}\,\mathrm{yr}^{-1}$, which is lower than the value inferred from GWTC-3 (Fig. 3.8). Hence our conclusion are not largely affected by this channel.

In addition, the BPASS code predicts that the channel involving CHE dominates the merging BBH population (Eldridge and Stanway, 2016). Different from the MESA model, the BPASS code computes rotational mixing in a parameterised way that CHE in the BPASS code is assumed to occur through accretion-induced spin up, while in our MESA model rotational mixing after mass transfer is inefficient due to the building up of chemical gradient. Eldridge and Stanway (2016) assumes that CHE can take place in 20 $M_\odot$ stars, while in our MESA model the minimum initial mass for CHE is $\sim 70\ M_\odot$, where stars are significantly spun down by wind braking (Paper I). Hence the BPASS code may overestimate the contribution of CHE.

3.6.5 Other uncertainties

Another potential uncertainty is related to the convergence errors in our model grid (white regions in Fig. 3.2). Figure 3.2 has shown that with increasing $\log M_{1,\mathrm{i}}$ convergence errors occur more frequently in the region with high q_i and low $\log P_{\mathrm{orb,i}}$. If these erroneous models could finally reach BBHs, the StableMT channel might be enhanced, which leads to a higher q_min to fit the GWTC-3 population.

In addition, our analysis only consider the evolutionary sequence presented in Fig. 3.1 such that the binaries undergo unstable mass transfer when the primary stars fill the Roche lobe are not included in Paper I and this work. We do not expect this channel can considerably change our SMC OB+BH and WR+BH populations since only a small fraction of these binaries can avoid merger (Sect. 4 in Pauli, 2020) but they may play an important role in forming merging BBHs (Briel, Stevance and Eldridge, 2022).

3.6.6 Fraction of WR stars having BH companions

Our fiducial model predicts 2.6 WR+BH binaries and 6.7 WR+O binaries (Paper I) in the SMC, resulting in a strikingly high fraction of WR stars that have BH companions. As already pointed out by (van den Heuvel, Portegies Zwart and S. E. de Mink, 2017b), this is due to the effect of lifetime that the WR stars in WR+O systems and the WR stars in WR+BH systems have comparable lifetimes.

Table 3.2 presents an example model, which is a wide-orbit system with initial masses of 63 $M_\odot$ and 56 $M_\odot$. This binary goes through the following stages, O+O, WR+O, BH+O, and BH+WR. The lifetime of the O+O phase is determined by the core hydrogen burning time of the primary star, which is about 3.89 Myrs. After a Case B mass transfer, the system enters the WR+O phase, whose lifetime is the core He burning time of the WR star, 0.30 Myrs. The WR star ends up with a BH, and the lifetime of the following BH+O phase is roughly equal to the difference between the main-sequence lifetimes between the primary star and secondary star, which is 0.23 Myrs. Then this binary goes into BH+WR phase, which has lifetime of 0.31 Myrs.

In this example, the WR stars formed from the primary star and secondary star have almost the same lifetime. With constant star formation, the chance to observe a object should be proportional to its lifetime (Sect. 3.2.6). Hence one can expect comparable numbers of the WR+O and WR+BH phases. Not all binaries have their secondary stars massive enough to form WR stars, and some binaries can not survive the common envelope evolution. This leads to a ratio of WR+BH/WR+O about 40%. In addition, in this example model, the lifetime of the O+BH phase is about 6% of the lifetime of O+O phase, which is consistent with the estimation by Langer, Schürmann et al. (2020) and X.-T. Xu, Schürmann et al. (2023).

For higher metallicity, the predicted population by Lommen et al. (2005) and Shao and X.-D. Li (2020) imply $\sim$ 30 WR+BH binaries in the MW, while there are $\sim$50 galactic WR+O binaries[5] (van der Hucht, 2001; van der Hucht, 2006; Crowther, 2015; Rosslowe and Crowther, 2015). It seems that the ratio of WR+BH/WR+O is rather metallicity-independent.

Table 3.2: Evolution of a wide binary with initial masses 63 $M_\odot$ and 56 $M_\odot$

Stage	O+O	WR+O	BH+O	BH+WR
Lifetime [Myrs]	3.89	0.30	0.23	0.31

3.6.7 Wind-fed X-ray binaries

To become a strong X-ray source, it requires an accretion disc formed around BH. The viscosity inside disc can efficiently convert potential energy into X-ray emission (Shakura and Sunyaev, 1973). We accordingly assume a WR+BH binaries becomes wind-fed X-ray binaries if an accretion disc formed around the BH, where we adopt the same criterion as in Sen, X.-T. Xu et al. (2021) (see App. B for detailed formulas) that a disc can be formed if the cricularization radius $R_{\rm disk}$ of captured wind material is larger than the radius of the innermost stable orbit $R_{\rm ISCO}$ (Shapiro and Lightman, 1976; Vanbeveren et al., 2020; Sen, X.-T. Xu et al., 2021). Figure 3.11 presents the distribution of $\log R_{\rm disk}/R_{\rm ISCO}$. The majority of WR+BH binaries have $R_{\rm disk}/R_{\rm ISCO}$ around 10^{-6} due to their wide orbits. We expect 0.11 out of 2.61 SMC WR+BH binaries can become wind-fed X-ray binaries, which

[5] http://pacrowther.staff.shef.ac.uk/WRcat/index.php

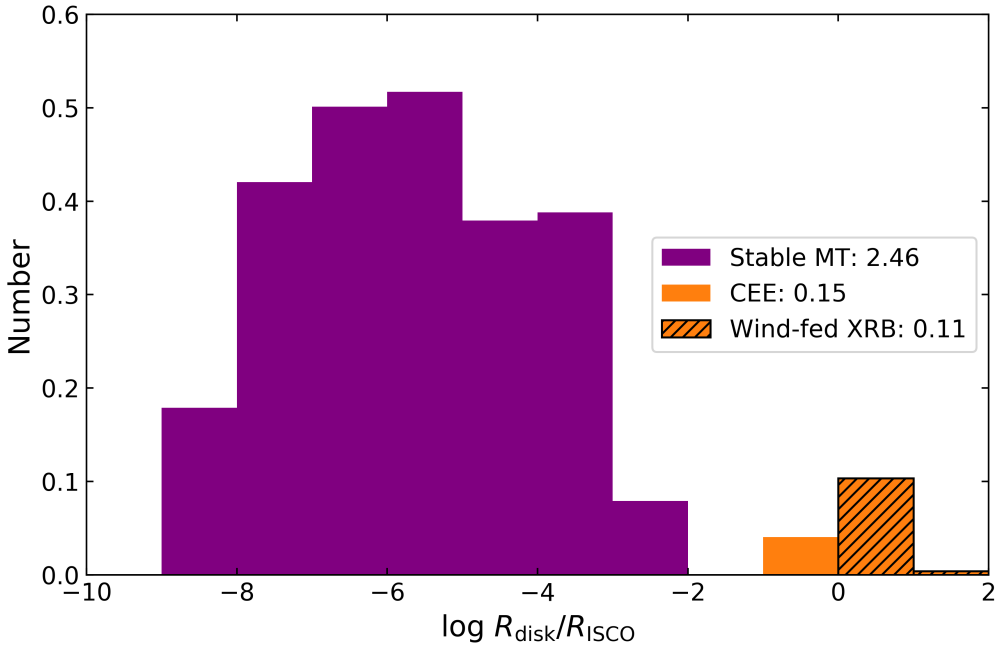

Figure 3.11: Predicted distribution of the ratio of the circularisation radius of captured material $R_{\rm disk}$ to the radius of the innermost stable orbit $R_{\rm ISCO}$. Different formation channels are coded in color (purple: StableMT channel, orange: CEE channel), and hatched histogram corresponds to $R_{\rm disk}/R_{\rm ISCO} > 1$, i.e., wind-fed X-ray binaries. The corresponding numbers are indicated in the legend.

is close to the fraction predicted by Lommen et al. (2005). The critical value $R_{\rm disk}/R_{\rm ISCO} = 1$ is related to a orbital period of 0.3 day, which can only be achieved by common envelope evolution in our fiducial.

We note that the observed WR X-ray binaries can have orbital periods up to 1.5 days (Tab. 3.1 and Fig. 3.3.2). Considering the uncertainties in metallicity, wind velocities, and the criterion for disc formation, this may not be a discrepancy.

3.6.8 Long Gamma-ray burst

While we ignore the effects of WR star winds and tides during the WR+BH phases, the orbital properties of WR+BH binaries can be largely changed by these two factors. Wolf-Rayet star's strong wind carries away a large amount of rotational angular momentum. If WR stars are tidally locked in close binaries, tidal interaction compensates for the angular momentum loss through stellar wind. This can cause strong orbital shrinkage, leading to merger and produce long Gamma-ray burst (LGRB) (Fryer, Woosley and Hartmann, 1999; Detmers et al., 2008).

To estimate the event rate of LGRB related to this scenario, we assume all WR+BH binaries below 1 day are tidally locked. The angular momentum loss rate through WR star wind $\dot{J}_{\rm WR}$ is taken to be

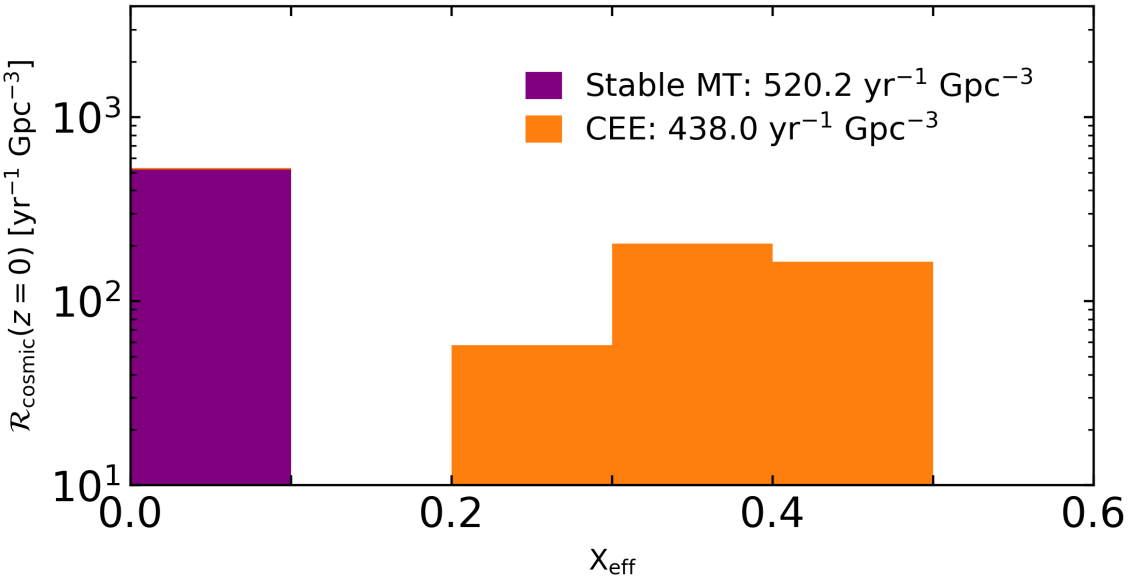

Figure 3.12: Predicted distribution of the effective spin parameter $X_{\rm eff}$ of the merging BBHs at $z = 0$. Different formation channels are coded in color (purple: StableMT channel, orange: CEE channel), and the corresponding total merger rate densities are indicated in the legend.

(Detmers et al., 2008)

$$\frac{J_{\rm WR}}{\dot{J}_{\rm WR}} = 0.1\frac{M_{\rm WR}}{\dot{M}_{\rm WR}}. \tag{3.20}$$

We expect a merger if the timescale of orbital shrinkage ($\tau_{\rm orb,wind} = |P_{\rm orb}/\dot{P}_{\rm orb}|$) is less than the lifetime of the WR+BH phase.

The above assumption gives a event rate of 4×10^{-7} yr^{-1} in the SMC, which is far below the event rate computed by Detmers et al. (2008). This may be due to the difference in treating common envelope evolution. Our estimated value is also below the intrinsic event rate by (Levan et al., 2016), $[1.6 \times 10^{-5},\ 6.6 \times 10^{-4}]$ yr^{-1} per galaxy [6]. Considering the uncertainties in tides, WR star wind, and our models, this discrepancy does not exclude WR+BH as main LGRB progenitors.

3.6.9 Effective spin parameter of binary black hole

Another effect of strong tide is to produce fast-rotating WR stars, which produce fast-rotating BHs. In our models, stellar core and envelope are strongly coupled through the Tayler-Spruit dynamo (Spruit, 2002), and the accretion onto a BH is limited by the Eddington limit. Hence the dimensionless spin parameter $a_{\rm spin}$ of the BH formed from the primary star is always close to zero and the $a_{\rm spin}$ of the BH formed from the secondary star can reach 1 only though the tide-induced spin-up during the WR+BH phase. Qin et al. (2018) found that there is a critical orbital period about 0.3 day. Below this value

[6] Levan et al. (2016) computed this value by multiplying the event rate obtained by Sun, Zhang and Z. Li (2015) with a fixed scaling factor of 10^7. Here a typical galaxy is assumed to have a B-band luminosity of 10^{10} $L_\odot$, and the B-band galaxy luminosity density is about 10^8 Mpc^{-3}. This value should be treated with caution since the effects of metallicity is ignored.

WR stars can be spun up to produce BH with $a_{\rm spin} = 1$. Otherwise, the outcome BHs can only have $a_{\rm spin}$ close to zero.

The effective spin of a BBH $X_{\rm eff}$ is the mass-averaged $a_{\rm spin}$ of two BHs. Figure 3.12 shows our estimated $X_{\rm eff}$ distribution at $z = 0$ by adopting the critical orbital period of 0.3 day found by Qin et al. (2018). All BBHs from the StableMT channel are expected to have zero $X_{\rm eff}$, while the BBHs from the CEE channel have $X_{\rm eff}$ between 0.2 and 0.5, which is roughly consistent with the results by Bavera et al. (2021). Observationally, the majority of merging BBHs have $X_{\rm eff}$ below 0.2 (R. Abbott et al., 2023), which may suggest the observed population is dominated by the StableMT channel.

3.6.10 Black hole as dark matter

The rotation curve of the SMC implies that the total mass of dark matter within 3 kpc of the SMC is about $3 \times 10^9\ M_\odot$. (Bekki and Stanimirović, 2009). Here we examine the probability that these dark matter are actually the BHs formed in the SMC. Taking a constant star formation rate of $0.05\ M_\odot\ {\rm yr}^{-1}$ (Sect. 3.2) and an age of 10 Gyrs (Harris and Zaritsky, 2004), our fiducial population synthesis model (Paper I and this work) gives a total BH mass of $\sim 6 \times 10^6\ M_\odot$. Our estimate suggests that the BHs formed in the SMC can not dominate the dark matter halo of the SMC otherwise it would require an unphysically high star formation rate or an age much longer than the Hubble time.

3.7 Conclusion

In this work, we have performed a population synthesis study on the properties of WR+BH binaries in the SMC with the dense detailed model grid computed by Wang, Langer et al. (2020). Then we discussed the role of stable mass transfer in producing merging BBHs by propagating our SMC population to all redshifts. We adopt the same assumptions as the fiducial model in Paper I. To evolve our SMC OB+BH binaries predicted in Paper I to the WR+BH phase, we further assume that the H-rich envelope of mass donor is completely stripped after mass transfer, and the accretion onto a BH is limited by the Eddington limit.

We expect 2-3 WR stars having BH companions in the SMC. We expect them to have orbital periods with periods about 50-300 days with a orbital velocity of $50\,{\rm km\,s^{-1}}$ for the WR star. In addition, we also expect a considerable fraction of WR stars above $150{\rm km\,s^{-1}}$. Comparing with the WR+O binaries predicted in Paper I, we find a strikingly high fraction of WR stars that have BH companion, which is not sensitive to our input parameters (see App. B). This can be explained by a simple argument that the WR stars in WR+BH binaries have comparable lifetimes as the WR stars in WR+O binaries. In addition, we find only 0.11 WR+BH binary can become wind-fed X-ray binaries by applying the criterion derived by Sen, X.-T. Xu et al. (2021).

We expect BBHs merging at a rate about 1.7 per Myr in the SMC, which is dominated by the CEE channel. Assuming all galaxies are SMC-like, the CEE and StableMT channels can contribute equally to the merging BBH population at zero redshift, where the StableMT channel is largely enhanced by high redshifts because of the rather high delay time. Different from the WR+BH population, the merging BBH population is highly sensitive to our assumption on the stability of mass transfer. Our model suggests that the StableMT channel may play an unignorable role in the observed merging BBH population.

There are 7 apparently single WR stars observed in the SMC (Shenar, Hainich, Todt, Sander et al.,

2016; Schootemeijer and Langer, 2018). We expect 2-3 of them are actually X-ray quiet WR+BH binaries. Identifying such systems can bring important insights on binary evolution and binary black hole merger.

CHAPTER 4

X-ray emission from BH+O star binaries expected to descend from the observed galactic WR+O binaries

Koushik Sen[a], Xiao-Tian Xu[a], Norbert Langer[a,b], Ileyk El Mellah[c], Christoph Schürmann[a,b], Martin Quast[a]

[a]Argelander-Institüt fur Astronomie, Universität Bonn, Auf dem Hugel 71, 53121 Bonn, Germany
[b]Max-Planck-Institüt fur Radioastronomie, Auf dem Hugel 69, 53121 Bonn, Germany
[c]Univ. Grenoble Alpes, CNRS, IPAG, 414 Rue de la Piscine, 38400 Saint-Martin-d'Hères, France

Astronomy and Astrophysics, 2021, 652, A138
DOI: 10.1051/0004-6361/202141214

Author contributions: K.S. and X.-T.X. contributed equally to this work. K.S. performed the analytical calculation together with X.-T.X. and wrote the first draft of this article. X.-T.X. performed the numerical calculation and produced the plots. N.L. found the discrepency between the literature and the work by M.Q.. K.S., X.-T.X., N.L., I.E.M., and C.S. interpreted the results. All authors reviewed the manuscript.

Summary: Black hole + O star (BH+O) binaries are thought to evolve from Wolf-Rayet + O star (WR+O) binaries. In Chapter 2, we predict 6-7 WR+O binaries and over 200 BH+OB binaries in the Small Magellanic Cloud. Observationally, there are 4 WR binaries observed but no BH+O binaries have so far been observed. This apparent lack of BH+O binaries also happens in the Milky Way (MW), where ~ 80 WR+O and one BH+O binaries (Cygnus X-1) have been found. To resolve this discrepency, it was suggested recently that the newborn BHs receive large momentum kicks (Vanbeveren et al., 2020), which disrupts most of the binaries.

Most of the observed BH+O binaries were found in X-ray band. Besides large BH kicks, it is also possible that most of BH+O binaries can not produce detectable X-ray emission and hence were missed in the past observations. Without a solid surface, a BH needs an accretion disc to become a strong X-ray emitter, where the potential energy of the accreted material is converted into X-ray emission

through viscosity. The formation of an accretion disc depends on how much the wind material from the O star companions that can be captured by the BHs and the angular momentum of the captured material. In this work, we revisit the analysis in Vanbeveren et al. (2020) with a particular emphasis on the uncertainty in the formation of accretion disc around BHs.

We assume that O star's wind is spherically symmetric, and the fraction of wind material can be accreted by the BH is determined by the accretion radius, which is given by the kinetic energy and potential energy of the wind material. The angular momentum of captured material can be described by the circularisation radius, which is the radius of the Keplerian orbit around the BHs that having the same specific angular momentum as the captured material. As a consequence of General Relativity, there is an innermost stable orbit around BHs, within which material can not form any stable structure. We expect an accretion disc around BHs if the circularisation radius is larger than the radius of the innermost stable orbit. If an accretion disc can form around the BHs, the X-ray luminosity is estimated by the release of the gravitational potential energy of the disc material, and we use 10^{-11} erg s^{-1} cm^{-2} as the threshold X-ray flux at Earth for observable X-ray binaries, which corresponds to the detection limit of non-focusing X-ray telescope. We use detailed stellar evolution models to follow the evolution of the O stars in the observed MW WR+O binaries.

There are 17 MW WR+O binaries having measurements of distances, masses, and orbital periods, from which our fiducial model predicts 2-3 wind-fed BH X-ray binaries, while Vanbeveren et al. (2020) predicted over one hundred due to an underestimation of O stars' wind velocity by a factor of 2.6. This slow wind makes BHs accrete much more material than the case with a typical O star wind. Besides wind velocity, we find that disc formation also sensitively depends on the amount of specific angular momentum carried by the wind, the efficiency of angular momentum accretion by the BH, and the spin of the BH. Varying these factors, our predicted number of wind-fed BH X-ray binaries changes from 0 to 33. In particular, we find that a high spin of the BH or a high Roche-lobe filling factor of the O star can boost the duration of the X-ray bright phase as well as the X-ray luminosity during this phase.

In conclusion, considering the uncertainties in accretion disc formation, we find that large BH formation kicks are not required to understand the sparsity of X-ray bright BH+O stars in the Milky Way. According to Chapter 2, there might be a large population of long-period BH+OB binaries, and the BHs can not produce observable X-ray due to their wide orbits. Probing for these X-ray silent BH binaries with alternative methods can likely inform us about BH kicks and the necessary conditions for high energy emission from high-mass BH binaries.

CHAPTER 5

Summary and outlook

Massive stars play an essential role in modern astrophysics, as they produce various important astrophysical phenomena, like Wolf-Rayet stars, supernovae, X-ray binaries, and gravitational waves. Most massive stars are believed to have nearby companions, which further enhances their importance in the era of gravitational wave. While our understanding of massive binaries has evolved rapidly over the past few decades, many crucial problems still remain unsolved, and more challenges arise from new observations, particularly the fast accumulating gravitational wave observations. Most of our knowledge of stars was built upon nearby isolated low-mass stars, while the observed gravitational-wave events may be produced by high-redshift massive binaries, where stars behave very differently from those in the local Universe.

While individual stars in the early Universe are not available for us, the Small Magellanic Cloud (SMC) provides unique laboratories to probe the early Universe. The SMC's metallicity is about 1/5 of the Solar value, corresponding to the average metallicity at a redshift of ~ 5. This also reduces the uncertainties related to stellar wind. The SMC is a star forming galaxy, whose rich population of massive stars is ideal for population synthesis study.

This thesis aims to constrain the uncertainties in massive binary evolution and understand the role of isolated binaries in forming BBHs by providing comprehensive population synthesis predictions for the massive star population in the SMC with a dense binary evolution model grid computed with a metallicity tailored for the SMC.

In Chapters 2 and 3, we present the results from our fiducial population synthesis model. Chapter 2 focuses on the evolution from the pre-interaction phase to the end of the main sequence phase of the initial secondary stars. Afterwards, in Chapter 3, we investigate the later evolutionary phases until the formation of BBH by using the BH binary population derived in Chapter 2 and analytical estimates for the mass transfer onto BHs. Our models can partly explain observations but also raise more questions.

In Chapter 2, our fiducial model predicts over one thousand O stars in the SMC with a constant star formation rate, which leads to the prediction of 6-7 WR+O and 211 OB+BH binaries. Most of our WR+O and OB+BH binaries have orbital periods of $\sim$100 days and orbital velocities of $\sim 50\,\mathrm{km\,s^{-1}}$. Our result suggests that we have a large chance of finding BHs in Oe star binaries. For NS binaries, our fiducial model predicts 25 OB+NS binaries in the SMC, showing a bimodal feature in their orbital period distribution.

Observationally, around 230 O stars are observed in the SMC. Schootemeijer, Langer, D. Lennon et al. (2021) suggest that this low number of O stars could be explained by a decreasing star formation

rate but, as shown in Chapter 2, this scenario can not produce enough WR+O binaries. The observed O+BH binaries and SMC WR+O binaries have orbital periods below 20 days, while our synthetic population is dominated by long-period binaries. These long-period binaries may be missing in past observations because of their low orbital velocities. Considering orbital inclination and orbital phase, 50 km s^{-1} would correspond to a radial velocity of 10 - 20 km s^{-1}, which is below the binarity threshold used in Foellmi, Moffat and Guerrero (2003). The observed SMC WR stars are much less massive than their O-type companions, while many of our close WR+O binaries have WR stars more massive than the O stars, where WR stars may outshine the O stars, making them not identified in past observations. We expect future monitoring campaign to find long-period O+BH and WR+O binaries in the SMC. For NS binaries, our predicted number is far below the observed one, suggesting that our merger criterion needs further investigation in the low-mass regime. In addition, we find a considerable fraction of NS binaries having orbital periods below the observed minimum value, which we expect to be X-ray quiet due to their rather low eccentricity.

As shown in Chapter 3, we predict 2-3 WR+BH binaries in the SMC, which show similar orbital properties to the WR+O and OB+BH binaries, i.e., having orbital periods of 100 days and orbital velocities of 50 km s^{-1} for the WR stars. Compared with our WR+O binaries, we find a strikingly high fraction of WR stars that have BH companions. This is because the lifetimes of WR+O and BH+WR phases are comparable, and the chance of finding an object is proportional to its lifetime if the star formation rate is constant. On the observational side, there is no WR+BH binary observed in the SMC yet, which may be hidden among the 7 apparently single WR stars. Our prediction on the merging BBHs at zero redshift is highly sensitive to the treatment of the stability of mass transfer and common envelope evolution. Our result suggests that the observed merging BBHs could be explained by isolated binaries. Unlike previous studies with rapid codes, we find Case A mass transfer can contribute a considerable fraction of merging BBHs at zero redshift.

Our main findings in Chapters 2 and 3 remain valid if we include non-extreme BH kicks. Recently, Vanbeveren et al. (2020) argued that the lack of wind-fed BH high-mass X-ray binaries implies that newborn BHs actually receive strong momentum kicks. We revisit the cterion of accretion disc formation in Vanbeveren et al. (2020), which is the key of producing strong X-ray emission for accreting BHs. We find that Vanbeveren et al. (2020) underestimate the wind velocity of O stars, which makes BHs accrete much more material than the case with a typical O star wind velocity. This leads to the prediction of over 100 wind-fed BH X-ray binaries in the Milky Way. With the updated criterion, we predict 2-3 wind-fed BH X-ray binaries. Therefore, considering the uncertainties in disc formation, strong BH kicks are not necessary to understand the dearth of wind-fed BH high-mass X-ray binaries.

In general, our findings highlight the importance of long-period massive evolved binaries (WR+O, BH+OB, and BH+WR binaries), which have large impacts on the merging BBH formation but have not yet been observed. The close massive binaries observed so far may be the tip of the iceberg. We do find NS binaries having orbital periods of over 100 days, so it is fair to believe that long-period WR binaries and BH binaries do exist. In addition, as we explain in Chapter 2, WR stars could outshine their O-type companions, making them hard to identify. In the future, we can make detailed predictions for the spectra of high-mass-ratio WR+O binaries to refine the searching of such systems.

A recent monitoring campaign (Schootemeijer, Shenar et al., in prep) suggests that the apparently single WR stars in the SMC are truly single, which means that long-period OB+BH binaries do not exist either, and the channel involving common envelope evolution for forming merging BBHs might be ruled out. In this campaign, each WR star has 6 spectra, which may not be enough to resolve the

orbital motion of long-period binaries. A two-year spectroscopic survey on the massive stars in the SMC was launched recently, which will give us more insights into the massive stars at low metallicity. While WR stars are not included in this survey, possible detections of long-period O+BH binaries can give us clues about their direct progenitors, O+WR binaries.

Another important question arising from our result is the stability of mass transfer. While our physical-motivated criterion can hardly explain the observed Be X-ray binary population, it can recover the observed SMC WR+O binaries. It seems that we are on the right direction. Theoretically, merger criterion, accretion efficiency, and stellar rotation are closely related. Previous studies on Be X-ray binaries found that a high accretion efficiency is required to explain the observed minimum mass for the Be stars, which could also be solved by a different merger criterion. If wide binaries do have high accretion efficiency, the following question is whether critically rotating stars can keep accreting mass. In the future, the newly launched SMC survey will enrich our knowledge about Be stars, and a new binary evolution model grid is needed to further investigate Be X-ray binaries.

Most of previous population studies find that common envelope evolution plays an important or even dominating role in forming merging BBHs, which is challenged by recent detailed simulations. Our studies confirm that stable mass transfer can contribute a significant fraction to the merging BBHs at zero redshift. We find that the fractions of these two channels are sensitive to various factors, like semiconvection, tide, accretion efficiency, and mass transfer stability, which needs further investigation in the future. The binary model grid adopted in this thesis suffers from numerical errors in the high-mass end. We also need to overcome these problems to better understand the role of stable mass transfer. All stars in our binary model grid are initially slow rotators since we assume they are initially tidally locked. However, the early B stars observed by VLT-FLAMES Survey (Dufton, Langer et al., 2013) suggests that young stars could rotate at 50% of their critical rotational velocities, which can induce chemically homogeneous evolution and may largely affect the properties of BBHs.

While the above discussion mainly focuses on massive binaries, there should be a large population of white dwarfs (WD) and less massive stripped stars (sdOB) according to the initial mass function. Currently, there are two Be+WD candidates reported in the SMC (Sturm et al., 2012; Coe, Kennea et al., 2020). In the Milky Way, around 17 sdOB stars and Be+sdOB candidates are observed so far (Schürmann, Langer, X. Xu et al., 2022). We expect more such objects to be identified in the future, providing more insights into binary evolution.

In this thesis we briefly investigate the properties of Be X-ray binaries and wind-fed BH high-mass X-ray binaries. X-ray binary population shows a large diversity (Reig, 2011), where low-mass X-ray binaries are believed to be common envelope survivors due to their tight orbits ($\sim$ 1 days) and low-mass main-sequence companions ($\sim$ 1 $M_{\odot}$) (Tauris and van den Heuvel, 2006). Currently, most of the detailed simulations do not consider the evolution before the compact object formation. We can also use our MESA binary evolution models to investigate low-mass X-ray binaries to obtain a better understanding of common envelope evolution.

Through this thesis, we have demonstrated many important features that are not found in previous rapid binary evolution codes, which raise more questions. On the observational side, new devices and observation campaigns, like James Webb Space Telescope (JWST), Transiting Exoplanet Survey Satellite (TESS), extended ROentgen Survey with an Imaging Telescope Array (eROSITA), and advanced Laser Interferometer Gravitational-Wave Observatory (aLIGO), will help us test our theory and bring more exciting science in the foreseeable future.

APPENDIX A

Appendix to Chapter 2

Calculations of statistical weights

We assume the distribution of the initial mass of primary star is described by the initial mass function (IMF), which is $f_{\rm IMF} \propto M_{1,\rm i}^{-\alpha}$, and the distributions of initial mass ratio and initial orbital period are $f_{q_{\rm i}} \propto q_{\rm i}^{-\beta}$ and $f_{\log P_{\rm orb,i}} \propto \log P_{\rm orb,i}^{-\gamma}$. The number of a binary $N_{\rm b}$ with initial parameter ($M_{1,\rm i}$, $q_{\rm i}$, $\log P_{\rm orb,i}$) is

$$N_{\rm b} \propto M_{1,\rm i}^{-\alpha} q_{\rm i}^{-\beta} \log P_{\rm orb,i}^{-\gamma}. \tag{A.1}$$

In order to take into account star formation rate, we rewrite Eq. (A.1) into mass fraction form,

$$F_{\rm b} \propto M_{1,\rm i}^{-\alpha} \times (M_{1,\rm i} + M_{1,\rm i}\, q_{\rm i}) q_{\rm i}^{-\beta} \log P_{\rm orb,i}^{-\gamma}. \tag{A.2}$$

Then from a constant star formation rate (SFR), the predicted number of a OB+cc binary is given by

$$N_{\rm b} = {\rm SFR} \times {\rm lifetime} \times \frac{\int_V F_{\rm b}\, {\rm d}\log M_{1,\rm i}\, {\rm d}q_{\rm i}\, {\rm d}\log P_{\rm orb,i}}{< M_{\rm b} >}, \tag{A.3}$$

where V is the parameter space enclosed by [$\log P_{\rm orb,i}$, $\log P_{\rm orb,i} + \Delta \log P_{\rm orb,i}$], [$q_{\rm i}$, $q_{\rm i} + \Delta q_{\rm i}$], and [$\log M_{1,\rm i}$, $\log M_{1,\rm i} + \Delta \log M_{1,\rm i}$], ($\Delta \log M_{1,\rm i}$, $\Delta q_{\rm i}$, $\Delta \log P_{\rm orb,i}$) are the intervals of our model grid, lifetime is the lifetime of the OB+cc phase, and $< M_{\rm b} >$ is the averaged mass of the binary in within the parameter space V weighted by the initial distributions, i.e.,

$$< M_{\rm b} >= \frac{\int_V N_{\rm b} (M_{1,\rm i} + q M_{1,\rm i})\, {\rm d}\log M_{1,\rm i}\, {\rm d}\, q_{\rm i}\, {\rm d}\log P_{\rm orb,i}}{\int_V N_{\rm b}\, {\rm d}\log M_{1,\rm i}\, {\rm d}\, q_{\rm i}\, {\rm d}\log P_{\rm orb,i}}. \tag{A.4}$$

Defining statistical weight W as following,

$$W(M_{1,\rm i},\, q_{\rm i},\, \log P_{\rm orb,i}) = \frac{\int_V F_{\rm b}\, {\rm d}\log M_{1,\rm i}\, {\rm d}q_{\rm i}\, {\rm d}\log P_{\rm orb,i}}{< M_{\rm b} >}, \tag{A.5}$$

Eq. (A.3) has the following form

$$N_{\rm b} = {\rm SFR}\times {\rm lifetime}\times W(M_{1,{\rm i}},\, q_{\rm i},\, \log P_{\rm orb,i}). \tag{A.6}$$

In order to include non-constant star formation rate, we introduce the factor SFH,

$${\rm SFH} = \frac{\int_{t_{\rm i,OB+cc}}^{t_{\rm f,OB+cc}} {\rm SFR}(t)\,{\rm d}t}{\rm lifetime}, \tag{A.7}$$

where the SFR is the function of lookback time t, i.e., $t = 0$ marks the observed status, $t_{\rm i/f,OB+cc}$ are the binary age of entering/ending OB+cc phase. The observed OB+cc population at $t = 0$ comes from the star formation starting at $t = t_{\rm f,OB+cc}$ and ending at $t = t_{\rm i,OB+cc}$. With this, the predicted number of a OB+cc binary with non-constant SFR is given by

$$N_{\rm b} = {\rm SFH}\times {\rm lifetime}\times W(M_{1,{\rm i}},\, q_{\rm i},\, \log P_{\rm orb,i}). \tag{A.8}$$

The number of O stars, He stars, and WR stars are computed with the same method except the lifetimes are determined by effective temperature hotter than 31.6 kK, core helium burning, and core helium burning with logarithmic luminosity higher than 5.6.

Tides during OB+cc phase

As mentioned in Sect. 2.2.1, after the formation of BH or NS, we evolve the secondary as a single star. However, during the OB+cc phase, the OBe star can be spun down by tides. Here we take into account tidal interaction by considering the synchronization timescale at the beginning of OB+cc phase. If the synchronization timescale is shorter than 10% of the lifetime of OB+cc phase[1], we expect in the following OB+cc phase the OB star is rapidly spun down by tides and can not form OBe stars.

In order to take into account the effect of eccentricity on tides, we introduce a different definition of synchronization timescale $\tau_{\rm sync}$ basing on Hut (1981) and Hurley, Tout and Pols (2002). The spin evolution of stars induced by tides is given by Hut (1981)

$$\begin{aligned}\frac{{\rm d}\,\Omega_{spin}}{{\rm d}\,t} = 3\left(\frac{k}{T}\right)_{\rm rad}\left(\frac{q^2}{r_{\rm g}^2}\right)\left(\frac{R}{a}\right)^6 \frac{\Omega_{orb}}{(1-e^2)^6} \\ \times\left[f_2(e^2) - (1-e^2)^{3/2}\, f_5(e^2)\frac{\Omega_{spin}}{\Omega_{orb}}\right],\end{aligned} \tag{A.9}$$

where Ω_{orb} and Ω_{spin} are the orbital angular velocities and spin angular velocities of OB star, mass ratio q is $M_{\rm cc}/M_{\rm OB}$, $r_{\rm g}$ is the ratio of gyration radius to stellar radius R, e is eccentricity,

$$\left(\frac{k}{T}\right)_{\rm rad} = 1.9782\times 10^4 \left(\frac{M_{\rm OB}R^2}{M_\odot R_\odot^2}\frac{R_\odot^5}{a^5}\right)^{1/2} (1+q)^{5/6} E_2\ {\rm yr}^{-1}, \tag{A.10}$$

[1] While we take 10% as the threshold value for strong tide, we also perform experiments with 30%, 50%, and 100% and the predicted OBe+cc binaries remain unchanged.

the numerical factor E_2 is

$$E_2 = 1.592 \times 10^{-9} \left(\frac{M_{\rm OB}}{M_\odot} \right)^{2.84}, \tag{A.11}$$

$f_2(e^2)$ and $f_5(e^2)$ are defined by Hut (1981),

$$f_2(e^2) = 1 + \frac{15}{2} e^2 + \frac{45}{8} e^4 + \frac{5}{16} e^6 \tag{A.12}$$

and

$$f_5(e^2) = 1 + 3e^2 + \frac{3}{8} e^4. \tag{A.13}$$

Basing on the above equations, we can define the synchronization timescale $\tau_{\rm sync}$ as

$$\begin{aligned} \tau_{\rm sync} &= \left| \frac{\Omega_{{\rm s}pin} - \Omega_{{\rm o}rb}}{\dot{\Omega}_{\rm spin}} \right| \\ &= \left[3 \left(\frac{k}{T} \right)_{\rm rad} \left(\frac{q^2}{r_{\rm g}^2} \right) \left(\frac{R}{a} \right)^6 \right]^{-1} \\ &\times \left| \frac{(1-e^2)^6 (\Omega_{{\rm s}pin} - \Omega_{{\rm o}rb})}{f_2(e^2)\Omega_{{\rm o}rb} - (1-e^2)^{3/2} f_5(e^2) \Omega_{{\rm s}pin}} \right|. \end{aligned} \tag{A.14}$$

For circular orbit, i.e., $e = 0$, Eq. (A.14) becomes the widely used form

$$\tau_{\rm sync}(e=0) = \left[3 \left(\frac{k}{T} \right)_{\rm rad} \left(\frac{q^2}{r_{\rm g}^2} \right) \left(\frac{R}{a} \right)^6 \right]^{-1}. \tag{A.15}$$

With the above assumption, we find that the tide interaction during the OB+BH phase is too weak to spin down the OB stars. In our fiducial model, 170.401 OBe+BH binaries are predicted. Without tide, 170.403 OBe+BH binaries are predicted.

Outcomes of our model grid

The outcomes of our detailed binary evolution models with initial primary mass from 5.0 $M_\odot$ to 15.8 $M_\odot$ (Fig. A.1) and from 20 $M_\odot$ to 100 $M_\odot$ (Fig. A.2), where each pixel represents one detailed MESA binary model, and the related evolutionary outcome is coded in color.

Supernova window

We adopt the ComBinE supernovae window through the following approach.

- We use the ComBinE code simulates binaries with flat distribution for initial primary mass $M_{1,\rm i}$, initial mass ratio $q_{\rm i}$, and initial logarithmic orbital period $\log P_{\rm orb,i}$.

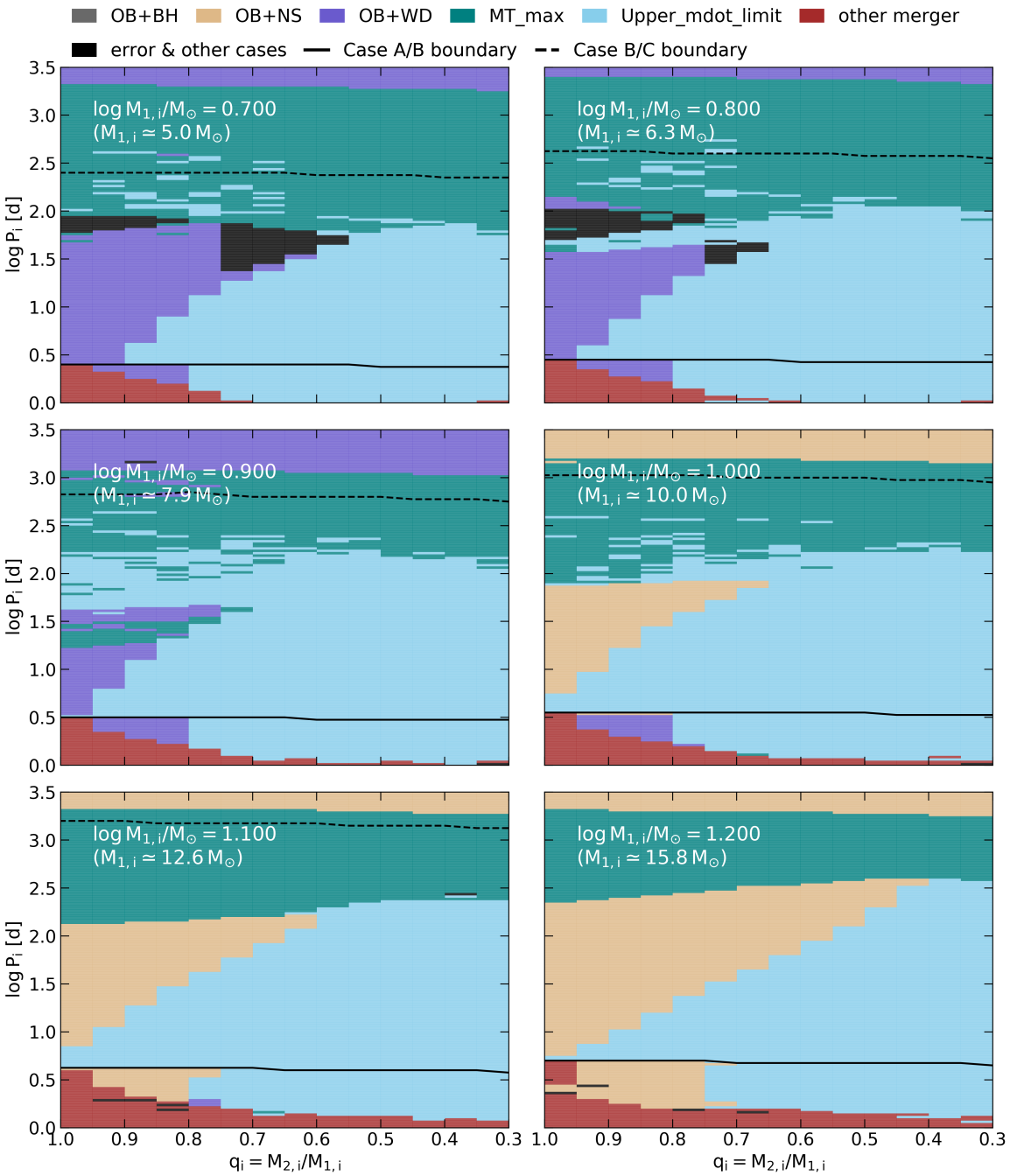

Figure A.1: The outcomes of our detailed binary evolution models. The same as Fig. 2.2 but for initial primary mass 5.0 $M_\odot$, 6.3 $M_\odot$, 7.9 $M_\odot$, 10.0 $M_\odot$, 12.6 $M_\odot$, and 15.8 $M_\odot$

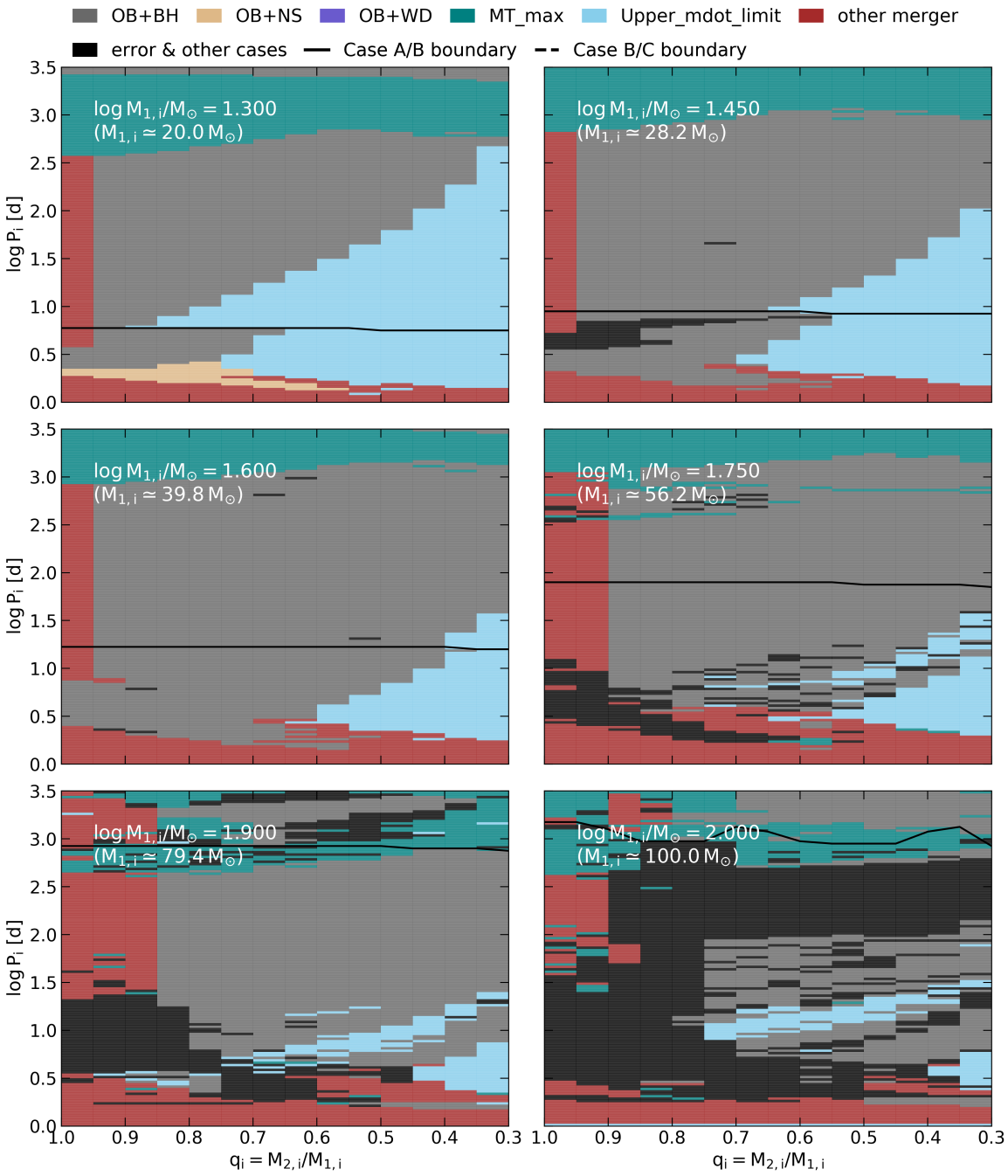

Figure A.2: The outcomes of our detailed binary evolution models. The same as Fig. 2.2 but for initial primary mass 20.0 $M_\odot$, 28.2 $M_\odot$, 39.8 $M_\odot$, 56.2 $M_\odot$, 79.4 $M_\odot$, and 100.0 $M_\odot$.

- We calculate the following statistical weight for all ComBinE models,

$$W = M_{1,i}^{-\alpha} q_i^{-\beta} \log P_{orb,i}^{-\gamma}, \tag{A.16}$$

  where (α, β, γ) are determined by initial distributions. For our fiducial (the Kroupa IMF and the Sana distribution), $(\alpha, \beta, \gamma) = (2.3, 0.1, 0.55)$, and for the logPq-flat model, $(\alpha, \beta, \gamma) = (2.3, 0, 0)$.

- With the above statistical weight, we calculate the fraction of different types of SNe in each pixel of our SMC model grid. Taking ECSN as an example, the ECSN fraction f_{ECSN} is evaluated as

$$f_{ECSN} = \frac{\sum_{j=1}^{N} \delta_{ECSN} W_j}{\sum_{j=1}^{N} W_j}, \tag{A.17}$$

  where N is the total number of ComBinE models inside the give grid pixel, and

$$\delta_{ECSN} = \begin{cases} 1 & \text{if the model undergoes ECSN} \\ 0 & \text{the other cases} \end{cases} . \tag{A.18}$$

- To apply the ECSN fraction to our calculations, we use the Monte Carlo method to generate a sample of kick velocities with sample size n, where $n \times f_{ECSN}$ of the sample are draw from the kick distribution corresponding to ECSN.

- We repeat the above steps to the other types of SNe.

Figure A.3 shows the ECSN fraction for each pixel in our model grid. With binary interaction, the ECSN still happens in a very narrow parameter space (initial primary mass in 8.91 - 10 $M_\odot$). We see that ECSN window behaves differently in case A/B systems. In Case B systems, mass transfer helps the donor star avoid the second dredge-up, which makes ECSNe become possible with relatively low-mass stars. In Case A systems, mass transfer happens when the primary stars are still on the main sequence, which limits the growth of the inner core in the post-main-sequence evolution, and consequently the minimum initial primary mass for ECSNe is shifted towards the high-end.

Further model details

Properties of OB+WR binary systems

Figure A.4 presents the OB+WR binaries in the mass ratio M_{WR}/M_{OB} - logarithmic orbital period $\log P_{orb}$ plane. Most of our OB+WR binaries have a M_{WR}/M_{OB} of 0.7. Below this values, binaries are formed with low initial orbital period and close-to-one initial mass ratio, where the mass gainer can accrete a large amount of mass. The number drop towards high $\log P_{orb}$ is related to the initial distribution (cf. Sect. 2.3.2).

Properties of OB+cc binary systems

We further distinguish different formation channels (Case A or Case B). Case A systems produce the most massive O stars reaching 100 $M_\odot$ and the slowest rotators, while Case B systems produce

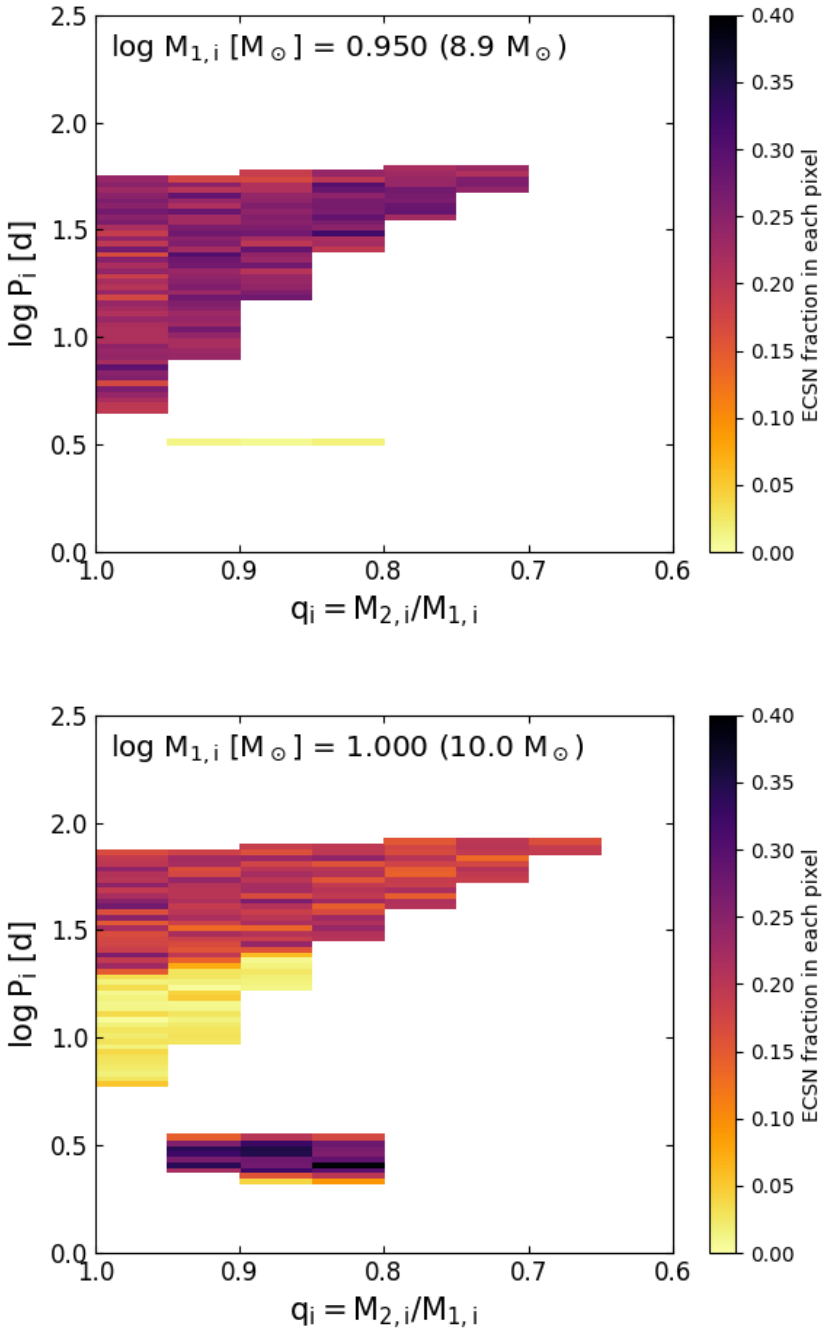

Figure A.3: ECSN fraction on the $q_{\mathrm{i}} - \log P_{\mathrm{orb,i}}$ plane with initial primary mass 8.91 $\mathrm{M}_{\odot}$ and 10 $\mathrm{M}_{\odot}$.

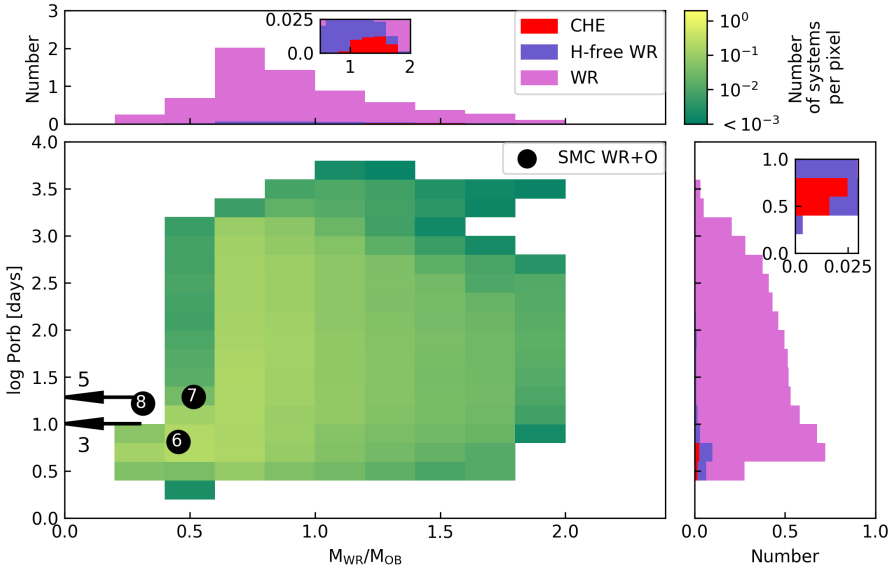

Figure A.4: Predicted distribution of OB+WR binaries in the mass ratio $M_{\rm WR}/M_{\rm OB}$ - logarithmic orbital period $\log P_{\rm orb}$ plane. The number in each pixel is coded in color. The H-free and CHE WR stars are identified in 1D projection. The observed WR binaries (Foellmi, Moffat and Guerrero, 2003; Foellmi, 2004; Koenigsberger et al., 2014; Hainich et al., 2015; Shenar, Hainich, Todt, Sander et al., 2016; Shenar, Hainich, Todt, Moffat et al., 2018) are plotted with black.

less massive OB stars and most of them are near-critically rotating. Case A systems usually have tight orbit, resulting in strong tidal interaction. As a result they have relative high accretion efficiency according to our rotation-dependent accretion efficiency. The opposite takes place in Case B systems, which results in near-zero accretion efficiency.

Masses and mass ratios

The top panel of Fig. A.5 shows the predicted distribution of $M_{\rm OB}$. The distribution peaks at $\sim 10 M_\odot$, below which stars have less chance to form BHs or NSs. Above $10\,M_\odot$ the number drop is due to the effects of the IMF and lifetime. Both BH systems and NS systems have a minimum companion mass about $6\,M_\odot$ (cf., Sect. 2.3.1).

The middle panel of Fig. A.5 shows the predicted distribution of $M_{\rm BH}$, which is mainly shaped by the IMF (cf. Sect. 2.3.4). In Case A systems, mass transfer begins when primary stars are still on the MS, which limits the growth of He core. Therefore, BH progenitors in Case A systems trend to higher initial primary mass than that in Case B systems. Towards the high-mass end, the orbital period window of Case A binaries becomes wider and wider due to the increasing importance of envelope inflation. These wide-orbit Case A systems produce the most massive BHs, which can have fast-rotating companions because of weak tide.

The bottom panel of Fig. A.5 presents the distribution of mass ratio of OB+cc binaries ($q = M_{\rm cc}/M_{\rm OB}$). In our calculations, the mass of NS is fixed to be $1.4\,M_\odot$, while most of their companions have mass around $10\,M_\odot$, leading to a peak in mass ratio at $\simeq 0.1$. Since our model predicts all OB

stars in OB(e)+NS binaries to be more massive than 6 $M_{\odot}$, the highest mass ratio of NS systems is about 0.2-0.3.

The mass ratio of OB+BH binaries peaks at ≃0.6-0.7, clearly separated from the NS systems. The drop in numbers towards high mass ratio is due to the increasing fraction of the binaries undergoing unstable mass transfer. The effects of decreasing lifetime cause the number drop towards low mass ratio. Case A systems contribute the lowest mass ratio ∼0.2 and highest mass ratio ∼1.8, corresponding to close binaries with high accretion efficiency and wide binaries with inflated primary stars respectively.

Orbital properties

The top panel of Fig. A.6 shows the distribution of orbital periods of OB+cc binaries $P_{\rm orb}$. Our merger criterion leads to a peak near $P_{\rm orb}$ = 100 days (cf. Sect. 2.3.4), which is dominated by Case B systems. Case A systems require close orbits, leading to a peak near 7 days. A small fraction of Case A systems have orbital periods above 100 days due to envelope inflation (BH binaries) or SN kick (NS binaries).

The bottom panel of Fig. A.6 shows the distribution of the semi-amplitude of orbital velocities of OB stars $K_{\rm OB}$. For BH systems, the $K_{\rm OB}$ distribution peaks at 30 - 40km s^{-1}, corresponding to Case B systems. Case A systems peaks at 80 - 90km s^{-1} since them have closer orbits. For NS systems, the OB stars are much more massive than the NSs, making $K_{\rm OB}$ less than 30km s^{-1}. A few NS binaries have $K_{\rm OB} > 200$km s^{-1} due to their high eccentricity.

Rotation of OB stars

Figure A.7 presents the distribution of rotational velocity $\upsilon_{\rm rot}$ of OB stars (top panel), which shows a fast-rotating peak around 600km s^{-1} with a slow-rotating tail extended to 100km s^{-1}. The fast-rotating peak reflect the critical rotation velocities of stars with mass around 10 $M_{\odot}$. In Case A systems, tidal interaction plays an important role, which makes $\upsilon_{\rm rot}$ distributed in $100 - 600$km s^{-1}. We note that some Case A BH and NS binaries can rotate critically. For BH binaries, these critically rotating systems have inflated primary stars and wide orbit. For NS binaries, the stripped star could not be massive enough to spin down the mass gainer.

We further present the distribution of the ratio of rotational velocity to critical velocity $\upsilon_{\rm rot}/\upsilon_{\rm crit}$ in the bottom panel of Fig. A.7. Similar with the top panel, the $\upsilon_{\rm rot}/\upsilon_{\rm crit}$ ratio shows a fast-rotating peak at 1 with a slow-rotating tail extended to 0.2, corresponding to Case B and Case A systems. In Case B systems, most of binaries have $\upsilon_{\rm rot}/\upsilon_{\rm crit} > 0.95$ as expected, while 18 of them with $\upsilon_{\rm rot}/\upsilon_{\rm crit} < 0.95$ are braked by stellar wind.

Surface abundance of OB stars

We present the predicted distribution of surface abundance of OB stars in Fig. A.8. Surface abundance can be enriched through two ways, internal mixing and mass transfer. For He, it is mainly enriched by mass transfer because the strong gradient in mean molecular weight between the core and the envelope prevents the transfer of He. Due to the near-zero accretion efficiency of wide binaries, most of OB stars have He unenriched. When the second mass transfer episode takes place, some accretors rotate sub-critically due to wind braking, allowing their surface He to be slightly enriched. In Case A systems, due to the effect of tidal braking, accretion efficiency can be up to 60%. Consequently, the most enriched star has surface helium mass fraction about 0.5. The unenriched Case A binaries have inflated primary stars.

The distribution of surface nitrogen enhancement factor (surface nitrogen mass fraction divided by initial surface nitrogen mass fraction) is presented in the lower panel of Fig. A.8. Different from helium, surface nitrogen can be enriched by both mixing and mass transfer because CN-equilibrium is reached before the establishment of the strong gradient in mean molecular weight so that nitrogen in core can be transferred throughout envelope. In Case B systems, surface nitrogen is mainly enriched by internal mixing, resulting in an enrichment factor about 2-3. In Case A systems, the unenriched peak is related to the effect of envelope inflation and mass transfer leads to an enrichment factor of 10 to 15. Hastings, Wang and Langer (2020) has shown that the surface abundance of nitrogen is sensitive with initial rotation velocity. An initially fast-rotating star can have its surface nitrogen enriched by a factor of 30. In our models, all secondary stars are initially slow rotators. Hence our results give an lower limit on the nitrogen enhancement.

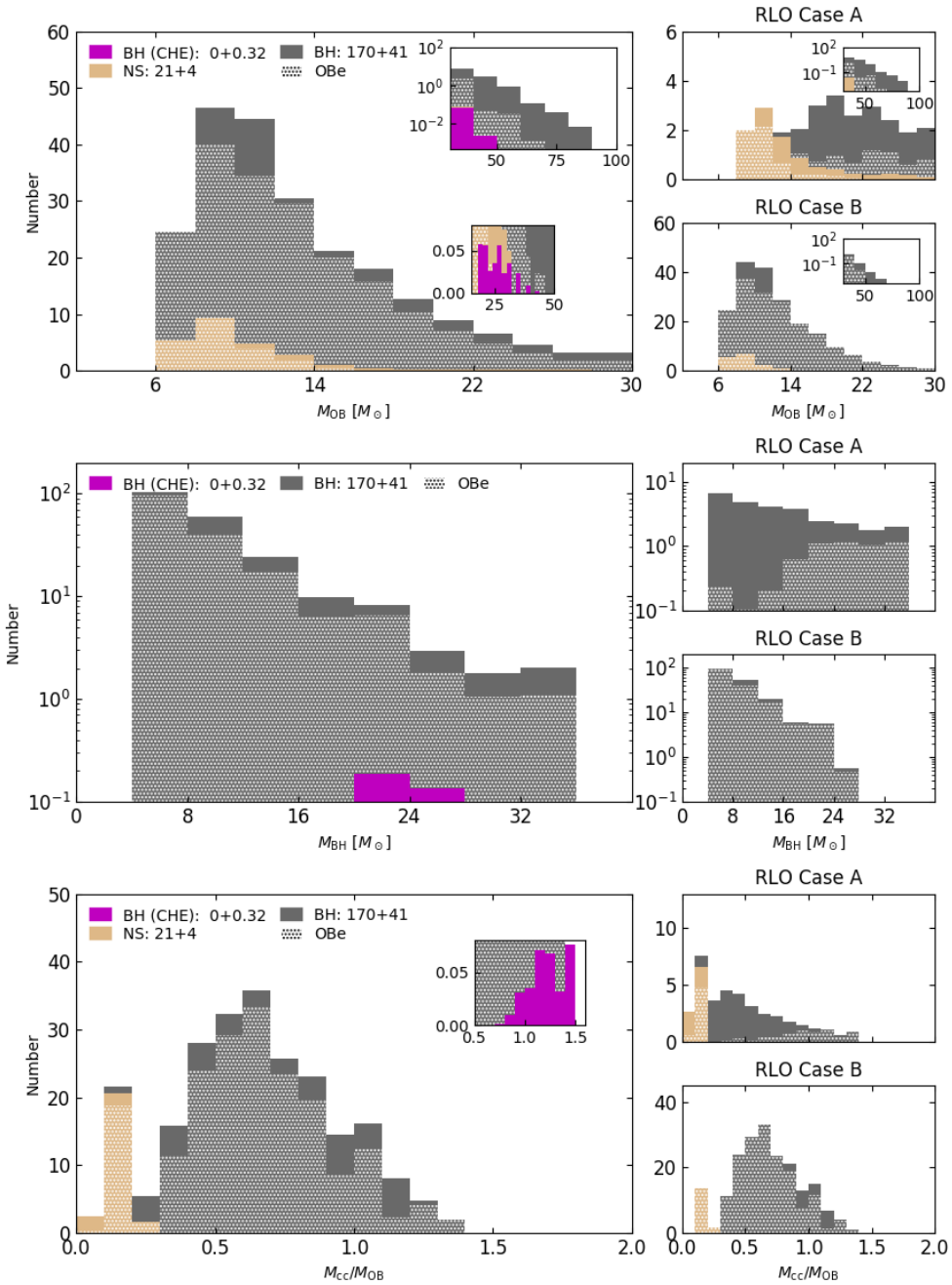

Figure A.5: Top panel: Distributions of OB star masses $M_{\rm OB}$ in OB+cc binaries. The types of compact objected are coded in color (BH: black, NS: brown), and the shaded area is related to the OBe feature. The OB+BH binaries formed from CHE are plotted with purple. The number is the legends is the predicted number of OBe stars and normal OB stars, e.g., "Black hole: 170+41" means 170 BH+OBe binaries and 41 BH+OB binaries. The in-layer plot in the top panel shows the distribution in the range 30 - 100 $M_\odot$ with bin width of 10 $M_\odot$, while the main plot is produced in 2 - 30 $M_\odot$ with bin width of 2 $M_\odot$. The left panel is the distribution of the total population, which is detangled into Case A systems and Case B systems in the right upper and lower panel respectively. Middle panel: Distributions of black hole masses. Bottom panel: Distributions of mass ratios of OB+cc binaries.

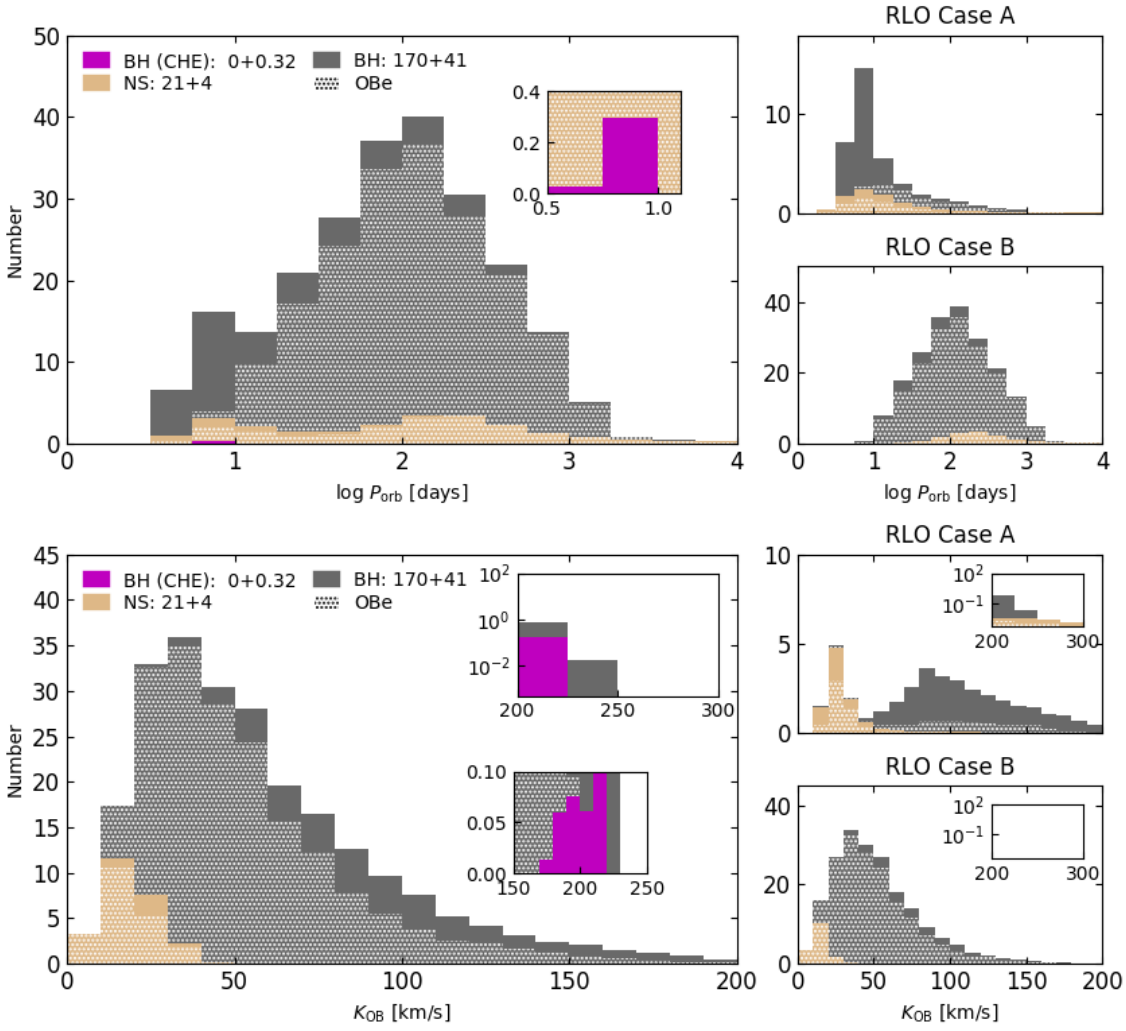

Figure A.6: Top panel: Distribution of logarithmic orbital periods log P_{orb} of OB+cc binaries. The colors and legends have the same meaning as Fig. A.5. Lower panel: Semi-amplitude of orbital velocity of OB stars K_{OB}.

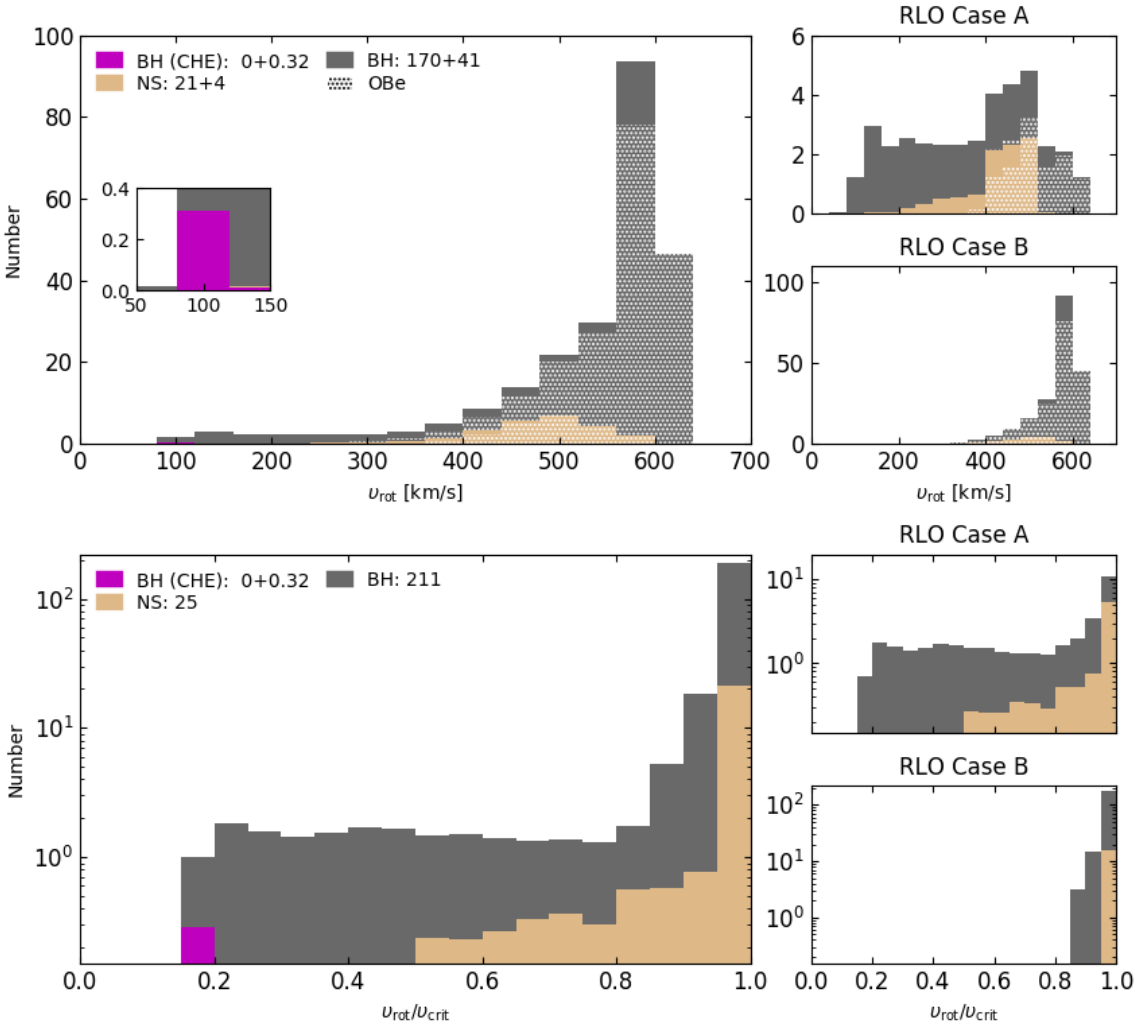

Figure A.7: Distribution of rotation velocities of OB stars $v_{\rm rot}$ (top) and ratios of rotation velocity to critical velocity $v_{\rm rot}/v_{\rm crit}$ of OB stars (bottom). The colors and legends have the same meaning as Fig. A.5

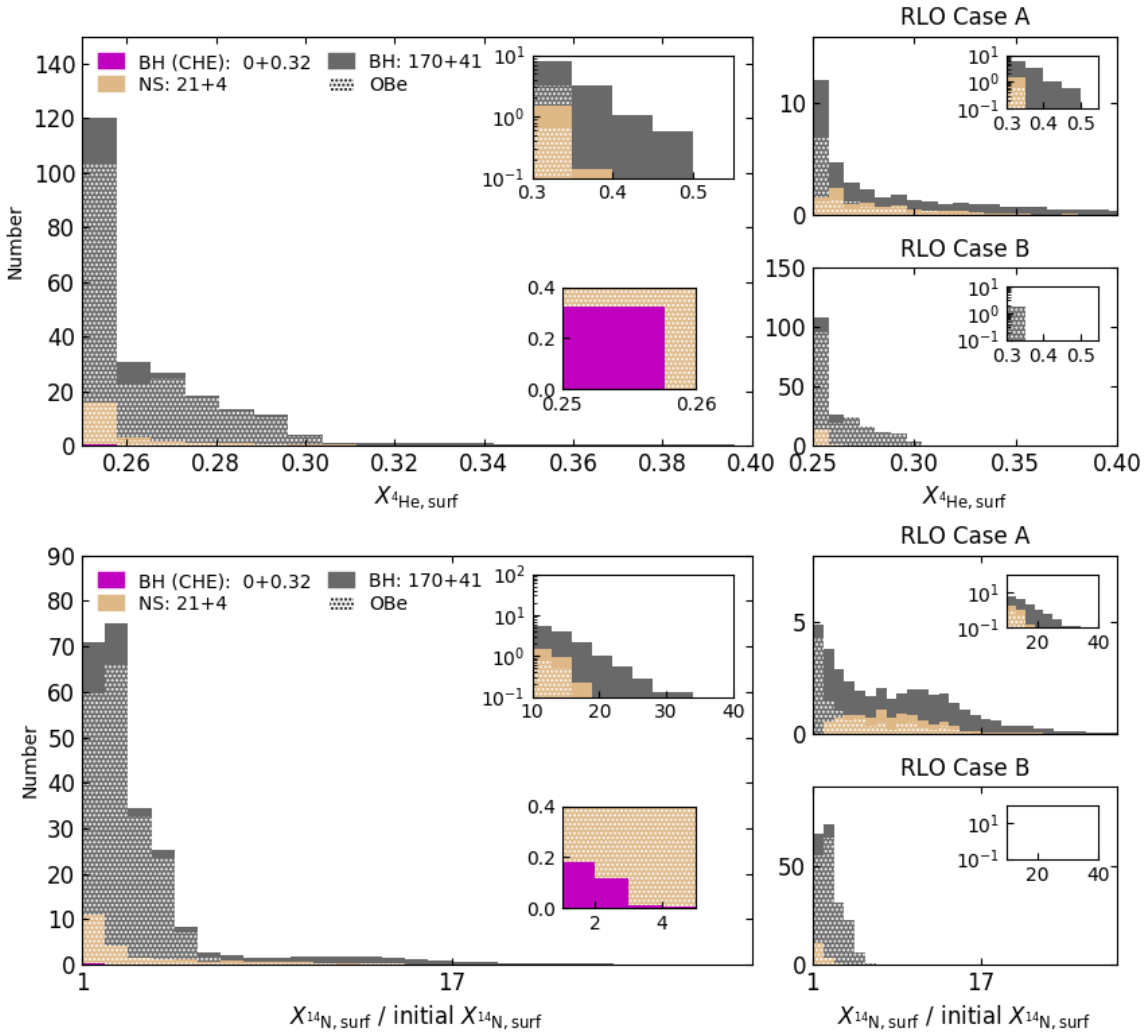

Figure A.8: The distributions of surface abundance of ^{4}He $X_{^4\mathrm{He,surf}}$ (top panel) and the enhancement factor of ^{14}N $X_{^{14}\mathrm{N,surf}}$/ initial $X_{^{14}\mathrm{N,surf}}$ (bottom panel) of OB stars. The colors and legends have the same meaning as Fig. A.5.

APPENDIX B

Appendix to Chapter 3

Eddington limit and mass transfer rate

In this appendix, we provide a comparison between the Eddington limit and the mass transfer rate under thermal timescale. We adopt the same formula for the Eddington luminosity $LEdd$ as in Sen,

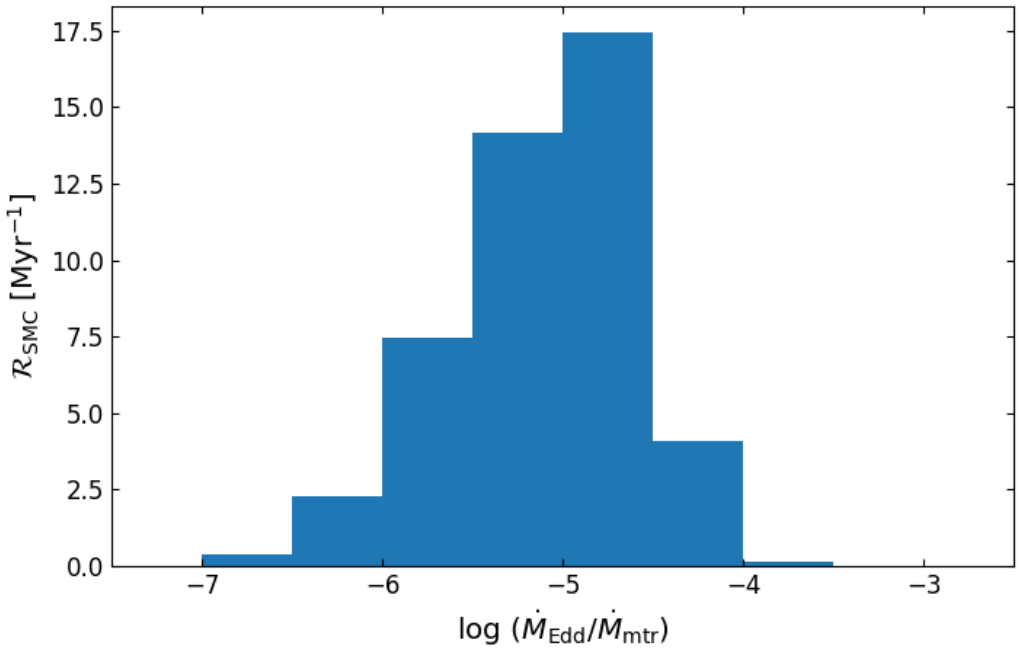

Figure B.1: Predicted distribution of the ratio of the Eddington accretion rate $\dot{M}_{\rm Edd}$ to the mass transfer rate $\dot{M}_{\rm mtr}$ estimated by Eq. (B.3). The Y-axis shows the birth rate in unit of Myr^{-1}.

X.-T. Xu et al. (2021), which is

$$L_{\rm Edd} = L_{\odot} \frac{65335}{1+X} \frac{M_{\rm BH}}{M_{\odot}}, \tag{B.1}$$

where X is the hydrogen abundance in the transferred material, and $M_{\rm BH}$ is the mass of BH. The corresponding mass accretion rate $\dot{M}_{\rm Edd}$ is estimated by (Frank, King and Raine, 2002b; El Mellah, 2017)

$$\dot{M}_{\rm Edd} = \frac{L_{\rm Edd}\, R_{\rm ISCO}}{G\, M_{\rm BH}}, \tag{B.2}$$

where $R_{\rm ISCO}$ is the radius of the innermost stable circular orbit around BH. The mass transfer rate $\dot{M}_{\rm mtr}$ under thermal timescale is estimated by (Eq. (60) in Hurley, Tout and Pols, 2002)

$$\dot{M}_{\rm mtr} = \frac{M_{\rm env}}{\tau_{\rm th}}, \tag{B.3}$$

where $M_{\rm env}$ is the mass of the H-rich envelope of the donor star and $\tau_{\rm th}$ is the thermal timescale, which is

$$\tau_{\rm th} = \frac{G M_{\rm d}^2}{2 R_{\rm d} L_{\rm d}}, \tag{B.4}$$

where $M_{\rm d}$, $R_{\rm d}$, and $L_{\rm d}$ are the the mass, radius, and luminosity of donor star. Figure B.1 presents that the distribution of $\dot{M}_{\rm Edd}/\dot{M}_{\rm mtr}$, which are always below 10^{-4}. This means that most of transferred material is expelled if assuming that a BH can only accrete at a rate below the Eddington limit.

Parameter Study

A parameter study is presented regarding the parameterised criterion for the stability of mass transfer ($q_{\rm min}$ and $P_{\rm orb,max}$), the fraction of mass lost from the BH accretor ($\beta_{\rm RLO}$), the efficiency of expelling envelope material during the common envelope evolution ($\eta_{\rm CE}$), and BH kick ($\upsilon_{\rm Kick,max}$). Here BH kicks are computed in the same way as in Paper I, and we adopt the same kick distribution as in Kruckow et al. (2018) that BH kicks are flatly distributed in $[0, \upsilon_{\rm Kick,max}]$. We assume that the eccentricity induced by kick is rapidly circularised just before the secondary star filling its Roche lobe (Kruckow et al., 2018) since the circularisation timescale is highly sensitive with the Roche lobe filling factor (Hurley, Tout and Pols, 2002). The circularised orbit is computed by assuming orbital angular momentum conservation during the circularisation process. The effect of eccentricity on the merger timescale of BBHs is included by the fitting formula in Mandel (2021).

Different from our fiducial models, early Case A mass transfer onto BH can take place if including BH kicks. In that case, stripped stars are given by fitting formulas based on our detailed models with zero accretion efficiency, which are

$$\begin{aligned} \log\left(M_{\rm He,core}/\,M_{\odot}\right) = &\left(a_1 + a_2 \log M_{1,\rm i} + a_3 q_{\rm i} + a_4 X_{\rm H,donor,RLO}\right) \\ &\times \left(1 + a_5 \log M_{1,\rm i} + a_6 q_{\rm i} + a_7 X_{\rm H,donor,RLO}\right) \end{aligned} \tag{B.5}$$

and

$$\begin{aligned} R_{\rm He,core}/R_{\odot} = &\left(b_1 + b_2 \log M_{1,\rm i} + b_3 q_{\rm i} + b_4 X_{\rm H,donor,RLO}\right) \\ &\times \left(1 + b_5 \log M_{1,\rm i} + b_6 q_{\rm i} + b_7 X_{\rm H,donor,RLO}\right), \end{aligned} \tag{B.6}$$

Table B.1: Predicted SMC WR+BH population by different input parameters.

	WR+BH		$f_{\rm WR+BH}$	$P_{\rm orb,peak}$ [day]		$V_{\rm orb,WR,peak}$ [km s^{-1}]	
	StableMT	CEE		StableMT	CEE	StableMT	CEE
fiducial model	2.46	0.15	28.1%	$42.17^{+14.06}_{-10.55}$	$0.07^{+0.03}_{-0.014}$	50^{+10}_{-10}	910^{+10}_{-10}
$q_{\rm min} = 0$	3.24	=	33.6%	=	=	=	=
$q_{\rm min} = 0.6$	0.96	=	14.2%	$237.14^{+79.09}_{-59.31}$	=	=	=
$P_{\rm orb,max} = 500$ days	2.26	=	26.5%	=	=	70^{+10}_{-10}	=
$P_{\rm orb,max} = 1500$ days	2.55	0.13	28.6%	=	=	=	=
$\beta_{\rm RLO} = 0.5$	=	=	=	=	=	70^{+10}_{-10}	=
$\eta_{\rm CE} = 0.1$	=	0.00	26.9%	=	merger	=	merger
$\eta_{\rm CE} = 0.5$	=	0.03	27.1%	=	=	=	1190^{+10}_{-10}
$\upsilon_{\rm K,max} = 200\,{\rm km\,s^{-1}}$	1.89	0.05	22.5%	=	=	90^{+10}_{-10}	930^{+30}_{-30}
$\upsilon_{\rm K,max} = 100\,{\rm km\,s^{-1}}$	2.34	0.10	26.7%	=	=	70^{+10}_{-10}	930^{+30}_{-30}

Notes. (1) The fiducial model is computed with $(q_{\rm min}, P_{\rm orb,max}, \beta_{\rm RLO}, \eta_{\rm CE}, \upsilon_{\rm Kick,max}) = (0.3,\ 1000\,{\rm days},\ 1,\ 1,\ 0\,{\rm km\,s^{-1}})$. (2) "=" means the same value as the fiducial model. (3) StableMT and CEE are related to the StableMT and CEE channels respectively. (4) $f_{\rm WR+BH}$ is the fraction of WR+BH, where the number of WR+O binaries is taken to be 6.7 (Paper I). (5) $P_{\rm orb,peak}$ and $V_{\rm orb,WR,peak}$ are the typical values of the orbital periods and the orbital velocities of WR stars, which are the center values of the bins with the highest predicted number, and the corresponding errors are given by the bin widths.

where $M_{\rm He,core}$ is the mass of stripped star in solar mass, $R_{\rm He,core}$ is the radius of stripped star in solar radius, $M_{1,\rm i}$ is the mass of donor star, $q_{\rm i}$ is the mass ratio before interaction, and $X_{\rm H,donor,RLO}$ is the core H abundance of the donor star at its Roche Lobe filling. The fitting parameters have values of -1.05735056, 1.35768157, 0.58722921, -1.02679054, 0.07968712, -0.41678739, 0.6213659 for a_1 to a_7, and -0.11959835, 0.1525386, 0.10325001, -0.1314212, 3.01077205, -2.49124461, 2.13141913 for b_1 to b_7.

Our fiducial model is defined by $q_{\rm min} = 0.3$, $P_{\rm orb,max} = 1000\,{\rm days}$, $\beta_{\rm RLO} = 1$, $\eta_{\rm CE} = 1$, and $\upsilon_{\rm Kick,max} = 0$. Here we consider $0.0 \ldots 0.6$ for $q_{\rm min}$, $500 \ldots 1500$ days for $P_{\rm orb,max}$, 0.5 for $\beta_{\rm RLO}$, $0.1 \ldots 0.5$ for $\eta_{\rm CE}$, and $(100, 200)\,{\rm km\,s^{-1}}$ for $\upsilon_{\rm Kick,max}$. In App. B we present the SMC WR+BH populations predicted by different parameters, and App. B for the cosmic merger rate density of BBHs. In App. B we fine-tune $q_{\rm min}$ and $P_{\rm orb,max}$ to match the merger rate density inferred from GWTC-3.

Wolf-Rayet + black hole binary

The predicted WR+BH populations from different input parameters are summarized in Tab. B.1. Expect the $q_{\rm min} = 0.6$ case, we always found 2-3 WR+BH binaries in the SMC with similar typical orbital periods and orbital velocities as the fiducial model[1].

For higher $q_{\rm min}$, more binaries below 1000 days undergo unstable mass transfer, which all end

[1] The typical values of the orbital periods and the orbital velocities are the center values of the bins with the highest predicted numbers in the corresponding distributions.

up with merger. For Roche-lobe overflow, orbit shrinks less if the pre-interaction binary have less extreme mass ratio. Hence in the $q_{\rm min} = 0.6$ case the typical orbital period is shifted to over 200 days. The $P_{\rm orb,max}$ determines the orbital period boundary between the StableMT and CEE channels. Taking $P_{\rm orb,max} = 500$ days does not change the number of CEE survivors since binaries with period between 500. . . 1000 days merge. This decreasing in the orbital period boundary also leads to a slight increasing in orbital velocities. Due to the similar reason, the number of CEE survivors decreases by 0.02 with $P_{\rm orb,max} = 1500$ days.

With $\beta_{\rm RLO} = 0.5$, less orbital angular momentum is lost through isotropic wind, and BHs are more massive than that in the fiducial model. Consequently, we obtain a larger typical orbital velocity for WR stars $70\,{\rm km\,s^{-1}}$, while $50\,{\rm km\,s^{-1}}$ in the fiducial model.

The variation of $\eta_{\rm CE}$ can largely change the number of the CEE survivors but have ignorable effects on the total number of our WR+BH binaries. Higher $\eta_{\rm CE}$ requires massive BHs to avoid merger. Consequently, we obtain a typical velocity of $1190\,{\rm km\,s^{-1}}$ with $\eta_{\rm CE} = 0.5$, while $910\,{\rm km\,s^{-1}}$ with $\eta_{\rm CE} = 1$. Taking $\eta_{\rm CE} = 0.1$, there is no CEE survivor anymore.

Black hole kicks have larger impact on the CEE channel than that on the StableMT channel since the all CEE survivors are wide binaries, which are easily disrupted. The BH kick survivors are usually close binaries, and hence the typical orbital velocities with kicks are generally higher than the zero kick case, $90\,{\rm km\,s^{-1}}$ for $\upsilon_{\rm Kick,max} = 200\,{\rm km\,s^{-1}}$ and $70\,{\rm km\,s^{-1}}$ for $\upsilon_{\rm Kick,max} = 100\,{\rm km\,s^{-1}}$. In addition, even with $\upsilon_{\rm Kick,max} = 200\,{\rm km\,s^{-1}}$ we still expected 2 WR+BH binaries in the SMC.

Binary black holes

Figure B.2 presents the cosmic merger rate density of merging BBHs $\mathcal{R}_{\rm cosmic}$ predicted by different input parameters. With $q_{\rm min} = 0.6$, the cosmic merger rate density does not change a lot since the StableMT channel becomes important only near the current universe. The StableMT channel dominates all redshifts with $q_{\rm min} = 0.0$ due to the large orbital shrinkage caused by extreme mass ratios. In consistent with Tab. B.1, changing $P_{\rm orb,max}$ from 500 days to 1500 days does not have significant effect on the predicted rates.

In the $\beta_{\rm RLO} = 0.5$ case, orbits shrink less since less material is ejected out of the systems comparing with $\beta_{\rm RLO} = 1$ (fiducial model). This results in longer delay time for the StableMT channel and causes a lower rate near $z = 0$. For the efficiency of expelling envelope $\eta_{\rm CE}$, the merger rate density at high redshifts can be reduced by several orders of magnitude by reducing $\eta_{\rm CE}$ from 1 to 0.3. Taking $\eta_{\rm CE} = 0.1$ there is no CEE survivor anymore.

We study the effects of BH kick in the panel (d) of Fig. B.2. The BH progenitors are more massive than the NS progenitors, and BH kicks are expected to be much weaker than NS kicks (Belczynski, Kalogera et al., 2008; Janka, 2017; Kruckow et al., 2018). Therefore, including BH kicks does not change the order of magnitude of our predicted rates. Particularly, in the $\upsilon_{\rm Kick,max} = 100\,{\rm km\,s^{-1}}$ case, the main effect of BH kick is to widen the orbits of BBHs instead of disruption. Consequently, merging BBHs at low redshift is enhanced.

Reproducing the merger rate inferred from GWTC-3

As already shown in Fig. 3.8 and Fig. B.2, the merger rate density expected by our fiducial model is much higher than that inferred rate from the GWTC-3 (R. Abbott et al., 2023), where both the StableMT and CEE channels expect a higher rate than GWTC-3. In this appendix we assume that

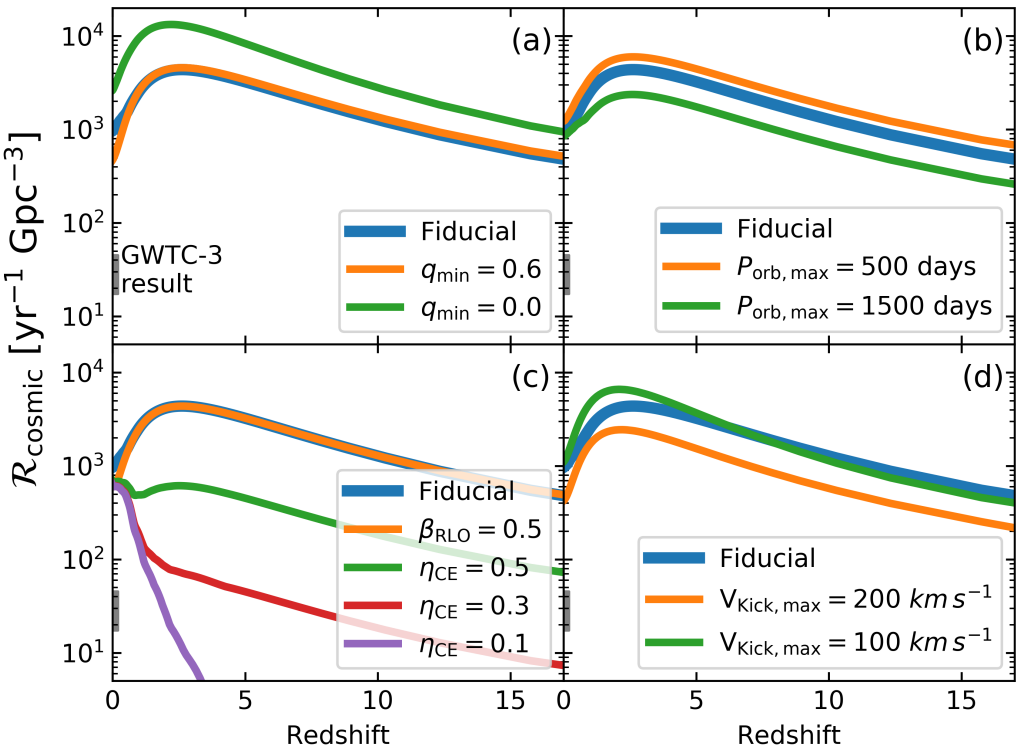

Figure B.2: Cosmic merger rate density predicted by our models using different input parameters. The fiducial case is computed with ($q_{\rm min}$, $P_{\rm orb,max}$, $\beta_{\rm RLO}$, $\eta_{\rm CE}$, $v_{\rm Kick,max}$) = (0.3, 1000 days, 1, 1, 0km s^{-1}). See text for the definitions of these parameters. Different parameters are coded in color, e.g. "$q_{\rm min} = 0.6$" means that the curve is computed with $q_{\rm min} = 0.6$ while other parameters are kept at their fiducial values. The Y-axis shows the merger rate density in unit of yr^{-1} Gpc^{-3}. The grey region means that the Y-axis shows the merger rate density inferred from GWTC-3 (R. Abbott et al., 2023).

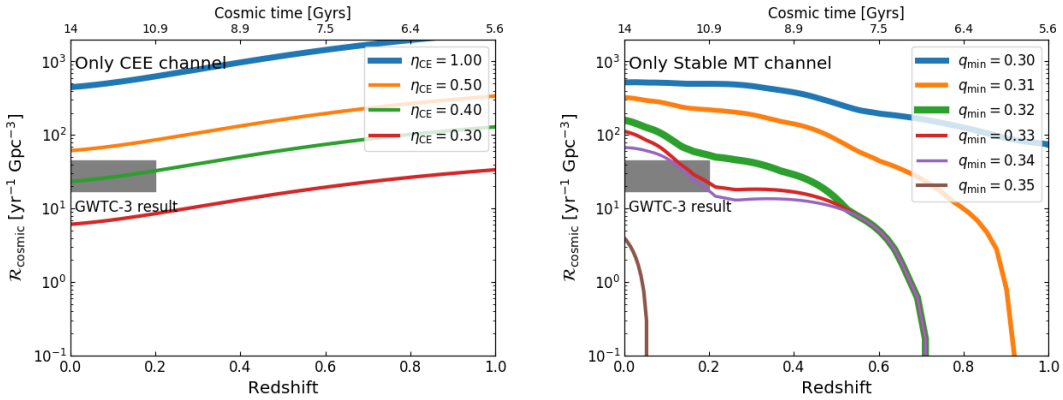

Figure B.3: Same as Fig. B.2 but for the merger rate densities predicted by the CEE (left panel) and Stable MT (right panel) channels. In left panel we vary $\eta_{\rm CE}$ from 0.3 to 1 and in the right panel we vary $q_{\rm min}$ from 0.30 to 0.35, where $\eta_{\rm CE} = 1$ and $q_{\rm min} = 0.3$ are the fiducial values.

the merging BBH population is either dominated by the StableMT channel or the CEE channel, and we fine-tune the minimum mass ratio for stable mass transfer $q_{\rm min}$ and the efficiency of expelling envelope during common envelope evolution $\eta_{\rm CE}$ to fit the merger rate inferred from GWTC-3.

Figure B.3 presents our fitting results. The CEE channel can reproduce the GWTC-3 value with $\eta_{\rm CE} = 0.4$, and the StableMT channel with $q_{\rm min} = 0.33$ or $q_{\rm min} = 0.34$. The cosmic rates expected by these two channels behavior differently near zero redshift (StableMT: $\mathcal{R}_{\rm cosmic}$ decreases with redshift, CEE: $\mathcal{R}_{\rm cosmic}$ increases with redshift). This feature may suggest the observed population is dominated by the CEE channel (see Fig. 13 in R. Abbott et al., 2023).

To better understand the merger rate near zero redshift predicted by the StableMT channel, we present the mass ratios of the OB+BH phase ($q_{\rm OB+BH} = M_{\rm BH}/M_{\rm OB}$) of the merging BBHs at $z = 0$ in Fig B.4. Here $q_{\rm OB+BH}$ can be directly compared with $q_{\rm min}$ that the binaries undergo CEE if $q_{\rm OB+BH} < q_{\rm min}$. Most of these merging BBHs are born within redshift of 2, whose corresponds to a delay time around 10 Gyrs and have $q_{\rm OB+BH}$ below 0.32. The model density rapidly decreases with increasing mass ratio, which leads to the behavior presented in Figs. B.3 and 3.8.

Wind-fed X-ray binaries

To determine whether WR+BH binaries can become wind-fed X-ray binaries, we adopt the criterion for accretion disc formation derived by Sen, X.-T. Xu et al. (2021) that an accretion disc is expected around the BH if $R_{\rm disk}/R_{\rm ISCO} > 1$, where $R_{\rm disk}$ is the circularisation radius of captured material, $R_{\rm ISCO}$ is the radius of the innermost stable orbit around BH, and $R_{\rm disk}/R_{\rm ISCO}$ is given by (Eq. (10) in Sen, X.-T. Xu et al., 2021)

$$\frac{R_{\rm disk}}{R_{\rm ISCO}} = \frac{2}{3}\frac{\eta_{\rm j}}{(1+M_{\rm WR}/M_{\rm BH})^2}\left(\frac{v_{\rm orb}}{c}\right)^{-2}\left(1+\frac{v_{\rm wind}^2}{v_{\rm orb}^2}\right)^{-4}\gamma_{\pm}, \tag{B.7}$$

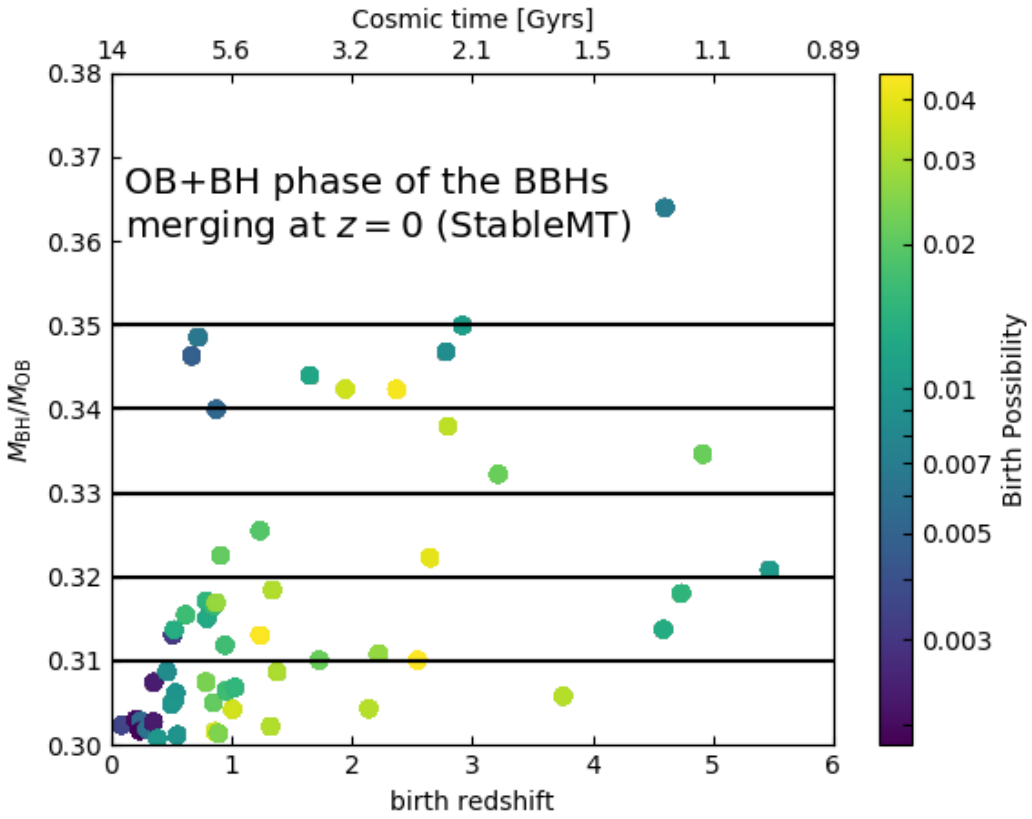

Figure B.4: The mass ratio $M_{\rm BH}/M_{\rm OB}$ during the OB+BH phase of the models producing BBHs merging at zero redshift through the StableMT channel as the function of their birth redshift. The X-axis is the birth redshift of these binaries and the corresponding cosmic time is indicated on the top. The horizontal lines mark mass ratios of 0.31, 0.32, 0.33, 0.34, and 0.35. The birth possibility of each model is coded in color, which is weighted by the initial mass function, the distributions of initial mass ratios and orbital periods, the star formation rate density at the birth redshift (Eq. (3.15)).

where $\eta_{\rm j}$ is the efficiency of angular momentum accretion, $M_{\rm WR}$ is the mass of WR star, $M_{\rm BH}$ is the mass of BH, c is the speed of light, $\upsilon_{\rm orb}$ is the relative orbital velocity of BH assuming circular orbit,

$$\upsilon_{\rm orb} = \sqrt{\frac{G(M_{\rm WR} + M_{\rm BH})}{a}}, \tag{B.8}$$

where G is the gravitational constant, a is the semi-major axis, $\upsilon_{\rm wind}$ is the velocity of WR star wind at the location of BH, given by (Gräfener et al., 2017)

$$\upsilon_{\rm wind} = 1.3\upsilon_{\rm esc}\left(1 - \frac{R_{\rm WR}}{a}\right), \tag{B.9}$$

$\upsilon_{\rm esc}$ is the escape velocity of WR star, $R_{\rm WR}$ is the radius of WR star, and $\gamma_{\pm}$ quantifies the effects of BH spin. While fast-rotating BHs have more chance to become strong X-ray emitters (Sen, X.-T. Xu et al., 2021), for simplicity we ignore the effects of BH spin ($\gamma_{\pm} = 1$) and take $\eta_{\rm j} = 1/3$.

APPENDIX C

Appendix to Chapter 4

A&A 652, A138 (2021)
https://doi.org/10.1051/0004-6361/202141214

Astronomy & Astrophysics

X-ray emission from BH+O star binaries expected to descend from the observed galactic WR+O binaries

K. Sen[1,2,⋆], X.-T. Xu[1,2,⋆], N. Langer[1,2], I. El Mellah[3], C. Schürmann[1,2], and M. Quast[1]

[1] Argelander-Institut fur Astronomie, Universitat Bonn, Auf dem Hugel 71, 53121 Bonn, Germany
e-mail: ksen@astro.uni-bonn.de
[2] Max-Planck-Institut fur Radioastronomie, Auf dem Hugel 69, 53121 Bonn, Germany
[3] Univ. Grenoble Alpes, CNRS, IPAG, 414 Rue de la Piscine, 38400 Saint-Martin-d'Hères, France

Received 30 April 2021 / Accepted 31 May 2021

ABSTRACT

Context. In the Milky Way, ∼18 Wolf-Rayet+O star (WR+O) binaries are known with estimates of their stellar and orbital parameters. Whereas black hole+O star (BH+O) binaries are thought to evolve from WR+O binaries, only one such system is known in the Milky Way. To resolve this disparity, it was suggested recently that upon core collapse, the WR stars receive large kicks such that most of the binaries are disrupted.
Aims. We reassess this issue, with a particular emphasis on the uncertainty in predicting the X-ray emission from wind-accreting BHs in BH+O binaries, which is key to identifying such systems.
Methods. BH+O systems are thought to be X-ray bright only when an accretion disk forms around the BHs. We followed the methodology of previous work and applied an improved analytic criterion for the formation of an accretion disk around wind accreting BHs. We then used stellar evolutionary models to predict the properties of the BH+O binaries which are expected to descend from the observed WR+O binaries if the WR stars would form BHs without a natal kick.
Results. We find that disk formation sensitively depends on the O stars' wind velocity, the amount of specific angular momentum carried by the wind, the efficiency of angular momentum accretion by the BH, and the spin of the BH. We show that whereas the assumption of a low wind velocity may lead to the prediction that most of the BH+O star binaries will have an extended X-ray bright period, this is not the case when typical wind velocities of O stars are considered. We find that a high spin of the BH can boost the duration of the X-ray active phase as well as the X-ray brightness during this phase. This produces a strong bias for detecting high mass BH binaries in X-rays with high BH spin parameters.
Conclusions. We find that large BH formation kicks are not required to understand the sparsity of X-ray bright BH+O stars in the Milky Way. Probing for a population of X-ray silent BH+O systems with alternative methods can likely inform us about BH kicks and the necessary conditions for high energy emission from high mass BH binaries.

Key words. stars: massive – stars: evolution – stars: black holes – X-rays: binaries – binaries: close

1. Introduction

The detection of gravitational waves by LIGO/VIRGO in the last decade has opened a new window to look at our Universe. Since the first observation by LIGO in 2015 (Abbott et al. 2016, 2019), most of these, now routine, events are associated with merging stellar mass black holes (BHs, Abbott et al. 2019). Thereby, the interest in the study of BHs has been revitalised (de Mink & Mandel 2016; Marchant et al. 2016; Belczynski et al. 2020; Woosley et al. 2020; du Buisson et al. 2020). But the evolution of massive star binaries towards binary compact object mergers is still riddled with uncertainties (Langer 2012; Crowther 2019).

Apart from gravitational wave signals from compact object mergers and direct imaging of the supermassive BH shadows (Akiyama 2019), BHs can be detected via microlensing (Minniti et al. 2015; Masuda & Hotokezaka 2019; Wyrzykowski & Mandel 2020), tidal disruption events (Perets et al. 2016; Kremer et al. 2019), and X-ray emission due to accretion on the BH. In the latter case, the source of material can be a dense interstellar medium (Fujita et al. 1998; Tsuna et al. 2018; Scarcella et al. 2021), or an orbiting stellar companion (Orosz et al. 2011).

A large number of binary population synthesis studies have been undertaken to predict the event rate of merging compact objects (Mennekens & Vanbeveren 2014; Belczynski et al. 2014; Stevenson et al. 2015; de Mink & Belczynski 2015; Kruckow et al. 2018). One of the major uncertainties in population synthesis studies (for a discussion, see O'Shaughnessy et al. 2008) is whether the formation of a BH is preceded by a supernova (SN) explosion and if so, whether the BH receives a natal kick high enough to disrupt the binary in which the BH formed (Mandel & Müller 2020; Mandel et al. 2021; Woosley et al. 2020). As expected, the presence or absence of a substantial kick during BH formation significantly affects the BH-BH merger rates calculated by population synthesis calculations (Mennekens & Vanbeveren 2014; Belczynski et al. 2016).

Direct evidence towards high or low BH kicks is inconclusive (Özel et al. 2010; Farr et al. 2011; Belczynski et al. 2012). On the one hand, in Galactic low mass X-ray binaries containing a BH, BHs were found to have formed with low or modest kick velocities (Brandt et al. 1995; Willems et al. 2005; Fragos et al. 2009; Wong et al. 2012). Belczynski et al. (2016) (table 7, and references therein) have given empirical evidence for low BH natal kicks. On the other hand, Repetto et al. (2012,

⋆ The first two authors have contributed equally to this work.

2017) found that their binary models can adequately explain the observed population of low mass BH binaries above the Galactic plane when high BH kick velocities, similar to the ones assumed for the formation of neutron stars (Hobbs et al. 2005), are adopted during BH formation. Moreover, some works have suggested a BH mass-dependent natal kick distribution (Mirabel & Rodrigues 2003; Dhawan et al. 2007), with more massive BHs receiving lower kicks.

Several teams have studied whether very massive stars can explode at the end of their lifetime (O'Connor & Ott 2011; Ugliano et al. 2012). Sukhbold et al. (2018) and Woosley (2019) predict that most of the hydrogen-free helium stars having masses between 7–30 $M_{\odot}$, which also manifest as Wolf-Rayet (WR) stars during helium burning, do not explode with an associated supernova but instead implode into BHs. Mirabel & Rodrigues (2003) provided evidence that WR stars might become BHs with little or no kick.

Langer et al. (2020) predict to find that approximately three out of every 100 massive binary stars host a BH. The average lifetime of the WR+O phase (~0.4 Myrs, given by the lifetime of the WR phase) is much smaller than the lifetime of the BH+O phase (which is given by the remaining main sequence lifetime of the O star). Hence, if the transition from the WR+O stage to the BH+O stage happens without the binary being disrupted, we expect the Milky Way to host more binaries containing BHs than WR stars. However, the observed number of WR+O star binaries are much larger than BH+O star binaries.

Vanbeveren et al. (2020) (hereafter V20) assessed this problem with the following two assumptions: (i) WR stars collapse to form BHs with no natal kick and (ii) a BH+O binary is detectable if the BH has an accretion disk and the X-ray flux emitted from the accretion disk is above the detection threshold of current X-ray telescopes. They predict to find over 200 wind-fed BH high mass X-ray binaries (HMXBs) in the Milky Way. There is only one observed in the Milky Way (Cygnus X-1, see e.g., Hirsch et al. 2019).

The large discrepancy between the predicted and observed number of wind-fed BH HMXBs led V20 to conclude that most of the WR stars must explode in a supernova to form neutron stars with an associated large natal kick that disrupts the binaries, or BH formation itself is associated with a high kick velocity that disrupts most of the progenitor WR+O binaries at the time of BH formation. This conclusion would greatly affect the merger rates of BH-BH and BH-NS mergers as many population synthesis results assume low kick velocities for BH formation.

In this work, we follow Shapiro & Lightman (1976) to formulate a condition for the formation of accretion disks and detectability of a BH+O system as a wind-fed BH HMXB. We investigate the effect of the stellar wind velocity, efficiency of angular momentum accretion from the stellar wind, and the spin of the BH on our prediction of the number of wind-fed BH HMXBs. We also revisit the assumptions and definitions of stellar parameters used to derive the accretion disk formation criterion in the work of V20.

In Sect. 2, we outline the definitions and assumptions used to derive our accretion disk formation criterion. We then predict the population of BH+O binaries and study the effect of uncertain parameters on our predictions in Sect. 3. We compare the assumptions and results in our work with the literature in Sect. 4. In Sect. 5, we critically discuss the implications of the uncertainties that are present in the calculation of the X-ray active lifetime of BH+O binaries and outline our main conclusions from this work in Sect. 6.

Table 1. Stellar parameters of the anticipated BH+O binaries obtained by V20 at BH formation, in order of increasing orbital period.

Progenitor system	Distance (kpc)	O star mass ($M_{\odot}$)	BH mass ($M_{\odot}$)	Orbital period (days)	$L/L_{\rm Edd}$ of O star
WR 155	2.99	30	12	2.6	0.161
WR 151	5.38	28	10	3.4	0.076
WR 139	1.31	28	6	5.0	0.101
WR 31	6.11	24	7	6.1	0.140
WR 42	2.44	27	14	8.7	0.156
WR 47	3.49	47	20	10.5	0.317
WR 79	1.37	24	7	10.7	0.076
WR 127	3.09	20	6	11.8	0.076
WR 21	3.99	37	10	11.8	0.341
WR 9	4.57	32	8	15.0	0.299
WR 97	2.15	30	9	18.3	0.304
WR 30	5.09	34	14	20.4	0.303
WR 113	1.80	22	8	35.9	0.054
WR 141	1.92	26	18	43.1	0.076
WR 35a	5.84	19	10	68.2	0.054
WR 11	0.34	31	8	86.8	0.107
WR 133	1.85	34	9	158.0	0.107

Notes. The BH is assumed to have formed at the end of core helium depletion of the WR star in the progenitor WR+O binaries.

2. Method

2.1. Sample selection

In the Milky Way, there are about ~53 observed WR+O type binaries[1] (van der Hucht 2001, 2006; Crowther et al. 2015; Rosslowe & Crowther 2015). Of them, 38 are designated as double-lined spectroscopic binaries (SB2). V20 consider a subpopulation of 17 SB2 binaries that have estimates of the masses of both components and orbital period of the binary. The present masses of both components and the orbital period of the selected sample of 17 binaries can be found in table 1 of V20. We find one more SB2 system, WR 22, that has estimates of its component masses and orbital period (Schweickhardt et al. 1999). This system has an orbital period around ~80 days. In this work, we further look at the distance of the systems from Earth using the catalogue of galactic WR stars (Rosslowe & Crowther 2015) (Table 1). To be consistent with the analysis of V20, we chose to analyse the sub-sample of the 17 WR+O binaries. We also explain later that the addition of WR 22 to the sample of 17 SB2 binaries reinforces the conclusions we derive from our work.

The orbital period distribution of WR+O binaries in the Large Magellanic Cloud (LMC) is expected to peak at ~100 days (Langer et al. 2020), which can be expected to be similar in the Milky Way. Observationally, short-period WR+O star binaries are much easier to detect than long-period ones. This implies that the sub-sample of ~17 mostly short-period WR+O binaries considered in this work may indeed account for nearly all short-period WR+O binaries expected for the ~53 WR+O binaries observed in the Milky Way. We see below that only short-period WR+O binaries can manifest as X-ray bright BH+O systems. In this sense, the sub-sample of 17 WR+O binaries can be used as a suitable proxy to analyse the detectability of anticipated BH+O binaries in the Milky Way.

[1] http://pacrowther.staff.shef.ac.uk/WRcat/index.php

2.2. Binary evolution

We describe the further modelling of the chosen WR+O binaries in the following sub-sections.

2.2.1. WR+O binary evolution up to BH formation

We adopt the stellar and orbital parameters of the anticipated BH+O binaries derived by V20 at the time of BH formation (Table 1). We describe the modelling of the evolution of the WR+O star binaries performed by V20 up to the point of BH formation briefly in the following paragraph.

The orbital periods of the considered WR+O star binaries suggest that most of them did in fact undergo mass transfer in the past, which stripped the hydrogen-rich envelope of the donor stars and the O star companions may have been rejuvenated due to accretion (Braun & Langer 1995). The expected masses of the WR stars at core helium depletion were calculated using the evolutionary tracks of hydrogen deficient, post-Roche Lobe overflow, core helium burning star models of Vanbeveren et al. (1998b). For a WR star of the nitrogen sequence (i.e., WN star), the WR star was assumed to be at the beginning of the helium burning. On the other hand, if a WR star was of the carbon sequence (WC star), the calculation was started from the point during core helium burning at which helium burning products appear at the stellar surface due to wind mass loss. This assumption neither affects the main results of V20 nor this study (see appendix of V20 for a discussion). Following this evolution, the expected mass of the WR star at the end of core helium burning was calculated. The orbital periods of the WR+O binaries at the end of core helium burning of the WR stars were estimated using the close binary evolutionary models of Vanbeveren et al. (1998a).

At the end of core helium depletion, we assumed that the WR stars will directly collapse into BHs of the same mass without any natal kick. This means that we did not account for the binary disruption which might be induced by high natal kicks. We also neglected the changes in orbital separation and eccentricity provoked by natal kicks. We thus expect the number of wind-fed BH HMXBs predicted from our analysis to be an upper limit on the actual number. Below, we test this assumption a posteriori by comparing our predicted number of wind-fed BH HMXBs with observations. We note that a small natal kick may not lead to the binary being disrupted, but introduce an eccentricity in the orbit that may result in the production of X-ray at periastron passage. In such a case, the X-ray emission is expected to be periodic and active only for a small fraction of the orbital period. Therefore, we do not expect a small natal kick to significantly alter our results.

2.2.2. The BH+O phase

After the formation of the BH, orbital evolution is driven by the mass loss from the O star companion, which reduces the mass of the O star and carries away orbital angular momentum (Quast et al. 2019; El Mellah et al. 2020a). Whether the orbit shrinks or expands depends on the mass ratio and the fraction of wind material escaping from the system (see Fig. 10 in El Mellah et al. 2020a). In our case, the ratio of O star masses to BH masses are below 5, and more than ∼99% of wind material escapes from the binary (see Fig. A.1). This implies that we can assume that the orbital parameters remain unchanged during the BH+O phase. Considering the fact that most of these systems might have undergone a mass transfer episode in the past, we also assumed that the orbit is circular.

We followed the subsequent evolution of the O star companions in the BH+O binaries by interpolating in the massive single star models of Ekström et al. (2012). Due to past mass transfer from the WR progenitors to the O star companions, the O stars can be found to be younger than the age of the binaries, by the process of rejuvenation (Braun & Langer 1995). This is the so-called rejuvenated ages of the O stars. The rejuvenated ages of the O stars were obtained by V20 from their observed mass, spectral type, and luminosity class. Here, we estimated the rejuvenated ages of the O stars at the time of BH formation by reproducing the results of V20 with their assumptions. For the systems that are not expected to become detectable BH+O binaries by V20, the rejuvenated ages of the O stars at the time of BH formation were set to be zero. This did not affect our results as we also found no X-ray emission from those systems during the BH+O phase. We assume that the BH+O phase lasts until the O stars leave the main sequence or fill their Roche lobes, whichever is earlier. On the other hand, V20 assumed that the BH+O phase lasts until the O stars fill its Roche lobes.

2.3. Wind-captured disks during the BH+O phase

Due to the gravitational field of the BH, a fraction of the stellar wind from the O star can be captured by the BH (Illarionov & Sunyaev 1975). As a result, a wind-captured disk may form around the BH (Shapiro & Lightman 1976; Iben & Tutukov 1996). Due to turbulent viscosity produced by instabilities such as the magneto-rotational instability (Balbus & Hawley 1991), accreting material moves inwards in an optically thick and geometrically thin accretion disk in which gravitational energy is efficiently converted into thermal energy, producing X-ray emission (Shakura & Sunyaev 1973).

2.3.1. Wind velocity

The O star wind velocity ($\upsilon_{\rm wind}$) at the location of the BH can be approximated as

$$\upsilon_{\rm wind} = \upsilon_{\infty}\left(1 - \frac{R_{\rm O}}{a}\right)^{\beta}, \tag{1}$$

where a is the orbital separation, υ_{∞} is the terminal velocity of stellar wind, and $R_{\rm O}$ is the radius of the O star. For O stars (effective temperature higher than 30 kK), the value of β is 0.8–1 (Groenewegen & Lamers 1989; Puls et al. 1996) and the terminal velocity is given by (Vink et al. 2001)

$$\upsilon_{\infty} \simeq 2.6\,\upsilon_{\rm esc}, \tag{2}$$

where $\upsilon_{\rm esc}$ is the modified escape velocity of the O star

$$\upsilon_{\rm esc} = \sqrt{\frac{2GM_{\rm O}}{R_{\rm O}}(1-\Gamma)}, \tag{3}$$

where Γ is the Eddington factor and $M_{\rm O}$ is the mass of the O star companion.

2.3.2. Disk formation

A necessary condition for the formation of a wind-captured disk around a BH is

$$\frac{R_{\rm disk}}{R_{\rm ISCO}} > 1, \tag{4}$$

where $R_{\rm ISCO}$ is the radius of the innermost stable orbit and $R_{\rm disk}$ is the circularisation radius of a Keplerian accretion disk, which is defined by

$$R_{\rm disk} = \frac{j^2}{GM_{\rm BH}}, \tag{5}$$

where j is the specific angular momentum of the captured wind material, G is the gravitational constant, and $M_{\rm BH}$ is the mass of the BH. The radius of the innermost circular orbit around a BH is evaluated by

$$R_{\rm ISCO} = \frac{6GM_{\rm BH}}{c^2}\gamma_{\pm}, \tag{6}$$

where c is the speed of light and $\gamma_{\pm}$ represents the modification caused by the BH spin with respect to the disk on the location of the innermost stable circular orbit. It ranges from 1/6 for a maximally rotating BH surrounded by a prograde disk to 3/2 for a maximally rotating BH surrounded by a retrograde disk, assuming the disk and BH angular momenta are aligned (El Mellah 2017). For a non-rotating BH, $\gamma_{\pm} = 1$. Qin et al. (2018) found that the spin of the first formed BH in a binary is usually very low. For a considerable change in the spin, the BH needs to accrete an amount of mass of the order of its own mass (Wong et al. 2012). Regardless of the birth spin of the BH, we assume that the spin of the BH does not change during the BH+O phase as only a small fraction of the BH mass is accreted during this phase.

The specific angular momentum (j) accreted by the BH from the O star wind can be written as (Shapiro & Lightman 1976, eq. 7)

$$j = \frac{1}{2}\eta\Omega_{\rm orb}R_{\rm acc}^2, \tag{7}$$

where $\Omega_{\rm orb}$ is the orbital angular velocity, η is a numerical factor which quantifies the efficiency of specific angular momentum accretion by the BH from the available wind matter, and $R_{\rm acc}$ is the accretion radius which is the typical distance to the BH at which the wind trajectory and/or speed is significantly altered by the gravitational field of the BH. It can be written as (Davidson & Ostriker 1973)

$$R_{\rm acc} = \frac{2GM_{\rm BH}}{\upsilon_{\rm rel}^2}, \tag{8}$$

where $\upsilon_{\rm rel} = \sqrt{\upsilon_{\rm wind}^2 + \upsilon_{\rm orb}^2}$ is the relative velocity of the stellar wind with respect to the BH for a circular orbit, $\upsilon_{\rm wind}$ is the wind velocity of the O star companion, and $\upsilon_{\rm orb}$ is the relative velocity of the BH with respect to the O star, that is, $\upsilon_{\rm orb} = \Omega_{\rm orb}a$.

Equation (7) was obtained under the assumption that the wind velocity is considerably larger than the orbital velocity, which is consistent with our further analysis (see Fig. B.1). If all wind material entering the accretion radius can be accreted by the BH, $\eta = 1$ (Shapiro & Lightman 1976). Detailed hydrodynamical simulations suggest that this efficiency factor can be lower, ∼1/3 (Livio et al. 1986; Ruffert 1999). In what follows, we consider these two values.

In defining the mass ratio $q = M_{\rm O}/M_{\rm BH}$ and combining Eqs. (5)–(8), the disk formation criterion can be converted into the dimensionless form

$$\frac{2}{3}\frac{\eta^2}{(1+q)^2} > \left(\frac{\upsilon_{\rm orb}}{c}\right)^2\left(1+\frac{\upsilon_{\rm wind}^2}{\upsilon_{\rm orb}^2}\right)^4\gamma_{\pm}, \tag{9}$$

or equivalently

$$\frac{R_{\rm disk}}{R_{\rm ISCO}} = \frac{2}{3}\frac{\eta^2}{(1+q)^2}\left(\frac{\upsilon_{\rm orb}}{c}\right)^{-2}\left(1+\frac{\upsilon_{\rm wind}^2}{\upsilon_{\rm orb}^2}\right)^{-4}\gamma_{\pm}^{-1} > 1. \tag{10}$$

Equations (9) and (10) suggest that a wind-captured disk can form around a BH if the captured material carries enough angular momentum, if the wind speed is low compared to the orbital speed, and if the orbital speed is high.

2.4. X-ray luminosity

We can distinguish the following three cases for the morphology of the accretion flow: sub-Eddington accretion via a disk, super-Eddington accretion via a disk, and spherical accretion. The first two happen only if enough angular momentum is carried by the accretion flow (see Sect. 2.3). Super-Eddington accretion occurs when the mass accretion rate is so high that the X-ray luminosity it produces exceeds the Eddington luminosity of the BH. Although super-Eddington accretion onto neutron stars has been observed in ultra-luminous X-ray sources (Bachetti et al. 2014; Fürst et al. 2016; Israel et al. 2017; Chandra et al. 2020), the typical mass accretion rate calculated in our study is much smaller than the Eddington accretion rate for the individual systems (Fig. A.1). Accretion disks with a sub-Eddington mass accretion rate are thought to be geometrically thin and optically thick, centrifugally-maintained structures (Shakura & Sunyaev 1973; Novikov & Thorne 1973). Notwithstanding minor relativistic corrections, such a disk around a BH mostly radiates in X-rays, and the maximum associated luminosity is (Frank et al. 2002; El Mellah 2017):

$$L_{\rm X} = \frac{1}{2}\frac{GM_{\rm BH}\dot{M}_{\rm acc}}{R_{\rm ISCO}}, \tag{11}$$

where $\dot{M}_{\rm acc}$ is the mass accretion rate.

In order to evaluate the mass accretion rate, we rely on the wind accretion formula introduced by Davidson & Ostriker (1973) (see also the review by Edgar 2004). It is valid in binary systems provided the wind speed at the binary orbital separation is larger than the orbital speed (El Mellah & Casse 2017). In this case, the fraction of the accreted wind can be approximated by

$$\frac{\dot{M}_{\rm acc}}{\dot{M}_{\rm wind}} = \frac{1}{4}\left(\frac{R_{\rm acc}}{a}\right)^2\frac{\upsilon_{\rm rel}}{\upsilon_{\rm wind}}, \tag{12}$$

where $\dot{M}_{\rm wind}$ is the O star wind mass loss rate.

Finally, in the case of spherical accretion, the mass accretion rate is not an independent variable. Instead, it is set by the location of the sonic point as described in the 1D spherical Bondi model (Bondi 1952). Without an accretion disk, thermal bremsstrahlung dominates the radiation from the optically thin wind material, which makes spherical accretion radiatively inefficient (Shapiro & Teukolsky 1983). We do not expect this regime to produce any X-ray emission above detectable levels.

2.5. Detectability of a BH+O system

The X-ray active lifetime ($\tau_{\rm Lx}$) of each BH+O binary model considered is defined as the amount of time during the BH+O phase when the system is detectable as a wind-fed BH HMXB. We assume that this is only the case when an accretion disk forms, that is, Eq. (10) is satisfied, and when the calculated X-ray luminosity (Eq. (11)) and the distance to the source yield a flux

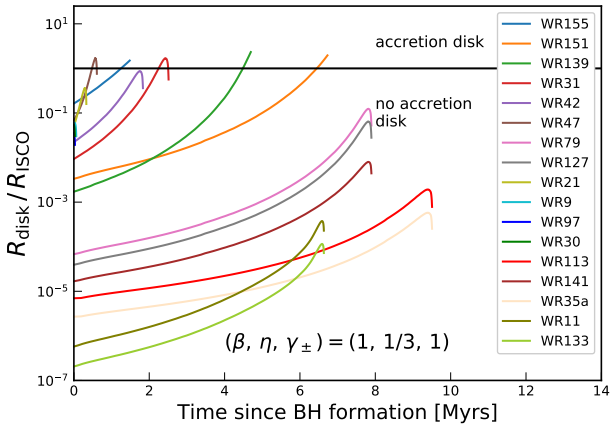

Fig. 1. Evolution of the ratio of the circularisation radius $R_{\rm disk}$ to the radius of the innermost stable circular orbit $R_{\rm ISCO}$ during the BH+O phase as a function of the time since the formation of the BH for $(\beta, \eta, \gamma_\pm) = (1, 1/3, 1)$. The black horizontal line shows the dividing line above which an accretion disk is expected. The colour coding in the legend identifies the 17 progenitor WR+O star systems that are expected to give rise to the BH+O binaries.

above a detection threshold that we set to $\sim 10^{-11}$ erg s^{-1} cm^{-2}. Our adopted threshold is similar to the flux detection limit of non-focussing X-ray telescopes with typical integration times (Wood et al. 1984; Bradt et al. 1991; In't Zand et al. 1994). We discuss the relevance of the X-ray flux threshold in the light of the sensitivity of current all-sky monitoring X-ray instruments in Sect. 5.

3. Results

3.1. Fiducial parameter set

Figure 1 shows the evolution of the ratio of the circularisation radius ($R_{\rm disk}$) to the radius of the innermost stable circular orbit ($R_{\rm ISCO}$) during the BH+O phase for the 17 progenitor WR+O star binaries. For our fiducial case, we adopted the value of $\beta = 1$ (Vink et al. 2001), $\eta = 1/3$ (El Mellah 2017), and $\gamma_\pm = 1$ (Qin et al. 2018). The O star expands during core hydrogen burning, leading to a decrease in its wind velocity, which makes the formation of a wind-captured disk easier during the late stages of its main sequence evolution. In most systems, there is a small decrease in the ratio of the circularisation radius to the innermost stable circular orbit towards the end of the BH+O star phase, which is related to the shrinkage of massive stars when they approach their core hydrogen depletion. WR139, WR151, and WR155 do not present this feature since their BH+O phases are terminated due to the Roche Lobe filling condition before their O stars complete core hydrogen burning. While the mass ratio of WR 139 suggests this system will merge at this time, the other two could undergo an SS433-like evolution leading to short-period WR+BH binaries (van den Heuvel et al. 2017), which lies outside the scope of our paper.

We find that no accretion disk forms in 12 of our BH+O models. Among them, three systems are not visible in this plot since the estimated rejuvenated age of their O stars are very close to the O stars' main sequence lifetime, such that the duration of their BH+O phase is very small. Importantly, we find that only in five BH+O models, all with orbital periods $\leq$10 days, can an accretion disk form for a small fraction of the total BH+O phase. For systems with higher orbital periods, an accretion disk does not form at all for the entire BH+O phase. Noting that the orbital

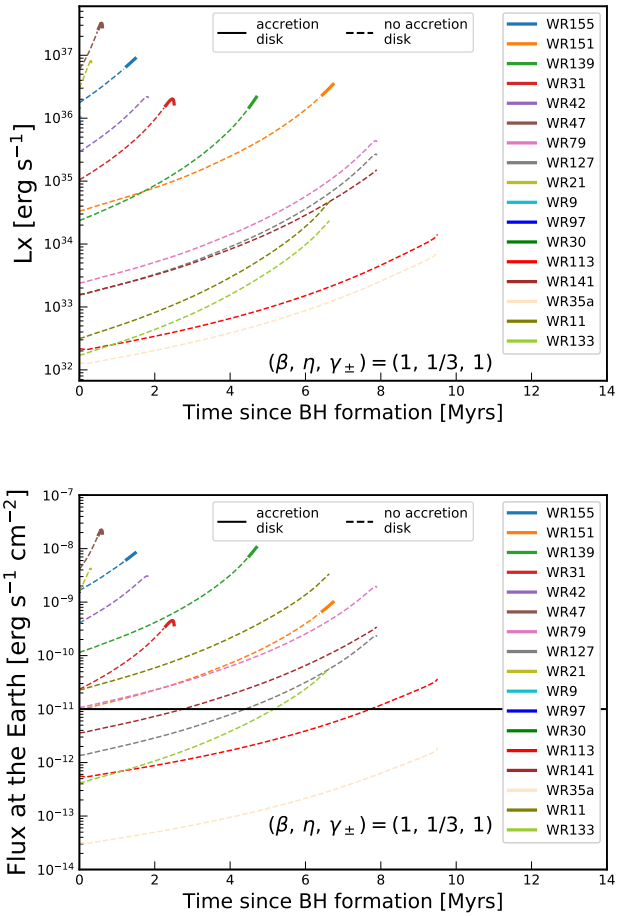

Fig. 2. Evolution of X-ray luminosity (*upper panel*) calculated using Eq. (11) and the corresponding X-ray flux at Earth (*lower panel*) for our BH+O models when an accretion disk can form according to our criterion (solid line). The dashed lines indicate the X-ray luminosity and flux evolution if an accretion disk could form for the entire BH+O phase. The black horizontal line shows our adopted flux detection limit.

period of WR 22 is ~80 days, we do not expect that the BH+O binary anticipated to form from WR 22 will be X-ray bright at any time.

Figure 2 shows the X-ray luminosity (top panel) and its corresponding flux at Earth (bottom panel), calculated using Eq. (11) for our BH+O models. We find that when an accretion disk can form, the predicted X-ray flux at Earth is well above the flux detection limit we have assumed. In other words, the X-ray luminosity from the accretion disk is not a bottleneck for our BH+O models to be detectable in X-rays. We note that Eq. (11) only holds when an accretion disk is present such that the dashed lines are only indicative of the X-ray luminosity and flux if an accretion disk could form for the entire BH+O phase. The X-ray luminosity from a BH+O system without an accretion disk is expected to be orders of magnitude lower than what is predicted by Eq. (11) (see discussion in Sect. 2.4).

For each system where an accretion disk can form, we calculated the duration for which it will be detectable as a wind-fed BH HMXB (i.e., the X-ray active lifetime). To predict the number of wind-fed BH HMXB systems that we expect based on the 17 progenitor WR+O star systems, we assume (as in V20) that the observed numbers of WR+O binaries and wind-fed BH HMXBs are proportional to the lifetime in the respective phases. One WR+O binary is thus representative of $\tau_{\rm Lx}/\tau_{\rm WR}$ wind-fed

Table 2. Predicted X-ray active lifetime ($\tau_{\rm Lx}$, in millions of years) of each of the 17 BH+O binary models and expected number of wind-fed BH HMXBs ($N_{\rm XRBs}$, last line), for various combinations of β, η, and $\gamma_{\pm}$.

	$(\beta,\eta)^{(a)}$= (1, 1)			(β,η) = (0.8, 1)			(β,η) = (1, 1/3)			(β,η) = (0.8, 1/3)		
$\gamma_{\pm}$	1/6	1	3/2	1/6	1	3/2	1/6	1	3/2	1/6	1	3/2
WR155	1.5	1.5	1.4	1.5	1.2	0.9	1.4	**0.2**	0.0	0.9	0.0	0.0
WR151	3.6	1.6	1.3	2.9	1.1	0.8	1.3	**0.3**	0.1	0.8	0.0	0.0
WR139	2.0	1.0	0.8	1.6	0.6	0.5	0.8	**0.2**	0.1	0.5	0.0	0.0
WR31	1.9	1.0	0.8	1.6	0.7	0.6	0.8	**0.2**	0.1	0.6	0.0	0.0
WR42	1.8	0.8	0.7	1.7	0.6	0.5	0.7	**0.0**	0.0	0.5	0.0	0.0
WR47	0.6	0.4	0.4	0.6	0.4	0.3	0.4	**0.1**	0.0	0.3	0.0	0.0
WR79	0.8	0.1	0.0	0.6	0.0	0.0	0.0	**0.0**	0.0	0.0	0.0	0.0
WR127	0.6	0.0	0.0	0.4	0.0	0.0	0.0	**0.0**	0.0	0.0	0.0	0.0
WR21	0.3	0.2	0.1	0.3	0.1	0.1	0.1	**0.0**	0.0	0.1	0.0	0.0
WR9	0.1	0.0	0.0	0.1	0.0	0.0	0.0	**0.0**	0.0	0.0	0.0	0.0
WR97	0.0	0.0	0.0	0.0	0.0	0.0	0.0	**0.0**	0.0	0.0	0.0	0.0
WR30	0.0	0.0	0.0	0.0	0.0	0.0	0.0	**0.0**	0.0	0.0	0.0	0.0
WR113	0.0	0.0	0.0	0.0	0.0	0.0	0.0	**0.0**	0.0	0.0	0.0	0.0
WR141	0.0	0.0	0.0	0.0	0.0	0.0	0.0	**0.0**	0.0	0.0	0.0	0.0
WR35a	0.0	0.0	0.0	0.0	0.0	0.0	0.0	**0.0**	0.0	0.0	0.0	0.0
WR11	0.0	0.0	0.0	0.0	0.0	0.0	0.0	**0.0**	0.0	0.0	0.0	0.0
WR133	0.0	0.0	0.0	0.0	0.0	0.0	0.0	**0.0**	0.0	0.0	0.0	0.0
$N_{\rm XRBs}{}^{(b)}$	33.0	16.6	13.4	28.3	11.8	9.0	13.4	2.5	0.7	9.0	0.0	0.0

Notes. The bold highlighted column represents our fiducial case. $^{(a)}$See Eqs. (1) and (7) for the definition of β and η, respectively. $^{(b)}N_{\rm XRBs}$ is the predicted number of wind-fed BH high mass X-ray binaries by considering 0.4 Myr to be the typical lifetime of WR stars. See Sect. 3 for more details.

BH HMXBs, where $\tau_{\rm WR}$ is the duration of the WR+O binary phase. Considering $\tau_{\rm WR}$ = 0.4 Myrs to be the typical lifetime of a WR star (V20), we expect ∼2.5 wind-fed BH HMXBs from the 17 WR+O binaries. Accounting for the observational and theoretical bias in the population of WR+O binaries (see discussion in Sect. 2.1), it is likely that the number of wind-fed BH HMXBs in the entire Milky Way would be ∼2–3.

3.2. Effects of parameter variations

The predicted number of wind-fed BH HMXBs is sensitive to the uncertainties in the parameters we have assumed. We explore the results computed using reasonable variations to our fiducial parameter set in Table 2. For a non-rotating BH ($\gamma_{\pm}$ = 1), by varying (β,η) from (0.8, 1/6) to (1, 1/2), the predicted number of wind-fed BH HMXBs out of 17 WR+O binaries varies from 0 to 16.6. Considering a maximally spinning BH with a prograde accretion disk, the predicted number can be boosted up to 33, suggesting an observational bias in favour of wind-fed BH HMXBs containing maximally rotating BHs surrounded by a prograde disk. In the following sub-sections, we discuss the effects of these parameters individually.

3.2.1. Efficiency of specific angular momentum accretion

From Eq. (10), the ratio of the circularisation radius to the radius of the innermost stable orbit varies with the square of the efficiency of specific angular momentum accretion

$$\frac{R_{\rm disk}}{R_{\rm ISCO}} \propto \eta^2. \tag{13}$$

The predicted X-ray luminosity when an accretion disk can form does not depend on the efficiency parameter. So, the likelihood of the formation of an accretion disk in our BH+O models increases with the increase in the efficiency of angular momentum accretion by the BH. In Fig. 3, we show the variation of the two above-mentioned quantities with the efficiency of specific angular momentum accretion for the BH+O model corresponding to WR 31. We find that the amount of time an accretion disk can form during the BH+O phase is significantly longer when the efficiency of angular momentum accretion increases by a factor of 3. On the other hand, the X-ray luminosity predicted from Eq. (11) is unaffected. From Table 2, we find that the number of predicted wind-fed BH HMXBs increases by 6.5 times when the η increases from 1/3 to 1, and the other two parameters are at their fiducial value.

3.2.2. BH spin

Our definition of the radius of the innermost stable circular orbit around a BH (Eq. (6)) accounts for the effect of the spin of the BH on the formation of an accretion disk (via $\gamma_{\pm}$). The spin parameter of BHs in observed wind-fed HMXBs can be quite high, as in Cyg X-1 (Gou et al. 2011; Zhao et al. 2021; Miller-Jones et al. 2021). To account for the spin of the BH, we calculated the predicted number of wind-fed BH HMXB derived from the 17 progenitor WR+O binaries for the following three cases (see Table 2): i) when the BHs are maximally rotating with a prograde accretion disk, ii) when the BHs are maximally rotating with a retrograde accretion disk, and iii) for a non-spinning BH.

Both the ratio of the circularisation radius to the radius of the innermost stable orbit, and the X-ray luminosity from an accretion disk vary inversely with our BH spin parameter

$$\frac{R_{\rm disk}}{R_{\rm ISCO}} \propto \gamma_{\pm}^{-1} \tag{14}$$

and

$$L_{\rm X} \propto \gamma_{\pm}^{-1}. \tag{15}$$

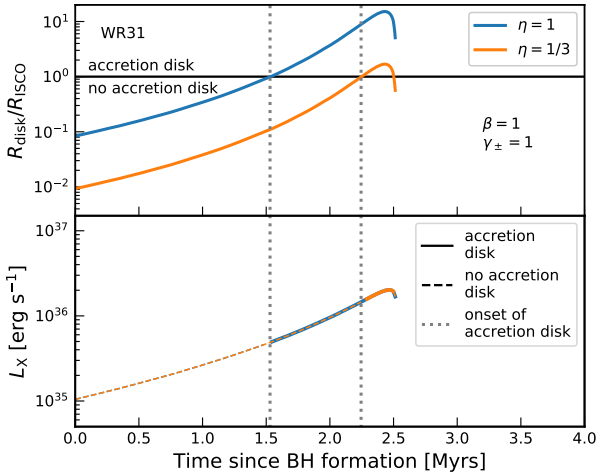

Fig. 3. Effects of η parameter on the ratio of the circularisation radius to the radius of the innermost stable circular orbit (*upper panel*) and the X-ray luminosity (*lower panel*). We take the BH+O binary derived from WR31 as an example. The η parameter is considered to be 1 and 1/3 (colour coded), and $(\beta, \gamma_\pm) = (1, 1)$. The line styles in the *lower panel* have the same meaning as in Fig. 2.

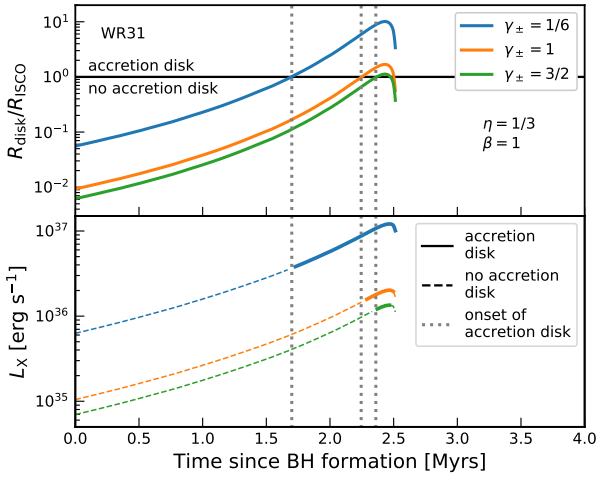

Fig. 4. Effects of the $\gamma_\pm$ parameter. The same as Fig. 3, but $\gamma_\pm$ is considered to be 1/6, 1, and 3/2 (colour coded), and $(\beta, \eta) = (1, 1/3)$. The line styles in the *lower panel* have the same meaning as in Fig. 2.

Figure 4 shows the effect of the BH spin on the formation of an accretion disk and the emitted X-ray luminosity during the BH+O phase of WR 31. For a BH maximally rotating with a prograde accretion disk, both the amount of time for which an accretion disk can form and the X-ray luminosity predicted from the accretion disk increase significantly. In Table 2, we find that the predicted number of wind-fed HMXBs increases by a factor of ∼5 for the case of a maximally rotating BH with a prograde disk, and it decreases by a factor of ∼3.5 for a maximally rotating BH with a retrograde disk, compared to a non-rotating BH, with the other two parameters being at their fiducial values.

The fact that we predict a short X-ray active lifetime for non-spinning BHs in BH+O systems, while the only observed wind-fed BH HMXB in the Milky Way is known to have high spin parameter, hints to the possibility that only BHs that were born with a very high spin are likely to be detectable as an X-ray source if they are associated with an O star in a close binary configuration. Qin et al. (2019) show that high spin BHs can be produced only if the efficiency of angular momentum transport in stellar models is reduced. As such, BHs with high birth spins might be rare, as is the case for observed wind-fed BH HMXBs.

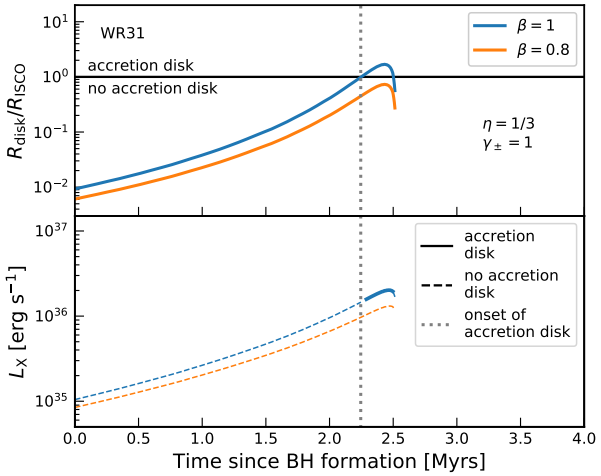

Fig. 5. Effects of the β parameter. The same as Fig. 3, but the β parameter is considered to be 0.8 and 1 (colour coded), and $(\eta, \gamma_\pm) = (1/3, 1)$. The line styles in the *lower panel* have the same meaning as in Fig. 2.

3.2.3. O star wind velocity law

The exponent β in the wind velocity law for O stars is constrained from observations to be 0.8–1 (Groenewegen & Lamers 1989; Lamers et al. 1995; Puls et al. 1996). Since wind velocity is always larger than orbital velocity in our work, Eqs. (10) and (11) suggest the following dependencies:

$$\frac{R_{\rm disk}}{R_{\rm ISCO}} \propto v_{\rm wind}^{-8} \propto \left(1 - \frac{R_{\rm O}}{a}\right)^{-8\beta}, \tag{16}$$

and

$$L_X \propto v_{\rm rel}^{-3} \propto \left(1 - \frac{R_{\rm O}}{a}\right)^{-3\beta}. \tag{17}$$

In our analysis, the ratio between the O star radius (obtained from the stellar tracks of Ekström et al. 2012) and orbital separation is generally below 0.4. Therefore, changing β from 1 to 0.8 can maximally reduce the ratio of the circularisation radius to the radius of the innermost stable circular orbit by a factor of ∼2, making the formation of the accretion disk more difficult. Likewise, the predicted X-ray luminosity from Eq. (11) is also decreased.

We present the effects of the β parameter on the formation of an accretion disk and the X-ray luminosity emitted from the disk in Fig. 5, where we use the BH+O model derived from WR 31 as an example. We find that even the change in the assumed β value from 1 to 0.8 makes the BH+O model of WR 31 become X-ray inactive due to the inability to form an accretion disk. The predicted X-ray luminosity and thereby the X-ray flux from an accretion disk, if it were to form, is also decreased, but not as significantly as to fall beyond our flux detection limit.

From Table 2, we see that when we change the value of the β from 1 to 0.8, while the other parameters remain at their fiducial values, our BH+O binary models do not have any X-ray bright phase. The predicted number of wind-fed BH HMXBs decreases from ∼2.5 to zero. This shows that the X-Ray active lifetime of the BH+O binaries analysed in our work is very sensitive to the assumed wind velocity of the O star companion.

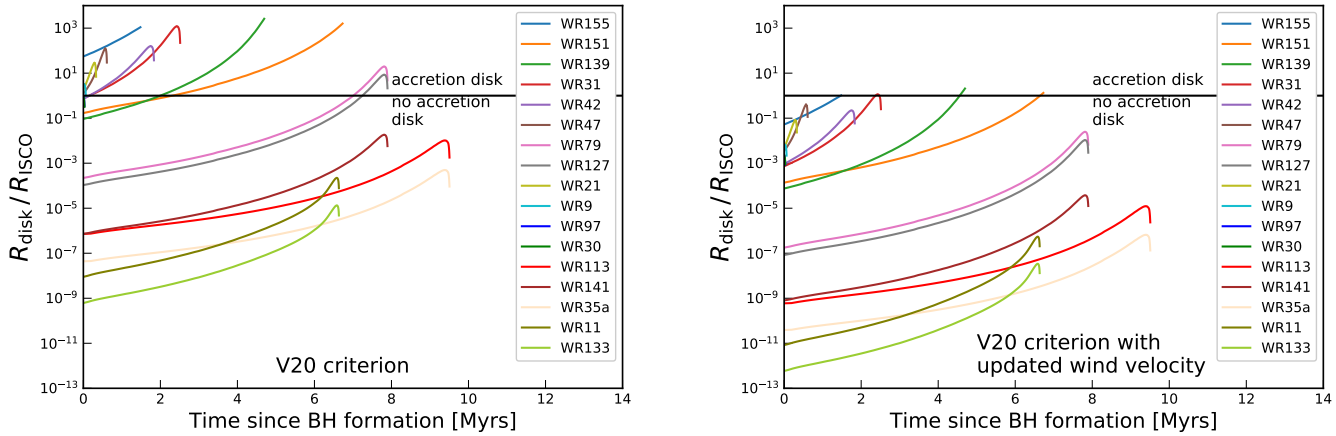

Fig. 6. Evolution of the ratio of the circularisation radius of the accreted wind matter from the O star to the radius of the innermost stable circular orbit of the BH for the 17 BH+O star binary models as a function of the time since the formation of the BH. *Left panel*: evolution as calculated by V20, which does not account for the orbital velocity of the companion and the typical wind velocity of O stars. *Right panel*: same evolution when we use the typical O star wind velocity (Eq. (1)), the mass of the BH, and the orbital velocity of the O star companion. The black horizontal line in both panels show the dividing line above which an accretion disk can form. The colour coding in the legend identifies the 17 progenitor WR+O star systems that are expected to give rise to the BH+O binaries.

4. Comparison with earlier work

Starting from the same 17 WR+O binaries, V20 performed a similar analysis and predicted to find over 200 wind-fed BH HMXBs in the Milky Way. Here, we compare the analysis of V20 with our work and discuss the factors that led to the difference in the predicted numbers.

V20 adopted the accretion disk formation criterion derived by Iben & Tutukov (1996). Iben & Tutukov (1996) primarily modelled accretion onto degenerate white dwarfs from red giant donors and their central idea remained the same in the sense that they assumed that an accretion disk forms when the specific angular momentum of the accreted matter exceeds that of the innermost stable circular orbit radius of the BH. Iben & Tutukov (1996) assumed that the specific angular momentum (j) accreted by the degenerate dwarf from the stellar wind of the giant companion is given by

$$j \sim \Omega_g R_g^2 \left(\frac{R_{acc}}{a}\right)^2, \tag{18}$$

where Ω_g and R_g are the angular velocity and radius of the giant star, respectively. Iben & Tutukov (1996) defined the accretion radius R_{acc} as

$$R_{acc} = \frac{2GM_{dd}}{\upsilon_{wind}^2}, \tag{19}$$

where M_{dd} is the mass of the degenerate dwarf. They further assumed that the companion star is tidally locked and the binary mass is dominated by the giant star mass (M_g). Comparing our work and V20, we note the difference of a factor $\sim R_g^2/a^2$ in the definition of specific angular momentum accretion, and the omission of the relative velocity of the BH with respect to the main sequence companion in the definition of the accretion radius. For the wind velocity, Iben & Tutukov (1996) assumed that the wind velocity from the giant companions is given by

$$\upsilon'_{wind} = \upsilon'_{esc}\left(1 - \frac{R_g}{a}\right), \tag{20}$$

where $\upsilon'_{esc} = \sqrt{2GM_g/R_g}$ is the escape velocity from the companion star. Effectively, they assumed that the terminal wind velocity is equal to the escape velocity from the surface of the star, and $\beta = 1$. They also did not take the Eddington factor into account.

Observational studies of the terminal wind velocities of O stars show that their terminal velocities are larger than their escape velocities, such that the appropriate expression for the wind velocity from O stars is given by Eq. (1) (Vink et al. 2001). However, V20 did not account for the typical wind velocity of the O stars when they adopted the disk formation criterion derived by Iben & Tutukov (1996) for their BH+O systems, that is, the terminal wind velocities used by V20 in their disk formation criterion are underestimated by a factor of 2.6.

Figure 6 shows the evolution of the ratio of the circularisation radius to the radius of the innermost stable circular orbit during the BH+O phase of the 17 progenitor WR+O binaries, with (right panel, Eq. (C.1)) and without (left panel, Eq. (C.3)) taking into consideration the typical O star wind velocity, the mass of the O star, and the orbital velocity in the definition of accretion radius. Comparing the left- and right-hand side panels, we see that in using the appropriate O star wind velocity, the fraction of the BH+O star phase when an accretion disk can form greatly decreases. This shows that the X-ray active lifetime is very sensitive to the wind velocity considered in the disk formation criterion.

From the modified criterion (Eq. (C.1)), we see that only four out of 17 progenitor WR+O binaries are to become wind-fed BH HMXBs for a short period during their lifetime as a BH+O star binary. All of them are close binaries with orbital periods of less than 10 days. The only observed wind-fed BH+O in the Milky Way, Cyg X-1, also has an orbital period of around ~5.6 days (Orosz et al. 2011; Hirsch et al. 2019). From the modified criterion, we expect to find approximately three wind-fed BH HMXBs for the 17 progenitor WR+O binaries instead of 44 as calculated in V20.

In the definition of the accretion radius (Eq. (19)), Iben & Tutukov (1996) only accounted for the wind velocity of the giant star companion and not for the relative velocity between the compact object and the red giant star. We find that this assumption does not play a significant role in most of our BH+O systems as the wind velocity is much larger than the orbital velocity (Fig. B.1). But for systems where the wind

velocity can be comparable to the orbital velocity, the inclusion of the orbital velocity can further reduce the X-ray active lifetime.

Iben & Tutukov (1996) also assumed the total mass of the binary system to be approximately equal to the mass of the giant star companion (see their Eq. (65)). Their work was primarily aimed at white dwarf or neutron star+red giant binary systems and hence this was a reasonable approximation. However, that approximation breaks down for BH+O systems. V20 did not correct for the mass of the BH in the equation of the orbital velocity. The inclusion of the mass of the BH in the expression for orbital velocity reduces the predicted X-ray active lifetime of the BH+O models for systems where the mass of the BH formed is comparable to the mass of the O star, which is most readily seen in Eq. (C.2). For an equal mass BH+O binary, accounting for the mass of the BH introduces a factor of ∼1.34 on the right-hand side of Eq. (C.2), which means that the radius of the O star has to be larger for an accretion disk to form, while all other parameters are fixed.

The luminosity of massive O stars can be a finite fraction of its Eddington luminosity (see Table 1). Accounting for this Eddington factor, defined as the ratio of the luminosity of the O star to its Eddington luminosity, in the wind velocity of O stars leads to a decrease in the calculated O star wind velocity. However, in many of our considered WR+O binaries, the Eddington factor of the O star is low (≤0.1). Hence, the inclusion of the Eddington factor does not have a significant effect on the predicted X-ray active lifetime of most of our BH+O models. On the other hand, for the few systems which have Eddington factors ∼0.3, accounting for the Eddington factor increased the X-ray active lifetime, but not as significantly so as to compensate for the updated O star terminal wind velocity.

For the X-ray emission from a BH+O model with an accretion disk to be detectable from Earth, V20 assumed a luminosity cut-off of 10^{35} erg s^{-1} for all the 17 systems regardless of their individual distances from Earth. But most of the 17 WR+O binaries considered are not located within 3–4 kpc. In our work, we assume a flux cut-off of $\sim 10^{-11}$ erg s^{-1} cm^{-2} and take the distance of each source from Earth into consideration individually. The consideration of the individual distances does not affect our results as the calculated X-ray flux is above our flux detection threshold for all the models that are predicted to have an X-ray active phase (Fig. 2).

The end of the BH+O phase in V20 is considered to be the point when the companion star fills its Roche lobe. This can lead to an over-prediction of $\tau_{\rm Lx}$ for comparatively wide systems where the O star can complete hydrogen burning and yet not fill its Roche lobe. Since the wind velocity of post-MS stars are low as well, some of these systems in the post-MS phase of the O star can become strong X-ray emitters, but they do not necessarily fall under the class of wind-fed BH HMXBs. Hence, V20 may have over-predicted the X-ray active lifetime for some of the progenitor WR+O binaries by including the post-MS phase.

A recent population synthesis study by Shao & Li (2020) based on the rapid binary evolution code predicted about 10–30 wind-fed BH HMXBs in the Milky Way (see also, Wiktorowicz et al. 2020). The mass loss rate in Vink et al. (2001) was adopted, and the accretion rate was evaluated by the Bondi-Hoyle-Lyttleton accretion model (Bondi & Hoyle 1944; Belczynski et al. 2008). To evaluate the detectability of their BH+O binary models, they also adopted the same threshold for X-ray luminosity at 10^{35} erg/s as V20. We note that they did not take the criterion for the formation of an accretion disk into account. Our work suggests that accretion disks can only exist for a limited period of the main sequence lifetime of the O stars, which mainly determines the X-ray active lifetime of the BH+O star binaries. Therefore, Shao & Li (2020) have likely overestimated the number of wind-fed BH HMXBs in the Milky Way.

5. Discussion

Here, we discuss the uncertainties in the predicted X-ray active lifetimes of our BH+O binary models.

5.1. Specific angular momentum accretion

The discrepancy between the predicted wind-fed BH HMXB populations of V20 and our work shows that the criterion for accretion disk formation is sensitive to variations of the parameters in the theory. In particular, accounting for a larger O star wind velocity changes the prediction of V20 drastically. More factors such as the accretion efficiency and the approximation of the specific angular momentum carried by the accreted matter introduce further uncertainties for the computation of the X-Ray bright lifetime of the BH+O star binaries (Sect. 3). Livio et al. (1986) and Soker et al. (1986) studied accretion onto compact objects using detailed hydrodynamic simulations and found that while the mass accretion rate is similar to that predicted by the Bondi-Hoyle theory, the amount of specific angular momentum accreted was only a few percent of that predicted by the analytical approximation obtained from the Bondi-Hoyle theory. A similar conclusion was drawn by Ruffert (1999).

Owing to these calculations, El Mellah (2017) adopted the analytical expression for specific angular momentum from Shapiro & Lightman (1976, Eq. (7)), but they introduced an efficiency factor of 1/3 to account for the reduced specific angular momentum accretion found in the detailed numerical hydrodynamic studies. We captured this uncertainty and studied its effects through our efficiency parameter η. Therefore, we need to compare the analytical approximations to the specific angular momentum carried by the accreted matter used in V20 and our work to detailed 3D numerical hydrodynamic simulations in order to assess the reliability of the approximations.

As a preliminary exercise, in Fig. 7, we compare the expression for specific angular momentum carried by the wind matter used in V20 (Eq. (62) of Iben & Tutukov 1996) to the analytical form derived by Shapiro & Lightman (1976) that is assumed in our work. We see that there are significant differences between the two definitions and to the third, which includes the typical O star wind velocity in expression for specific angular momentum carried by the wind matter given by Iben & Tutukov (1996).

Due to the line-deshadowing instability and sub-photospheric turbulence, stellar winds from hot stars are prone to form overdense regions called 'clumps' (Owocki & Rybicki 1984; Owocki et al. 1988; Feldmeier 1995; Grassitelli et al. 2015). These clumps produce stochastic variations in the instantaneous amount of specific angular momentum of the accreted material. These variations take place on time scales of the order of hundreds to thousands of seconds, much shorter than the evolutionary time scales (Grinberg et al. 2017; El Mellah et al. 2020b). For clump sizes derived from first principles (Sundqvist et al. 2018), clumps are small compared to the accretion radius when they reach the orbital separation (El Mellah et al. 2018). As a consequence, they induce a limited peak-to-peak variability. However, when the wind is sufficiently fast, the net amount of angular momentum provided to the flow is so small (and so is the accretion radius) that the serendipitous capture of clumps becomes relatively more important and can

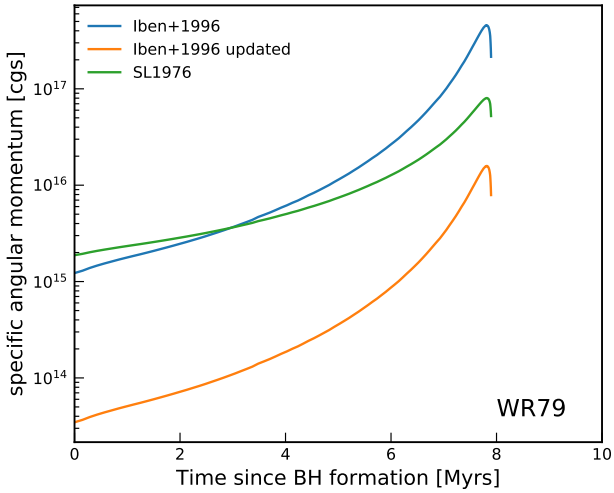

Fig. 7. Comparison of the specific angular momentum of the accreted wind matter used in V20 (Eq. (18), Iben+1996) to the analytical value derived by Shapiro & Lightman (1976) (SL1976) for the stellar and binary parameters of WR79, as a function of the time since BH formation. We also show the decrease in the amount of specific angular momentum carried by the wind when the typical wind velocity for O type stars is introduced in Eq. (18), denoted by 'Iben+1996 updated'.

produce a transient accretion disk. However, in Cygnus X-1, the wind-captured disk is permanent and so far, the only wind-fed HMXB where a transient wind-captured disk has been observed is Vela X-1 (Liao et al. 2020). In the latter case, the disk formation is believed to be associated with variations at the periastron induced by the slightly eccentric orbital motion, rather than with clump capture (Kretschmar et al. 2021). Therefore, including wind clumping is not expected to significantly modify the results obtained in this paper.

5.2. Properties of the WR star companion

In many of the investigated WR+O star binaries, in particular in the shorter-period ones, the WR star likely formed via Roche-lobe overflow from its progenitor O star (e.g., Vanbeveren et al. 1998a; Wellstein & Langer 1999). The companion O star may thus accrete mass from the WR star progenitor, which could lead to properties which are different from those of single O stars. Important properties in this respect are the helium abundance and spin of the mass gaining O star.

An enhancement of the surface helium mass fraction of the mass gainer of a few percent is predicted from conservative (Wellstein & Langer 1999) as well as non-conservative (Petrovic et al. 2005a; Langer et al. 2020) massive binary evolution models. This enrichment leads to a slight overluminosity of the mass gainer (Langer 1992), which may affect the stellar wind properties. However, quantitatively, this effect is not expected to exceed the uncertainty in the average wind properties of O stars (Vink & Sander 2021).

Independent of the mass transfer efficiency, the angular momentum gain of the accretor during the mass transfer is expected to spin up the mass gainer significantly (Packet 1981; Petrovic et al. 2005b; Langer et al. 2020). The observed population of Be/X-ray binaries (Reig 2011) signifies that this spin-up may achieve near-critical rotation, with strong consequences for the mass outflow from the spun-up star, and the mass accretion onto the compact companion. The Galactic and LMC WR+O binaries do indeed also contain rapidly rotating O stars (Vanbeveren et al. 2018; Shara et al. 2020). However, while faster than average O stars, the analysed WR companions rotate on average with less than 50% of their critical rotational velocity, implying that the centrifugal force remains below 25% of the surface gravity at the stellar equator. Whereas this may lead to a slight wind anisotropy, a disk-like outflow is not expected in this case.

In our analysis above, we adopted a wind velocity of the O star companions as expected for single stars. However, in Be/X-ray binaries (Waters et al. 1988) as well as in supergiant X-ray binaries (Manousakis et al. 2012), abnormally slow stellar winds are observed. While in the first case, this may relate to the stars' extreme rotation, a reduced wind acceleration due to the X-ray irradiation of the stellar atmosphere is thought to be responsible in the latter case (see also, Vilhu et al. 2021). For the conclusions we draw above, the consequences would be small, since neither of the two effects is expected in the majority of the investigated binaries. For the few cases where disk formation and significant X-ray emission is predicted, a slower wind would, however, lead to an increased accretion rate and a higher X-ray luminosity.

5.3. Other uncertainties

The lifetime of the WR+O star binary phase is considered to be constant for all the different considered WR+O binaries, whereas it actually depends on the core helium burning lifetime of the WR star, which in turn depends on the individual masses of the WR star. However, we do not expect this simplifying assumption to affect our predicted number of wind-fed BH HMXBs significantly. The mass of the WR stars at the end of core helium depletion is also uncertain due to the uncertainty about the mass loss rate during the WR phase (Neijssel et al. 2021). In both works, that is ours and V20, it is assumed that the properties of the WR stars do not change after core helium depletion. However, it has been shown recently (Laplace et al. 2020) that WR stars that have an outer hydrogen envelope may expand after helium depletion and the binary can undergo another mass transfer phase before core collapse (see also Laplace et al. 2021). Therefore, the formation of wind-fed BH HMXBs needs further investigation, both using detailed binary evolution models that calculate the binary evolution up to the core collapse of the WR star as well as into accurate modelling of the physics of accretion onto BHs.

We have shown (Fig. A.1) that the predicted mass accretion rates calculated for the anticipated BH+O binaries are much lower than the Eddington mass accretion rates. Hence, we do not consider super-Eddington accretion to be relevant for our work. Due to the same reason, the X-ray emission should be isotropic and we do not need to consider the case of beaming (King 2008). LOBSTER eye telescopes can reach a flux cut-off of 10^{-12} erg s^{-1} cm^{-2} (Priedhorsky et al. 1996; Hudec et al. 2007). The recently launched eROSITA X-ray telescope is stated to have a flux detection threshold of $\sim 10^{-14}$ erg s^{-1} cm^{-2} (Merloni et al. 2012) in the average all-sky survey mode. However, changing the flux limit to these lower values does not change our predicted X-ray active lifetime since once a wind-captured disk can form around the BH, the expected to X-ray flux at Earth is higher than 10^{-11} erg s^{-1} cm^{-2} (Fig. 2). On the other hand, if there is significant extinction at X-ray wavelengths in the Galactic plane, our predicted X-ray active lifetime of the BH+O binary models can get reduced.

The predicted X-ray luminosity of an accreting BH in our models is a few percent of the Eddington luminosity. In such a case, the X-ray spectrum can switch from a soft state to a

hard state and the X-ray emission becomes radiatively inefficient (Yuan & Narayan 2014). This is well-described by a distended and tenuous advection-dominated accretion flow (ADAF, see Narayan & Yi 1994, 1995a,b). In this accretion regime, the bulk of the accretion energy is carried by the accreting gas in the form of thermal energy, which can vanish through the event horizon of the BH. Hence, the BHs in the ADAF regime can be fainter by a factor of ∼100–1000 (Narayan & McClintock 2008). In such a case, we do not expect the binary to be detectable in X-rays. The inclusion of this effect can only reduce our prediction of the X-ray active lifetime during the BH+O phase.

6. Conclusion

WR+O binaries are expected to be progenitors of BH+O binaries. V20 investigated 17 galactic WR+O star binaries and predicted that there should be more than 200 wind-fed BH HMXBs in the Milky Way, while only one has been observed. They concluded that BHs receive much higher natal kick velocities or WR stars explode with supernova explosions to form neutron stars, which lead to a break-up of the binary systems.

We applied a similar methodology as in V20 with an improved analytical criterion to study the formation of accretion disks around BHs in BH+O binaries and the detectability of X-ray emission from such systems. We also investigated the effect of uncertain physics parameters, such as the β value in the O star wind velocity law, the efficiency of angular momentum accretion (η) and the spin of the BH ($\gamma_{\pm}$) on the predicted number of wind-fed BH HMXBs. We find that this calculated number is sensitive to plausible variations in the assumed parameters.

For our fiducial parameter set $(\beta, \eta, \gamma) = (1, 1/3, 1)$ (see Sect. 3, and Fig. 1), we predict only approximately two to three wind-fed BH HMXBs based on the 17 progenitor WR+O systems. While we still over-predict the number of wind-fed BH HMXBs, accounting for the theoretical and observational biases in the population of WR+O binaries (see Sect. 2.1) suggest that we should expect approximately two to three wind-fed BH HMXBs in the entire Milky Way. We remind the reader that only one wind-fed BH+O X-ray binary has been observed (Cyg X-1).

We then revisited the derivation of the accretion disk formation criterion used by V20 and found that, in particular, the assumed O star wind velocity was underestimated. Accounting for the appropriate O star wind velocity (Vink et al. 2001), we find most of BH+O binary models will have negligible X-ray bright lifetimes due to the absence of an accretion disk around the BH (see Fig. 6). As such, any conclusion drawn from the seemingly discrepant number of observed WR+O binaries and wind-fed BH HMXBs has to be re-evaluated.

Furthermore, our analysis shows that a high BH spin parameter can lead to significantly longer and brighter X-ray phases in wind-accreting BH+O binaries. The corresponding bias in detecting such binaries with rapidly spinning BHs may help to alleviate the tension between the rather low BH spin values generally predicted from binary stellar evolution models (Qin et al. 2018) and the high BH spin values observationally deduced from BH+O binaries in the Local Group (Qin et al. 2019).

We conclude that high BH formation kicks are not necessary to understand the number discrepancy between the populations of observed WR+O binaries and wind-fed BH HMXBs in the Milky Way. With our current understanding of O star wind velocities, we have shown that possibly the vast majority of Galactic BH+O star binaries may not form BH accretion disks and hence remain undetected in X-Ray surveys. Recent studies have shown that the *Gaia* satellite offers an excellent opportunity to observe such X-ray quiet BH+O binaries via periodic astrometric variations (Breivik et al. 2017; Mashian & Loeb 2017; Yalinewich et al. 2018; Yamaguchi et al. 2018; Andrews et al. 2019). Furthermore, BH+O binaries can also be detected from photometric variability of the O star induced by the BH companion (Zucker et al. 2007; Masuda & Hotokezaka 2019), or spectroscopically via the periodic shift in radial velocity of the O star.

Acknowledgements. We thank Pablo Marchant and Krzysztof Belczynski for meaningful discussions, and Dany Vanbeveren for helpful comments on an earlier version of this manuscript. I.E.M. has received funding from the European Research Council (ERC) under the European Union's Horizon 2020 research and innovation programme (Spawn ERC, grant agreement No 863412). This research has made use of NASA's Astrophysics Data System.

References

Abbott, B. P., Abbott, R., Abbott, T. D., et al. 2016, Phys. Rev. X, 6, 041015
Abbott, B. P., Abbott, R., Abbott, T. D., et al. 2019, Phys. Rev. X, 9, 031040
Andrews, J. J., Breivik, K., & Chatterjee, S. 2019, ApJ, 886, 68
Bachetti, M., Harrison, F. A., Walton, D. J., et al. 2014, Nature, 514, 202
Balbus, S. A., & Hawley, J. F. 1991, ApJ, 376, 214
Belczynski, K., Kalogera, V., Rasio, F. A., et al. 2008, ApJS, 174, 223
Belczynski, K., Wiktorowicz, G., Fryer, C. L., Holz, D. E., & Kalogera, V. 2012, ApJ, 757, 91
Belczynski, K., Buonanno, A., Cantiello, M., et al. 2014, ApJ, 789, 120
Belczynski, K., Repetto, S., Holz, D. E., et al. 2016, ApJ, 819, 108
Belczynski, K., Klencki, J., Fields, C. E., et al. 2020, A&A, 636, A104
Bondi, H. 1952, MNRAS, 112, 195
Bondi, H., & Hoyle, F. 1944, MNRAS, 104, 273
Bradt, H. V., Swank, J. H., & Rothschild, R. E. 1991, Adv. Space Res., 11, 243
Brandt, W. N., Podsiadlowski, P., & Sigurdsson, S. 1995, MNRAS, 277, L35
Braun, H., & Langer, N. 1995, A&A, 297, 483
Breivik, K., Chatterjee, S., & Larson, S. L. 2017, ApJ, 850, L13
Chandra, A. D., Roy, J., Agrawal, P. C., & Choudhury, M. 2020, MNRAS, 495, 2664
Crowther, P. A. 2015, in Wolf-Rayet Stars, eds. W. R. Hamann, A. Sander, & H. Todt, 21
Crowther, P. A. 2019, Galaxies, 7, 88
Davidson, K., & Ostriker, J. P. 1973, ApJ, 179, 585
de Mink, S. E., & Belczynski, K. 2015, ApJ, 814, 58
de Mink, S. E., & Mandel, I. 2016, MNRAS, 460, 3545
Dhawan, V., Mirabel, I. F., Ribó, M., & Rodrigues, I. 2007, ApJ, 668, 430
du Buisson, L., Marchant, P., Podsiadlowski, P., et al. 2020, MNRAS, 499, 5941
Edgar, R. 2004, New Astron. Rev., 48, 843
Ekström, S., Georgy, C., Eggenberger, P., et al. 2012, A&A, 537, A146
El Mellah, I. 2017, ArXiv e-prints [arXiv:1707.09165]
El Mellah, I., & Casse, F. 2017, MNRAS, 467, 2585
El Mellah, I., Sundqvist, J. O., & Keppens, R. 2018, MNRAS, 475, 3240
El Mellah, I., Bolte, J., Decin, L., Homan, W., & Keppens, R. 2020a, A&A, 637, A91
El Mellah, I., Grinberg, V., Sundqvist, J. O., Driessen, F. A., & Leutenegger, M. A. 2020b, A&A, 643, A9
Event Horizon Telescope Collaboration (Akiyama, K., et al.) 2019, ApJ, 875, L1
Farr, W. M., Sravan, N., Cantrell, A., et al. 2011, ApJ, 741, 103
Feldmeier, A. 1995, A&A, 299, 523
Fragos, T., Willems, B., Kalogera, V., et al. 2009, ApJ, 697, 1057
Frank, J., King, A., & Raine, D. J. 2002, Accretion Power in Astrophysics (Third Edition)
Fujita, Y., Inoue, S., Nakamura, T., Manmoto, T., & Nakamura, K. E. 1998, ApJ, 495, L85
Fürst, F., Walton, D. J., Harrison, F. A., et al. 2016, ApJ, 831, L14
Gou, L., McClintock, J. E., Reid, M. J., et al. 2011, ApJ, 742, 85
Grassitelli, L., Fossati, L., Simón-Díáz, S., et al. 2015, ApJ, 808, L31
Grinberg, V., Hell, N., El Mellah, I., et al. 2017, A&A, 608, A143
Groenewegen, M. A. T., & Lamers, H. J. G. L. M. 1989, A&AS, 79, 359
Hirsch, M., Hell, N., Grinberg, V., et al. 2019, A&A, 626, A64
Hobbs, G., Lorimer, D. R., Lyne, A. G., & Kramer, M. 2005, MNRAS, 360, 974
Hudec, R., Pina, L., Šimon, V., et al. 2007, Nucl. Phys. B Proc. Suppl., 166, 229
Iben, I. J., & Tutukov, A. V. 1996, ApJS, 105, 145
Illarionov, A. F., & Sunyaev, R. A. 1975, A&A, 39, 185
In't Zand, J. J., Priedhorsky, W. C., Moss, C. E., et al. 1994, in Advances in Multilayer and Grazing Incidence X-Ray/EUV/FUV Optics, eds.

R. B. Hoover, & A. B. Walker, Society of Photo-Optical Instrumentation Engineers (SPIE) Conference Series, 2279, 458
Israel, G. L., Belfiore, A., Stella, L., et al. 2017, Science, 355, 817
King, A. R. 2008, MNRAS, 385, L113
Kremer, K., Lu, W., Rodriguez, C. L., Lachat, M., & Rasio, F. A. 2019, ApJ, 881, 75
Kretschmar, P., El Mellah, I., Martínez-Núñez, S., et al. 2021, A&A, 652, A95
Kruckow, M. U., Tauris, T. M., Langer, N., Kramer, M., & Izzard, R. G. 2018, MNRAS, 481, 1908
Lamers, H. J. G. L. M., Snow, T. P., & Lindholm, D. M. 1995, ApJ, 455, 269
Langer, N. 1992, A&A, 265, L17
Langer, N. 2012, ARA&A, 50, 107
Langer, N., Schürmann, C., Stoll, K., et al. 2020, A&A, 638, A39
Laplace, E., Götberg, Y., de Mink, S. E., Justham, S., & Farmer, R. 2020, A&A, 637, A6
Laplace, E., Justham, S., Renzo, M., et al. 2021, A&A, submitted [arXiv:2102.05036]
Liao, Z., Liu, J., Zheng, X., & Gou, L. 2020, MNRAS, 492, 5922
Livio, M., Soker, N., de Kool, M., & Savonije, G. J. 1986, MNRAS, 222, 235
Mandel, I., & Müller, B. 2020, MNRAS, 499, 3214
Mandel, I., Müller, B., Riley, J., et al. 2021, MNRAS, 500, 1380
Manousakis, A., Walter, R., & Blondin, J. M. 2012, A&A, 547, A20
Marchant, P., Langer, N., Podsiadlowski, P., Tauris, T. M., & Moriya, T. J. 2016, A&A, 588, A50
Mashian, N., & Loeb, A. 2017, MNRAS, 470, 2611
Masuda, K., & Hotokezaka, K. 2019, ApJ, 883, 169
Mennekens, N., & Vanbeveren, D. 2014, A&A, 564, A134
Merloni, A., Predehl, P., Becker, W., et al. 2012, ArXiv e-prints [arXiv:1209.3114]
Miller-Jones, J. C. A., Bahramian, A., Orosz, J. A., et al. 2021, Science, 371, 1046
Minniti, D., Contreras Ramos, R., Alonso-García, J., et al. 2015, ApJ, 810, L20
Mirabel, I. F., & Rodrigues, I. 2003, Science, 300, 1119
Narayan, R., & Yi, I. 1994, ApJ, 428, L13
Narayan, R., & Yi, I. 1995a, ApJ, 444, 231
Narayan, R., & Yi, I. 1995b, ApJ, 452, 710
Narayan, R., & McClintock, J. E. 2008, New Astron. Rev., 51, 733
Neijssel, C. J., Vinciguerra, S., Vigna-Gómez, A., et al. 2021, ApJ, 908, 118
Novikov, I. D., & Thorne, K. S. 1973, in Black Holes (Les Astres Occlus), 343
O'Connor, E., & Ott, C. D. 2011, ApJ, 730, 70
Orosz, J. A., McClintock, J. E., Aufdenberg, J. P., et al. 2011, ApJ, 742, 84
O'Shaughnessy, R., Kim, C., Kalogera, V., & Belczynski, K. 2008, ApJ, 672, 479
Owocki, S. P., & Rybicki, G. B. 1984, ApJ, 284, 337
Owocki, S. P., Castor, J. I., & Rybicki, G. B. 1988, ApJ, 335, 914
Özel, F., Psaltis, D., Narayan, R., & McClintock, J. E. 2010, ApJ, 725, 1918
Packet, W. 1981, A&A, 102, 17
Perets, H. B., Li, Z., Lombardi, J. C., Jr., & Stephen, R. M., Jr. 2016, ApJ, 823, 113
Petrovic, J., Langer, N., & van der Hucht, K. A. 2005a, A&A, 435, 1013
Petrovic, J., Langer, N., Yoon, S. C., & Heger, A. 2005b, A&A, 435, 247
Priedhorsky, W. C., Peele, A. G., & Nugent, K. A. 1996, MNRAS, 279, 733
Puls, J., Kudritzki, R. P., Herrero, A., et al. 1996, A&A, 305, 171
Qin, Y., Fragos, T., Meynet, G., et al. 2018, A&A, 616, A28
Qin, Y., Marchant, P., Fragos, T., Meynet, G., & Kalogera, V. 2019, ApJ, 870, L18
Quast, M., Langer, N., & Tauris, T. M. 2019, A&A, 628, A19
Reig, P. 2011, Ap&SS, 332, 1
Repetto, S., Davies, M. B., & Sigurdsson, S. 2012, MNRAS, 425, 2799
Repetto, S., Igoshev, A. P., & Nelemans, G. 2017, MNRAS, 467, 298
Rosslowe, C. K., & Crowther, P. A. 2015, MNRAS, 447, 2322
Ruffert, M. 1999, A&A, 346, 861
Scarcella, F., Gaggero, D., Connors, R., et al. 2021, MNRAS, 505, 4036
Schweickhardt, J., Schmutz, W., Stahl, O., Szeifert, T., & Wolf, B. 1999, A&A, 347, 127
Shakura, N. I., & Sunyaev, R. A. 1973, A&A, 500, 33
Shao, Y., & Li, X.-D. 2020, ApJ, 898, 143
Shapiro, S. L., & Lightman, A. P. 1976, ApJ, 204, 555
Shapiro, S. L., & Teukolsky, S. A. 1983, Black holes, white dwarfs, and neutron stars : the physics of compact objects
Shara, M. M., Crawford, S. M., Vanbeveren, D., et al. 2020, MNRAS, 492, 4430
Soker, N., Livio, M., de Kool, M., & Savonije, G. J. 1986, MNRAS, 221, 445
Stevenson, S., Ohme, F., & Fairhurst, S. 2015, ApJ, 810, 58
Sukhbold, T., Woosley, S. E., & Heger, A. 2018, ApJ, 860, 93
Sundqvist, J. O., Owocki, S. P., & Puls, J. 2018, A&A, 611, A17
Tsuna, D., Kawanaka, N., & Totani, T. 2018, MNRAS, 477, 791
Ugliano, M., Janka, H.-T., Marek, A., & Arcones, A. 2012, ApJ, 757, 69
van den Heuvel, E. P. J., Portegies Zwart, S. F., & de Mink, S. E. 2017, MNRAS, 471, 4256
van der Hucht, K. A. 2001, VizieR Online Data Catalog:III/215
van der Hucht, K. A. 2006, A&A, 458, 453
Vanbeveren, D., De Donder, E., Van Bever, J., Van Rensbergen, W., & De Loore, C. 1998a, New Astron., 3, 443
Vanbeveren, D., De Loore, C., & Van Rensbergen, W. 1998b, A&ARv, 9, 63
Vanbeveren, D., Mennekens, N., Shara, M. M., & Moffat, A. F. J. 2018, A&A, 615, A65
Vanbeveren, D., Mennekens, N., van den Heuvel, E. P. J., & Van Bever, J. 2020, A&A, 636, A99
Vilhu, O., Kallman, T. R., Koljonen, K. I., & Hannikainen, D. C. 2021, A&A, 649, A176
Vink, J. S., & Sander, A. A. C. 2021, MNRAS, 504, 2051
Vink, J. S., de Koter, A., & Lamers, H. J. G. L. M. 2001, A&A, 369, 574
Waters, L. B. F. M., van den Heuvel, E. P. J., Taylor, A. R., Habets, G. M. H. J., & Persi, P. 1988, A&A, 198, 200
Wellstein, S., & Langer, N. 1999, A&A, 350, 148
Wiktorowicz, G., Lu, Y., Wyrzykowski, Ł., et al. 2020, ApJ, 905, 134
Willems, B., Henninger, M., Levin, T., et al. 2005, ApJ, 625, 324
Wong, T.-W., Valsecchi, F., Fragos, T., & Kalogera, V. 2012, ApJ, 747, 111
Wood, K. S., Meekins, J. F., Yentis, D. J., et al. 1984, ApJS, 56, 507
Woosley, S. E. 2019, ApJ, 878, 49
Woosley, S. E., Sukhbold, T., & Janka, H. T. 2020, ApJ, 896, 56
Wyrzykowski, Ł., & Mandel, I. 2020, A&A, 636, A20
Yalinewich, A., Beniamini, P., Hotokezaka, K., & Zhu, W. 2018, MNRAS, 481, 930
Yamaguchi, M. S., Kawanaka, N., Bulik, T., & Piran, T. 2018, ApJ, 861, 21
Yuan, F., & Narayan, R. 2014, ARA&A, 52, 529
Zhao, X., Gou, L., Dong, Y., et al. 2021, ApJ, 908, 117
Zucker, S., Mazeh, T., & Alexander, T. 2007, ApJ, 670, 1326

Appendix A: Mass accretion rate

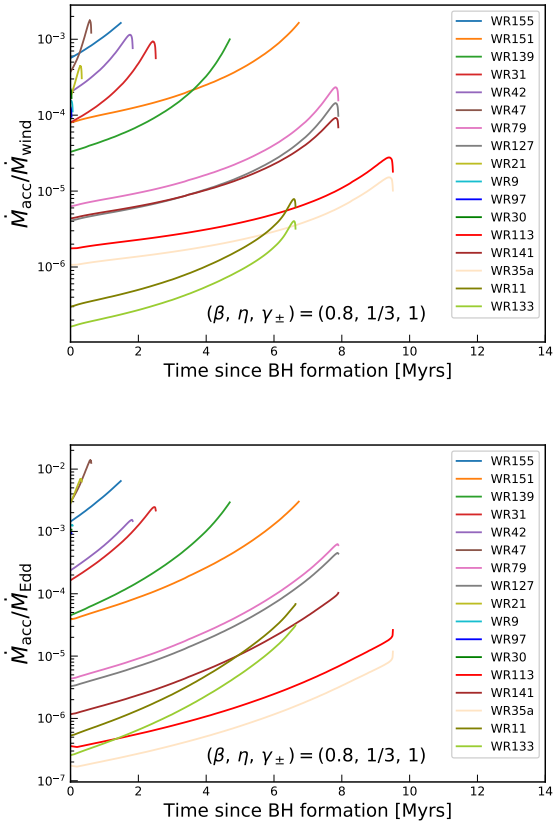

Fig. A.1. Comparison of mass accretion rate $\dot{M}_{\rm acc}$, mass loss rate of the O star $\dot{M}_{\rm wind}$, and Eddington accretion rate of the BH $\dot{M}_{\rm Edd}$ during the BH+O binary phase modelled from the 17 observed progenitor WR+O binaries for $(\beta,\eta,\gamma_\pm) = (0.8,1/3,1)$. The *upper and lower panels* present $\dot{M}_{\rm acc}/\dot{M}_{\rm wind}$ and $\dot{M}_{\rm acc}/\dot{M}_{\rm Edd}$, respectively. The colour coding in the legend denotes the 17 WR+O systems that are expected to form BH+O binaries.

Figure A.1 presents the comparison among the mass accretion rate, mass loss rate from the O star, and the Eddington accretion rate of the BH. The Eddington mass accretion rate is defined as

$$\dot{M}_{\rm Edd} = \frac{L_{\rm Edd}\, R_{\rm ISCO}}{G\, M_{\rm BH}}, \tag{A.1}$$

where $R_{\rm ISCO}$ is the radius of the innermost stable circular orbit around BH, G is the gravitational constant, $M_{\rm BH}$ is the mass of BH, and $L_{\rm Edd}$ is the Eddington luminosity, evaluated by

$$L_{\rm Edd} = L_\odot \frac{65335}{1+X}\frac{M_{\rm BH}}{M_\odot}, \tag{A.2}$$

where X is the hydrogen abundance in the accreted material, which is expected to be the hydrogen abundance at the surface of the donor star.

The upper panel shows that over 99% of wind material escapes the BH+O system, which means the typical timescale of orbital evolution $|a/\dot{a}|$ is longer than that of mass loss from the O star $|M_{\rm O}/\dot{M}_{\rm O}|$ (El Mellah et al. 2020a). The mass loss rate of the O star is about 10^{-7}–$10^{-6}\,M_\odot\,{\rm yr}^{-1}$. Therefore the orbital period of BH+O binary models can be safely treated as constant. The lower panel shows that the $\dot{M}_{\rm acc}$ is far below $\dot{M}_{\rm Edd}$. Hence super-Eddington winds from the accretor do not occur in our models.

Appendix B: Ratio of O star wind velocity to the orbital velocity

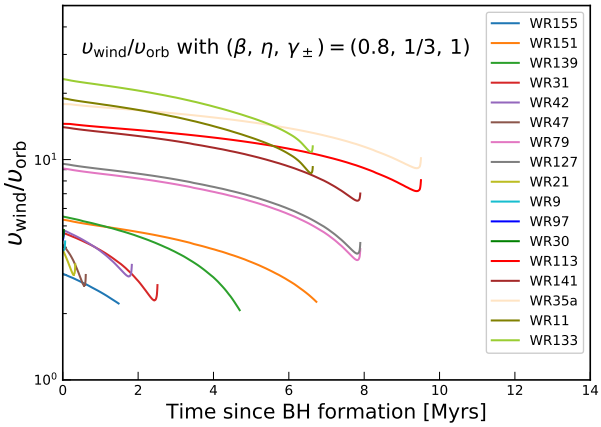

Fig. B.1. Evolution of the ratio of the O star wind velocity to the orbital velocity during the BH+O binary phase modelled from the 17 observed progenitor WR+O binaries for $(\beta,\eta,\gamma_\pm) = (0.8,1/3,1)$. The colour coding in the legend denotes the 17 WR+O systems that are expected to form BH+O binaries.

Figure B.1 presents the ratio wind velocity divided by orbital velocity $\upsilon_{\rm wind}/\upsilon_{\rm orb}$. The specific angular momentum obtained by SL76 only works in the fast-wind regime ($\upsilon_{\rm wind}/\upsilon_{\rm orb} > 1$), which is consistent with our model that we always have $\upsilon_{\rm wind} > \upsilon_{\rm orb}$.

Appendix C: Modifications on the disk formation criterion from Iben & Tutukov (1996)

Adopting the specific angular momentum as shown in Eq. (18) (Iben & Tutukov 1996) as well as the updated wind velocity from Eqs. (1)–(3), the ratio of $R_{\rm disk}/R_{\rm ISCO}$ is

$$\frac{R_{\rm disk}}{R_{\rm ISCO}} = \frac{8}{3}\frac{(R_{\rm O}/a)^4}{(1+q)^2}\left(\frac{\upsilon_{\rm orb}}{c}\right)^{-2}\left(1+\frac{\upsilon_{\rm wind}^2}{\upsilon_{\rm orb}^2}\right)^{-4}\gamma_\pm^{-1}, \tag{C.1}$$

where $q = M_{\rm O}/M_{\rm BH}$. Comparing this with Eq. (10), the efficiency parameter η for angular momentum accretion is replaced by $(R_{\rm O}/a)^4$. For the WR+O binaries considered in this work, $(R_{\rm O}/a)^4$ is much smaller than η. Hence, we expect that this updated criterion Eq. (C.1) predicts fewer wind-fed BH HMXBs than that by Eq. (10).

Taking the β parameter for wind velocity law and the BH spin parameter $\gamma_\pm$ to be equal to 1 in Eq. (C.1), the accretion disk formation criterion (Eq. (4)) can be rewritten as

$$\frac{R_{\rm O}}{a} \geq \left(2.6\sqrt{1-\Gamma}\right)^{8/7}\left(\frac{R_{\rm ISCO}}{R_{\rm O}}\right)^{1/7}(1+q)^{3/7}\left(1-\frac{R_{\rm O}}{a}\right)^{8/7}. \tag{C.2}$$

The wind velocity defined by Iben & Tutukov (1996) does not take into account the effect of the Eddington factor on the escape velocity and it underestimates the ratio of the terminal velocity to the escape velocity. Furthermore, assuming that the binary mass is equal to the mass of the non-compact companion, we obtain

$$\frac{R_{\rm disk}}{R_{\rm ISCO}} = \frac{8}{3}\left(\frac{R_{\rm O}}{a}\right)^4 q^{-2}\left(\frac{\upsilon'_{\rm orb}}{c}\right)^{-2}\left(\frac{\upsilon'^{\,2}_{\rm wind}}{\upsilon'^{\,2}_{\rm orb}}\right)^{-4}, \tag{C.3}$$

where $\upsilon'_{\rm orb}$ is the orbital velocity assuming the binary mass is equal to the donor star mass and $\upsilon'_{\rm wind}$ is the wind velocity

defined by Iben & Tutukov (1996), that is Eq. (20). Combining Eqs. (4) and (C.3) leads to the disk formation criterion obtained by Iben & Tutukov (1996) (c.f. Eq. (2) of V20),

$$\frac{R_{\rm O}}{a} \geq \left(\frac{R_{\rm ISCO}}{R_{\rm O}}\right)^{1/7} q^{3/7} \left(1 - \frac{R_{\rm O}}{a}\right)^{8/7}, \tag{C.4}$$

which makes the disk formation much easier than Eq. (C.2). For example, in the BH+O model corresponding to WR 155, with $\Gamma = 0.16$ and $q = 2.5$ at the BH formation time, taking $\gamma_{\pm} = 1$ and $\beta = 0.8$, adopting the typical O star wind velocity reduces the ratio of $R_{\rm disk}/R_{\rm ISCO}$ obtained from Eq. (C.1) by three orders of magnitude in comparison to that predicted from Eq. (C.3).

Bibliography

Abbott, B. P., R. Abbott, T. D. Abbott, M. R. Abernathy et al. (2016), Observation of Gravitational Waves from a Binary Black Hole Merger, Phys. Rev. Lett. 116, 061102 061102, arXiv: 1602.03837 [gr-qc] (cit. on pp. 3, 22).

Abbott, B. P., R. Abbott, T. D. Abbott, F. Acernese et al. (2017), Multi-messenger Observations of a Binary Neutron Star Merger, ApJ 848, L12 L12, arXiv: 1710.05833 [astro-ph.HE] (cit. on p. 3).

Abbott, R. et al. (2023), Population of Merging Compact Binaries Inferred Using Gravitational Waves through GWTC-3, Physical Review X 13, 011048 011048, arXiv: 2111.03634 [astro-ph.HE] (cit. on pp. 56, 73, 75, 76, 84, 110–112, 151, 153).

Antokhin, I. I., A. M. Cherepashchuk, E. A. Antokhina and A. M. Tatarnikov (2022), Near-IR and X-Ray Variability of Cyg X-3: Evidence for a Compact IR Source and Complex Wind Structures, ApJ 926, 123 123, arXiv: 2112.04805 [astro-ph.HE] (cit. on pp. 56, 57, 73).

Antoniou, V., A. Zezas, D. Hatzidimitriou and V. Kalogera (2010), STAR FORMATION HISTORY AND X-RAY BINARY POPULATIONS: THE CASE OF THE SMALL MAGELLANIC CLOUD, The Astrophysical Journal 716 L140, url: https://doi.org/10.1088/2041-8205/716/2/l140 (cit. on p. 43).

Antoniou, V., A. Zezas, J. J. Drake et al. (2019), Deep Chandra Survey of the Small Magellanic Cloud. III. Formation Efficiency of High-mass X-Ray Binaries, ApJ 887, 20 20, arXiv: 1901.01237 [astro-ph.HE] (cit. on p. 43).

El-Badry, K. et al. (2022), Birth of a Be star: an APOGEE search for Be stars forming through binary mass transfer, arXiv e-prints, arXiv:2201.05614 arXiv:2201.05614, arXiv: 2201.05614 [astro-ph.SR] (cit. on pp. 26, 33).

Barnard, R., J. S. Clark and U. C. Kolb (2008), NGC 300 X-1 and IC 10 X-1: a new breed of black hole binary?, A&A 488 697, arXiv: 0807.0606 [astro-ph] (cit. on p. 72).

Bauer, F. E. and W. N. Brandt (2004), Chandra and Hubble Space Telescope Confirmation of the Luminous and Variable X-Ray Source IC 10 X-1 as a Possible Wolf-Rayet, Black Hole Binary, The Astrophysical Journal 601 L67, url: https://dx.doi.org/10.1086/380107 (cit. on pp. 56, 72).

Bavera, S. S. et al. (2021), The impact of mass-transfer physics on the observable properties of field binary black hole populations, A&A 647, A153 A153, arXiv: 2010.16333 [astro-ph.HE] (cit. on p. 84).

Bekki, K. and S. Stanimirović (2009), The total mass and dark halo properties of the Small Magellanic Cloud, MNRAS 395 342, arXiv: 0807.2102 [astro-ph] (cit. on p. 84).

Belczynski, K., A. Buonanno et al. (2014), The Formation and Gravitational-wave Detection of Massive Stellar Black Hole Binaries, ApJ 789, 120 120, arXiv: 1403.0677 [astro-ph.HE] (cit. on p. 56).

Belczynski, K., Z. Doctor et al. (2022), Black Hole–Black Hole Total Merger Mass and the Origin of LIGO/Virgo Sources, The Astrophysical Journal 935 126, url: https://dx.doi.org/10.3847/1538-4357/ac8167 (cit. on p. 56).

Belczynski, K., D. E. Holz, T. Bulik and R. O'Shaughnessy (2016), The first gravitational-wave source from the isolated evolution of two stars in the 40-100 solar mass range, Nature 534 512, arXiv: 1602.04531 [astro-ph.HE] (cit. on p. 30).

Belczynski, K., V. Kalogera et al. (2008), Compact Object Modeling with the StarTrack Population Synthesis Code, ApJS 174 223, arXiv: astro-ph/0511811 [astro-ph] (cit. on pp. 10, 16, 30, 57, 110).

Bell, J. F., M. S. Bessell, B. W. Stappers, M. Bailes and V. M. Kaspi (1995), PSR J0045-7319: A Dual-Line Binary Radio Pulsar, ApJ 447 L117, arXiv: astro-ph/9505044 [astro-ph] (cit. on pp. 36, 38, 49, 149).

Binder, B. et al. (2011), A Deep Chandra Observation of the Wolf-Rayet + Black Hole Binary NGC 300 X-1, ApJ 742, 128 128 (cit. on pp. 56, 72).

Binder, B. A. et al. (2021), The Wolf–Rayet + Black Hole Binary NGC 300 X-1: What is the Mass of the Black Hole?, The Astrophysical Journal 910 74, url: https://dx.doi.org/10.3847/1538-4357/abe6a9 (cit. on pp. 57, 72, 73).

Blaauw, A. (1961), On the origin of the O- and B-type stars with high velocities (the "run-away" stars), and some related problems, Bull. Astron. Inst. Netherlands 15 265 (cit. on p. 30).

Bodensteiner, J., T. Shenar and H. Sana (2020), Investigating the lack of main-sequence companions to massive Be stars, A&A 641, A42 A42, arXiv: 2006.13229 [astro-ph.SR] (cit. on p. 13).

Böhm-Vitense, E. (1958), Über die Wasserstoffkonvektionszone in Sternen verschiedener Effektivtemperaturen und Leuchtkräfte. Mit 5 Textabbildungen, ZAp 46 108 (cit. on pp. 6, 25, 52).

Bonanos, A. Z. et al. (2010), Spitzer SAGE-SMC Infrared Photometry of Massive Stars in the Small Magellanic Cloud, AJ 140 416, arXiv: 1004.0949 [astro-ph.SR] (cit. on p. 49).

Briel, M. M., H. F. Stevance and J. J. Eldridge (2022), Understanding the high-mass binary black hole population from stable mass transfer and super-Eddington accretion in BPASS, arXiv e-prints, arXiv:2206.13842 arXiv:2206.13842, arXiv: 2206.13842 [astro-ph.HE] (cit. on pp. 56, 80).

Brott, I. et al. (2011), Rotating massive main-sequence stars. I. Grids of evolutionary models and isochrones, A&A 530, A115 A115, arXiv: 1102.0530 [astro-ph.SR] (cit. on pp. 7, 8, 23, 25, 59, 73).

Cantiello, M. and N. Langer (2010), Thermohaline mixing in evolved low-mass stars, A&A 521, A9 A9, arXiv: 1006.1354 [astro-ph.SR] (cit. on p. 25).

Carmeli, M., J. G. Hartnett and F. J. Oliveira (2006), The Cosmic Time in Terms of the Redshift, Foundations of Physics Letters 19 277, arXiv: gr-qc/0506079 [gr-qc] (cit. on p. 63).

Casares, J. et al. (2014), A Be-type star with a black-hole companion, Nature 505 378, arXiv: 1401.3711 [astro-ph.SR] (cit. on pp. 15, 23, 40, 49, 57, 149).

Chatzopoulos, E. and J. C. Wheeler (2012), Effects of Rotation on the Minimum Mass of Primordial Progenitors of Pair-instability Supernovae, ApJ 748, 42 42, arXiv: 1201.1328 [astro-ph.HE] (cit. on p. 28).

Cheng, Z. .-., Y. Shao and X. .-. Li (2014), On the Spin Period Distribution in Be/X-Ray Binaries, ApJ 786, 128 128, arXiv: 1404.0219 [astro-ph.HE] (cit. on p. 48).

Chiosi, C. and C. Summa (1970), On the Evolution of OB Stars from the Main Sequence to the Helium Exhaustion Phase, Ap&SS 8 478 (cit. on p. 8).
Choi, J. et al. (2016), Mesa Isochrones and Stellar Tracks (MIST). I. Solar-scaled Models, ApJ 823, 102 102, arXiv: 1604.08592 [astro-ph.SR] (cit. on p. 41).
Clark, J. S. and P. A. Crowther (2004), On the Wolf-Rayet counterpart to IC 10 X-1, A&A 414 L45 (cit. on pp. 56, 72, 73).
Coe, M. J., J. A. Kennea, P. A. Evans and A. Udalski (2020), Swift J004427.3 − 734801 - a probable Be/white dwarf system in the Small Magellanic Cloud, MNRAS 497 L50, arXiv: 2005.02891 [astro-ph.HE] (cit. on p. 91).
Coe, M. J. and J. Kirk (2015), Catalogue of Be/X-ray binary systems in the Small Magellanic Cloud: X-ray, optical and IR properties, MNRAS 452 969, arXiv: 1506.01920 [astro-ph.HE] (cit. on pp. 38, 48, 149).
Coleiro, A. and S. Chaty (2013), DISTRIBUTION OF HIGH-MASS X-RAY BINARIES IN THE MILKY WAY, ApJ 764 185, url: https://doi.org/10.1088/0004-637x/764/2/185 (cit. on p. 30).
Crowther, P. A. (2015), "Wolf-Rayet content of the Milky Way", Wolf-Rayet Stars, ed. by W.-R. Hamann, A. Sander and H. Todt 21, arXiv: 1509.00495 [astro-ph.SR] (cit. on p. 81).
Crowther, P. A., R. Barnard et al. (2010), NGC 300 X-1 is a Wolf-Rayet/black hole binary, MNRAS 403 L41, arXiv: 1001.4616 [astro-ph.SR] (cit. on p. 72).
Crowther, P. A., S. Carpano, L. J. Hadfield and A. M. T. Pollock (2007), On the optical counterpart of NGC 300 X-1 and the global Wolf-Rayet content of NGC 300, A&A 469 L31, arXiv: 0705.1544 [astro-ph] (cit. on pp. 56, 72).
Davies, B. et al. (2015), Red Supergiants as Cosmic Abundance Probes: The Magellanic Clouds, ApJ 806, 21 21, arXiv: 1504.03694 [astro-ph.GA] (cit. on pp. 22, 56).
de Grijs, R. and G. Bono (2015), Clustering of Local Group Distances: Publication Bias or Correlated Measurements? III. The Small Magellanic Cloud, AJ 149, 179 179, arXiv: 1504.00417 [astro-ph.SR] (cit. on p. 22).
de Kool, M. (1990), Common Envelope Evolution and Double Cores of Planetary Nebulae, ApJ 358 189 (cit. on p. 61).
de Mink, S. E., M. Cantiello et al. (2008), "Rotational mixing in close binaries", The Art of Modeling Stars in the 21st Century, ed. by L. Deng and K. L. Chan, vol. 252, IAU Symposium 365, arXiv: 0805.2544 [astro-ph] (cit. on p. 12).
de Mink, S. E. and I. Mandel (2016), The chemically homogeneous evolutionary channel for binary black hole mergers: rates and properties of gravitational-wave events detectable by advanced LIGO, MNRAS 460 3545, arXiv: 1603.02291 [astro-ph.HE] (cit. on p. 47).
de Mink, S. E., O. R. Pols and R. W. Hilditch (2007), Efficiency of mass transfer in massive close binaries. Tests from double-lined eclipsing binaries in the SMC, A&A 467 1181, arXiv: astro-ph/0703480 [astro-ph] (cit. on pp. 12, 32, 51, 61, 77).
Detmers, R. G., N. Langer, P. Podsiadlowski and R. G. Izzard (2008), Gamma-ray bursts from tidally spun-up Wolf-Rayet stars?, A&A 484 831, arXiv: 0804.0014 [astro-ph] (cit. on pp. 25, 82, 83).
Dewi, J. D. M., O. R. Pols, G. J. Savonije and E. P. J. van den Heuvel (2002), The evolution of naked helium stars with a neutron star companion in close binary systems, MNRAS 331 1027, arXiv: astro-ph/0201239 [astro-ph] (cit. on p. 57).
Dominik, M. et al. (2013), Double Compact Objects. II. Cosmological Merger Rates, ApJ 779, 72 72, arXiv: 1308.1546 [astro-ph.HE] (cit. on pp. 56, 57, 62, 77).

Dotter, A. (2016), MESA Isochrones and Stellar Tracks (MIST) 0: Methods for the Construction of Stellar Isochrones, ApJS 222, 8 8, arXiv: 1601.05144 [astro-ph.SR] (cit. on p. 41).

du Buisson, L. et al. (2020), Cosmic rates of black hole mergers and pair-instability supernovae from chemically homogeneous binary evolution, MNRAS 499 5941, arXiv: 2002.11630 [astro-ph.HE] (cit. on p. 80).

Dufton, P. L., N. Langer et al. (2013), The VLT-FLAMES Tarantula Survey. X. Evidence for a bimodal distribution of rotational velocities for the single early B-type stars, A&A 550, A109 A109, arXiv: 1212.2424 [astro-ph.SR] (cit. on p. 91).

Dufton, P. L., D. J. Lennon et al. (2022), Properties of the Be-type stars in 30 Doradus, arXiv e-prints, arXiv:2203.02440 arXiv:2203.02440, arXiv: 2203.02440 [astro-ph.SR] (cit. on pp. 28, 43).

Eddington, A. S. (1929), Internal circulation in rotating stars, MNRAS 90 54 (cit. on pp. 7, 25).

Eggleton, P. P. (1983), Approximations to the radii of Roche lobes, ApJ 268 368 (cit. on pp. 10, 25, 60).

Eggleton, P. P. (1971), The evolution of low mass stars, MNRAS 151 351 (cit. on p. 16).

El Mellah, I., J. Bolte, L. Decin, W. Homan and R. Keppens (2020), Wind morphology around cool evolved stars in binaries. The case of slowly accelerating oxygen-rich outflows, A&A 637, A91 A91, arXiv: 2001.04482 [astro-ph.SR] (cit. on pp. 11, 31).

El Mellah, I., V. Grinberg, J. O. Sundqvist, F. A. Driessen and M. A. Leutenegger (2020), Radiography in high mass X-ray binaries. Micro-structure of the stellar wind through variability of the column density, A&A 643, A9 A9, arXiv: 2006.16216 [astro-ph.HE] (cit. on p. 59).

El Mellah, I. (2017), Wind accretion onto compact objects, arXiv e-prints, arXiv:1707.09165 arXiv:1707.09165, arXiv: 1707.09165 [astro-ph.HE] (cit. on p. 108).

Eldridge, J. J. and E. R. Stanway (2016), BPASS predictions for binary black hole mergers, MNRAS 462 3302, arXiv: 1602.03790 [astro-ph.HE] (cit. on pp. 56, 57, 80).

Eldridge, J. J., E. R. Stanway et al. (2017), Binary Population and Spectral Synthesis Version 2.1: Construction, Observational Verification, and New Results, PASA 34, e058 e058, arXiv: 1710.02154 [astro-ph.SR] (cit. on p. 16).

Endal, A. S. and S. Sofia (1978), The evolution of rotating stars. II. Calculations with time-dependent redistribution of angular momentum for 7 and 10 M sun stars., ApJ 220 279 (cit. on p. 25).

Ercolino, A., H. Jin, N. Langer, L. Dessart and D. Aguilera-Dena (in prep), Interacting supernovae from wide massive binary systems, A&A (cit. on p. 52).

Fabrika, S., Y. Ueda, A. Vinokurov, O. Sholukhova and M. Shidatsu (2015), Supercritical accretion disks in ultraluminous X-ray sources and SS 433, Nature Physics 11 551, arXiv: 1512.00435 [astro-ph.HE] (cit. on p. 79).

Falanga, M. et al. (2015), Ephemeris, orbital decay, and masses of ten eclipsing high-mass X-ray binaries, A&A 577, A130 A130, arXiv: 1502.07126 [astro-ph.HE] (cit. on pp. 36, 48, 149).

Fichtner, Y. A., L. Grassitelli, E. Romano-Díaz and C. Porciani (2022), Mechanical feedback from stellar winds with an application to galaxy formation at high redshift, MNRAS 512 4573, arXiv: 2201.07244 [astro-ph.GA] (cit. on p. 22).

Finkelstein, S. L. et al. (2023), CEERS Key Paper. I. An Early Look into the First 500 Myr of Galaxy Formation with JWST, ApJ 946, L13 L13, arXiv: 2211.05792 [astro-ph.GA] (cit. on p. 22).

Foellmi, C. (2004), Another single hydrogen-rich Wolf-Rayet star in the SMC?, A&A 416 291, arXiv: astro-ph/0310153 [astro-ph] (cit. on pp. 35, 45, 100, 148, 152).

Foellmi, C., A. F. J. Moffat and M. A. Guerrero (2003), Wolf-Rayet binaries in the Magellanic Clouds and implications for massive-star evolution - I. Small Magellanic Cloud, MNRAS 338 360 (cit. on pp. 35, 45, 75, 90, 100, 148, 152).
Fragos, T. et al. (2023), POSYDON: A General-purpose Population Synthesis Code with Detailed Binary-evolution Simulations, ApJS 264, 45 45, arXiv: 2202.05892 [astro-ph.SR] (cit. on p. 16).
Frank, J., A. King and D. J. Raine (2002a), Accretion Power in Astrophysics: Third Edition (cit. on pp. 10, 147).
– (2002b), Accretion Power in Astrophysics: Third Edition (cit. on p. 108).
Fricke, K. (1968), Instabilität stationärer Rotation in Sternen, ZAp 68 317 (cit. on pp. 6, 25).
Fryer, C. L., K. Belczynski et al. (2012), COMPACT REMNANT MASS FUNCTION: DEPENDENCE ON THE EXPLOSION MECHANISM AND METALLICITY, ApJ 749 91, url: https://doi.org/10.1088/0004-637x/749/1/91 (cit. on p. 30).
Fryer, C. L., S. E. Woosley and D. H. Hartmann (1999), Formation Rates of Black Hole Accretion Disk Gamma-Ray Bursts, ApJ 526 152, arXiv: astro-ph/9904122 [astro-ph] (cit. on p. 82).
Gaia Collaboration et al. (2018), Gaia Data Release 2. Observational Hertzsprung-Russell diagrams, A&A 616, A10 A10, arXiv: 1804.09378 [astro-ph.SR] (cit. on pp. 8, 147).
Gallegos-Garcia, M., C. P. L. Berry, P. Marchant and V. Kalogera (2021), Binary Black Hole Formation with Detailed Modeling: Stable Mass Transfer Leads to Lower Merger Rates, arXiv e-prints, arXiv:2107.05702 arXiv:2107.05702, arXiv: 2107.05702 [astro-ph.HE] (cit. on pp. 57, 78, 79).
Ge, H., R. F. Webbink and Z. Han (2020), The Thermal Equilibrium Mass-loss Model and Its Applications in Binary Evolution, ApJS 249, 9 9, arXiv: 2006.00774 [astro-ph.SR] (cit. on p. 78).
Gilkis, A., J. S. Vink, J. J. Eldridge and C. A. Tout (2019), Effects of winds on the leftover hydrogen in massive stars following Roche lobe overflow, MNRAS 486 4451, arXiv: 1904.09221 [astro-ph.SR] (cit. on p. 34).
Golden-Marx, J. B., M. S. Oey, J. B. Lamb, A. S. Graus and A. S. White (2016), Classical Oe Stars in the Field of the Small Magellanic Cloud, ApJ 819, 55 55, arXiv: 1601.03405 [astro-ph.SR] (cit. on p. 28).
Goldreich, P. and G. Schubert (1967), Differential Rotation in Stars, ApJ 150 571 (cit. on pp. 6, 25).
Götberg, Y., S. E. de Mink et al. (2018), Spectral models for binary products: Unifying subdwarfs and Wolf-Rayet stars as a sequence of stripped-envelope stars, A&A 615, A78 A78, arXiv: 1802.03018 [astro-ph.SR] (cit. on p. 23).
Götberg, Y., V. Korol et al. (2020), Stars Stripped in Binaries: The Living Gravitational-wave Sources, ApJ 904, 56 56, arXiv: 2006.07382 [astro-ph.SR] (cit. on pp. 57, 77).
Graczyk, D. et al. (2020), A Distance Determination to the Small Magellanic Cloud with an Accuracy of Better than Two Percent Based on Late-type Eclipsing Binary Stars, ApJ 904, 13 13, arXiv: 2010.08754 [astro-ph.GA] (cit. on p. 15).
Gräfener, G., S. P. Owocki, L. Grassitelli and N. Langer (2017), On the optically thick winds of Wolf-Rayet stars, A&A 608, A34 A34, arXiv: 1710.04543 [astro-ph.SR] (cit. on p. 114).
Green, D. A. and F. R. Stephenson (2003), "Historical Supernovae", Supernovae and Gamma-Ray Bursters, ed. by K. Weiler, vol. 598 7 (cit. on p. 1).
Haberl, F. and R. Sturm (2016), High-mass X-ray binaries in the Small Magellanic Cloud, A&A 586, A81 A81, arXiv: 1511.00445 [astro-ph.GA] (cit. on pp. 15, 23, 36, 42, 48, 56, 78, 149).

Hagen, L. M. Z. et al. (2017), Swift Ultraviolet Survey of the Magellanic Clouds (SUMaC) - I. Shape of the ultraviolet dust extinction law and recent star formation history of the Small Magellanic Cloud, MNRAS 466 4540, arXiv: 1611.00064 [astro-ph.GA] (cit. on pp. 22, 31, 56, 63).

Hainich, R. et al. (2015), Wolf-Rayet stars in the Small Magellanic Cloud. I. Analysis of the single WN stars, A&A 581, A21 A21, arXiv: 1507.04000 [astro-ph.SR] (cit. on pp. 35, 45, 100, 148, 152).

Hamann, W. .-., L. Koesterke and U. Wessolowski (1995), Spectral analyses of the Galactic Wolf-Rayet stars: hydrogen-helium abundances and improved stellar parameters for the WN class, A&A 299 151 (cit. on p. 25).

Harris, J. and D. Zaritsky (2004), The Star Formation History of the Small Magellanic Cloud, AJ 127 1531, arXiv: astro-ph/0312100 [astro-ph] (cit. on pp. 22, 31, 56, 63, 84).

Hastings, B., N. Langer and J. Puls (2023), A model of anisotropic winds from rotating stars for evolutionary calculations, A&A 672, A60 A60, arXiv: 2302.10992 [astro-ph.SR] (cit. on p. 25).

Hastings, B., N. Langer, C. Wang, A. Schootemeijer and A. P. Milone (2021), Stringent upper limit on Be star fractions produced by binary interaction, A&A 653, A144 A144, arXiv: 2106.12263 [astro-ph.SR] (cit. on pp. 51, 78).

Hastings, B., C. Wang and N. Langer (2020), The single star path to Be stars, A&A 633, A165 A165, arXiv: 1912.05290 [astro-ph.SR] (cit. on pp. 13, 102).

Heger, A. and N. Langer (2000), Presupernova Evolution of Rotating Massive Stars. II. Evolution of the Surface Properties, ApJ 544 1016, arXiv: astro-ph/0005110 [astro-ph] (cit. on pp. 6, 25).

Heger, A. and S. E. Woosley (2002), The Nucleosynthetic Signature of Population III, ApJ 567 532, arXiv: astro-ph/0107037 [astro-ph] (cit. on p. 28).

Hilditch, R. W., I. D. Howarth and T. J. Harries (2005), Forty eclipsing binaries in the Small Magellanic Cloud: fundamental parameters and Cloud distance, MNRAS 357 304, arXiv: astro-ph/0411672 [astro-ph] (cit. on p. 41).

Hill, V., S. Andrievsky and M. Spite (1995), Chemical evolution of the Magellanic Clouds. VI. Chemical composition of nine F supergiants from different regions of the large Magellanic Cloud., A&A 293 347 (cit. on pp. 22, 56).

Hobbs, G., D. R. Lorimer, A. G. Lyne and M. Kramer (2005), A statistical study of 233 pulsar proper motions, MNRAS 360 974, arXiv: astro-ph/0504584 [astro-ph] (cit. on pp. 29, 41).

Huang, W., D. R. Gies and M. V. McSwain (2010), A Stellar Rotation Census of B Stars: From ZAMS to TAMS, ApJ 722 605, arXiv: 1008.1761 [astro-ph.SR] (cit. on p. 26).

Hulse, R. A. and J. H. Taylor (1975), Discovery of a pulsar in a binary system., ApJ 195 L51 (cit. on p. 2).

Hurley, J. R., O. R. Pols and C. A. Tout (2000), Comprehensive analytic formulae for stellar evolution as a function of mass and metallicity, MNRAS 315 543, arXiv: astro-ph/0001295 [astro-ph] (cit. on p. 16).

Hurley, J. R., C. A. Tout and O. R. Pols (2002), Evolution of binary stars and the effect of tides on binary populations, MNRAS 329 897, arXiv: astro-ph/0201220 [astro-ph] (cit. on pp. 10, 16, 25, 30, 50, 51, 61, 77, 94, 108).

Hut, P. (1981), Tidal evolution in close binary systems., A&A 99 126 (cit. on pp. 11, 25, 94, 95).

Iben Icko, J. and A. V. Tutukov (1996), On the Evolution of Symbiotic Stars and Other Binaries with Accreting Degenerate Dwarfs, ApJS 105 145 (cit. on p. 15).

Ivanova, N. et al. (2013), Common envelope evolution: where we stand and how we can move forward, A&A Rev. 21, 59 59, arXiv: 1209.4302 [astro-ph.HE] (cit. on pp. 12, 56, 61, 79).
Izzard, R. G., L. M. Dray, A. I. Karakas, M. Lugaro and C. A. Tout (2006), Population nucleosynthesis in single and binary stars. I. Model, A&A 460 565 (cit. on p. 16).
Janka, H.-T. (2012), Explosion Mechanisms of Core-Collapse Supernovae, Annual Review of Nuclear and Particle Science 62 407, arXiv: 1206.2503 [astro-ph.SR] (cit. on pp. 29, 41, 56).
– (2017), Neutron Star Kicks by the Gravitational Tug-boat Mechanism in Asymmetric Supernova Explosions: Progenitor and Explosion Dependence, ApJ 837, 84 84, arXiv: 1611.07562 [astro-ph.HE] (cit. on pp. 29, 30, 110).
Janssens, S. et al. (2022), Uncovering astrometric black hole binaries with massive main-sequence companions with Gaia, A&A 658, A129 A129, arXiv: 2111.06427 [astro-ph.SR] (cit. on p. 23).
Jewitt, D. C., S. Sheppard and C. Porco (2004), "Jupiter's outer satellites and Trojans", Jupiter. The Planet, Satellites and Magnetosphere, ed. by F. Bagenal, T. E. Dowling and W. B. McKinnon, vol. 1 263 (cit. on pp. 10, 147).
Kaspi, V. M. et al. (1994), A Massive Radio Pulsar Binary in the Small Magellanic Cloud, ApJ 423 L43 (cit. on pp. 38, 49, 149).
Kato, S. (1966), Overstable Convection in a Medium Stratified in Mean Molecular Weight, PASJ 18 374 (cit. on p. 6).
Kippenhahn, R., K. Kohl and A. Weigert (1967), Entwicklung in engen Doppelstern systemen II., ZAp 66 58 (cit. on p. 11).
Klencki, J., G. Nelemans, A. G. Istrate and O. Pols (2020), Massive donors in interacting binaries: effect of metallicity, A&A 638, A55 A55, arXiv: 2004.00628 [astro-ph.SR] (cit. on pp. 12, 57, 78–80).
Knigge, C., M. J. Coe and P. Podsiadlowski (2011), Two populations of X-ray pulsars produced by two types of supernova, Nature 479 372, arXiv: 1111.2051 [astro-ph.SR] (cit. on p. 48).
Koenigsberger, G. et al. (2014), The HD 5980 Multiple System: Masses and Evolutionary Status, AJ 148, 62 62, arXiv: 1408.0556 [astro-ph.SR] (cit. on pp. 35, 45, 100, 148, 152).
Korn, A. J., S. R. Becker, C. A. Gummersbach and B. Wolf (2000), Chemical abundances from Magellanic cloud B stars, A&A 353 655 (cit. on pp. 22, 56).
Kroupa, P. (2001), On the variation of the initial mass function, MNRAS 322 231, arXiv: astro-ph/0009005 [astro-ph] (cit. on pp. 31, 63).
Kruckow, M. U., T. M. Tauris, N. Langer, M. Kramer and R. G. Izzard (2018), Progenitors of gravitational wave mergers: binary evolution with the stellar grid-based code COMBINE, MNRAS 481 1908, arXiv: 1801.05433 [astro-ph.SR] (cit. on pp. 16, 18, 23, 24, 28, 39, 49–51, 53, 56–59, 61, 77, 78, 108, 110, 148, 150).
Kudritzki, R.-P. et al. (2008), Quantitative Spectroscopy of 24 A Supergiants in the Sculptor Galaxy NGC 300: Flux-weighted Gravity-Luminosity Relationship, Metallicity, and Metallicity Gradient, ApJ 681 269, arXiv: 0803.3654 [astro-ph] (cit. on p. 73).
Langer, N. (1991), Evolution of massive stars in the Large Magellanic Cloud : models with semiconvection., A&A 252 669 (cit. on p. 25).
– (2012), Presupernova Evolution of Massive Single and Binary Stars, ARA&A 50 107, arXiv: 1206.5443 [astro-ph.SR] (cit. on pp. 9, 29, 56).
Langer, N., D. Baade et al. (2020), γ Cas stars: Normal Be stars with discs impacted by the wind of a helium-star companion?, A&A 633, A40 A40, arXiv: 1911.06508 [astro-ph.SR] (cit. on p. 23).

Langer, N., M. F. El Eid and K. J. Fricke (1985), Evolution of massive stars with semiconvective diffusion, A&A 145 179 (cit. on p. 8).

Langer, N., K. J. Fricke and D. Sugimoto (1983), Semiconvective diffusion and energy transport, A&A 126 207 (cit. on p. 6).

Langer, N. and C. A. Norman (2006), On the Collapsar Model of Long Gamma-Ray Bursts:Constraints from Cosmic Metallicity Evolution, ApJ 638 L63, arXiv: astro-ph/0512271 [astro-ph] (cit. on pp. 22, 56).

Langer, N., C. Schürmann et al. (2020), Properties of OB star-black hole systems derived from detailed binary evolution models, A&A 638, A39 A39, arXiv: 1912.09826 [astro-ph.SR] (cit. on pp. 23, 28, 50, 52, 81).

Laplace, E., Y. Götberg, S. E. de Mink, S. Justham and R. Farmer (2020), The expansion of stripped-envelope stars: Consequences for supernovae and gravitational-wave progenitors, A&A 637, A6 A6, arXiv: 2003.01120 [astro-ph.SR] (cit. on pp. 16, 34, 50, 52, 56, 61).

Laplace, E., S. Justham et al. (2021), Different to the core: the pre-supernova structures of massive single and binary-stripped stars, arXiv e-prints, arXiv:2102.05036 arXiv:2102.05036, arXiv: 2102.05036 [astro-ph.SR] (cit. on p. 56).

Laycock, S. G. T., R. C. Cappallo and M. J. Moro (2015), Chandra and XMM monitoring of the black hole X-ray binary IC 10 X-1, MNRAS 446 1399, arXiv: 1410.3417 [astro-ph.HE] (cit. on pp. 56, 72).

Laycock, S. G. T., T. J. Maccarone and D. M. Christodoulou (2015), Revisiting the dynamical case for a massive black hole in IC10 X-1, MNRAS 452 L31, arXiv: 1506.03882 [astro-ph.HE] (cit. on pp. 57, 72, 73).

Levan, A. et al. (2016), Gamma-Ray Burst Progenitors, Space Sci. Rev. 202 33, arXiv: 1611.03091 [astro-ph.HE] (cit. on p. 83).

Linden, T., F. Valsecchi and V. Kalogera (2012), ON THE RARITY OF X-RAY BINARIES WITH NAKED HELIUM DONORS, ApJ 748 114, url: https://dx.doi.org/10.1088/0004-637X/748/2/114 (cit. on p. 57).

Lommen, D., L. Yungelson, E. van den Heuvel, G. Nelemans and S. Portegies Zwart (2005), Cygnus X-3 and the problem of the missing Wolf-Rayet X-ray binaries, A&A 443 231, arXiv: astro-ph/0507304 [astro-ph] (cit. on pp. 56, 57, 72, 77, 81, 82).

Maeder, A. (1997), Stellar evolution with rotation. II. A new approach for shear mixing., A&A 321 134 (cit. on p. 25).

Magrini, L. and D. R. Gonçalves (2009), IC10: the history of the nearest starburst galaxy through its Planetary Nebula and HII region populations, MNRAS 398 280, arXiv: 0905.3630 [astro-ph.CO] (cit. on p. 73).

Mandel, I. (2021), An Accurate Analytical Fit to the Gravitational-wave Inspiral Duration for Eccentric Binaries, Research Notes of the American Astronomical Society 5, 223 223, arXiv: 2110.09254 [astro-ph.HE] (cit. on p. 108).

Mandel, I. and S. E. de Mink (2016), Merging binary black holes formed through chemically homogeneous evolution in short-period stellar binaries, MNRAS 458 2634, arXiv: 1601.00007 [astro-ph.HE] (cit. on p. 80).

Mandel, I. and B. Müller (2020), Simple recipes for compact remnant masses and natal kicks, arXiv e-prints, arXiv:2006.08360 arXiv:2006.08360, arXiv: 2006.08360 [astro-ph.HE] (cit. on p. 30).

Mapelli, M. (2020), Binary black hole mergers: formation and populations, Frontiers in Astronomy and Space Sciences 7, 38 38, arXiv: 2105.12455 [astro-ph.HE] (cit. on pp. 3, 22, 56).

Mapelli, M. and N. Giacobbo (2018), The cosmic merger rate of neutron stars and black holes, MNRAS 479 4391, arXiv: 1806.04866 [astro-ph.HE] (cit. on p. 16).
Mapelli, M., N. Giacobbo, E. Ripamonti and M. Spera (2017), The cosmic merger rate of stellar black hole binaries from the Illustris simulation, MNRAS 472 2422, arXiv: 1708.05722 [astro-ph.GA] (cit. on pp. 56, 57).
Marchant, P. (2017), The impact of tides and mass transfer on the evolution of metal-poor massive binary stars, PhD thesis
https://astro.uni-bonn.de/~nlanger/thesis/pablo.pdf (cit. on pp. 25, 59, 78).
Marchant, P., N. Langer, P. Podsiadlowski, T. M. Tauris, S. de Mink et al. (2017), Ultra-luminous X-ray sources and neutron-star-black-hole mergers from very massive close binaries at low metallicity, A&A 604, A55 A55, arXiv: 1705.04734 [astro-ph.HE] (cit. on p. 80).
Marchant, P., N. Langer, P. Podsiadlowski, T. M. Tauris and T. J. Moriya (2016), A new route towards merging massive black holes, A&A 588, A50 A50, arXiv: 1601.03718 [astro-ph.SR] (cit. on pp. 25, 47, 80).
Marchant, P., K. M. W. Pappas et al. (2021), The role of mass transfer and common envelope evolution in the formation of merging binary black holes, A&A 650, A107 A107, arXiv: 2103.09243 [astro-ph.SR] (cit. on pp. 56, 57, 78, 79).
Marchant, P., M. Renzo et al. (2019), Pulsational Pair-instability Supernovae in Very Close Binaries, ApJ 882, 36 36, arXiv: 1810.13412 [astro-ph.HE] (cit. on pp. 28, 37, 59).
McBride, V. A., M. J. Coe, I. Negueruela, M. P. E. Schurch and K. E. McGowan (2008), Spectral distribution of Be/X-ray binaries in the Small Magellanic Cloud, MNRAS 388 1198, arXiv: 0805.0008 [astro-ph] (cit. on p. 37).
Mokiem, M. R. et al. (2007), The empirical metallicity dependence of the mass-loss rate of O- and early B-type stars, A&A 473 603, arXiv: 0708.2042 [astro-ph] (cit. on pp. 23, 56).
Nieuwenhuijzen, H. and C. de Jager (1990), Parametrization of stellar rates of mass loss as functions of the fundamental stellar parameters M, L, and R., A&A 231 134 (cit. on p. 25).
Nomoto, K. (1984), Evolution of 8-10 solar mass stars toward electron capture supernovae. I - Formation of electron-degenerate O + NE + MG cores., ApJ 277 791 (cit. on p. 29).
O'Connor, E. and C. D. Ott (2011), Black Hole Formation in Failing Core-Collapse Supernovae, ApJ 730, 70 70, arXiv: 1010.5550 [astro-ph.HE] (cit. on p. 28).
Okazaki, A. T. and I. Negueruela (2001), A natural explanation for periodic X-ray outbursts in Be/X-ray binaries, A&A 377 161, arXiv: astro-ph/0108037 [astro-ph] (cit. on p. 48).
Olejak, A., C. L. Fryer, K. Belczynski and V. Baibhav (2022), The role of supernova convection for the lower mass gap in the isolated binary formation of gravitational wave sources, MNRAS 516 2252, arXiv: 2204.09061 [astro-ph.HE] (cit. on p. 75).
Orosz, J. A., J. E. McClintock, J. P. Aufdenberg et al. (2011), THE MASS OF THE BLACK HOLE IN CYGNUS X-1, The Astrophysical Journal 742 84, url: https://dx.doi.org/10.1088/0004-637X/742/2/84 (cit. on pp. 18, 23, 40, 49, 57, 149).
Orosz, J. A., J. E. McClintock, R. Narayan et al. (2007), A 15.65-solar-mass black hole in an eclipsing binary in the nearby spiral galaxy M 33, Nature 449 872, arXiv: 0710.3165 [astro-ph] (cit. on pp. 18, 49, 57).
Orosz, J. A., D. Steeghs et al. (2009), A NEW DYNAMICAL MODEL FOR THE BLACK HOLE BINARY LMC X-1*, The Astrophysical Journal 697 573, url: https://dx.doi.org/10.1088/0004-637X/697/1/573 (cit. on pp. 18, 23, 40, 49, 57, 149).

Packet, W. (1981), On the spin-up of the mass accreting component in a close binary system, A&A 102 17 (cit. on pp. 12, 25, 59).

Paczynski, B. (1976), "Common Envelope Binaries", Structure and Evolution of Close Binary Systems, ed. by P. Eggleton, S. Mitton and J. Whelan, vol. 73 75 (cit. on p. 12).

Pauli, D. et al. (2023), Spectroscopic and evolutionary analyses of the binary system AzV 14 outline paths toward the WR stage at low metallicity, A&A 673, A40 A40, arXiv: 2303.03989 [astro-ph.SR] (cit. on p. 48).

Pauli, D. (2020), Evolution of Very Massive Binary Systems, master thesis https://astro.uni-bonn.de/~nlanger/thesis/PauliDaniel_Master_Thesis.pdf (cit. on pp. 51, 80).

Paxton, B., L. Bildsten et al. (2011), Modules for Experiments in Stellar Astrophysics (MESA), ApJS 192, 3 3, arXiv: 1009.1622 [astro-ph.SR] (cit. on pp. 16, 23, 59).

Paxton, B., M. Cantiello et al. (2013), Modules for Experiments in Stellar Astrophysics (MESA): Planets, Oscillations, Rotation, and Massive Stars, ApJS 208, 4 4, arXiv: 1301.0319 [astro-ph.SR] (cit. on pp. 16, 23, 52, 59).

Paxton, B., P. Marchant et al. (2015), Modules for Experiments in Stellar Astrophysics (MESA): Binaries, Pulsations, and Explosions, ApJS 220, 15 15, arXiv: 1506.03146 [astro-ph.SR] (cit. on pp. 10, 17, 23, 59).

Petrovic, J., N. Langer and K. A. van der Hucht (2005), Constraining the mass transfer in massive binaries through progenitor evolution models of Wolf-Rayet+O binaries, A&A 435 1013, arXiv: astro-ph/0504242 [astro-ph] (cit. on p. 51).

Pfahl, E., S. Rappaport, P. Podsiadlowski and H. Spruit (2002), A New Class of High-Mass X-Ray Binaries: Implications for Core Collapse and Neutron Star Recoil, ApJ 574 364, arXiv: astro-ph/0109521 [astro-ph] (cit. on pp. 30, 41).

Podsiadlowski, P. et al. (2004), The Effects of Binary Evolution on the Dynamics of Core Collapse and Neutron Star Kicks, ApJ 612 1044, arXiv: astro-ph/0309588 [astro-ph] (cit. on pp. 29, 30, 37, 51).

Poelarends, A. J. T., F. Herwig, N. Langer and A. Heger (2008), The Supernova Channel of Super-AGB Stars, ApJ 675 614, arXiv: 0705.4643 [astro-ph] (cit. on p. 29).

Poelarends, A. J. T., S. Wurtz, J. Tarka, L. Cole Adams and S. T. Hills (2017), Electron Capture Supernovae from Close Binary Systems, ApJ 850, 197 197, arXiv: 1710.11143 [astro-ph.HE] (cit. on pp. 29, 51).

Pols, O. R. (1994), Case A evolution of massive close binaries: formation of contact systems and possible reversal of the supernova order, A&A 290 119 (cit. on p. 32).

Pols, O. R., J. Cote, L. B. F. M. Waters and J. Heise (1991), The formation of Be stars through close binary evolution., A&A 241 419 (cit. on p. 51).

Pols, O. R., K.-P. Schröder, J. R. Hurley, C. A. Tout and P. P. Eggleton (1998), Stellar evolution models for Z = 0.0001 to 0.03, MNRAS 298 525 (cit. on p. 16).

Poutanen, J., G. Lipunova, S. Fabrika, A. G. Butkevich and P. Abolmasov (2007), Supercritically accreting stellar mass black holes as ultraluminous X-ray sources, MNRAS 377 1187, arXiv: astro-ph/0609274 [astro-ph] (cit. on p. 79).

Qin, Y. et al. (2018), The spin of the second-born black hole in coalescing binary black holes, A&A 616, A28 A28, arXiv: 1802.05738 [astro-ph.SR] (cit. on pp. 83, 84).

Quast, M., N. Langer and T. M. Tauris (2019), Mass transfer on a nuclear timescale in models of supergiant and ultra-luminous X-ray binaries, A&A 628, A19 A19, arXiv: 1903.04995 [astro-ph.SR] (cit. on p. 31).

Ramachandran, V. et al. (2022), Phase-resolved spectroscopic analysis of the eclipsing black hole X-ray binary M33 X-7: System properties, accretion, and evolution, A&A 667, A77 A77, arXiv: 2208.07773 [astro-ph.HE] (cit. on pp. 18, 40, 49, 57, 149).
Rappaport, S., F. Verbunt and P. C. Joss (1983), A new technique for calculations of binary stellar evolution application to magnetic braking., ApJ 275 713 (cit. on p. 11).
Rawls, M. L. et al. (2011), Refined Neutron Star Mass Determinations for Six Eclipsing X-Ray Pulsar Binaries, ApJ 730, 25 25, arXiv: 1101.2465 [astro-ph.SR] (cit. on pp. 36, 48, 149).
Reig, P. (2011), Be/X-ray binaries, Ap&SS 332 1, arXiv: 1101.5036 [astro-ph.HE] (cit. on pp. 26, 91).
Rivinius, T., R. Klement et al. (2022), MWC656: A Be+BH or a Be+sdO?, arXiv e-prints, arXiv:2208.12315 arXiv:2208.12315, arXiv: 2208.12315 [astro-ph.SR] (cit. on p. 49).
Rivinius, T., A. C. Carciofi and C. Martayan (2013), Classical Be stars. Rapidly rotating B stars with viscous Keplerian decretion disks, A&A Rev. 21, 69 69, arXiv: 1310.3962 [astro-ph.SR] (cit. on pp. 13, 26, 43).
Rosslowe, C. K. and P. A. Crowther (2015), Spatial distribution of Galactic Wolf-Rayet stars and implications for the global population, MNRAS 447 2322, arXiv: 1412.0699 [astro-ph.SR] (cit. on p. 81).
Rubele, S., L. Girardi et al. (2015), The VMC survey - XIV. First results on the look-back time star formation rate tomography of the Small Magellanic Cloud, MNRAS 449 639, arXiv: 1501.05347 [astro-ph.SR] (cit. on pp. 22, 31, 39, 43, 44, 56, 63, 150).
Rubele, S., G. Pastorelli et al. (2018), The VMC survey - XXXI: The spatially resolved star formation history of the main body of the Small Magellanic Cloud, MNRAS 478 5017, arXiv: 1805.04516 [astro-ph.GA] (cit. on pp. 22, 31, 43, 56, 63).
Sana, H. et al. (2012), Binary Interaction Dominates the Evolution of Massive Stars, Science 337 444, arXiv: 1207.6397 [astro-ph.SR] (cit. on pp. 3, 9, 15, 22, 31, 41, 63, 75).
Sanyal, D., L. Grassitelli, N. Langer and J. M. Bestenlehner (2015), Massive main-sequence stars evolving at the Eddington limit, A&A 580, A20 A20, arXiv: 1506.02997 [astro-ph.SR] (cit. on pp. 26, 52).
Saulson, P. R. (2011), Josh Goldberg and the physical reality of gravitational waves, General Relativity and Gravitation 43 3289 (cit. on p. 2).
Schneider, F. R. N. et al. (2019), Stellar mergers as the origin of magnetic massive stars, Nature 574 211, arXiv: 1910.14058 [astro-ph.SR] (cit. on p. 79).
Schootemeijer, A. and N. Langer (2018), Wolf-Rayet stars in the Small Magellanic Cloud as testbed for massive star evolution, A&A 611, A75 A75, arXiv: 1709.08727 [astro-ph.SR] (cit. on pp. 15, 45, 48, 57, 78, 85).
Schootemeijer, A., N. Langer, N. J. Grin and C. Wang (2019), Constraining mixing in massive stars in the Small Magellanic Cloud, A&A 625, A132 A132, arXiv: 1903.10423 [astro-ph.SR] (cit. on pp. 8, 56, 57, 79).
Schootemeijer, A., N. Langer, D. Lennon et al. (2021), A dearth of young and bright massive stars in the Small Magellanic Cloud, A&A 646, A106 A106, arXiv: 2012.05913 [astro-ph.GA] (cit. on pp. 15, 22, 23, 31, 39, 43–45, 49, 56, 63, 89, 150).
Schootemeijer, A., D. Lennon et al. (2022), A census of OBe stars in nearby metal-poor dwarf galaxies reveals a high fraction of extreme rotators, A&A 667, A100 A100, arXiv: 2209.04943 [astro-ph.GA] (cit. on pp. 23, 45, 47, 56, 150).

Schootemeijer, A., T. Shenar, N. Langer and G. Gräfener (in prep), High-precision radial velocity monitoring shows that truly single Wolf-Rayet stars exist in the Small Magnellanic Cloud, A&A (cit. on pp. 75, 90).

Schürmann, C., N. Langer, X. Xu and C. Wang (2022), The spins of stripped B stars support magnetic internal angular momentum transport, A&A 667, A122 A122, arXiv: 2208.03129 [astro-ph.SR] (cit. on p. 91).

Schürmann, C., N. Langer, X.-T. Xu and D. Lennon (2023), A&A, in prep (cit. on pp. 12, 18, 23, 28, 39, 43, 49–51, 53, 78).

Schwarzschild, M. and R. Härm (1958), Evolution of Very Massive Stars., ApJ 128 348 (cit. on p. 8).

Sen, K., N. Langer et al. (2022), Detailed models of interacting short-period massive binary stars, A&A 659, A98 A98, arXiv: 2111.03329 [astro-ph.SR] (cit. on p. 12).

Sen, K., X.-T. Xu et al. (2021), X-ray emission from BH+O star binaries expected to descend from the observed galactic WR+O binaries, arXiv e-prints, arXiv:2106.01395 arXiv:2106.01395, arXiv: 2106.01395 [astro-ph.SR] (cit. on pp. 15, 23, 51, 81, 84, 107, 112, 114).

Sepinsky, J. F., B. Willems, V. Kalogera and F. A. Rasio (2007), Interacting Binaries with Eccentric Orbits: Secular Orbital Evolution Due to Conservative Mass Transfer, ApJ 667 1170, arXiv: 0706.4312 [astro-ph] (cit. on p. 25).

Shakura, N. I. and R. A. Sunyaev (1973), Reprint of 1973A&A....24..337S. Black holes in binary systems. Observational appearance., A&A 500 33 (cit. on p. 81).

Shao, Y. and X.-D. Li (2014), On the Formation of Be Stars through Binary Interaction, ApJ 796, 37 37, arXiv: 1410.0100 [astro-ph.HE] (cit. on pp. 10, 12, 16, 23, 29, 51, 61, 78).

– (2016), Nonconservative Mass Transfer in Massive Binaries and the Formation of Wolf-Rayet+O Binaries, ApJ 833, 108 108, arXiv: 1610.04307 [astro-ph.SR] (cit. on pp. 51, 78).

– (2019), Population Synthesis of Black Hole Binaries with Normal-star Companions. I. Detached Systems, ApJ 885, 151 151, arXiv: 1909.11328 [astro-ph.SR] (cit. on p. 23).

– (2020), Population Synthesis of Black Hole X-Ray Binaries, ApJ 898 143, url: https://doi.org/10.3847%5C%2F1538-4357%5C%2Faba118 (cit. on pp. 57, 77, 81).

– (2021), Population Synthesis of Black Hole Binaries with Compact Star Companions, ApJ 920, 81 81, arXiv: 2107.03565 [astro-ph.HE] (cit. on pp. 56, 57, 77, 79).

Shapiro, S. L. and A. P. Lightman (1976), Black holes in X-ray binaries: marginal existence and rotation reversals of accretion disks., ApJ 204 555 (cit. on p. 81).

Shapiro, S. L. and S. A. Teukolsky (1986), Black Holes, White Dwarfs and Neutron Stars: The Physics of Compact Objects (cit. on p. 2).

Shenar, T., A. Gilkis, J. S. Vink, H. Sana and A. A. C. Sander (2020), Why binary interaction does not necessarily dominate the formation of Wolf-Rayet stars at low metallicity, A&A 634, A79 A79, arXiv: 2001.04476 [astro-ph.SR] (cit. on pp. 13, 28, 56, 62).

Shenar, T., R. Hainich, H. Todt, A. F. J. Moffat et al. (2018), The shortest-period Wolf-Rayet binary in the Small Magellanic Cloud: Part of a high-order multiple system. Spectral and orbital analysis of SMC AB 6, A&A 616, A103 A103, arXiv: 1805.00952 [astro-ph.SR] (cit. on pp. 35, 45, 47, 56, 57, 100, 148, 152).

Shenar, T., R. Hainich, H. Todt, A. Sander et al. (2016), Wolf-Rayet stars in the Small Magellanic Cloud. II. Analysis of the binaries, A&A 591, A22 A22, arXiv: 1604.01022 [astro-ph.SR] (cit. on pp. 23, 28, 35, 45, 47, 56, 57, 78, 84, 100, 148, 152).

Shenar, T., H. Sana et al. (2022), An X-ray-quiet black hole born with a negligible kick in a massive binary within the Large Magellanic Cloud, Nature Astronomy 6 1085, arXiv: 2207.07675 [astro-ph.HE] (cit. on pp. 23, 40, 49, 57, 149).
Siess, L. and U. Lebreuilly (2018), Case A and B evolution towards electron capture supernova, A&A 614, A99 A99, arXiv: 1807.04008 [astro-ph.SR] (cit. on pp. 29, 51).
Soberman, G. E., E. S. Phinney and E. P. J. van den Heuvel (1997), Stability criteria for mass transfer in binary stellar evolution., A&A 327 620, arXiv: astro-ph/9703016 [astro-ph] (cit. on pp. 12, 50, 60).
Spera, M. et al. (2019), Merging black hole binaries with the SEVN code, MNRAS 485 889, arXiv: 1809.04605 [astro-ph.HE] (cit. on p. 77).
Spruit, H. C. (2002), Dynamo action by differential rotation in a stably stratified stellar interior, A&A 381 923, arXiv: astro-ph/0108207 [astro-ph] (cit. on pp. 6, 25, 83).
Strolger, L.-G. et al. (2004), The Hubble Higher z Supernova Search: Supernovae to z ≈ 1.6 and Constraints on Type Ia Progenitor Models*, The Astrophysical Journal 613 200, url: https://dx.doi.org/10.1086/422901 (cit. on pp. 63, 72).
Sturm, R. et al. (2012), A new super-soft X-ray source in the Small Magellanic Cloud: Discovery of the first Be/white dwarf system in the SMC?, A&A 537, A76 A76, arXiv: 1112.0176 [astro-ph.HE] (cit. on p. 91).
Sukhbold, T., T. Ertl, S. E. Woosley, J. M. Brown and H. .-. Janka (2016), Core-collapse Supernovae from 9 to 120 Solar Masses Based on Neutrino-powered Explosions, ApJ 821, 38 38, arXiv: 1510.04643 [astro-ph.HE] (cit. on p. 28).
Sukhbold, T., S. E. Woosley and A. Heger (2018), A High-resolution Study of Presupernova Core Structure, ApJ 860, 93 93, arXiv: 1710.03243 [astro-ph.HE] (cit. on pp. 28, 45, 59).
Sun, H., B. Zhang and Z. Li (2015), Extragalactic High-energy Transients: Event Rate Densities and Luminosity Functions, ApJ 812, 33 33, arXiv: 1509.01592 [astro-ph.HE] (cit. on p. 83).
Sweet, P. A. (1950), The importance of rotation in stellar evolution, MNRAS 110 548 (cit. on p. 7).
Tauris, T. M., M. Kramer et al. (2017), Formation of Double Neutron Star Systems, ApJ 846, 170 170, arXiv: 1706.09438 [astro-ph.HE] (cit. on p. 30).
Tauris, T. M. and E. P. J. van den Heuvel (2006), "Formation and evolution of compact stellar X-ray sources", Compact stellar X-ray sources, vol. 39 623 (cit. on pp. 25, 60, 62, 91).
The LIGO Scientific Collaboration et al. (2021), GWTC-3: Compact Binary Coalescences Observed by LIGO and Virgo During the Second Part of the Third Observing Run, arXiv e-prints, arXiv:2111.03606 arXiv:2111.03606, arXiv: 2111.03606 [gr-qc] (cit. on p. 22).
Townsend, L. J., M. J. Coe, R. H. D. Corbet and A. B. Hill (2011), On the orbital parameters of Be/X-ray binaries in the Small Magellanic Cloud, MNRAS 416 1556, arXiv: 1106.0194 [astro-ph.HE] (cit. on pp. 38, 149).
Townsend, R. H. D., S. P. Owocki and I. D. Howarth (2004), Be-star rotation: how close to critical?, MNRAS 350 189, arXiv: astro-ph/0312113 [astro-ph] (cit. on pp. 26, 28, 43, 48).
Tutukov, A. V., A. V. Fedorova and A. M. Cherepashchuk (2013), Wolf-Rayet stars with relativistic companions, Astronomy Reports 57 657 (cit. on p. 57).
van den Heuvel, E. P. J. and C. De Loore (1973), The nature of X-ray binaries III. Evolution of massive close binaries with one collapsed component - with a possible application to Cygnus X-3., A&A 25 387 (cit. on pp. 57, 75).

van den Heuvel, E. P. J., S. F. Portegies Zwart and S. E. de Mink (2017a), Forming short-period Wolf-Rayet X-ray binaries and double black holes through stable mass transfer, MNRAS 471 4256, arXiv: 1701.02355 [astro-ph.SR] (cit. on p. 16).
– (2017b), Forming short-period Wolf-Rayet X-ray binaries and double black holes through stable mass transfer, MNRAS 471 4256, arXiv: 1701.02355 [astro-ph.SR] (cit. on pp. 57, 81).
van der Hucht, K. A. (2001), VizieR Online Data Catalog: 7th Catalog of Galactic Wolf-Rayet stars (van der Hucht, 2001), VizieR Online Data Catalog, III/215 III/215 (cit. on p. 81).
– (2006), New Galactic Wolf-Rayet stars, and candidates. An annex to The VIIth Catalogue of Galactic Wolf-Rayet Stars, A&A 458 453, arXiv: astro-ph/0609008 [astro-ph] (cit. on p. 81).
Vanbeveren, D., N. Mennekens, E. P. J. van den Heuvel and J. Van Bever (2020), Evidence from high-mass X-ray binaries that Galactic WR components of WR+O binaries end their life with a supernova explosion, A&A 636, A99 A99, arXiv: 1912.01256 [astro-ph.SR] (cit. on pp. 15, 19, 20, 81, 87, 88, 90).
Veledina, A. et al. (2023), Astronomical puzzle Cyg X-3 is a hidden Galactic ultraluminous X-ray source, arXiv e-prints, arXiv:2303.01174 arXiv:2303.01174, arXiv: 2303.01174 [astro-ph.HE] (cit. on p. 72).
Verbunt, F. and C. Zwaan (1981), Magnetic braking in low-mass X-ray binaries., A&A 100 L7 (cit. on p. 11).
Verbunt, F., A. Igoshev and E. Cator (2017), The observed velocity distribution of young pulsars, A&A 608, A57 A57, arXiv: 1708.08281 [astro-ph.HE] (cit. on p. 41).
Vigna-Gómez, A. et al. (2018), On the formation history of Galactic double neutron stars, MNRAS 481 4009, arXiv: 1805.07974 [astro-ph.SR] (cit. on p. 41).
Vinciguerra, S. et al. (2020), Be X-ray binaries in the SMC as indicators of mass-transfer efficiency, MNRAS 498 4705, arXiv: 2003.00195 [astro-ph.HE] (cit. on pp. 12, 29, 50, 51, 78).
Vink, J. S., A. de Koter and H. J. G. L. M. Lamers (1999), On the nature of the bi-stability jump in the winds of early-type supergiants, A&A 350 181, arXiv: astro-ph/9908196 [astro-ph] (cit. on p. 25).
– (2000), New theoretical mass-loss rates of O and B stars, A&A 362 295, arXiv: astro-ph/0008183 [astro-ph] (cit. on p. 25).
Vink, J. S., A. de Koter and H. J. G. L. M. Lamers (2001), Mass-loss predictions for O and B stars as a function of metallicity, A&A 369 574, arXiv: astro-ph/0101509 [astro-ph] (cit. on p. 25).
Wang, C., K. Jia and X.-D. Li (2016), The binding energy parameter for common envelope evolution, Research in Astronomy and Astrophysics 16, 126 126 (cit. on p. 79).
Wang, C., N. Langer et al. (2020), Effects of Close Binary Evolution on the Main-sequence Morphology of Young Star Clusters, ApJ 888, L12 L12, arXiv: 1912.07294 [astro-ph.SR] (cit. on pp. 17, 23, 26, 59, 78, 79, 84).
Webbink, R. F. (1984), Double white dwarfs as progenitors of R Coronae Borealis stars and type I supernovae., ApJ 277 355 (cit. on pp. 13, 61).
Weisberg, J. M., D. J. Nice and J. H. Taylor (2010), Timing Measurements of the Relativistic Binary Pulsar PSR B1913+16, ApJ 722 1030, arXiv: 1011.0718 [astro-ph.GA] (cit. on p. 10).
Wellstein, S., N. Langer and H. Braun (2001), Formation of contact in massive close binaries, A&A 369 939, arXiv: astro-ph/0102244 [astro-ph] (cit. on pp. 23, 32).
Xu, X.-T., C. Schürmann et al. (2023), Populations of evolved massive binary stars in the Small Magellanic Cloud I: Predictions from detailed binary evolution models, A&A, in prep (cit. on pp. 57, 59, 60, 78, 81).

Xu, X.-T. and X.-D. Li (2019), On the Bimodal Spin-period Distribution of Be/X-Ray Pulsars, ApJ 872, 102 102, arXiv: 1901.04707 [astro-ph.HE] (cit. on p. 48).
Zahn, J. .-. (1977), Tidal friction in close binary systems., A&A 57 383 (cit. on p. 11).
Zdziarski, A. A., J. Mikolajewska and K. Belczynski (2013), Cyg X-3: a low-mass black hole or a neutron star., MNRAS 429 L104, arXiv: 1208.5455 [astro-ph.HE] (cit. on pp. 56, 57, 72, 73).

List of Figures

List of Tables

Acknowledgements

It took me four years to finally finish this thesis, which was not an easy journey, especially with the covid pandemic adding more challenges and uncertainties. I am quite happy with the outcome. It would have been impossible to achieve this without the support of many people. Here I want to express my sincere gratitude to those who have helped and accompanied me along the way.

First of all, I would like to deeply thank my supervisor Prof. Dr. Norbert Langer for giving me the opportunity to study in Bonn and providing all the necessary support through my doctoral work. His expertise in massive stars significantly broadened my scientific horizon. He is passionate, open-minded, and also strict in science, which taught me how to be a good scientist. Whenever I faced difficulties or felt unproductive, he was always patient and willing to provide help. I benefited a lot from our weekly meetings, and I hope to keep in touch and keep learning from him in the future. Thank you, Norbert!

Then I would like to thank my collaborators and our group members, Abel, Andrea, my officemate Ben, Chen, Christoph, Daniel, Götz, Harim, John, and Koushik. I learned a lot from the discussion with them, and they gave me many insightful comments on my work. In particular, I want to acknowledge Abel, Christoph, and Koushik for their close cooperation with me and Chen for teaching me a lot about the MESA code. The model grid computed by her forms the foundation of my research project. To Ben: I am happy to have an officemate like you. Hope to see you again in the future. I want to mention our lunch group as well. Even though I skipped many times or did not talk much, I really enjoyed our lunch time. I would also like to thank Elisabeth. Thanks to her help, I never had any problems with the paperwork.

Finally, I would like to thank my friends Gao-Yuan Zhang and Kenny Tse, who supported me a lot during the Covid-19 period. We met frequently through Skype and the Gathertown website, which helped me overcome my little mental issue during the Covid quarantine. I also received plenty of support from my family in China, whom I miss dearly. I am sure that there are people who supported me in ways that I cannot remember. I want to express my deepest gratitude to all the people who helped me during these years.

List of Publications

Published in refereed journals

- Langer, N., Schürmann, C., ...Xu, X.-T., 2020, A&A, 638, 39:
  "Properties of OB star-black hole systems derived from detailed binary evolution models"
  DOI: 10.1051/0004-6361/201937375

- Sen, K., Xu, X.-T., Langer, N., et al., 2021, A&A, 652, A138:
  "X-ray emission from BH+O star binaries expected to descend from the observed galactic WR+O binaries"
  DOI: 10.1051/0004-6361/202141214

- Schürmann, C., Langer, N., Xu, X.-T., Wang, C., 2022, A&A, 667, A122:
  "The spins of stripped B stars support magnetic internal angular momentum transport"
  DOI: 10.1051/0004-6361/202244153

- Sen, K., Langer, N., ...Xu, X.-T., 2022, A&A, 659, A98:
  "Detailed models of interacting short-period massive binary stars"
  DOI: 10.1051/0004-6361/202142574

- Wang, C., Langer, N., ...Xu, X.-T., et al., 2022, Nature Astronomy, 6, 480:
  "Stellar mergers as the origin of the blue main-sequence band in young star clusters"
  DOI: 10.1038/s41550-021-01597-5

- Antoniadis, J., Aguilera-Dena, D. R., ... Xu, X.-T., 2022, A&A, 657, L6:
  "Explodability fluctuations of massive stellar cores enable asymmetric compact object mergers like GW190814"
  DOI: 10.1051/0004-6361/202142322